NUREG/CR-0309
ORNL/NUREG-38

Test of 6-in.-thick Pressure Vessels. Series 3: Intermediate Test Vessel V-7B

R. H. Bryan
P. P. Holz
J. G. Merkle
G. C. Smith
J. E. Smith
W. J. Stelzman

Prepared for the U.S. Nuclear Regulatory Commission
Office of Nuclear Regulatory Research
Under Interagency Agreements DOE 40-551-75 and 40-552-75

OAK RIDGE NATIONAL LABORATORY

OPERATED BY UNION CARBIDE CORPORATION · FOR THE DEPARTMENT OF ENERGY

Printed in the United States of America. Available from
National Technical Information Service
U.S. Department of Commerce
5285 Port Royal Road, Springfield, Virginia 22161

NUREG/CR-0309
ORNL/NUREG-38
Dist. Category R5

Contract No. W-7405-eng-26

Engineering Technology Division

Test of 6-in.-thick Pressure Vessels. Series 3: Intermediate Test Vessel V-7B

R. H. Bryan *G. C. Smith*
P. P. Holz *J. E. Smith*
J. G. Merkle *W. J. Stelzman*

Manuscript Completed – October 6, 1978
Date Published – October 1978

Prepared for the
U.S. Nuclear Regulatory Commission
Office of Nuclear Regulatory Research
Under Interagency Agreements DOE 40-551-75 and 40-552-75

NRC FIN No. B0119

Prepared by the
OAK RIDGE NATIONAL LABORATORY
Oak Ridge, Tennessee 37830
operated by
UNION CARBIDE CORPORATION
for the
DEPARTMENT OF ENERGY

Contents

Foreword

The work reported here was performed mostly at Oak Ridge National Laboratory (ORNL) under sponsorship of the U.S. Nuclear Regulatory Commission's (NRC) Heavy-Section Steel Technology (HSST) Program, which is directed by ORNL. The program is conducted as part of the ORNL Pressure Vessel Technology Program, of which G. D. Whitman is manager. The manager for the NRC is E. K. Lynn.

This report is designated Heavy-Section Steel Technology Program Technical Report No. 51. Prior reports in this series are listed below.

1. S. Yukawa, *Evaluation of Periodic Proof Testing and Warm Prestressing Procedures for Nuclear Reactor Vessels,* HSSTP-TR-1, General Electric Company, Schenectady, N.Y. (July 1, 1969).
2. L. W. Loechel, *The Effect of Section Size on the Transition Temperature in Steel,* MCR-69-189, Martin Marietta Corporation, Denver, Colo. (Nov. 20, 1969).
3. P. N. Randall, *Gross Strain Measure of Fracture Toughness of Steels,* HSSTP-TR-3, TRW Systems Group, Redondo Beach, Calif. (Nov. 1, 1969).
4. C. Visser, S. E. Gabrielse, and W. VanBuren, *A Two-Dimensional Elastic-Plastic Analysis of Fracture Test Specimens,* WCAP-7368, Westinghouse Electric Corporation, PWR Systems Division, Pittsburgh, Pa. (October 1969).
5. T. R. Mager, F. O. Thomas, and W. S. Hazelton, *Evaluation by Linear Elastic Fracture Mechanics of Radiation Damage to Pressure Vessel Steels,* WCAP-7328 (Rev.), Westinghouse Electric Corporation, PWR Systems Division, Pittsburgh, Pa. (October 1969).
6. W. O. Shabbits, W. H. Pryle, and E. T. Wessel, *Heavy Section Fracture Toughness Properties of A533 Grade B Class 1 Steel Plate and Submerged Arc Weldment,* WCAP-7414, Westinghouse Electric Corporation, PWR Systems Division, Pittsburgh, Pa. (December 1969).
7. F. J. Loss, *Dynamic Tear Test Investigations of the Fracture Toughness of Thick-Section Steel,* NRL-7056, U.S. Naval Research Laboratory, Washington, D.C. (May 14, 1970).
8. P. B. Crosley and E. J. Ripling, *Crack Arrest Fracture Toughness of A533 Grade B Class 1 Pressure Vessel Steel,* HSSTP-TR-8, Materials Research Laboratory, Inc., Glenwood, Ill. (March 1970).
9. T. R. Mager, *Post-Irradiation Testing of 2T Compact Tension Specimens,* WCAP-7561, Westinghouse Electric Corporation, PWR Systems Division, Pittsburgh, Pa. (August 1970).
10. T. R. Mager, *Fracture Toughness Characterization Study of A533, Grade B, Class 1 Steel,* WCAP-7578, Westinghouse Electric Corporation, PWR Systems Division, Pittsburgh, Pa. (October 1970).
11. T. R. Mager, *Notch Preparation in Compact Tension Specimens,* WCAP-7579, Westinghouse Electric Corporation, PWR Systems Division, Pittsburgh, Pa. (November 1970).

12. N. Levy and P. V. Marcal, *Three-Dimensional Elastic-Plastic Stress and Strain Analysis for Fracture Mechanics, Phase I: Simple Flawed Specimens,* HSSTP-TR-12, Brown University, Providence, R.I. (December 1970).
13. W. O. Shabbits, *Dynamic Fracture Toughness Properties of Heavy Section A533 Grade B, Class 1 Steel Plate,* WCAP-7623, Westinghouse Electric Corporation, PWR Systems Division, Pittsburgh, Pa. (December 1970).
14. P. N. Randall, *Gross Strain Crack Tolerance of A533-B Steel,* HSSTP-TR-14, TRW Systems Group, Redondo Beach, Calif. (May 1, 1971).
15. H. T. Corten and R. H. Sailors, *Relationship Between Material Fracture Toughness Using Fracture Mechanics and Transition Temperature Tests,* T&AM Report 346, University of Illinois, Urbana, Ill. (Aug. 1, 1971).
16. T. R. Mager and V. J. McLoughlin, *The Effect of an Environment of High Temperature Primary Grade Nuclear Reactor Water on the Fatigue Crack Growth Characteristics of A533 Grade B Class 1 Plate and Weldment Material,* WCAP-7776, Westinghouse Electric Corporation, PWR Systems Division, Pittsburgh, Pa. (October 1971).
17. N. Levy and P. V. Marcal, *Three-Dimensional Elastic-Plastic Stress and Strain Analysis for Fracture Mechanics, Phase II: Improved Modeling,* HSSTP-TR-17, Brown University, Providence, R.I. (November 1971).
18. S. C. Grigory, *Six-inch-thick Flawed Tensile Tests, First Technical Summary Report, Longitudinal Specimens 1 through 7,* HSSTP-TR-18, Southwest Research Institute, San Antonio, Tex. (June 1972).
19. P. N. Randall, *Effects of Strain Gradients on the Gross Strain Crack Tolerance of A533-B Steel,* HSSTP-TR-19, TRW Systems Group, Redondo Beach, Calif. (May 1, 1972).
20. S. C. Grigory, *Tests of Six-inch-thick Flawed Tensile Specimens, Second Technical Summary Report, Transverse Specimens Numbers 8 through 10, Welded Specimens Numbers 11 through 13,* HSSTP-TR-20, Southwest Research Institute, San Antonio, Tex. (June 1972).
21. L. A. James and J. A. Williams, *Heavy-Section Steel Technology Program Technical Report No. 21, The Effect of Temperature and Neutron Irradiation upon the Fatigue-Crack Propagation Behavior of ASTM A533, Grade B, Class 1 Steel,* HEDL-TME-72-132, Hanford Engineering Development Laboratory, Richland, Wash. (September 1972).
22. S. C. Grigory, *Tests of Six-inch-thick Flawed Tensile Specimens, Third Technical Summary Report, Longitudinal Specimens Numbers 14 through 16, Unflawed Specimen Number 17,* HSSTP-TR-22, Southwest Research Institute, San Antonio, Tex. (October 1972).
23. S. C. Grigory, *Tests of Six-inch-thick Flawed Tensile Specimens, Fourth Technical Summary Report, Tests of One-inch-thick Flawed Tensile Specimens for Size Effect Evaluation,* HSSTP-TR-23, Southwest Research Institute, San Antonio, Tex. (June 1973).
24. S. P. Ying and S. C. Grigory, *Tests of Six-inch-thick Tensile Specimens, Fifth Technical Summary Report, Acoustic Emission Monitoring of One-inch and Six-inch-thick Tensile Specimens,* HSSTP-TR-24, Southwest Research Institute, San Antonio, Tex. (November 1972).
25. R. W. Derby et al., *Test of 6-inch-thick Pressure Vessels. Series 1: Intermediate Test Vessels V-1 and V-2,* ORNL-4895 (February 1974).
26. W. J. Stelzman and R. G. Berggren, *Radiation Strengthening and Embrittlement in Heavy Section Plates and Welds,* ORNL-4871 (June 1973).
27. P. B. Crosley and E. J. Ripling, *Crack Arrest in an Increasing K-Field,* HSSTP-TR-27, Materials Research Laboratory, Glenwood, Ill. (January 1973).

28. P. V. Marcal, P. M. Stuart, and R. S. Bettes, *Elastic-Plastic Behavior of a Longitudinal Semi-Elliptical Crack in a Thick Pressure Vessel*, Brown University, Providence, R.I. (June 1973).
29. W. J. Stelzman, Characterization of HSST Plates 01, 02, and 03 (in preparation).
30. D. A. Canonico, Characterization of Heavy Section Weldments in Pressure Vessel Steels (in preparation).
31. J. A. Williams, *The Irradiation and Temperature Dependence of Tensile and Fracture Properties of ASTM A533, Grade B, Class 1 Steel Plate and Weldment*, HEDL-TME 73–75, Hanford Engineering Development Laboratory, Richland, Wash. (August 1973).
32. J. M. Steichen and J. A. Williams, *High Strain Rate Tensile Properties of Irradiated ASTM A533 Grade B Class 1 Pressure Vessel Steel*, HEDL-TME 73–74, Hanford Engineering Development Laboratory, Richland, Wash. (July 1973).
33. P. C. Riccardella and J. L. Swedlow, *A Combined Analytical-Experimental Fracture Study*, WCAP-8224, Westinghouse Electric Corporation, PWR Systems Division, Pittsburgh, Pa. (October 1973).
34. R. J. Podlasek and R. J. Eiber, *Final Report on Investigation of Mode III Crack Extension in Reactor Piping*, Battelle Columbus Laboratories, Columbus, Ohio (May 1974).
35. T. R. Mager et al., *Interim Report on the Effect of Low Frequencies on the Fatigue Crack Growth Characteristics of A533 Grade B Class 1 Plate in an Environment of High-Temperature Primary Grade Nuclear Reactor Water*, WCAP-8256, Westinghouse Electric Corporation, Pittsburgh, Pa. (December 1973).
36. J. A. Williams, *The Irradiated Fracture Toughness of ASTM A533, Grade B, Class 1 Steel Measured with a Four-inch-thick Compact Tension Specimen*, HEDL-TME 75–10, Hanford Engineering Development Laboratory, Richland, Wash. (January 1975).
37. R. H. Bryan et al., *Test of 6-in.-thick Pressure Vessels, Series 2: Intermediate Test Vessels V-3, V-4, and V-6*, ORNL-5059 (November 1975).
38. T. R. Mager, S. E. Yanichko, and L. R. Singer, *Fracture Toughness Characterization of HSST Intermediate Pressure Vessel Material*, WCAP-8456, Westinghouse Electric Corporation, Pittsburgh, Pa. (December 1974).
39. J. G. Merkle, G. D. Whitman, and R. H. Bryan, *An Evaluation of the HSST Program Intermediate Pressure Vessel Tests in Terms of Light-Water Reactor Pressure Vessel Safety*, ORNL/TM-5090 (November 1975).
40. J. G. Merkle et al., *Test of 6-in.-thick Pressure Vessels, Series 3: Intermediate Test Vessel V-7*, ORNL/NUREG-1 (August 1976).
41. J. A. Davidson, L. J. Cheschini, R. P. Shogan, and G. V. Rao, *The Irradiated Dynamic Fracture Toughness of ASTM A533, Grade B, Class 1 Steel Plate and Submerged-Arc Weldment*, WCAP-8775, Westinghouse Electric Corp., Pittsburgh, Pa. (October 1976).
42. R. D. Cheverton, *Pressure Vessel Fracture Studies Pertaining to a PWR LOCA-ECC Thermal Shock: Experiments TSE-1 and TSE-2*, ORNL/NUREG/TM-3 (September 1976).
43. J. G. Merkle et al., *Test of 6-inch-thick Pressure Vessels. Series 4: Intermediate Test Vessels V-5 and V-9*, ORNL/NUREG-7 (August 1977).
44. J. A. Williams, *The Ductile Fracture Toughness of Heavy Section Steel Plate*, Hanford Engineering Development Laboratory, Richland, Wash. (in preparation).
45. R. H. Bryan et al., *Test of 6-in.-thick Pressure Vessels. Series 3: Intermediate Test Vessel V-7A under Sustained Loading*, ORNL/NUREG-9 (February 1978).

46. R. D. Cheverton and S. E. Bolt, *Pressure Vessel Fracture Studies Pertaining to a PWR LOCA-ECC Thermal Shock: Experiments TSE-3 and TSE-4, and Update of TSE-1 and TSE-2 Analysis*, ORNL/NUREG-22 (December 1977).
47. D. A. Canonico, *Significance of Reheat Cracks to the Integrity of Pressure Vessels for Light-Water Reactors*, ORNL/NUREG-15 (July 1977).
48. G. C. Smith and P. P. Holz, *Repair Weld Induced Residual Stresses in Thick-Walled Steel Pressure Vessels*, ORNL/NUREG/TM-153 (in preparation).
49. S. W. Wismer and P. P. Holz, *Half-Bead (Temper) Repair Welding for Heavy-Section Steel Technology Program Vessels*, ORNL/NUREG/TM-177 (June 1978).
50. G. C. Smith, P. P. Holz, and W. J. Stelzman, *Crack Extension and Arrest Tests of Axially Flawed Steel Model Pressure Vessels*, ORNL/NUREG/TM-196 (in preparation).

Test of 6-in.-thick Pressure Vessels. Series 3: Intermediate Test Vessel V-7B*

R. H. Bryan
P. P. Holz
J. G. Merkle
G. C. Smith
J. E. Smith
W. J. Stelzman

Abstract

Intermediate test vessel V-7 was repaired a second time and retested hydrostatically as vessel V-7B. The flaw for this test had the same geometry as that for the first two tests, that is, a sharp outside surface flaw 547 mm long by about 135 mm deep in the 152-mm-thick test cylinder. The V-7B flaw was situated in the heat-affected zone of a half-bead weld repair made according to Section XI of the ASME Boiler and Pressure Vessel Code. The vessel failed as expected by ligament rupture at a pressure of 152 MPa, which is slightly higher than that observed in the two previous tests. The rupture pressure was sustained for a short time, during which the flaw continued to tear slowly. The test demonstrated that the flaw in the weld repair region was as stable as those in the original base metal at the test pressures. The test also demonstrated that the repaired and flawed vessel was capable of carrying more than twice the design load without failure. Pretest analyses and test data are included.

---

*The use of English and SI units is inconsistent in this report. To aid the reader and also for expediency, conversion factors are included on a foldout at the end of the report.

1

Introduction

The Heavy-Section Steel Technology (HSST) program was instituted at the Oak Ridge National Laboratory (ORNL) to accelerate investigations of the thick-section pressure vessels used in light-water nuclear reactors. The program is especially concerned with developing the understanding and information necessary for assessing the influence of flaws on safety and serviceability. Both analytical and experimental methods have been developed for fracture evaluation, and many specimen types and sizes have been tested under a wide range of loading conditions. The importance of the size of test specimens and structures in the proper characterization of behavior has been demonstrated in many parts of the program. The confidence in methods of analysis used in safety evaluations of nuclear vessels depends substantially on a thorough understanding of material behavior and the effects of constraint imposed by thick sections. Consequently, the HSST program has focused its efforts on simulated service tests of thick-walled pressure vessels, which are referred to as intermediate vessel tests. Nine of these tests[1–5] had been conducted prior to the intermediate vessel V-7B test, which is the subject of this report.

If a flaw requiring corrective action were to be found in an operating nuclear pressure vessel, there would be considerable safety and economic implications. One possible corrective action would be an in-situ repair weld, which would presumably involve grinding away material in a region encompassing the flaw and then filling the resulting cavity with weld metal. Relieving thermal stress under these conditions could lead to serious difficulties associated with thermal expansion and warpage and would therefore probably be avoided. Such a departure from normal procedure presents problems relating to residual stresses and material toughness levels that would have to be assessed before a repair could be recommended or approved.

To provide baseline information to aid in an assessment, should such a repair ever have to be seriously considered, three weld repairs were made in HSST test vessels without postrepair stress relief. The first two were made in intermediate test vessel V-7 and were subjected to the V-7A and V-7B test sequences, and the third was made in vessel V-8. The V-7A and V-7B tests were conducted at temperatures associated with upper-shelf material toughnesses, while the V-8 test was planned as a transition temperature test.

An in-situ repair weld in a nuclear pressure vessel would probably be made in accordance with provisions of the ASME Boiler and Pressure Vessel Code. Section XI, Subsubarticle IWB-4420, of the code describes a repair weld procedure that does not require a high-temperature postweld heat treatment. This procedure is premised on the tempering of the heat-affected zone (HAZ) of the base metal by the controlled deposition of weld metal. The procedure includes the requirement for grinding away half of the first layer of weld material in order to facilitate tempering of the HAZ by subsequent weld passes. The procedure is commonly referred to as a "half-bead" or a "temper-bead" repair weld.

The half-bead repair procedure was used to repair the V-7 intermediate test vessel on two separate occasions, the first of which occurred after the initial V-7 test.[3] The failure mode for that test was a slow stable tear through the remaining ligament at the base of the V-7 flaw. A leak developed when the tear penetrated through the vessel wall, and the test was terminated. Since the vessel had remained essentially intact, it was possible to repair the vessel and use it for a retest. The second test of the V-7 vessel, known as the V-7A test,[5] was basically a repetition of the first except that the vessel internal pressure was sustained after the initial indication of a leak. Since the damage to the vessel was again only slight and localized about the flaw, it was possible to repair the vessel a second time in preparation for the V-7B test.

In order to facilitate comparisons, the test temperature and flaw geometry for the V-7B test were made the same as those for the first two tests in the V-7 vessel (i.e., tests V-7 and V-7A). The significant difference between the V-7B test and the other two V-7 tests was that the V-7B flaw was placed in the HAZ of the second half-bead repair weld, while the flaws for the first two tests were located in plate material that had not been exposed to high temperatures after having received the prescribed postweld heat treatment during fabrication.

The test vessel and details relating to the repair weld and the flawing of the vessel are described in Chapter 2, along with the results of pretest material characterization and residual stress assessment. Chapter 3 discusses the test facilities, the data acquisition system, and the test procedures. Chapter 4 describes the pretest fracture analysis and summarizes the test results. Although high residual stresses were measured in the repair weld region, they were not expected to appreciably affect the outcome of the V-7B test. This expectation stemmed from the fact that very high local strains preceded rupture in V-7 and V-7A, while the relevant material toughness values and strengths in V-7B were comparable to those of the base metal in the two earlier tests. Since those tests were accompanied by extensive yielding and stable tearing in the vicinity of the flaw, it was hypothesized that any residual stresses in that region would be rapidly dissipated as yielding developed and therefore would be inconsequential in this test. The fact that the leak pressure for the V-7B test was nearly the same as that for the V-7 and V-7A tests tends to support that hypothesis. Chapter 5 contains the conclusions from this work.

Several organizations participated in this effort. The Advisory Task Group on Weld Repairs of the Pressure Vessel Research Committee reviewed, and provided suggestions for, the welding specification that was used for the V-7B repair. The repair welding was accomplished by the Westinghouse Electric Corporation's Tampa Division (WTD) under subcontract. Two independent acoustic emission systems were used to monitor the V-7B test, one each provided and monitored by the Battelle Northwest Laboratories and by ORNL. The acoustic-emission data are given in Appendices B and C.

References

1. R. W. Derby et al., *Test of 6-inch-thick Pressure Vessels. Series 1: Intermediate Test Vessels V-1 and V-2*, ORNL-4895 (February 1974).

2. R. H. Bryan et al., *Test of 6-inch-thick Pressure Vessels. Series 2: Intermediate Test Vessels V-3, V-4, and V-6*, ORNL-4049 (November 1975).

3. J. G. Merkle et al., *Test of 6-inch-thick Pressure Vessels. Series 3: Intermediate Test Vessel V-7*, ORNL/NUREG-1 (August 1976).

4. J. G. Merkle et al., *Test of 6-inch-thick Pressure Vessels. Series 4: Intermediate Test Vessels V-5 and V-9 with Inside Nozzle Corner Cracks*, ORNL/NUREG-7 (August 1977).

5. R. H. Bryan, J. G. Merkle, and G. C. Smith, *Test of 6-inch-thick Pressure Vessels. Series 3: Intermediate Test Vessel V-7A under Sustained Loading*, ORNL/NUREG-9 (July 1977).

2

Preparation of Vessel

2.1 Description of Vessel

The cylindrical test section of vessel V-7 was fabricated of 152-mm-thick (6-in.) steel plate meeting ASTM A533, grade B, class 1 specifications.[1] The configuration of the vessel for the V-7A test is shown in Fig. 2.1, along with the flaw locations for the V-7 and V-7A tests.

Upon depressurization, the first two tests of the vessel produced residual strains[2] characterized generally by a slight bulging near the flaws. After the V-7A test, a block of material about 490 mm long by 130 mm wide (19.2 by [illegible] in.) containing the flaw was cut from the vessel (Fig. 2.2). The removal of this

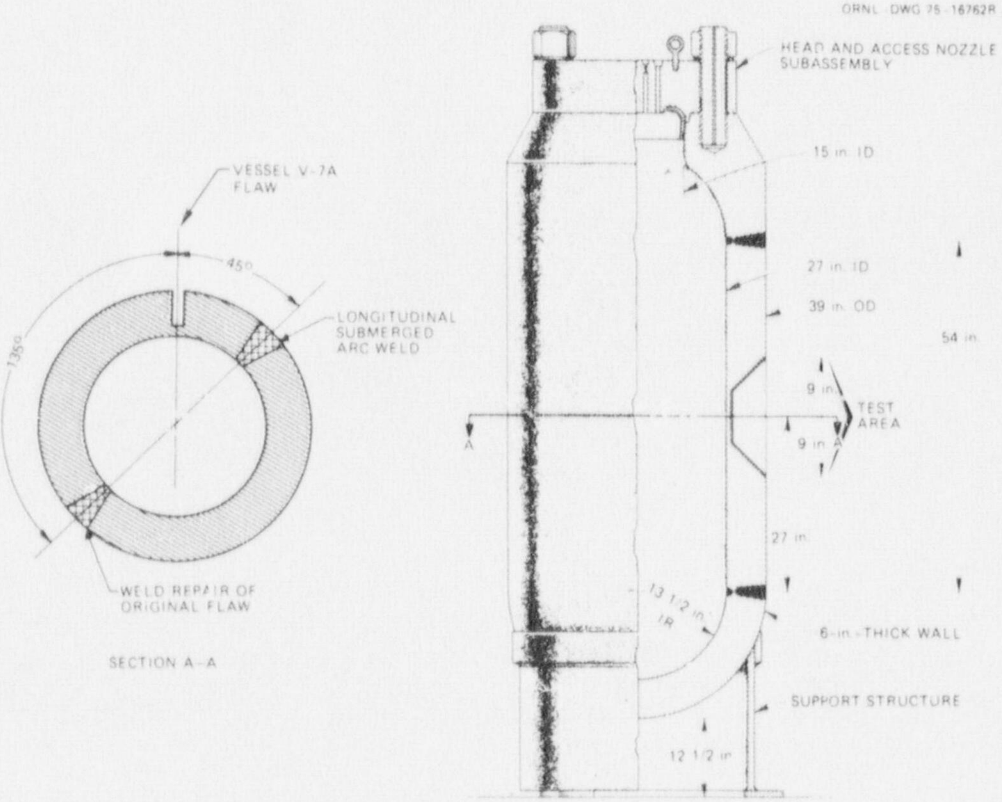

Fig. 2.1. Intermediate test vessel V-7A.

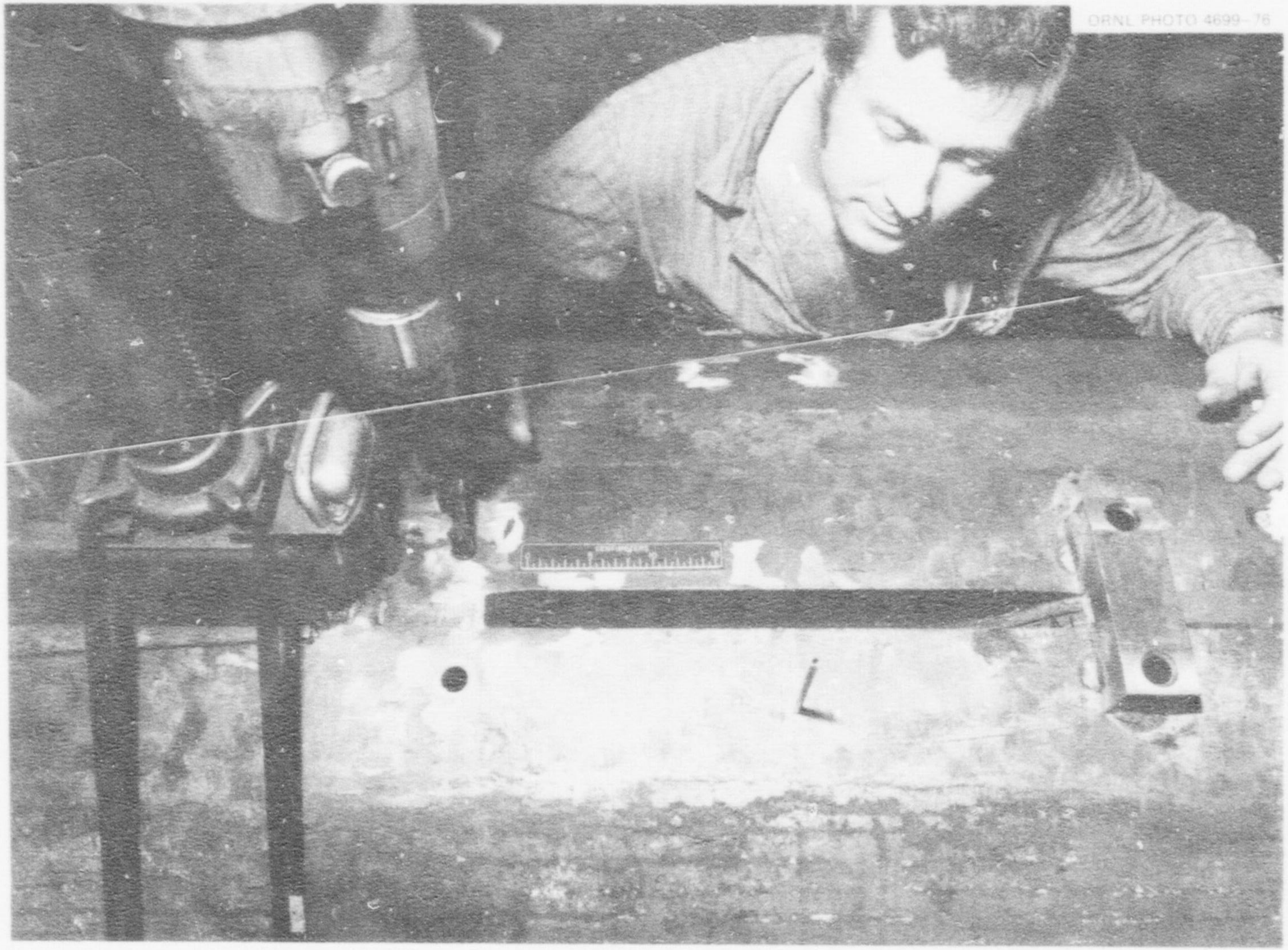

ORNL PHOTO 4699–76

Fig. 2.2. Removal of the flaw region from vessel V-7A after the test. Drilled holes mark the corners of the block flame-cut from the vessel.

material relieved the residual stresses induced by the V-7A test to some degree. Thus, the preparation of the vessel for the V-7B test commenced with probably small residual stresses associated with the previous tests.

The relative locations of the flaws in the V-7 series are shown in Fig. 2.3. The objectives of test V-7B necessitated placing the flaw very near the plane of the V-7A flaw. In this location the flaw would be in the heat-affected zone (HAZ) of the weld required to fill up the cavity formed by removal of the V-7A flaw. The tasks involved in making the repair, introducing a sharp flaw precisely in the desired position, and characterizing the material around the flaw are discussed in the remainder of this chapter.

ORNL DWG 78 2460

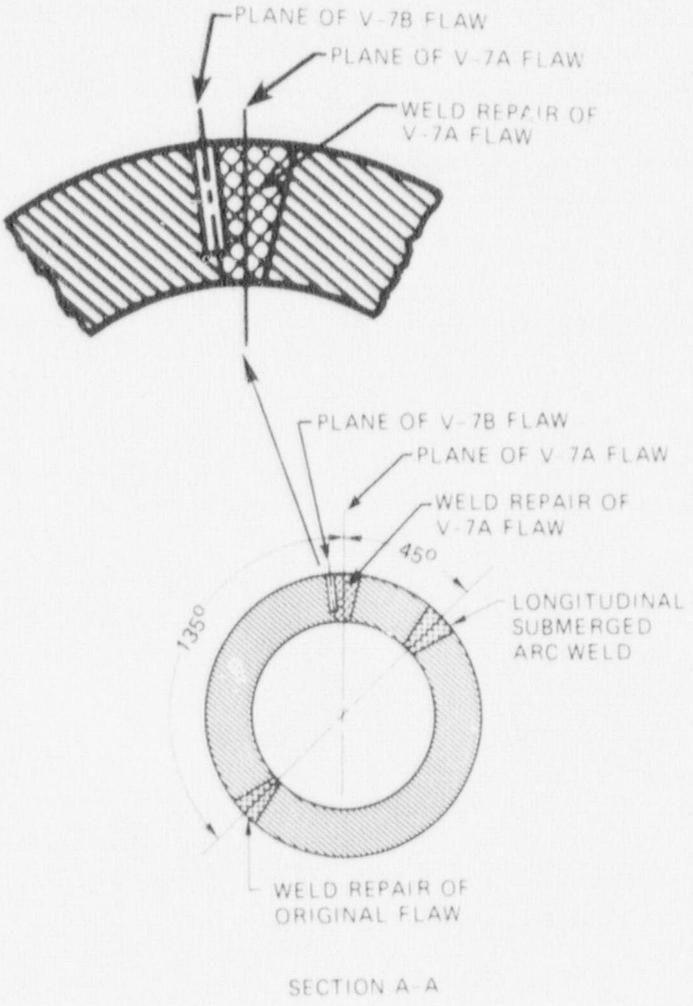

Fig. 2.3. Relative locations of the flaws and weld zones in vessel V-7.

2.2 Repair Weld

The general plan for the second repair of the V-7 vessel was to use the same welding procedure and the same filler metal, insofar as was practicable, as in the first repair of the vessel.[2,3] However, it was desired that the cavity be set in a different position for welding. This change and the plan for placing the flaw in the repair zone necessitated changes in the cavity preparation and in the welding specification.

The longitudinal sides of the cavity were machined in a Union Carbide Corporation Nuclear Division (UCCND) shop in Oak Ridge. This operation removed a layer about 8 mm thick ($^5/_{16}$ in.) from the flame-cut surface and precisely established the longitudinal sides of the cavity along two radial-axial planes 15° apart. These planes were indexed with permanent markings on the vessel so that they could be relocated after the welding was complete. The cavity was enlarged to the final shape for welding by air-arc gouging and grinding by the welding subcontractor. The ends of the cavity were shaped so that the welding could be accomplished with the axis of the cavity vertical with the orientation shown in Fig. 2.4. The finished surface of the cavity, except for the machined sides, was ground to remove at least 6.4 mm ($^1/_4$ in.) of material beyond the gouged surface. This assured removal of the entire HAZ created by the thermal cutting process.

The Westinghouse Tampa Division (WTD) of the Westinghouse Electric Corporation, under subcontract to the UCCND, made the second repair weld in the V-7 vessel and also made and supplied prototypical welds in the 610-mm-long (24-in.) cylindrical prolongation of intermediate test vessel V-8 and a total length of 1.2 m (48 in.) of weld metal test plates. At the same time, WTD made a weld repair in vessel V-8. Details of this work, including welding specifications, are reported in Ref. 4. The prototypical welds were used in the residual stress studies described in Section 2.4 of this report, and portions of the cylinder and weld metal test plates were cut into specimens for the material characterizations discussed in Section 2.3.

Welding was done with covered low-alloy steel electrodes conforming to Specification SFA-5.5, AWS Classification E8018-C3, of Section II of the ASME Boiler and Pressure Vessel Code. Vessel and prolongation cavities were filled in accordance with the sequence prescribed by Section XI, Subsubarticle IWB-4420, for the half-bead weld repair without postweld heat treatment at high temperature. During the 408 hr of continuous welding, the repair zone was maintained within the specified preheat range of 177 to 260°C (350 to 500°F), after which the temperature was raised to and maintained within the postweld heat treatment range of 232 to 288°C (450 to 550°F) for 4 hr.

After the cavity was filled and the backing plates were removed, a region of porosity at the inside surface of the vessel at the 112.5° corner of the cavity (see Fig. 2.4) was found and repaired. The repaired zone was about 127 mm wide (5 in.), 25 mm high (1 in.), and 22 mm deep ($^7/_8$ in.) The weldment was inspected ultrasonically and radiographically after all welding was completed and the vessel had been at ambient temperature for at least 48 hr. No indications of imperfections of rejectable magnitude were found, although several regions of small porosity were found and studied intensively.

The report of Wismer and Holz[4] includes general observations and recommendations regarding practical applications of the half-bead procedure to nuclear vessels in service. The principal conclusion drawn from use of this procedure on HSST vessels is that it has produced acceptable repairs but is difficult to execute in deep cavities. Consequently, modifications to the procedure that would eliminate some of the slow and tedious work, such as grinding the first butter layer, are recommended.

2.3 Materials Investigation

The properties of the A533, grade B, class 1 steel used for the cylindrical section of vessel V-7 were reported previously.[2,5] This section presents new data that characterize the V-7B repair weld. The material used in this characterization was obtained from the prototypical weldment in the V-8 prolongation and a qualification weldment (weld metal test plate) in HSST plate 01MS. Two diametrically opposed weldments were made in the V-8 prolongation, one of which was the V-7B prototype. The welds used in this investigation were made using the same lots of electrodes, welding procedures, and postweld heat treatments that were used in the actual vessel repair. The completed weldments were returned to ORNL for sectioning and study. The prolongation was sawed into two cylinders, and the part of the weldment used in

ORNL DWG 78 16487

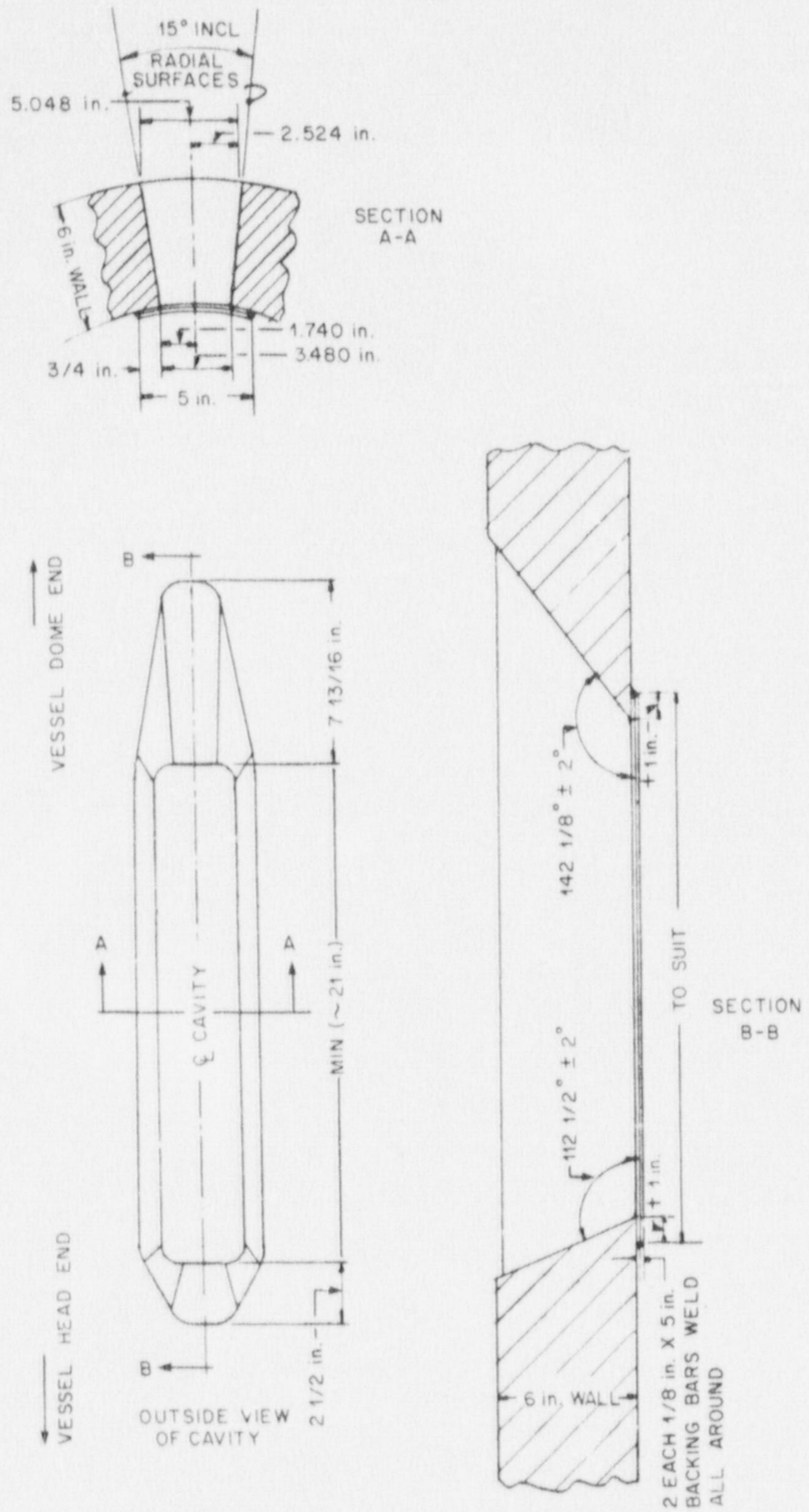

Fig. 2.4. Design of the V-7B weld repair cavity in vessel V-7.

the characterization (part of V8P1C) was removed as shown in Figs. 2.5 and 2.6. The V-7B prototypical weld and the qualification weld (identified as 4W in this report) were then sectioned into parts transverse to the long axis of the weld, as shown in Figs. 2.6 through 2.8, to obtain metallographic and specimen sections.

One metallurgical section from each weldment was then surface ground and chemically etched to bring out the HAZ and the weld bead pattern. Cross sections of the V-7B prototypical weldment at the ramp portion of the weld cavity and the qualification weld are shown in Figs. 2.9 and 2.10, respectively. The dark etchant band (HAZ) abutting the weld metal and the weld bead pattern are clearly visible.

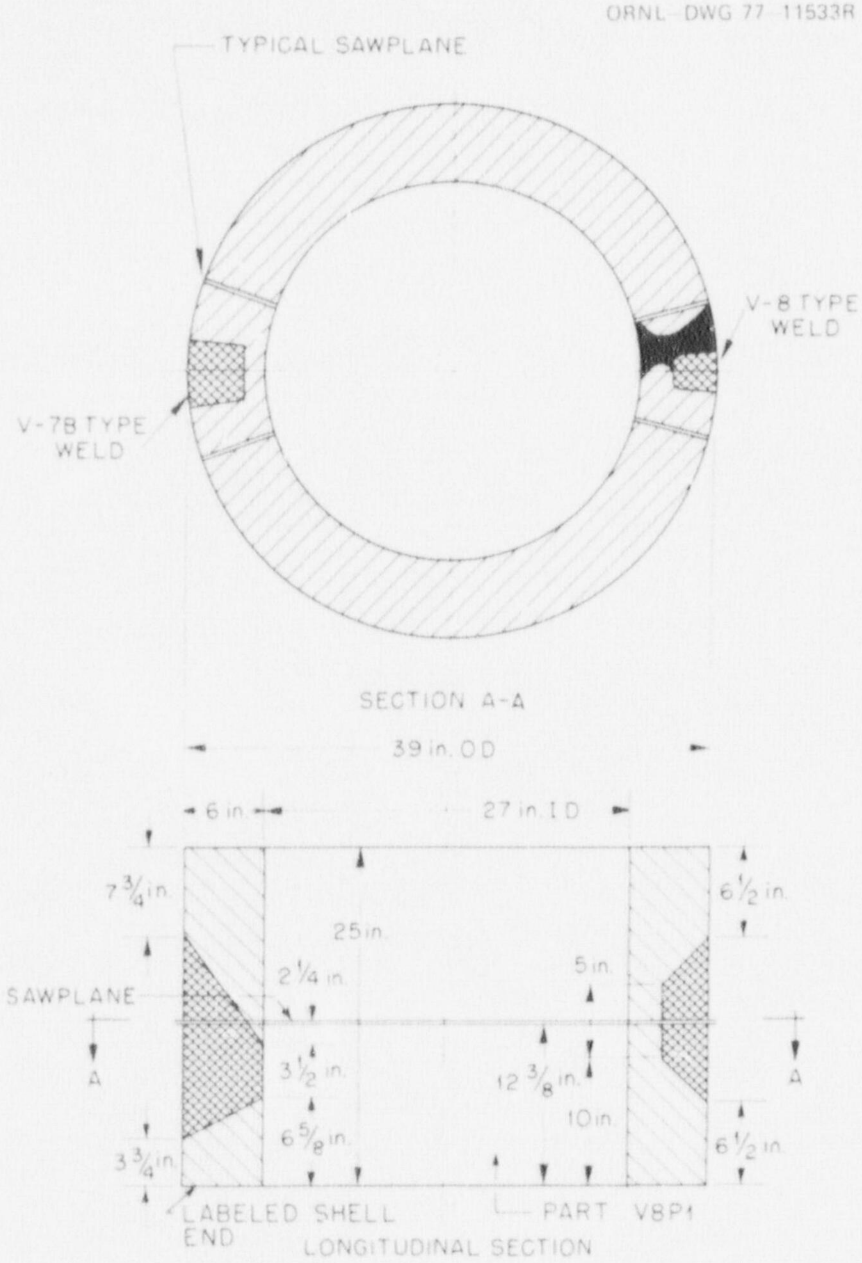

Fig. 2.5. Cutting plan for the V-8 prolongation.

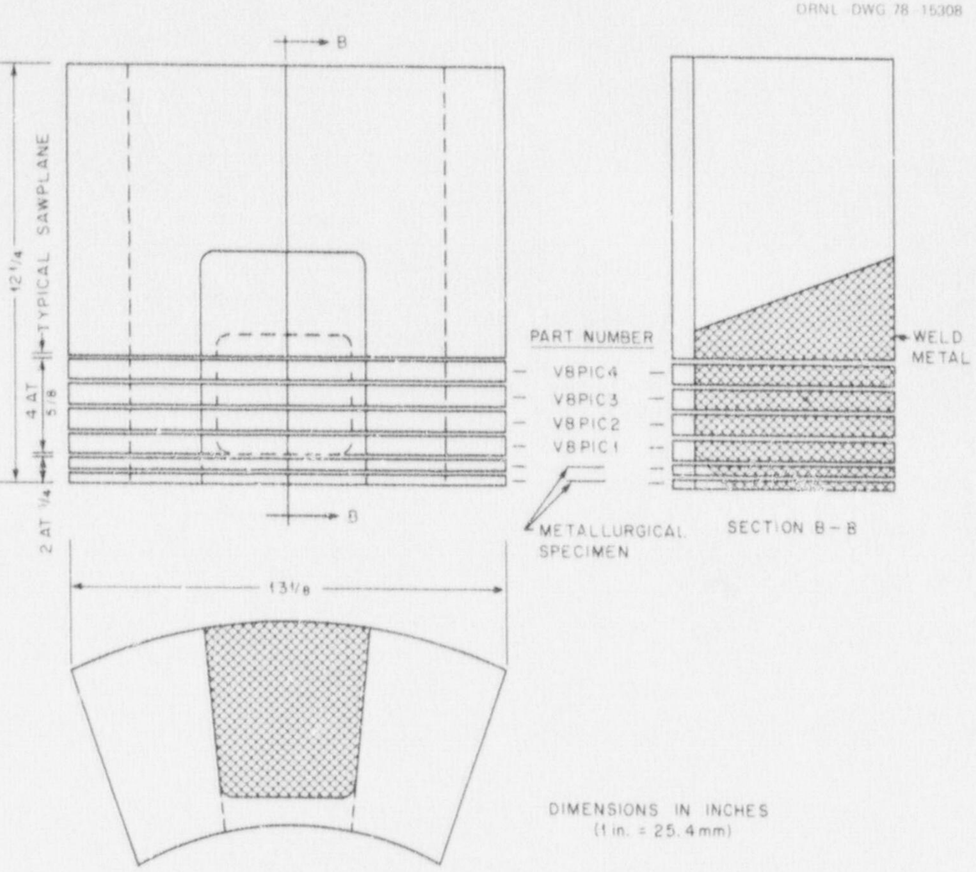

Fig. 2.6. Cutting plan for part V8P1C of the V-7B prototypical repair weldment.

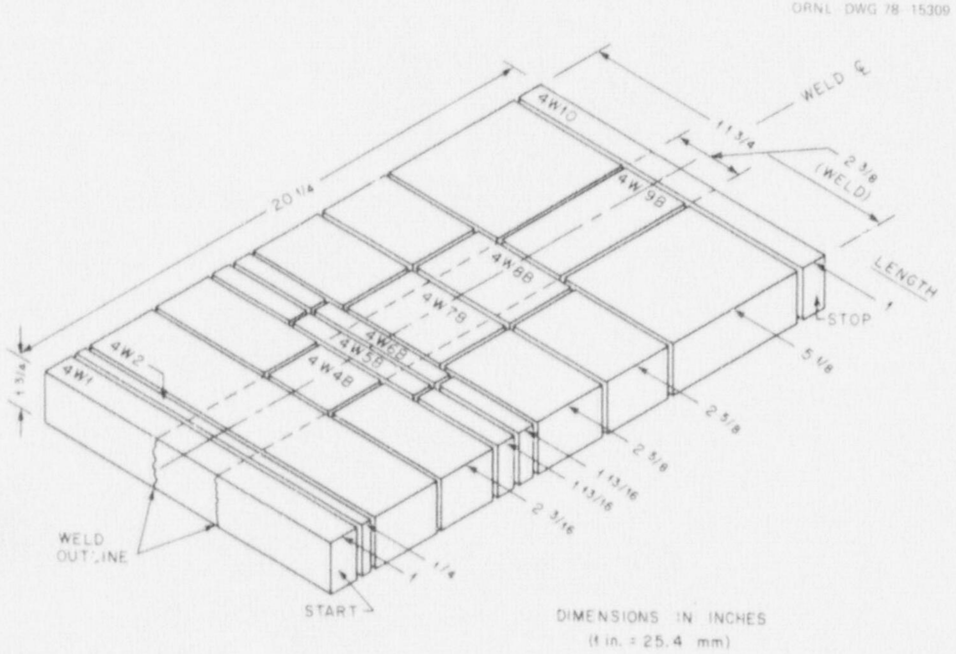

Fig. 2.7. Cutting plan for qualification weldment 4W (plate 01MS-C).

ORNL DWG 78 15310

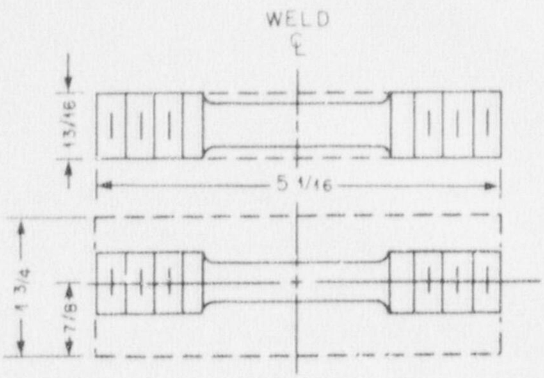

(a) TYPICAL LAYOUT OF PARTS 4W5B AND 4W6B

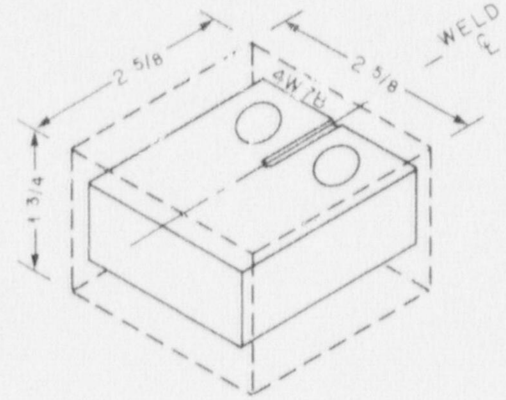

(b) TYPICAL LAYOUT OF PARTS 4W7B AND 4W8B

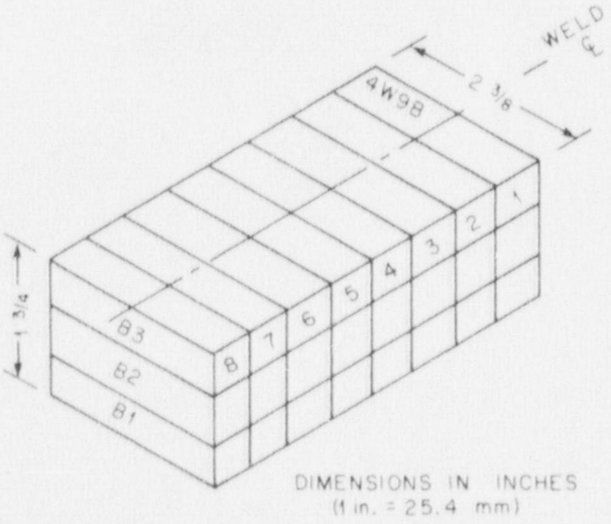

(c) TYPICAL LAYOUT OF PARTS 4W9B AND 4W4B

Fig. 2.8. Cutting plan for specimens from qualification weldment 4W.

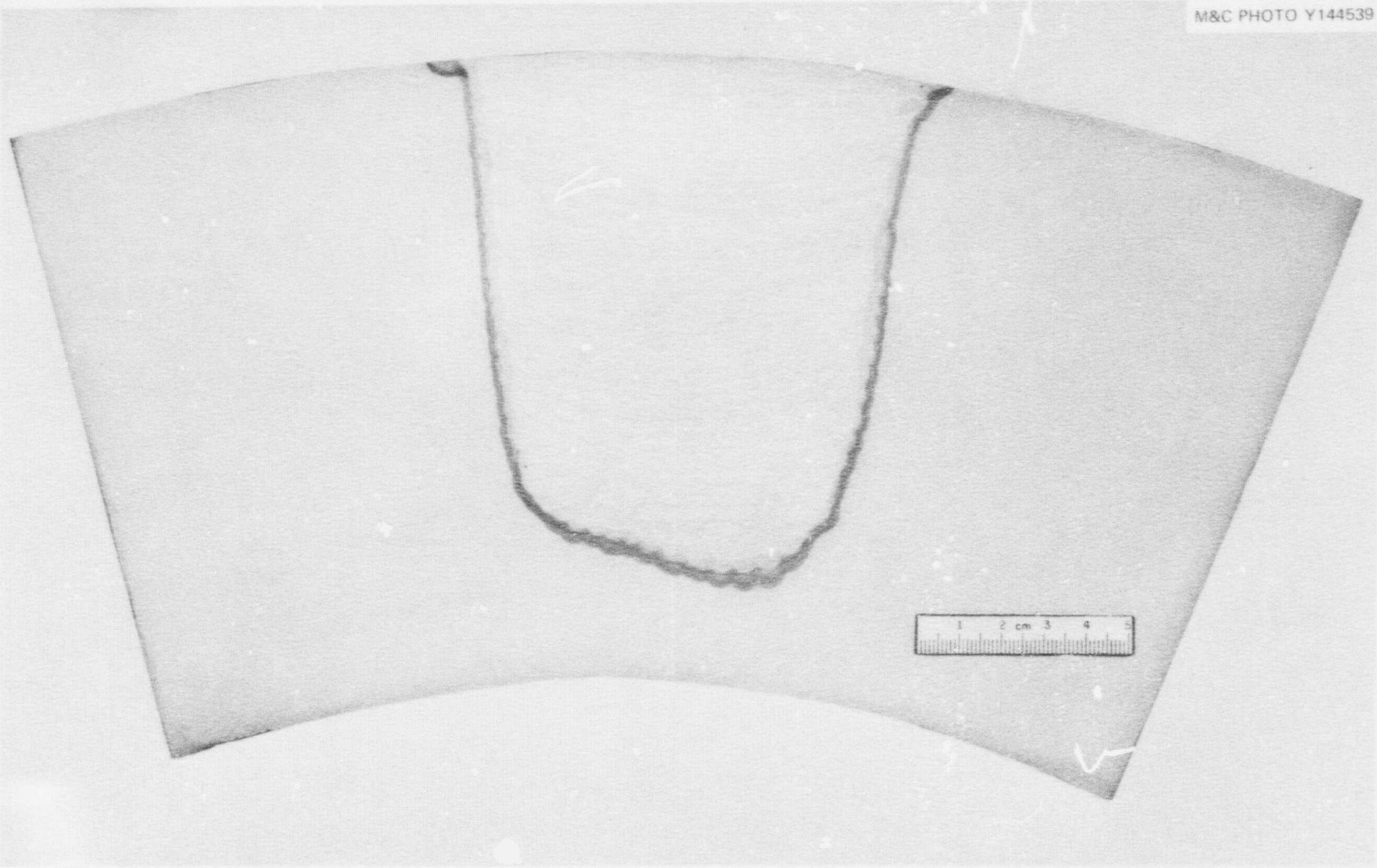

M&C PHOTO Y144539

Fig. 2.9. Cross section of the prototypical half-bead weld repair for vessel V-7B. The sides of the cavity in this piece are more irregular than in the vessel because the V-7B cavity was not machined.

M&C PHOTO Y144977

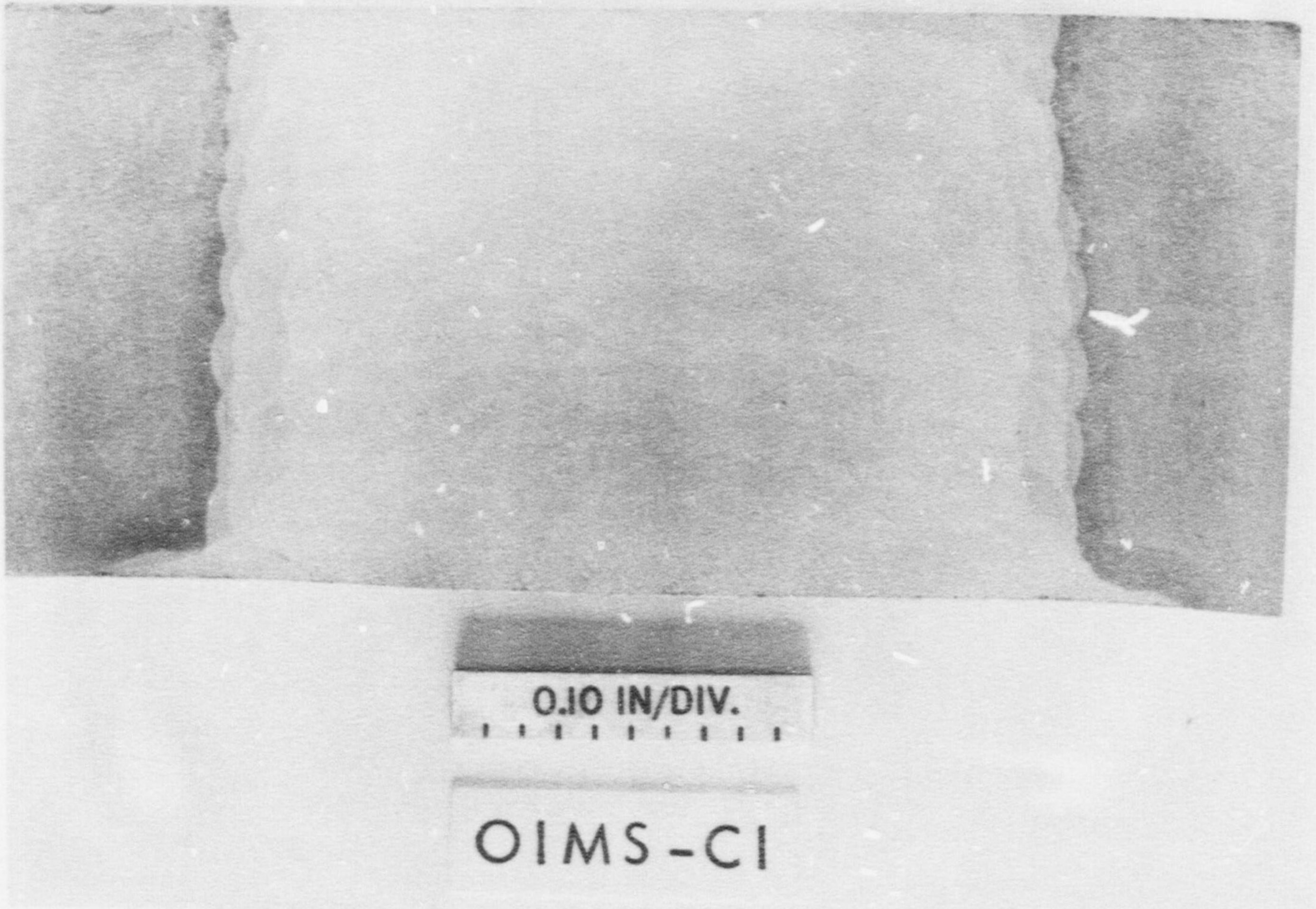

Fig. 2.10. Cross section of the half-bead qualification weld 4W in test plate 01MS-C.

The plates from which the V-7B weldment test specimens were taken were then surface ground to Charpy specimen thickness (10 mm) and chemically etched to locate the HAZ on both sides of the weld. A typical etched plate is shown in Fig. 2.11. After the HAZ had been located, the specimen positions were indicated directly on the plates and numbered, and the specimens were sawed out and machined to size. The specimen layouts are shown in Figs. 2.12 through 2.15. The sections from the qualification weldment, 4W, were machined into specimens. A correlation between the specimen number and its location in the original weldment is presented in Table 2.1.

Table 2.1. Qualification weldment 4W specimen and part number schedule

Specimen numbers	Part	Layer and[a] location
4W1–4W8	4W9B	B1-1–B1-8
4W9–4W12	4W4B	B1-1–B1-4
4W13–4W20	4W9B	B2-1–B2-8
4W21–4W24	4W4B	B2-1–B2-4
4W25–4W32	4W9B	B3-1–B3-8
4W33–4W36	4W4B	B3-1–B3-4
4W37	4W5B	
4W38	4W6B	
4W39	4W7B	
4W40	4W8B	

[a] See Figs. 2.7 and 2.8.

2.3.1 Tensile properties

Tensile properties of the prototypical and the qualification weldments were obtained with a subsize tensile specimen ($L/D = 7$) having a 31.7-mm gage length (1.25 in.) and a 4.50-mm gage diameter (0.177 in.). These specimens were tested at a strain rate of 0.016/min. In addition, standard 12.83-mm-gage-diam (0.505-in.) by 50-mm-gage-length (2.0-in.) tensile specimens with threaded ends conforming to ASTM A 370-74 (Ref. 6) were tested. These tests allowed a correlation between the tensile results obtained with two different specimen cross-sectional areas. The 12.83-mm-diam specimens were tested at a strain rate of 0.025/min. All the specimens were machined with the long axis transverse to the direction of welding. The weld metal specimens were taken from the center of the qualification weld (4W), and the tensile specimens used to determine the strength of the HAZ were removed from the prototypical weld (V-7B). The HAZ was located at the center of the gage length; the gage length contained base metal, the HAZ, and weld metal.

The tensile results from the V-7B prototypical and the qualification welds are presented in Table 2.2. The tensile results from the qualification weld are plotted in Fig. 2.16. There is good agreement between results from the 4.50- and 12.83-mm-gage-diam specimens from the qualification weld metal at room temperature. The tensile properties from the prototypical weldment were obtained with 4.50-mm-gage-diam specimens at 93.3°C (200°F) (the V-7B test temperature was 87°C). There is good agreement between the two weldments at 93.3°C.

2.3.2 Charpy V-notch impact properties

Charpy V-notch impact (C_V) tests were performed on the qualification weld metal (4W) using WL-oriented specimens (long axis of the specimen transverse to the major welding direction and parallel to

Fig. 2.11. Cross section of the prototypical half-bead weld repair to be used in intermediate test vessel V-7B.

ORNL DWG 78 15311

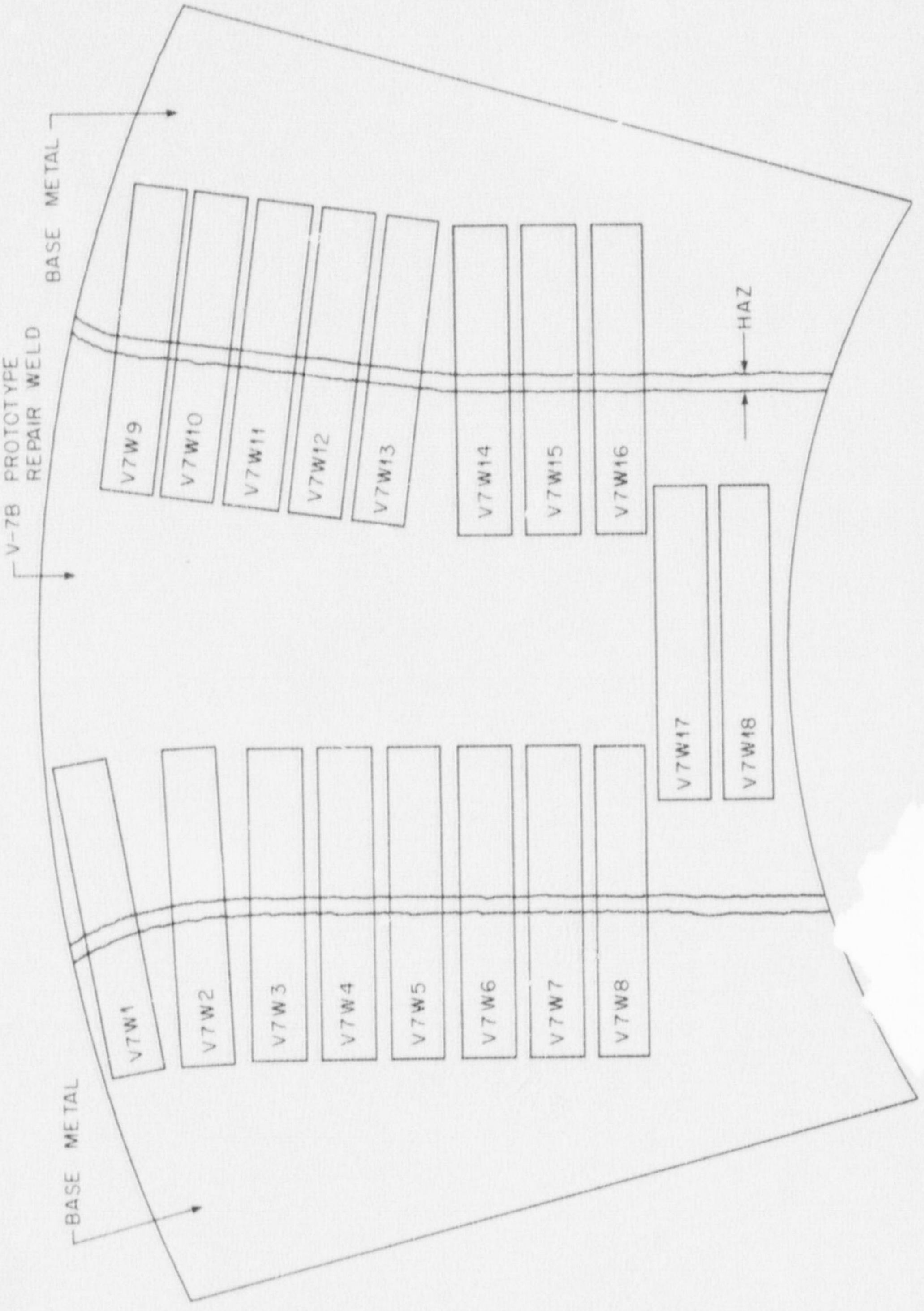

[illegible]g. 2.12. Specimen locations in part V8P1C1.

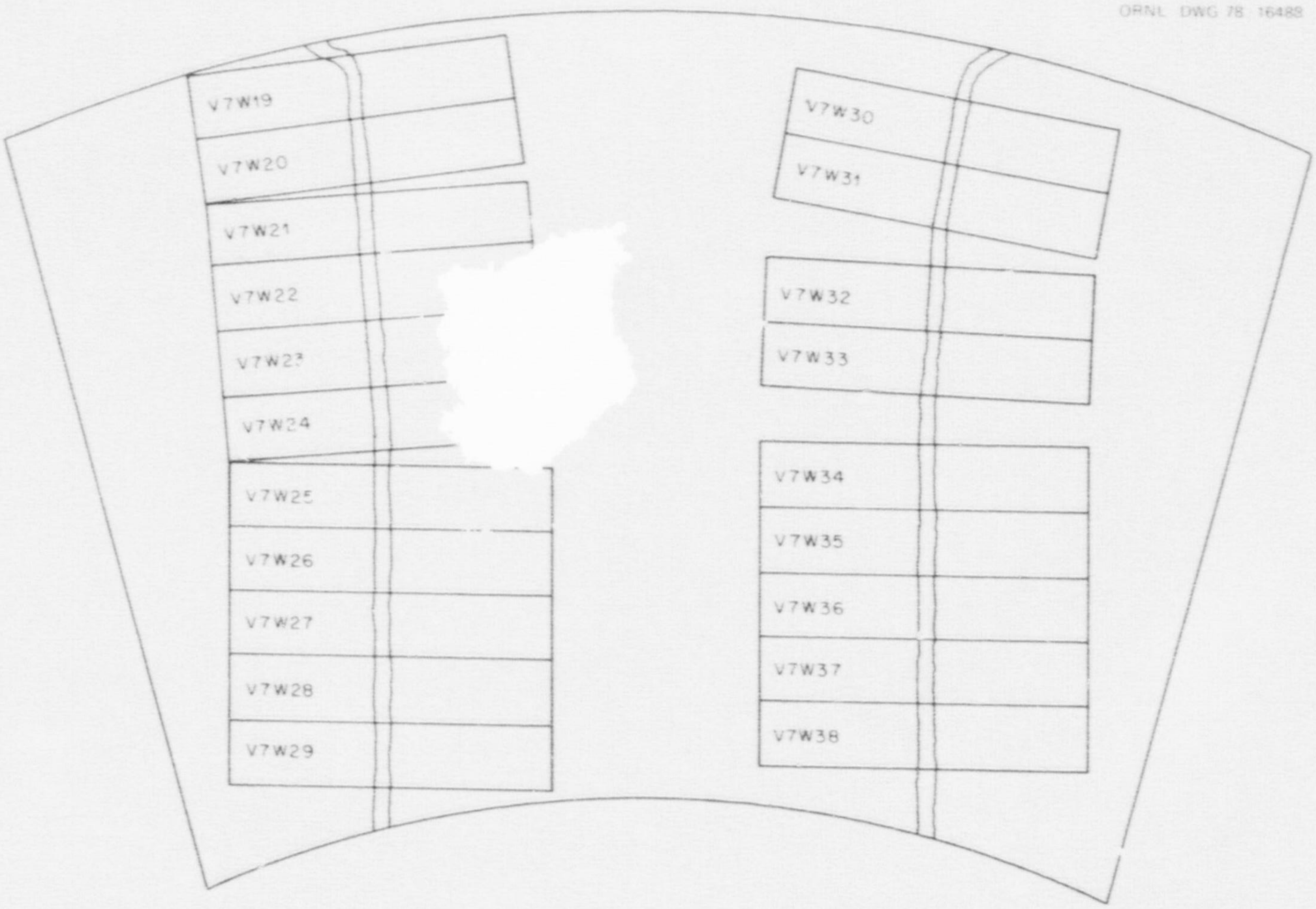

Fig. 2.13. Specimen locations in part V8P1C2.

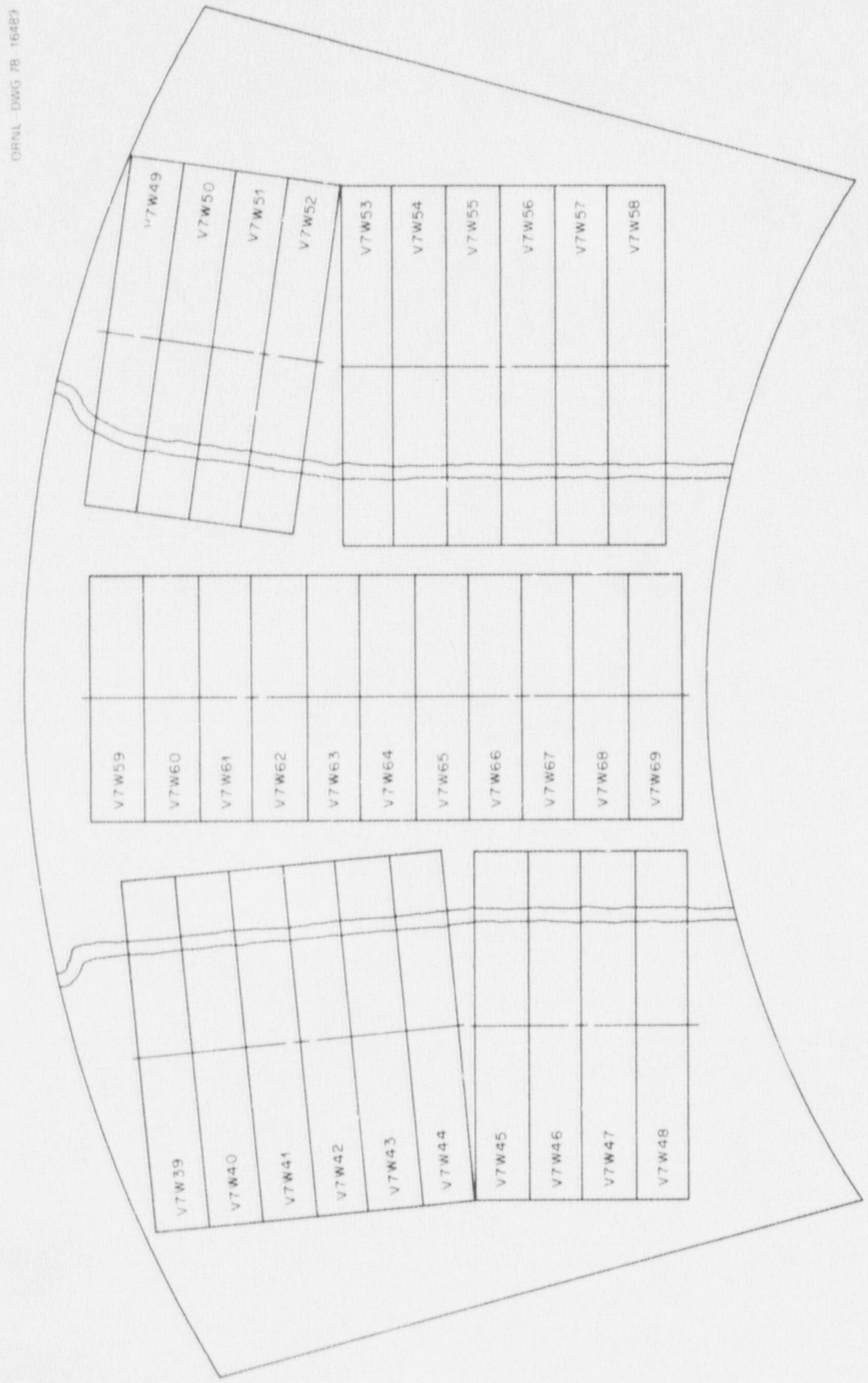

Fig. 2.14. Specimen locations in part V8P1C3.

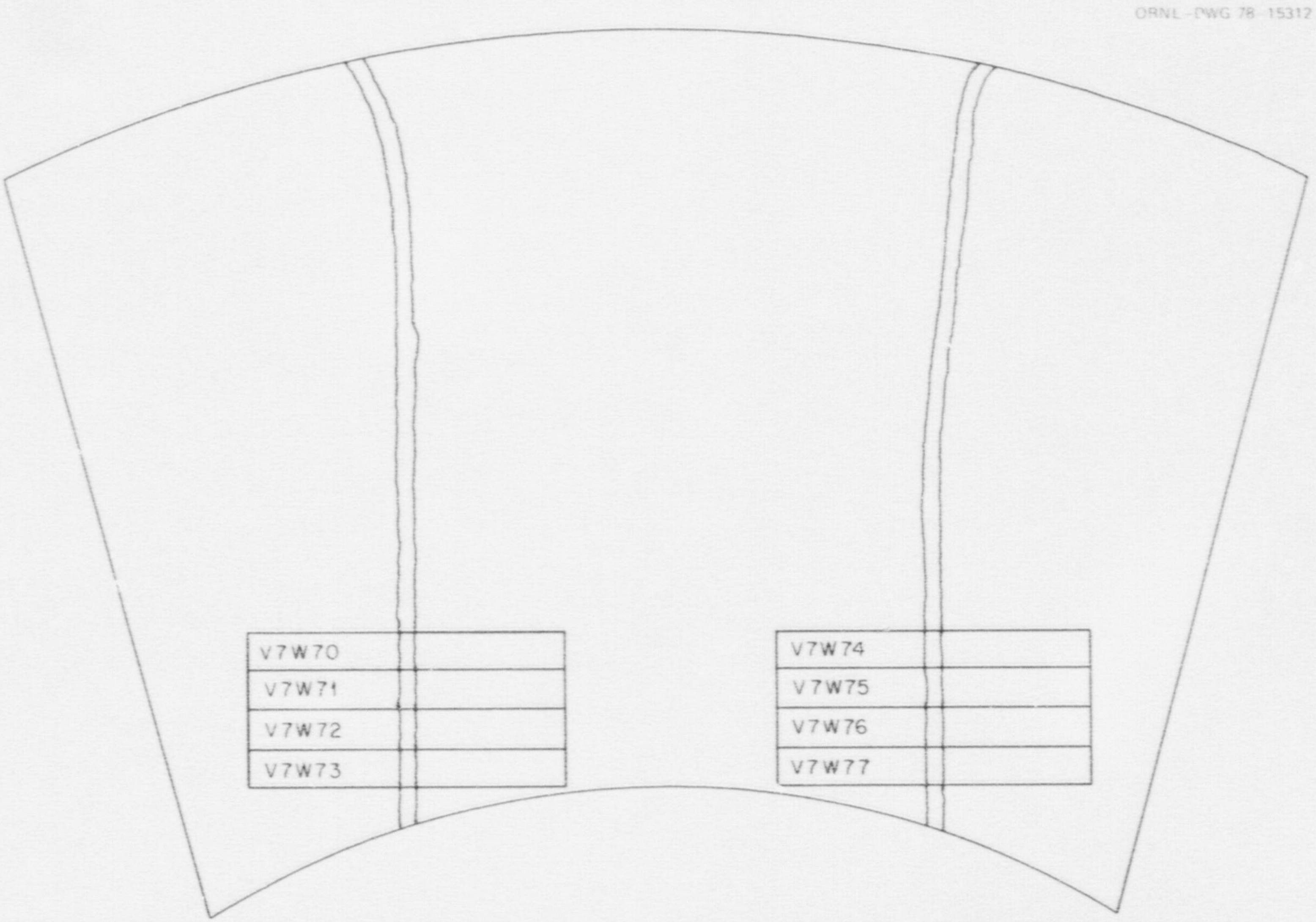

Fig. 2.15. Specimen locations in part V8P1C4.

Table 2.2. Tensile values from W-oriented specimens from the prototypical V-7B half-bead repair weld in the V-8 prolongation and the qualification weldment 4W

Specimen No.	Depth	Test temperature (°C)	Strength (MPa)			Total elongation (%)		Reduction in area (%)
			Upper yield	Lower[a] yield	Ultimate	$L/D = 7$	$L/D = 4$[b]	
			V-7B prototypical repair weld					
			HAZ					
V7W21	0.3T	93.3		432	560	14	(30)	72
			Weld metal					
V7W67	0.8T	93.3	485	467	567	14	(30)	71
V7W68	0.8T	93.3	490	463	578	14	(29)	73
			Qualification weld 4W					
			Weld metal					
4W11	0.2T	−101	625	550	656	26	(58)	74
4W12	0.2T	93.3	490	459	567	17	(36)	72
4W23	0.5T	149		478	653	14	(29)	64
4W24	0.5T	22.2	507	479	574	21	(45)	77
4W35	0.8T	−17.8	490	487	592	24	(51)	76
4W36	0.8T	204		437	610	16	(34)	67
4W37[c]	0.5T	21.1	502	485	576		24	63
4W38[c]	0.5T	21.1	492	488	563		*d*	*d*

[a] Absence of upper yield denotes 0.2% yield.

[b] Values of total elongation, e_{T4}, in parentheses are calculated from measured total and uniform elongations e_{T7} and e_{U7}, respectively, for specimens with $L/D = 7$ by the formula $e_{T4} = 1.75e_{T7} - 0.75e_{U7}$.

[c] 12.83-mm-gage-diam specimens; remainder 4.50 mm specimens.

[d] Fracture did not permit reassembly.

ORNL DWG 78 15313

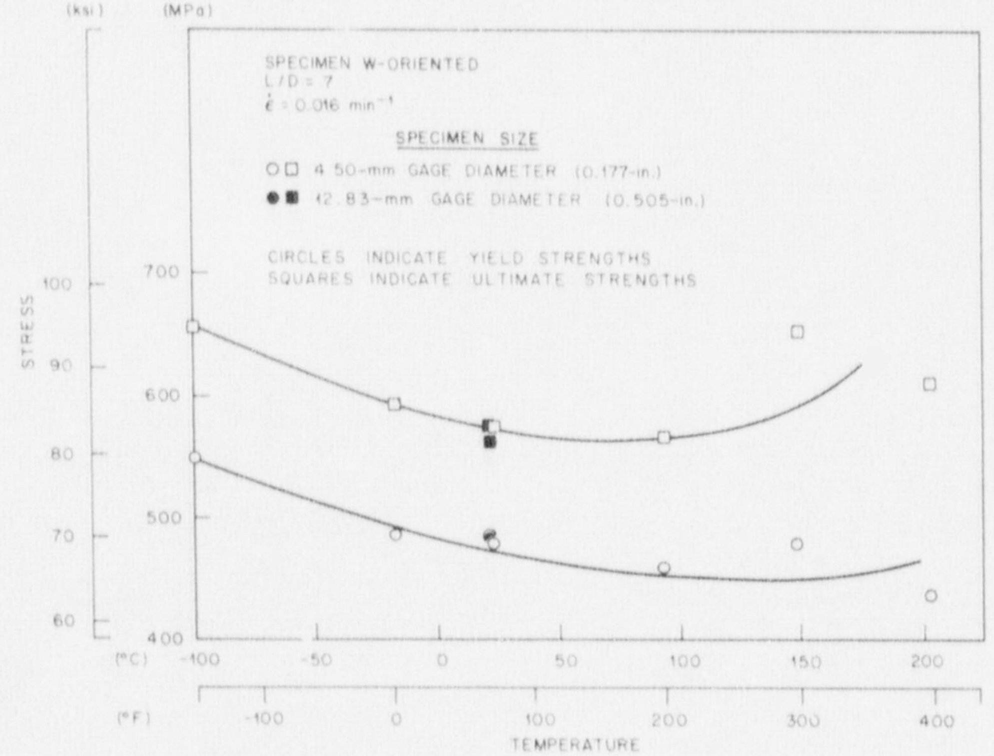

Fig. 2.16. Variation of tensile properties with temperature for 44-mm-thick (1¾-in.) half-bead qualification weld 4W in test plate 01MS-C.

the plate surface). The specimens were notched so the fracture progressed along the major welding direction. The C_V tests were run at a temperature range of −73.3 to 204°C (−100 to 400°F). The results, presented in Table 2.3, indicate that the weld metal fracture was fully ductile slightly below 37.8°C (100°F). The toughness of the weld metal exceeded the machine measuring capacity of 325 J (240 ft-lb) at 149°C (300°F). The toughness values at 177°C (350°F) and 204°C (400°F) are within the machine measuring capacity and indicate decreasing upper-shelf energies with increasing test temperatures.

Table 2.3. Charpy-V impact results from WL-oriented weld metal specimens from the qualification weldment 4W in test plate 01MS-C

Specimen No.	Depth[a]	Test temperature (°C)	Energy (J)	Lateral expansion (mm)	Fracture appearance (% fibrous)
4W1	0.3	−73.3	4	0.07	0
4W13	0.5	−45.6	81	1.57	20
4W25	0.8	−17.8	141	1.85	60
4W2	0.3	37.8	211	1.93	100
4W14	0.5	65.6	193	2.11	100
4W26	0.8	93.3	222	1.88	100
4W3	0.3	149	>324	[b,c]	100
4W15	0.5	177	321	[c]	100
4W27	0.8	204	310	[c]	100

[a] Fraction of plate thickness from the weld outer surfaces to the center of the specimen. Plate thickness is 4.4 cm (1¾ in.).

[b] Specimen stopped hammer.

[c] Specimen did not separate upon impact.

2.3.3 Static fracture toughness

Static fracture toughness (K_{Icd}) data were obtained from the V-7B prototypical and the qualification welds (4W) using precracked Charpy-V specimens (PCC_V). The fatigued precracks in the V-7B prototypical weld specimens are located in the base metal, the HAZ, and weld metal. All the fatigued crack tip location measurements were made from the edge of the dark etched band (HAZ) abutting the weld metal. This is clearly illustrated in Fig. 2.17. Figure 2.18, a photograph of the individual PCC_V specimens, shows the relationship between the V-notch and the HAZ reference edge (the fatigued precrack generally extends along the notch centerline from the apex of the V-notch). The actual orientation and depth location of each V-7B prototypical weld specimen are shown in Figs. 2.12 through 2.15 and in Table 2.4. The specimen orientations are identified in terms of the weld, even for specimens with precracks in base metal, for which the rolling direction is synonymous with the W direction of the weld. The fatigued precracks in the 4W weld specimens were located on the weld centerline.

The information obtained during fracture toughness testing is presented in Table 2.4. Specimen deflection was measured by deflectometers attached directly to the specimen. The displacement rate for all tests was 2.54 mm (0.100 in.)/min. All calculations for K_{Icd} were made in accordance with the expression given in ASTM E399-74 (Ref. 7) for bend specimens, with the load P_Q being given the value P_{EE} prescribed by the equivalent-energy method developed by Witt and Mager,[8,9]

$$P_{EE} = \sqrt{2mE_{\max}} , \qquad (1)$$

Table 2.4. Precracked Charpy-V static fracture toughness results for the prototypical V-7B half-bead repair weldment in the V-8 prolongation and the qualification weldment 4W

Specimen No.	Depth (T)	Specimen orientation	Test temperature (°F)	K_{Icd} (ksi $\sqrt{\text{in.}}$)	Average crack data				Load (lb)			Deflection (in.)		Energy (ft-lb)		Slope of linear load-displacement curve ($\times 10^4$ lb/in.)
					a (in.)	b (in.)	a/w	$f(a/w)$	Maximum	Start of fracture	Fracture arrest	Maximum load	Start of fracture	Maximum load	Start of fracture	
Prototypical V-7B repair weldment																
V7W4	0.41	WT	150	219	0.205	0.187	0.524	3.04	1380			0.078		6.9		11.6
V7W5	0.49	WT	200	279	0.198	0.196	0.502	2.85	1560			0.083		9.3		16.0
V7W10	0.21	WT	-50	271	0.232	0.161	0.590	3.81	1150	920	350	0.070		5.8		13.6
V7W11	0.29	WT	-50	172	0.228	0.164	0.581	3.70	1025	920	370	0.040	0.075	2.9		11.7
V7W13	0.45	WT	-150	217	0.216	0.177	0.549	3.30		1380	1080		0.044		4.1	16.4
V7W17	0.86	WT	200	199	0.216	0.177	0.550	3.31	1100			0.074		5.8		9.8
V7W18	0.92	WT	100	157	0.200	0.193	0.509	2.91		1290	1190		0.046		4.0	11.3
V7W26	0.68	WT	150	328	0.225	0.169	0.571	3.56	1250			0.124		11.2		12.3
V7W27	0.76	WT	250	272	0.223	0.171	0.566	3.49	1260			0.083		7.6		12.8
V7W28	0.84	WT	200	248	0.229	0.165	0.582	3.70	1100			0.075		6.1		11.9
V7W29	0.92	WT	200	255	0.227	0.167	0.576	3.62	1100			0.086		6.8		11.7
V7W31	0.22	WT	50	274	0.209	0.185	0.530	3.10	1410	1350	375	0.081	0.123	8.2		15.2
V7W33	0.42	WT	-50	258	0.201	0.193	0.510	2.91	1550	1530	350	0.068	0.091	7.5		17.0
V7W34	0.57	WT	-50	215	0.219	0.176	0.554	3.36	1300	1300	425	0.054	0.060	4.9	5.6	13.3
V7W35	0.65	WT	-50	157	0.216	0.178	0.548	3.29		1300	1230		0.030		2.6	14.4
V7W36	0.73	WT	50	260	0.205	0.189	0.520	3.01	1510	1510	210	0.072	0.095	7.8		15.3
V7W37	0.81	WT	-50	247	0.206	0.188	0.523	3.03		1450	380		0.071		7.1	15.0
V7W38	0.90	WT	-50	255	0.200	0.194	0.507	2.89	1470	1245	200	0.084		8.6		14.6
V7W39	0.09	WT	-50	184	0.195	0.199	0.494	2.78		1370	490		0.054		4.9	14.2
V7W40	0.19	WT	-50	225	0.199	0.195	0.506	2.88	1375			0.088		8.2		11.8
V7W41	0.27	WT	-50	213	0.198	0.196	0.502	2.84	1420	1420	350	0.087	0.090	8.4		10.6
V7W42	0.35	WT	-50	204	0.205	0.189	0.521	3.02	1380	980	180	0.079		6.8		10.6
V7W43	0.43	WT	-50	185	0.190	0.204	0.482	2.68		1460	325		0.061		5.9	12.7
V7W44	0.52	WT	50	214	0.208	0.186	0.528	3.08	1270	1200	270	0.077	0.125	6.6		11.6
V7W52	0.32	WL	50	193	0.211	0.182	0.537	3.17		1240	520		0.057		4.7	12.4
V7W72	0.86	WT	200	329	0.219	0.175	0.556	3.38	1280			0.121		11.4		13.3
V7W76	0.87	WT	200	231	0.233	0.162	0.592	3.84	1070			0.071		5.4		10.8
Qualification weldment 4W																
4W4	0.2	WL	100	194	0.202	0.192	0.512	2.97		1390	40		0.042		4.1	16.7
4W5	0.2	WL	100	276	0.211	0.182	0.537	3.18	1140			0.101		8.3		14.4
4W6	0.2	WL	300	185	0.221	0.172	0.562	3.45	1025			0.056		3.9		11.8
4W16	0.5	WL	-50	101	0.203	0.190	0.516	2.97		1080	660		0.022		1.5	12.1
4W17	0.5	WL	150	214	0.217	0.176	0.553	3.34	1080			0.066		5.1		12.8
4W28	0.8	WL	0	244	0.202	0.191	0.513	2.94	1325	1220	520	0.078		7.3		14.7
4W29	0.8	WL	200	238	0.196	0.197	0.500	2.83	1270			0.080		7.2		15.2
4W30	0.8	WL	400	163	0.214	0.179	0.544	3.25	1160			0.039		3.0		13.1

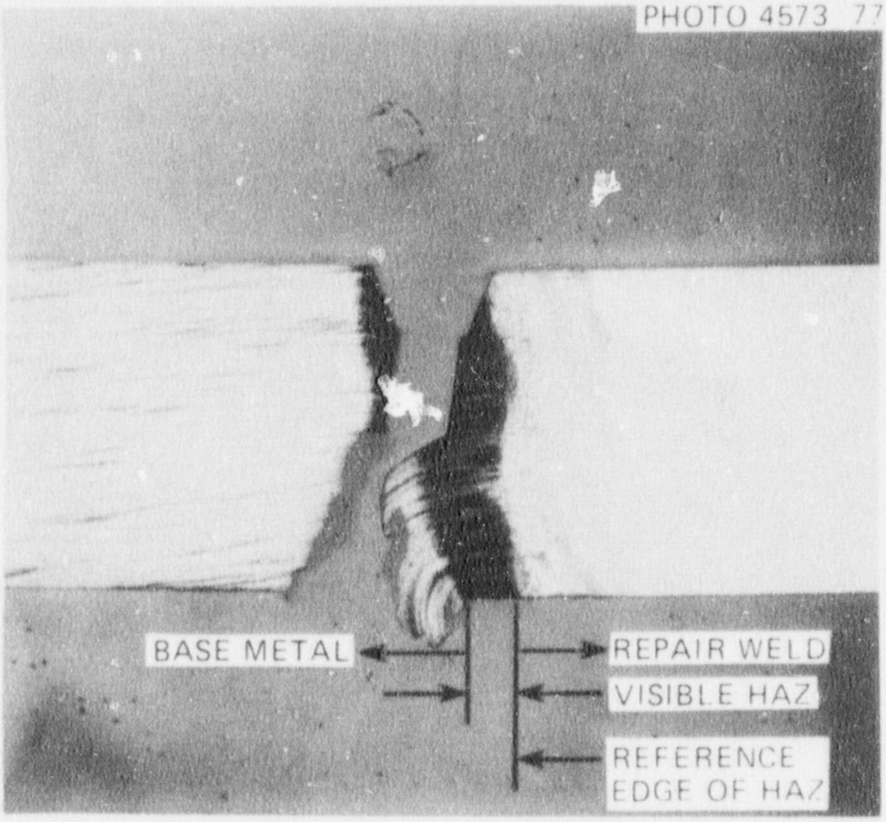

Fig. 2.17. Identification of reference edge cited in Table 2.5.

where m is the slope of the linear portion of the load-deflection curve and E_{max} is the area under the curve up to maximum load. The dimensional parameters shown in Table 2.4 are defined in ASTM E399-74. The function $f(a/W)$ was calculated from the expression

$$f\left(\frac{a}{W}\right) = \left(1 - \frac{a}{W}\right)^{-3/2} \qquad (2)$$

for a square beam rather than the series recommended in ASTM E-399-74 for a rectangular beam. All load and deflection data were obtained from the load-displacement record.

Two temperature ranges were investigated in the V-7B prototypical weldment, 66 to 121°C (150 to 250°F) and −45.6 to −101°C (−50 to −150°F). These ranges bracket the proposed V-7B and V-8 test temperatures, respectively. The latter range was included because of a shortage of similar HAZ material in the V-8 prototypical repair weld. The temperature range investigated for the 4W weld metal was −73.3 to 204°C (−100 to 400°F). The K_{Icd} results are listed in Table 2.5. The PCC_V results from the prototypical weld are shown in Fig. 2.19.

In the 66 to 121°C (150 to 250°F) temperature range, the K_{Icd} values from the prototypical weldment ranged between 219 $MN{\cdot}m^{-3/2}$ (199 ksi$\sqrt{\text{in.}}$) in the weld metal to 362 $MN{\cdot}m^{-3/2}$ (329 ksi$\sqrt{\text{in.}}$) in the base metal–repair weld HAZ. The K_{Icd} values in the −45.6 to −101°C (−50 to −150°F) temperature range varied between 173 and 301 $MN{\cdot}m^{-3/2}$ (157 to 274 ksi$\sqrt{\text{in.}}$).

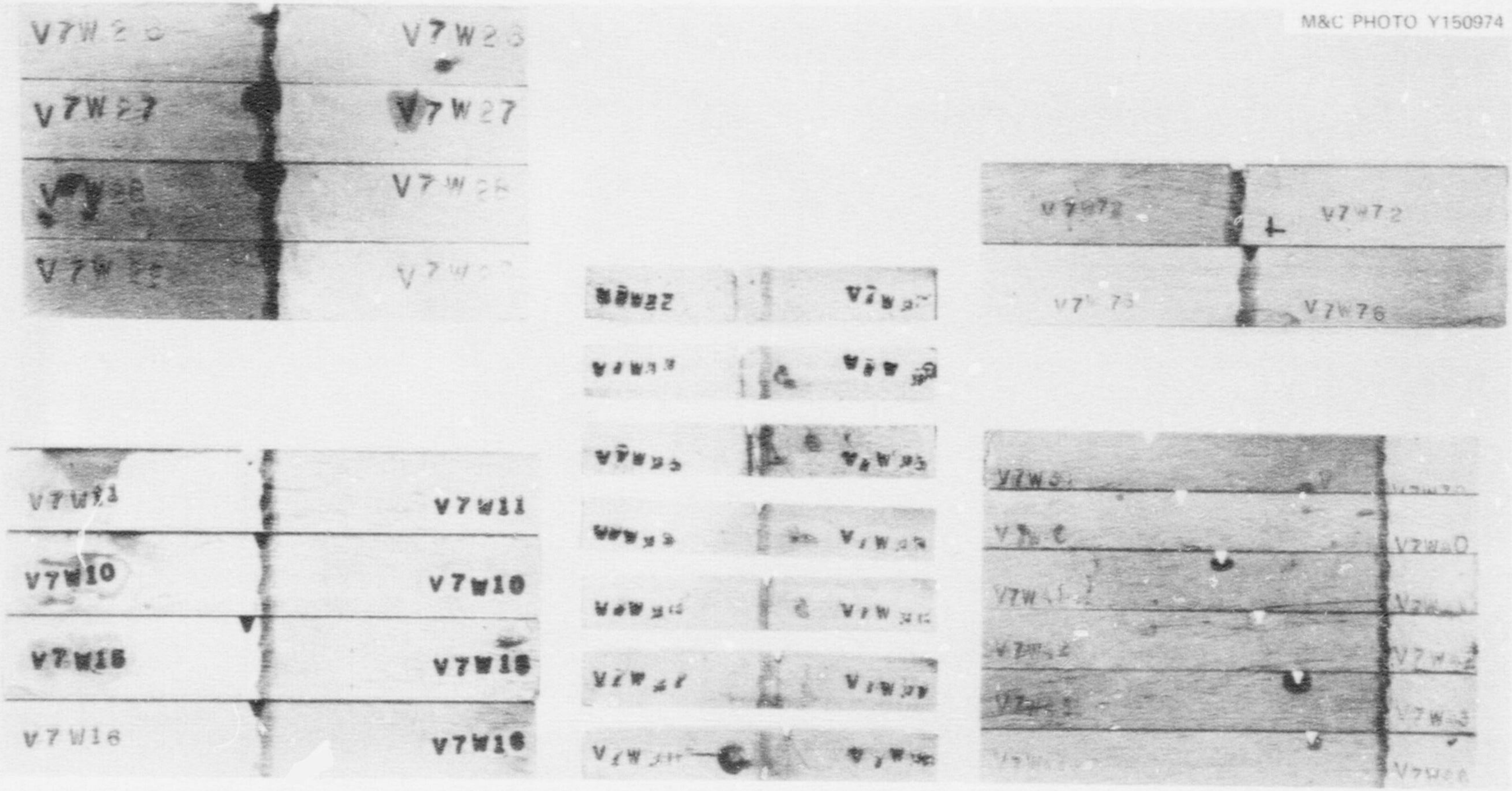

M&C PHOTO Y150974

Fig. 2.18. Locations of the Charpy V-notches in the prototypical V-7B weld relative to the HAZ.

Table 2.5. Precracked Charpy-V static fracture toughness at various distances from the visible HAZ of the prototypical V-7B half-bead repair weld in the V-8 prolongation and weld metal from the qualification weldment 4W

Specimen No.	Depth[a] (T)	Temperature (°C)	Static fracture[b] toughness, K_{Icd} ($MN \cdot m^{-3/2}$)	Distance of fatigued crack tip from HAZ reference edge (mm)
		V-7B type weld repair **In HAZ**		
V7W10	0.21	−45.6	298	0.0
V7W4	0.41	65.6	241	1.6
V7W5	0.49	93.3	307	1.1
V7W35	0.65	−45.6	173	0.0
V7W26	0.68	65.6	360	1.4
V7W36	0.73	−45.6	286	1.5
V7W27	0.76	121	299	0.6
V7W28	0.84	93.3	273	0.9
V7W72	0.86	93.3	362	0.4
V7W76	0.87	93.3	254	1.3
V7W29	0.92	93.3	280	0.6
		In base metal		
V7W39	0.09	−45.6	202	38.9
V7W40	0.19	−45.6	247	34.0
V7W41	0.27	−45.6	234	25.6
V7W42	0.35	−45.6	224	21.0
V7W43	0.43	−45.6	203	14.0
V7W44	0.52	−45.6	235	12.1
V7W37	0.81	−45.6	271	2.8
V7W38	0.90	−45.6	280	4.8
		In repair weld metal		
V7W31	0.22	−45.6	301	4.1
V7W11	0.29	−45.6	189	1.5
V7W33	0.42	−45.6	284	2.8
V7W13	0.45	−101	238	0.4
V7W34	0.57	−45.6	236	1.9
		Weld centerline		
V7W17	0.86	93.3	219	
V7W18	0.92	−73.3	173	
		Qualification weld 4W **Weld centerline**		
4W4	0.2	−73.3	213	
4W5	0.2	37.8	303	
4W6	6.2	149	203	
4W16	0.5	−45.6	111	
4W17	0.5	65.6	235	
4W28	0.8	−17.8	268	
4W29	0.8	93.3	262	
4W30	0.8	204	179	

[a] Fraction of wall thickness from outer surface to tip of fatigued crack. Wall thickness is 154 mm and 44 mm.

[b] Displacement rate is 2.5 mm/min.

ORNL–DWG 78–15314

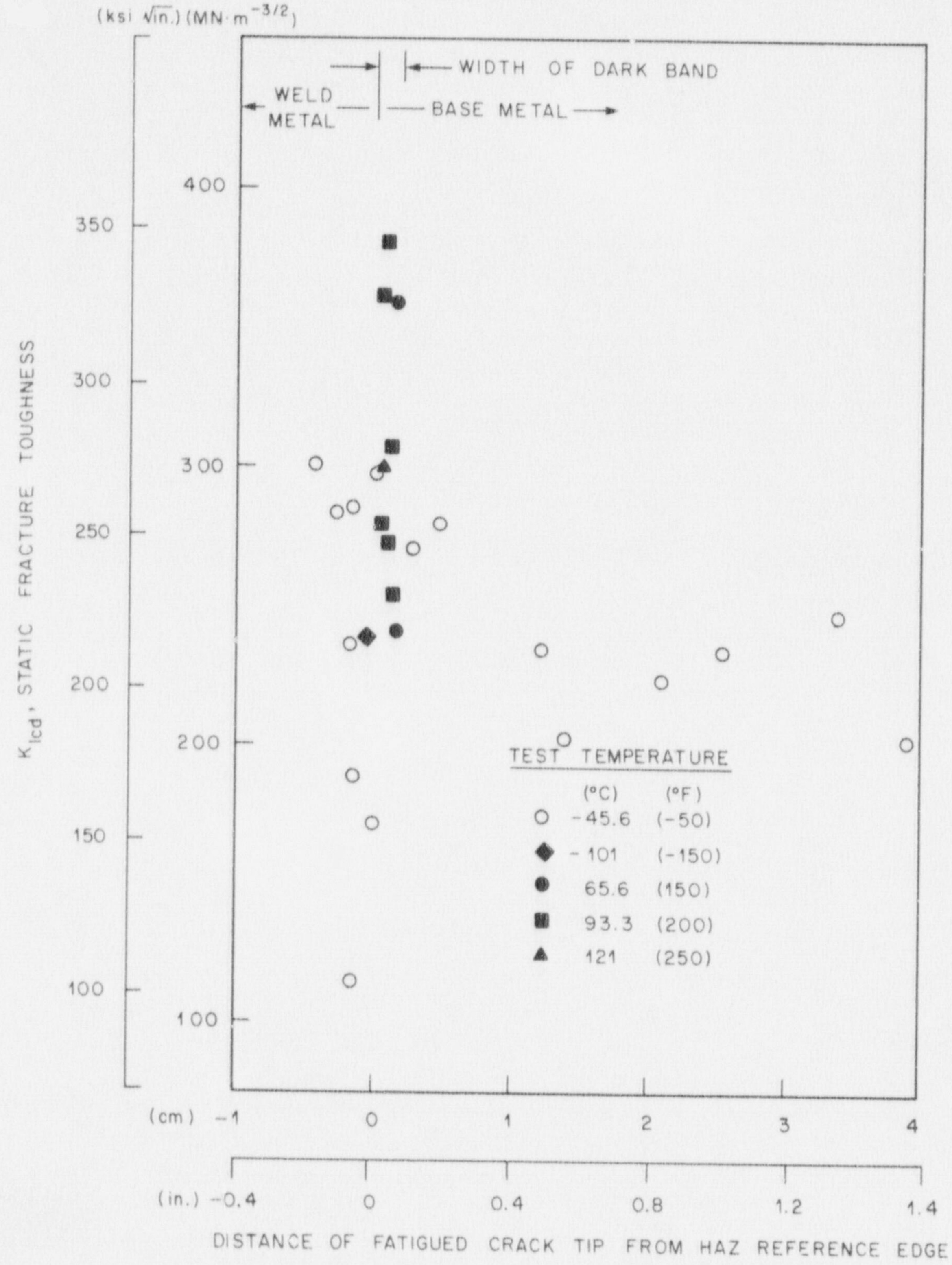

Fig. 2.19. Variation of static fracture toughness from precracked Charpy-V specimens with temperature and distance from the HAZ in the prototypical half-bead weld in the V-8 prolongation.

The test results from weld 4W listed in Tables 2.4 and 2.5 are plotted in Fig. 2.20. The K_{Icd} toughness of the weld metal is dependent on the depth in the weld from which the specimens were obtained. Lower values were noted for midthickness specimens for a given test temperature than for specimens from the quarter and three-quarter depth levels. The values for the latter thickness levels correlate very well with each other. The maximum K_{Icd} value, 303 $MN \cdot m^{-3/2}$ (276 $\text{ksi}\sqrt{\text{in.}}$), occurred at 37.8°C (100°F) at the quarter and three-quarter levels. Higher toughness values may occur at the midthickness at temperatures above 24°C (75°F), but no tests were made at these higher temperatures.

Static fracture toughness results from two WL-oriented 1T compact specimens of weld metal from the qualification weld were obtained. Specimens 4W39 and 4W40, tested at −17.8 and −45.6°C (0 and −50°F), gave values of 129 and 114 $MN \cdot m^{-3/2}$ (117 and 103 $\text{ksi}\sqrt{\text{in.}}$), respectively. Both specimens were from the midthickness depth in the weld as shown in Fig. 2.8. These data are included in Fig. 2.20.

Metallographic examination of specimens from the V-7B prototype weldment, in which the fatigued cracks reside in the visible HAZ identified in Fig. 2.17, indicates that the crack propagation is through the base metal. Figure 2.21 illustrates the type of fracture behavior noted in the study. The fatigue crack front

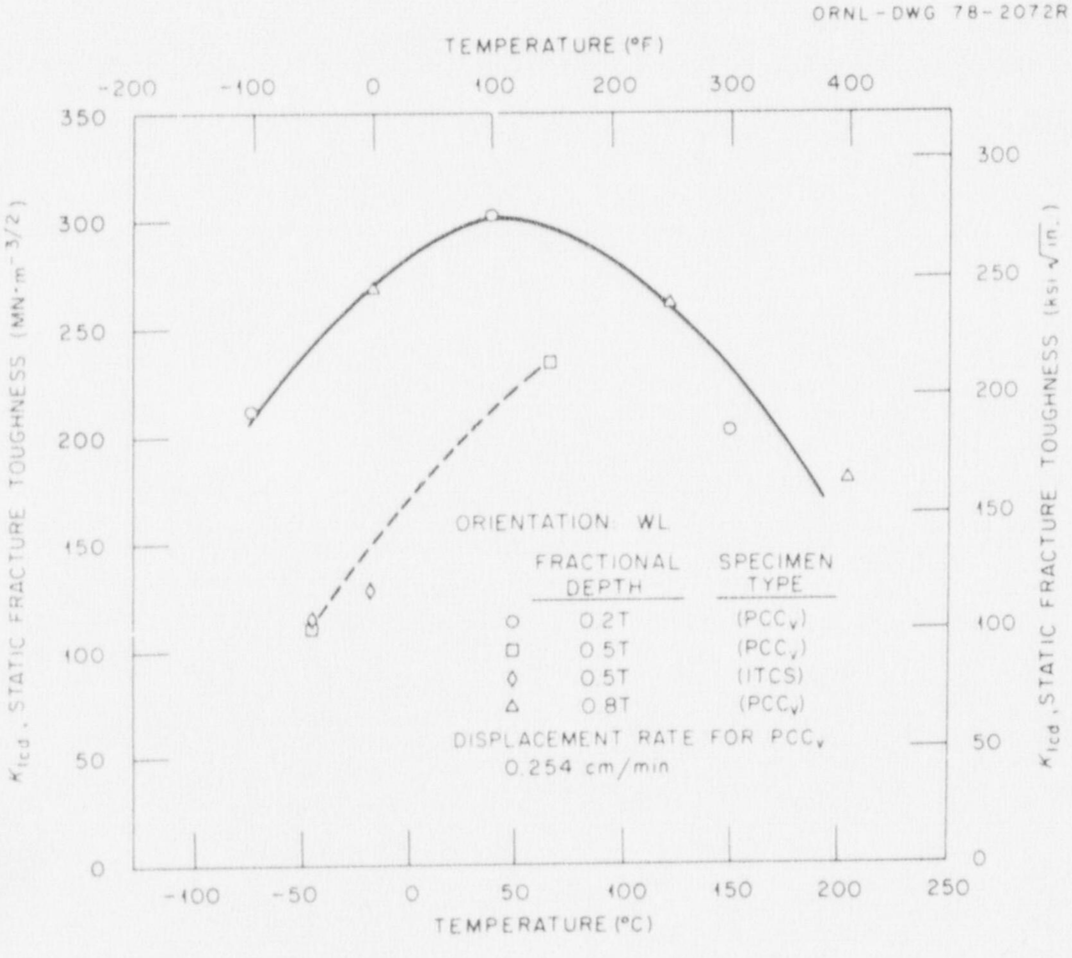

Fig. 2.20. Variation of static fracture toughness with temperature for 44-mm-thick (1¾-in.) half-bead qualification weldment 4W.

M&C PHOTO Y148536

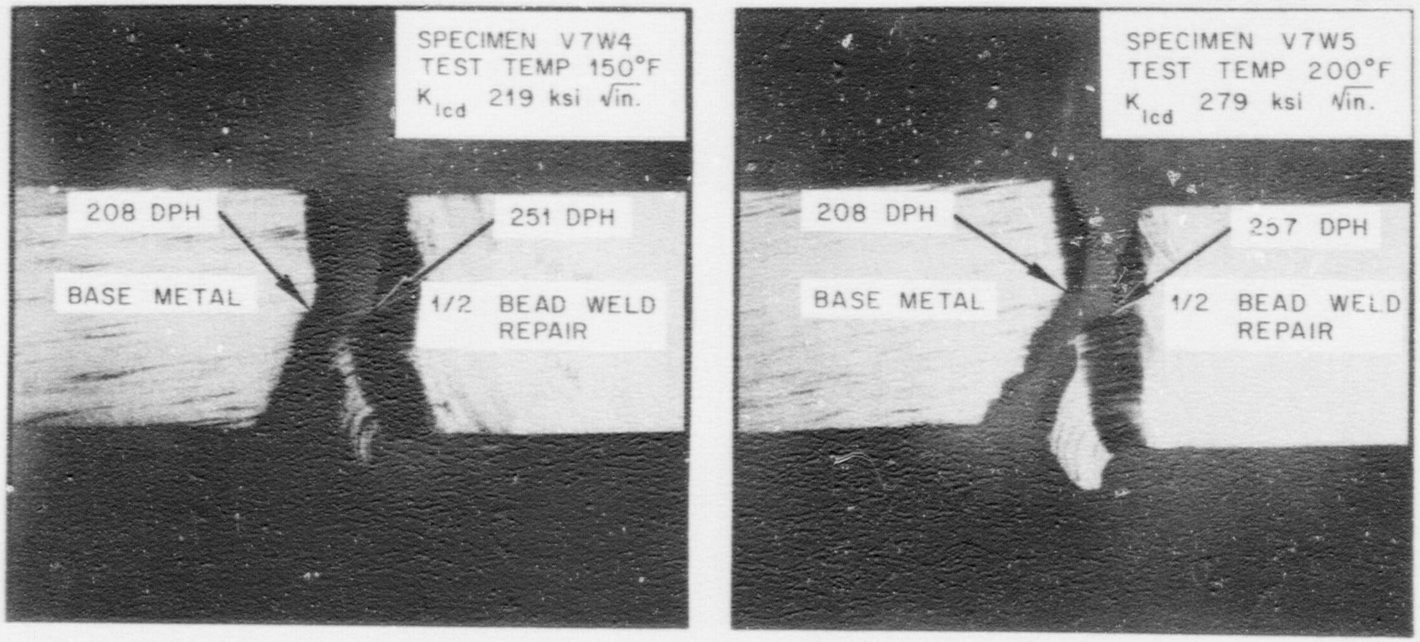

Fig. 2.21. Specimens having crack tips in the dark etching region of the HAZ.

resides near the middle of the visible HAZ, a region with a fairly high hardness, approximately 250 to 300 DPH (diamond pyramid hardness). The crack propagation is along the interface between the visible HAZ (dark band) and the (apparently) unaffected base metal. The hardness in the region where the crack propagated is approximately 210 DPH. The hardness values are approximated from the traverse shown in Fig. 2.22. Similar fracture behavior was not noted for specimens with fatigue crack fronts in the weld

M&C PHOTO Y150569

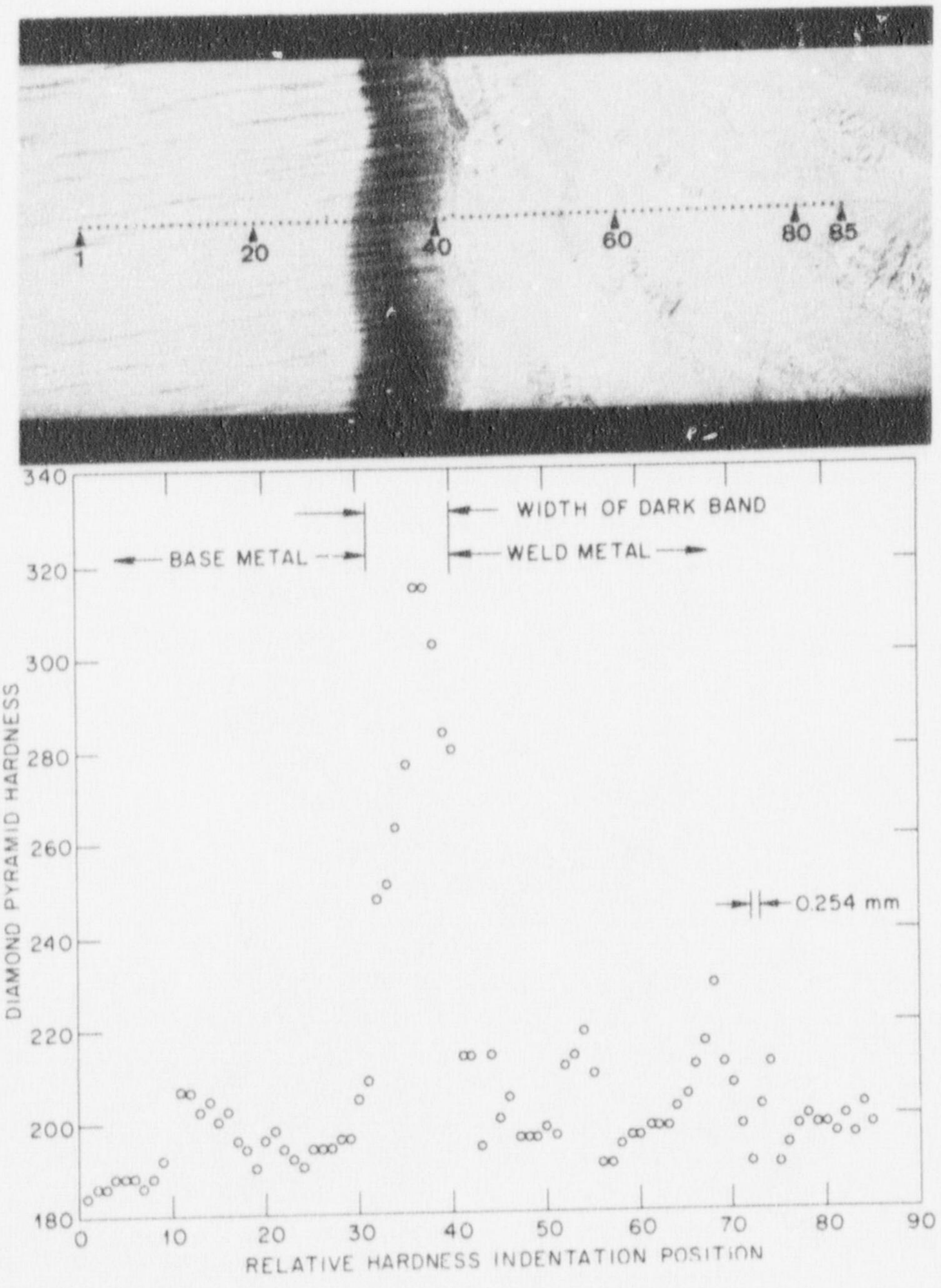

Fig. 2.22. Hardness traverse of the heat-affected zone and adjacent areas of a cross section of the V-7B prototypical half-bead weld repair in the V-8 prolongation.

metal. Those specimens tended to propagate in a more direct path or to follow the contour of a weld pass. Figure 2.23 contains a photomacrograph of a specimen with the crack tip in the repair weld adjacent to the half-bead repair and base metal fusion line. The propagation path is essentially straight through the specimen.

2.3.4 Hardness measurements

A microhardness traverse across the base metal–repair weld in specimen V7W7 was also obtained. Figure 2.22 is an enlargement of the region where the penetrations were made identifying the location of indentations and a plot of the hardness values associated with these locations. The actual hardness values are listed in Table 2.6. The highest hardness values occur in a 2.29-mm-wide (0.090-in.) region, which is the approximate width of the dark etchant band that identifies the HAZ in the base metal. The highest DPH value, 314 (R_c 31.6), occurred twice within 0.254 mm (0.010 in.) of each other. This is in agreement with three previous hardness traverses[2] across a similar HAZ in the V-7A prototype weld.

M&C PHOTO Y148584

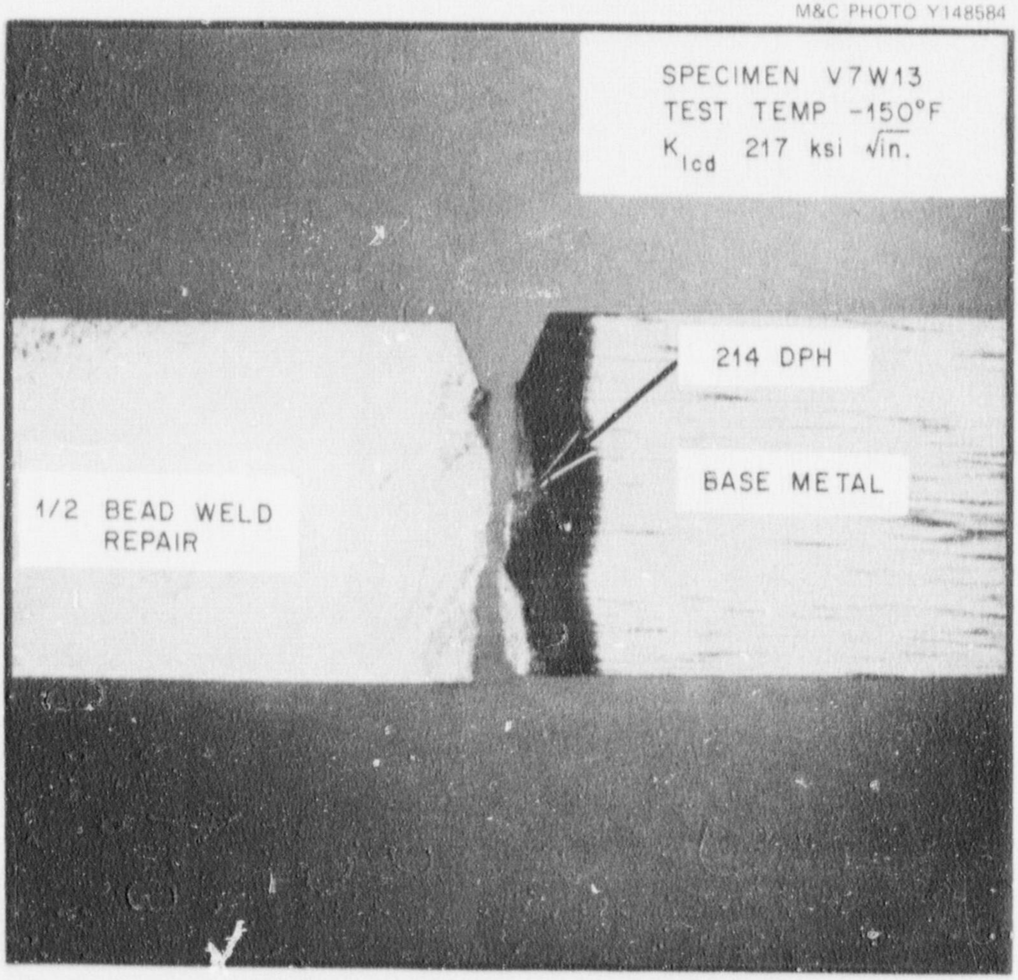

Fig. 2.23. Specimen with crack tip in the weld metal.

Table 2.6. DPH values across the HAZ and adjacent areas of the V-7B prototype half-bead repair weld in the V-8 prolongation

Indentation location No.	DPH	Rockwell B	Indentation location No.	DPH	Rockwell B	Rockwell C	Indentation location No.	DPH	Rockwell B
1	184	88.2	30	204	92.3		59	196	90.8
2	186	88.7	31	288		28.1	60	196	90.8
3	186	88.7	32	248		21.8	61	198	91.2
4	188	89.1	33	251		22.2	62	198	91.2
5	188	89.1	34	263		24.2	63	198	91.2
6	188	89.1	35	276		26.2	64	202	92.0
7	186	88.7	36	314		31.6	65	204	92.3
8	188	89.1	37	314		31.6	66	211	93.6
9	192	90.0	38	302		30.0	67	216	94.5
10	200	91.6	39	283		27.6	68	228	96.3
11	207	92.8	40	280		27.0	69	211	93.6
12	207	92.8	41	214	94.0		70	207	92.8
13	202	92.0	42	214	94.0		71	198	91.2
14	204	92.3	43	194	90.3		72	190	89.5
15	200	91.6	44	214	94.0		73	202	92.0
16	202	92.0	45	200	91.6		74	211	93.6
17	196	90.8	46	204	92.3		75	190	89.5
18	194	90.3	47	196	90.8		76	194	90.3
19	190	89.5	48	196	90.8		77	198	91.2
20	196	90.8	49	196	90.8		78	200	91.6
21	198	91.2	50	198	91.2		79	198	91.2
22	194	90.3	51	196	90.8		80	198	91.2
23	192	90.0	52	211	93.6		81	196	90.8
24	190	89.5	53	214	94.0		82	200	91.6
25	194	90.3	54	218	94.8		83	196	90.8
26	194	90.3	55	209	93.2		84	202	92.0
27	194	90.3	56	190	89.5		85	198	91.2
28	196	90.8	57	190	89.5				
29	196	90.8	58	194	90.3				

2.4 Residual Stress Measurements

The half-bead repair technique as previously discussed is accomplished without thermal stress relief. It would therefore be expected that significant residual stresses would result when the technique is employed. This section contains a description of, and the results from, an effort to assess the level and distribution of those stresses. The emphasis in that effort was on circumferential stresses in the vicinity of the repair weld because those would most directly affect the outcome of the V-7B test. A detailed discussion of the measurement techniques as well as results from two other half-bead repairs made to HSST intermediate test vessels and prolongations are contained in Ref. 10.

Most of the residual stress measurements on the V-7B vessel and the V-7B prototypical weld in the V-8 prolongation were made by means of weldable-type strain gages. After the cavities in the vessel and prolongation were ground to their final contour, and before the repair weld was begun, weldable gages were attached to the outside and inside surfaces of the V-7B vessel and the corresponding prolongation. Ailtech SG425 gages, which are stable at temperatures below 482°C (900°F), were used. No part of any gage was located closer than 38 mm (1.5 in.) to the weld cavity. Thermocouples were attached in the vicinity of the strain gages to control temperature. When temperatures indicated by the thermocouples began to approach 316°C (600°F), the rate of depositing weld metal was decreased or temporarily suspended.

The gages were initially zeroed at room temperature. The vessel and prolongation were then brought to a nominal 260°C (500°F), which was maintained approximately until the repair weld was complete. The gages were checked for drift during a 3-hr preweld hold and a 3-hr postweld hold when no welding was being done. There were no indications of drift with the exception of four gages on the prolongation which had become erratic during welding and had gone off-scale. Upon completion of the repair weld and the return of the vessel and prolongation to room temperature, a final strain gage reading was made. This final value of strain was used to calculate the change in stress which had resulted from the weld repair.

The gages were generally configured in clusters of three with two circumferential gages straddling an axial gage. This arrangement permitted the calculation of stresses by means of the following equations,

$$\sigma_a = \frac{E}{1 - \upsilon^2} (\epsilon_a + \upsilon\epsilon_c) \tag{3}$$

and

$$\sigma_c = \frac{E}{1 - \upsilon^2} (\epsilon_c + \upsilon\epsilon_a) , \tag{4}$$

where the subscripts *a* and *c* denote the axial and circumferential directions, respectively. Young's modulus was taken as 200,000 MPa (29×10^6 psi) and Poisson's ratio was taken as 0.29. The circumferential strain, ϵ_c, used in Eq. (3) was the average of the two circumferential strains taken from gages straddling the single axial gage. There were no significant differences between two such circumferential strains that were used for averaging.

Figures 2.24 and 2.25 show the stresses computed by the method described above for the V-7B vessel repair weld and its simulation in the prolongation, respectively. The figures show plan views, drawn to scale, of the repair zones as viewed from the outside of the vessel and prolongation. The weld cavity outline of the outside surface is shown as a solid line and that of the inside surface is shown as a dashed line. The gage lengths, orientations, and the locations of gages relative to the actual weld cavity outlines are drawn to scale and are indicated by the short solid lines. The number by each gage indicates the stresses (in MPa) that were calculated, and the orientation designates whether a stress is axial or circumferential. Stresses denoted by an asterisk pertain to gages located on the inside surface, with all other stresses pertaining to the outside surface. If it is assumed that the stresses existing in the vessel and prolongation prior to the weld repairs were negligible, the stress change due to the repair weld can be taken as an absolute residual stress. That assumption is considered reasonable because the operation of cutting the large cavities would tend to relieve residual stresses near those cavities. The assumption is also supported by the observation that the stresses measured in the vessel are not significantly different from those measured in the prolongation, which did not have a prior loading history and which had been stress relieved during original fabrication.

In addition to the weldable-gage-type measurements, five hole-drilling type measurements were made on the V-7B simulation repair weld at depths of 38 mm (1.5 in.) relative to the prolongation outside surface. The hole-drilling technique is a commonly used method that involves the attachment of a strain rosette to a surface where stresses are to be measured.[11] The rosette gages are initially zeroed and a small hole [e.g., 1.6 mm diam ($^1/_{16}$ in.)] is drilled into the specimen at the center of the rosette pattern. The depth of the hole is of the order of the hole diameter. The removal of material, which presumably was stressed, results in relaxation strains being indicated by the rosette gages. By means of calibration coefficients, it is possible to calculate the stresses that existed at the hole site prior to drilling.

ORNL-DWG 78-16490

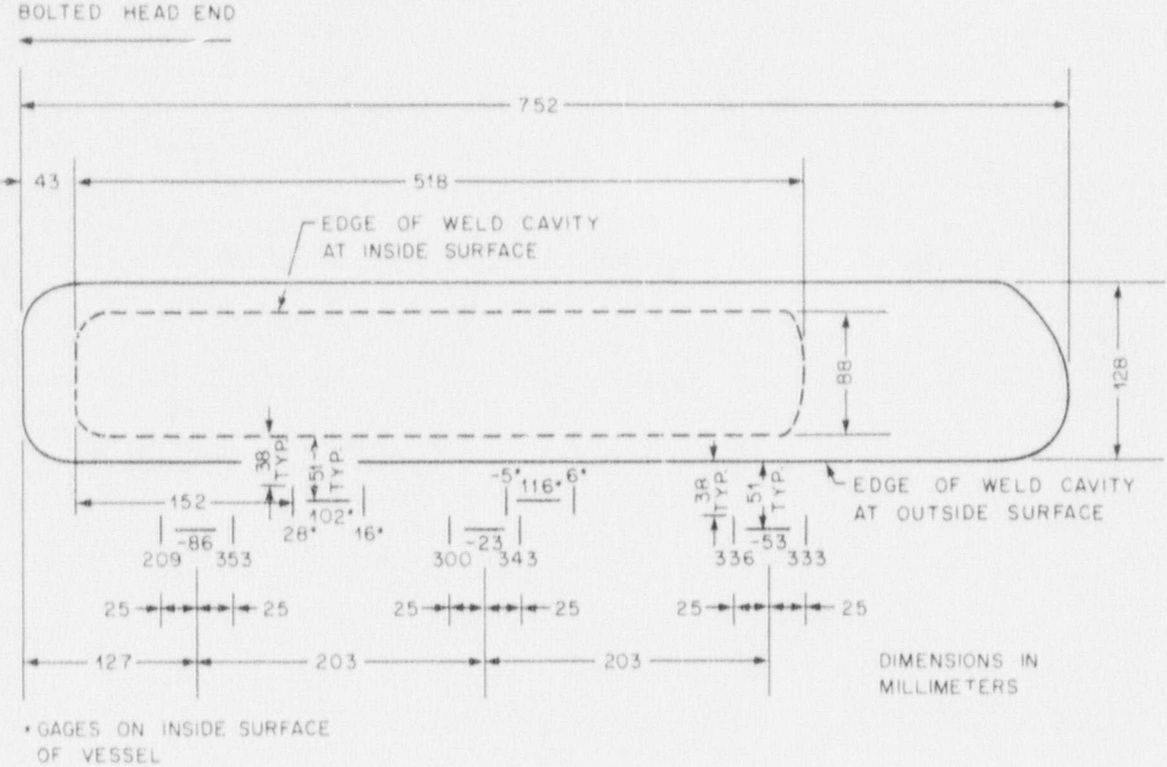

Fig. 2.24. V-7B repair weld residual stresses (MPa) determined from weldable strain gage measurements.

ORNL-DWG 78-4006

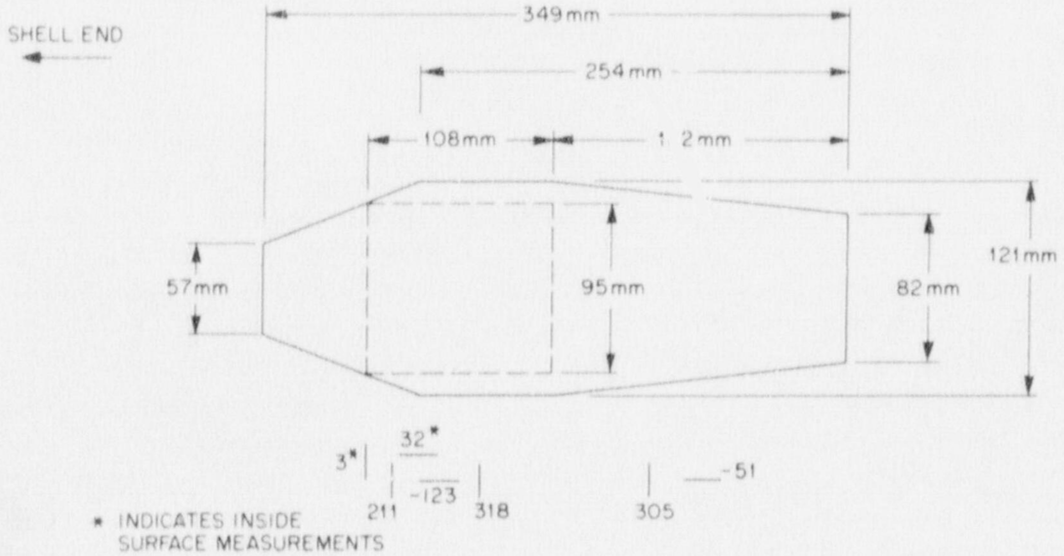

Fig. 2.25. V-7B prototypical repair weld residual stresses (MPa) determined from weldable strain gage measurements.

The hole-drilling method has been used extensively on the V-7A and V-8 simulation repair welds that were made in prolongations. Those measurements, which are contained in Ref. 10, indicated that, in the circumferential direction at least, large tensile residual stresses existed in the base metal surrounding the repair welds and low residual stresses existed in the weld metal itself. In the case of the V-7B repair weld, the hole-drilling method was used to provide a qualitative check of that behavior. Only a qualitative check of V-7B could be made because a conflicting measurement requirement for the V-8 repair weld dictated sectioning of the prolongation containing both simulations to best suit measuring residual stresses about the V-8 simulation repair weld. The location of the cut plane relative to the V-7B simulation repair weld is shown in Fig. 2.5. Figure 2.26 shows the prolongation, which contained the two simulation repair welds (180° apart), being sawed in half. Figure 2.27 shows a hole-drilling measurement being made on a ring that resulted from the prolongation being sawed in half. The results of the five hole-drilling measurements are shown in Figs. 2.28 and 2.29. The weld shown schematically in those figures does not penetrate through the entire prolongation wall because the saw cut bisecting the prolongation intersected with the sloping portion of the weld cavity. The circumferential values shown in Fig. 2.28 tend to confirm the conclusions[10] relative to high residual circumferential stresses in base metal surrounding the repair weld.

The V-7B vessel had a flaw deliberately introduced along the HAZ of the repair weld. The flawing, described in detail in Section 2.5, was accomplished in two steps. The first step involved machining a large deep slot in the vessel that approximated the final flaw geometry. Before the machining was begun, nine foil-type strain gages were attached to the inside surface of the V-7B vessel directly under the HAZ of interest. The location of the gages [6.4 mm (0.25 in.) gage length] relative to the weld cavity outline on the vessel inside surface is shown in Fig. 2.30. The gages were zeroed prior to machining and were used to monitor the strain induced in the ligament at the base of the flaw as a result of machining the deep cavity.

The recorded strains and the stresses calculated according to Eqs. 3 and 4 are listed in Table 2.7.* The compressive stresses that developed as a result of the machining operation suggest that the rotation resulting from cutting had a greater effect on the stress in the remaining ligament than did the translation of the free surfaces forming the sides of the flaw cavity. Thus, the development of compressive stresses in the remaining ligament as a result of machining in the flaw is not inconsistent with previous data indicating the existence of tensile stresses in and normal to the plane of the V-7B flaw prior to the introduction of the

---

*When possible, an average of the two adjacent gages was used for the Poisson term in Eqs. (3) and (4).

Table 2.7. Stresses on the V-7B inside surface beneath the flaw caused by machining the V-7B slot

Gage location[a]	Orientation	Microstrain	Stress (MPa)
1	Circumferential	−731	−183
2	Axial	−373	−129
3	Circumferential	−757	−192
4	Axial	−464	−148
5	Circumferential	−720	−187
6	Axial	−478	−152
7	Circumferential	−788	−200
8	Axial	−399	−137
9	Circumferential	−802	−200

[a] See Fig. 2.30.

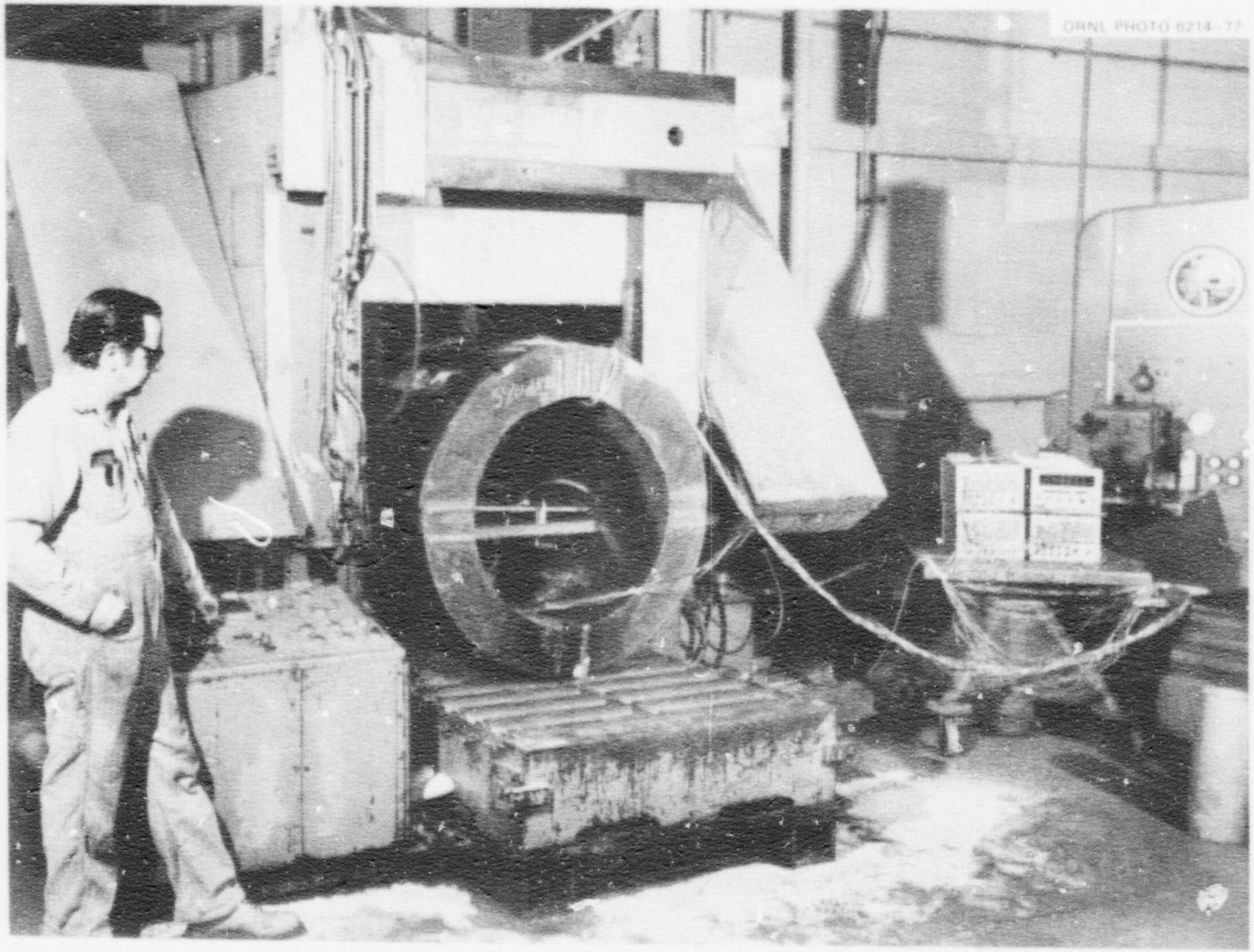

ORNL PHOTO 6214-77

Fig. 2.26. The prolongation containing the V-7B repair weld being sawed in half in order to allow through-thickness residual stress measurements.

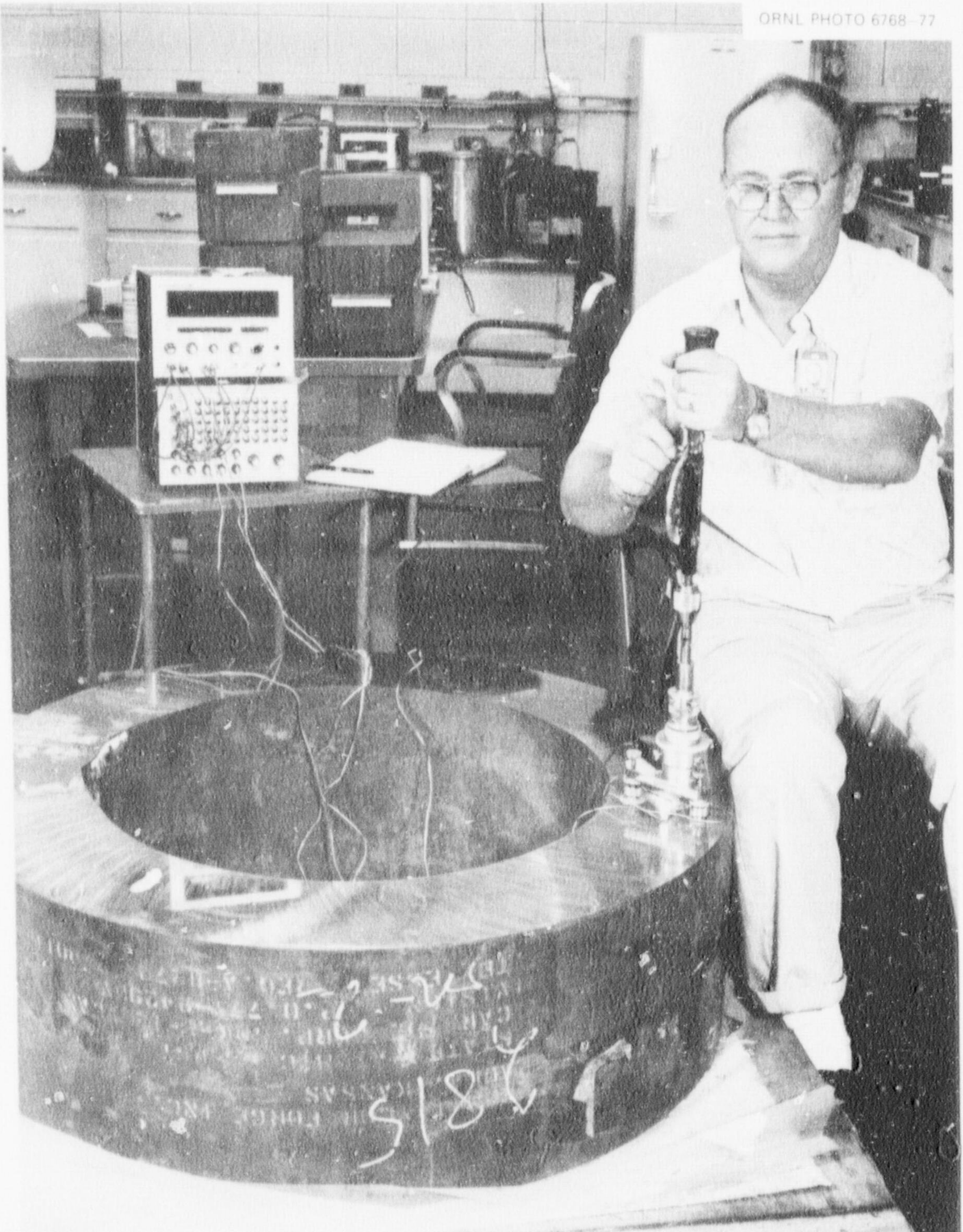
ORNL PHOTO 6768–77

Fig. 2.27. Through-thickness residual stress measurements being made on the V-7B prototypical repair weld by means of the hole-drilling technique.

ORNL-DWG 78-4030

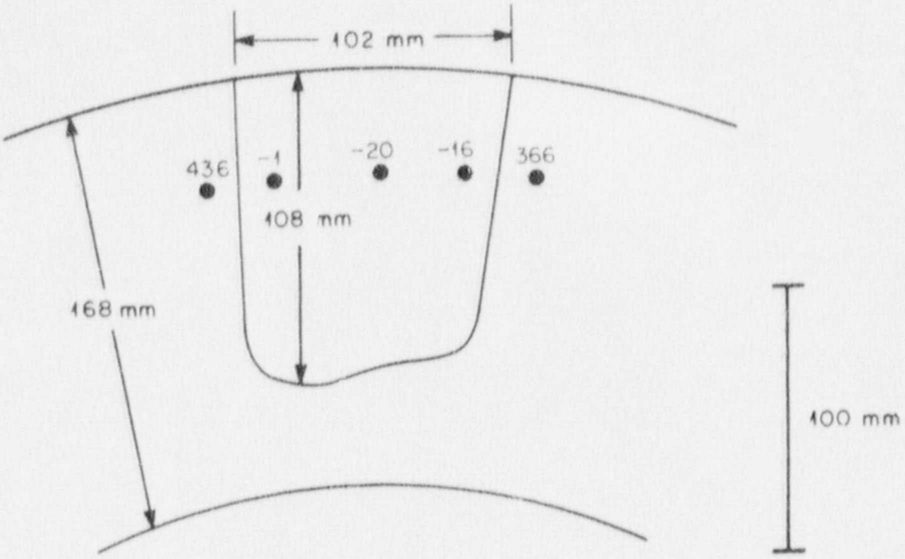

Fig. 2.28. Circumferential residual stresses (MPa) in the V-7B simulation repair weld (no correction for sectioning was applied).

ORNL-DWG 78-4031

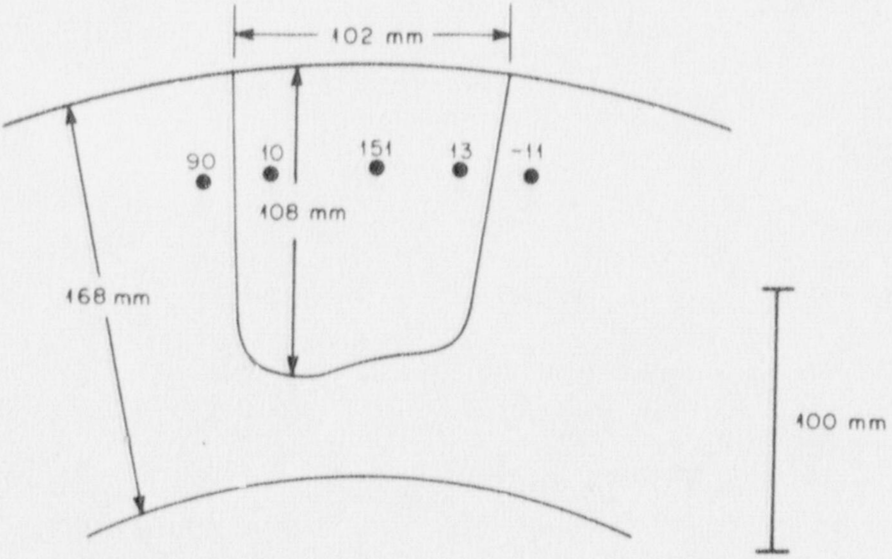

Fig. 2.29. Radial residual stresses (MPa) in the V-7B simulation repair weld (no correction for sectioning was applied).

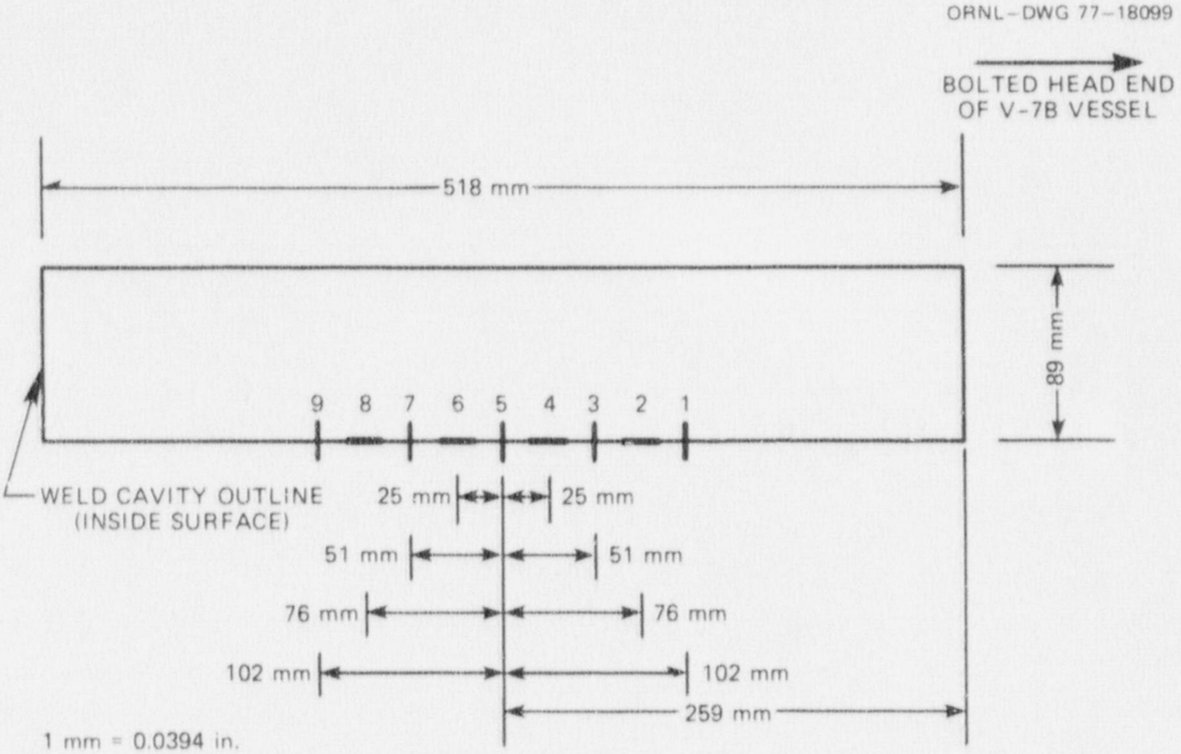

Fig. 2.30. Gage locations on the inside surface of the V-7B repair weld that were used to calculate stresses induced by machining the V-7B slot in the vessel. See Table 2.7 for results.

flaw. The absolute values of these compressive stresses are equal to or greater than any of the tensile stresses that were determined from the weldable gages or the hole-drilling measurements in comparable vicinities near the V-7B repair weld, the V-7B simulation repair weld, or the similarly shaped V-7A simulation repair weld. It is therefore concluded that compressive stresses with values that could have ranged from −16 MPa (−2 ksi) to −205 MPa (−30 ksi) were present in the ligament at the base of the V-7B flaw prior to the start of the V-7B test.

2.5 Flaw Preparation for the V-7B Test

The repaired vessel was flawed in UCCND facilities at the Y-12 Plant by the same means and with the same flaw geometry used in the vessel for the V-7 and V-7A tests.[2,5] The flaw geometry is shown in Fig. 2.31. The flaw was produced in three steps: machining a 25-mm-wide (1-in.) notch to within about 10 mm (0.4 in.) of the desired crack depth, making a narrow electron-beam (EB) weld along the periphery of the notch, and charging the EB weld with hydrogen until a sharp crack popped in.

The EB welding and hydrogen-charging combination had been used many times for producing sharp flaws; however, before proceeding with the repair of the vessel, it had to be demonstrated that a sharp flaw could be generated in the HAZ of a repair weld of this geometry. Accordingly, a series of tests was conducted to establish the feasibility of using this procedure. A portion of a test weldment made by Combustion Engineering in the course of the original V-7 half-head repair was used.

A 125-mm-long (5-in.) bar was cut from one end of the test weldment, and both ends were ground and etched to display the HAZ in the transverse cross section of the weld. (See Fig. 2.32.) The surface of the

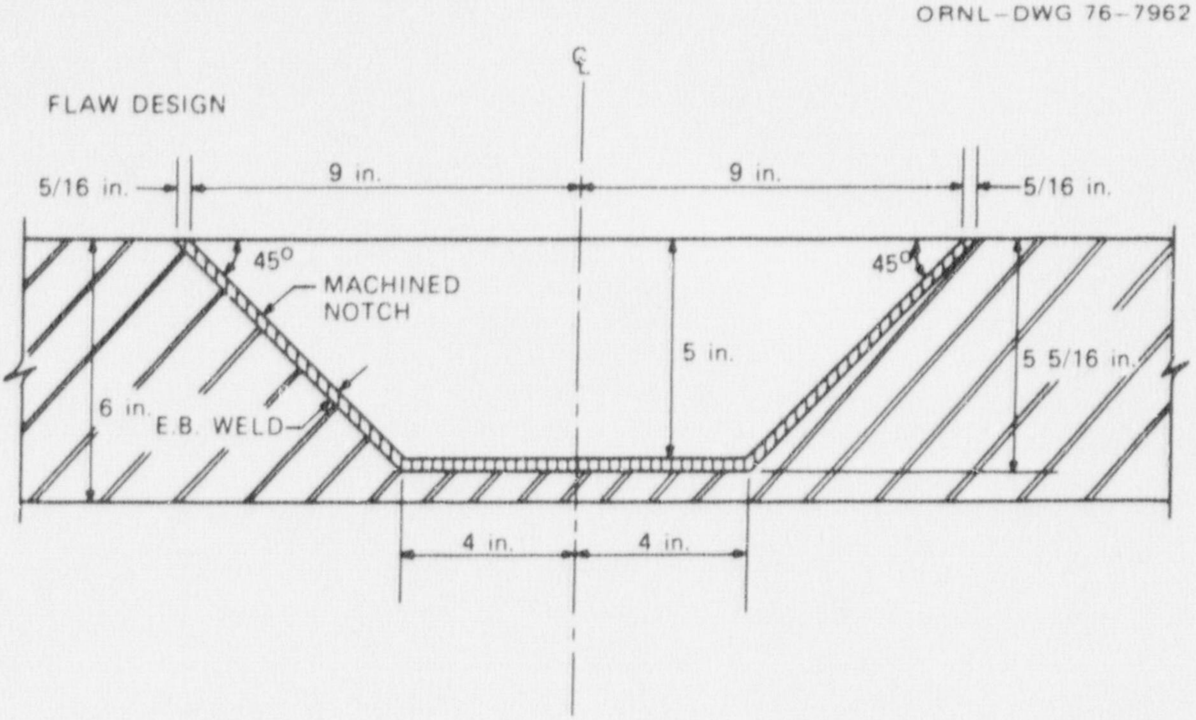

Fig. 2.31. Flaw design for vessels V-7, V-7A, and V-7B.

bar was machined to eliminate unevenness and curvature caused by final weld crowning passes and to form surfaces perpendicular to the desired direction of the EB. The bar was next mounted below the EB gun, and attempts were made to place two flaw welds centered within the two heat-affected zones of the weld. A third flaw weld was placed into the central portion of the weld metal of the bar. The EB welds were made only 100 mm long (4 in.) in order to retain end boundaries for restraint during the subsequent hydrogen charging. Figure 2.32 represents a slice from the bar and indicates the cracks that formed in the HAZ welds during the charging. The EB weld placed into the center of the weld did not crack during charging. The figure also illustrates the waviness of the HAZ and its narrow [2-mm ($^5/_{64}$-in.)] width, which can make the preparation of a long flaw difficult.

This preliminary investigation established the feasibility of producing a sharp crack in the HAZ of the second repair in vessel V-7, provided that the EB weld could be properly aligned with the HAZ. Experience with EB welding in the machined notches for the V-7 and V-7A tests provided some confidence that proper alignment could be accomplished if the procedures were carried out carefully and precisely. The necessary dimensional controls for finding the approximate locations of the heat-affected zones were assured by having the sides of the weld cavity prepared by machining and indexed with markings on the vessel surface. The axial centerline of the machined notch was located tentatively along the nominal centerline of one HAZ, as shown in Fig. 2.33.

Two beam saddle supports were welded to the vessel to index and align it for both the milling of the trapezoidal flaw notch and for subsequent EB flaw-welding operations. The procedure for aligning the notch along the actual centerline of the HAZ required alternative machining cuts, etching of the bottom of the notch, and recentering of the cutters. This was accomplished with the vessel on the bed of the large horizontal boring mill used to cut the notch. Position checks and appropriate minor tool centering

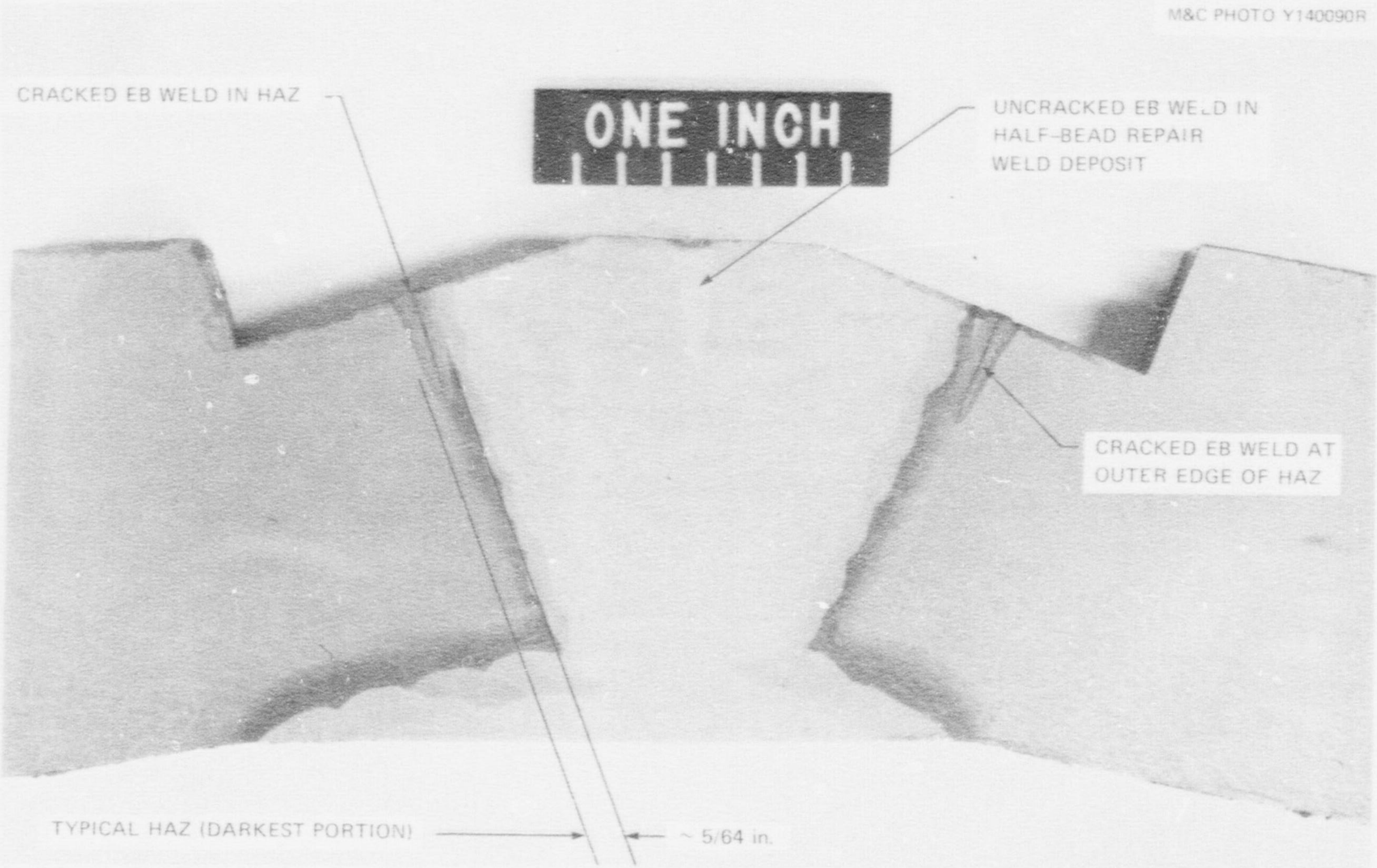

Fig. 2.32. Test piece for determining feasibility of flawing a half-bead weld repair zone by the electron-beam welding and hydrogen-charging procedure.

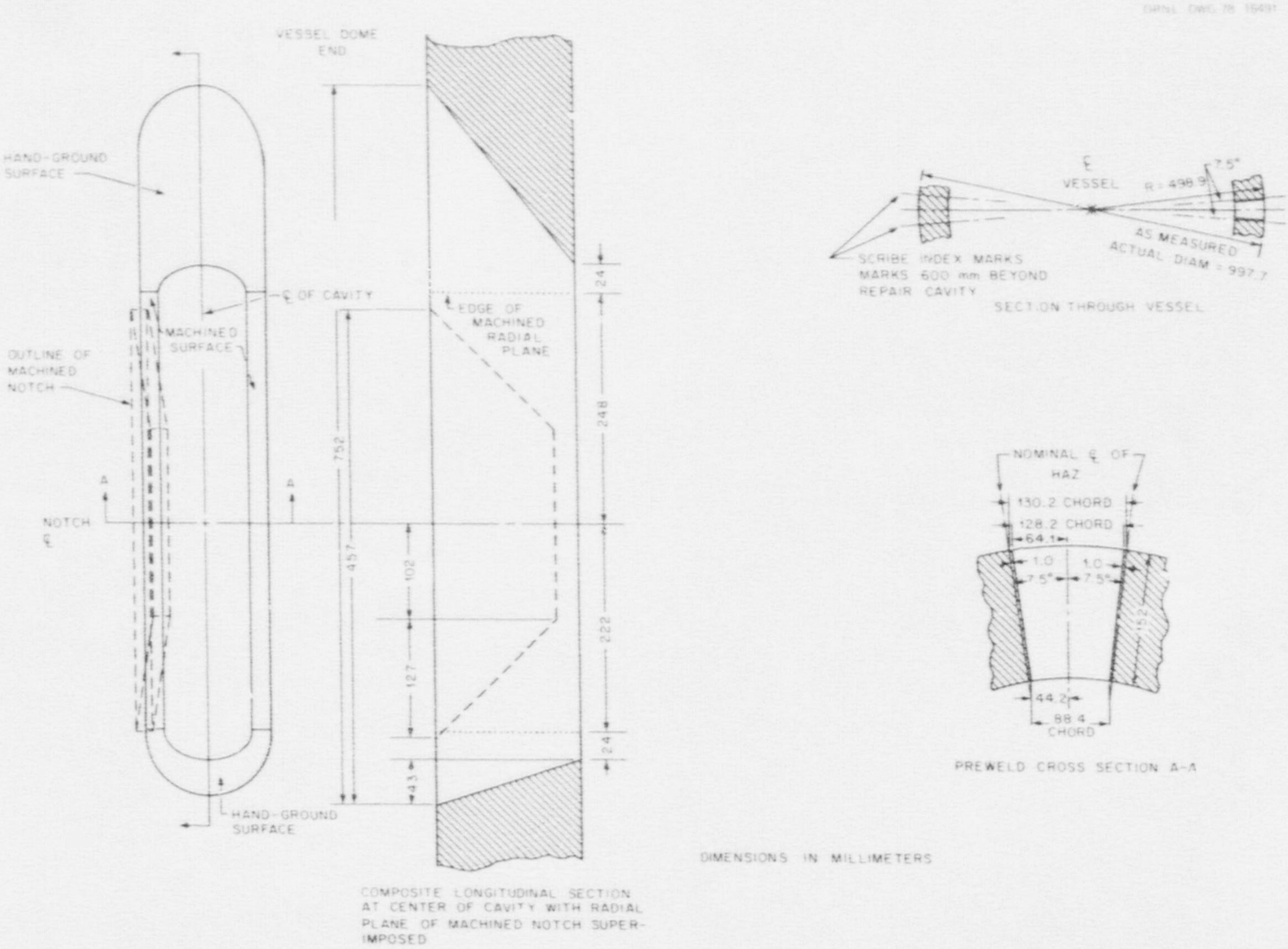

Fig. 2.33. Vessel V-7B as-built repair cavity and machined notch details.

adjustments were made using 9.5- and 12.7-mm-diam (0.375- and 0.5-in.) cutters at depths of 12.7, 25.4, and 63.5 mm (0.5, 1.0, and 2.5 in.) from the surface. The centers of the HAZ and the finished notch were within 0.25 and 0.89 mm (0.010 to 0.035 in.) of each other, both along the slopes and the bottom of the trapezoid. The HAZ band width varied from 1.7 to 2.0 mm (0.065 to 0.080 in.).

Four 50-mm-thick (2-in.) brick-shaped test blocks of A533 material with premachined cavities to simulate the vessel cavity geometry were repair welded by WTD to half-bead technique welding standards at the same time the vessel was repaired. These blocks were ground and etched and used to develop and establish EB programming input, to test magnetic beam deflection effects, and to verify hydrogen-charge flawing methods and detection of EB weld cracking by acoustic emission (AE). A steel model of a trapezoidal notch was also prepared and used in the final check of EB programming for the end slopes.

Precise placement of the weld bead along the bottom of the machined notch in vessel V-7A was complicated by the residual magnetism of the vessel.[2] Practice trials on blocks indicated that the EB bead positioning can be controlled in fields up to 3×10^{-4} T. Gaussmeter checks within the notch of vessel V-7B again revealed nonuniform magnetic flux densities, with the highest readings 8×10^{-4} T (8 G) longitudinally and 5×10^{-4} T (5 G) transversely. These readings were about one-tenth the magnitude of the magnetic flux densities encountered with the V-7A repair weld. This improvement in the residual magnetism may have been the result of the planned symmetrical grounding connections used in the V-7B repair. Both of the two electrical grounding connections were located 90° from the cavity along its transverse centerline. An arbitrarily located single ground had previously been used for the V-7A repair.

Two ceramic 0.1-T (1000-G) magnets were machined by electrical discharge to fit within the trapezoidal notch. These magnets permitted flux trimming by varying orientations and locations so as to reduce and even the flux distribution along the EB traverse. By this means, the magnetic flux densities for vessel V-7B were held to a maximum of 2.6×10^{-4} T before EB welding.

Actual forming of the EB weld bead in the notch had to be done in three separate steps: first along the deepest segment of the trapezoidal notch and then an upward pass along each slope. Tungsten target blocks were used to segment the overall weld. Upslope welding is necessary to maintain the molten metal puddle behind the weld gun. The proper combination of welding speed and power is needed to attain a uniform, rapid chilling of the weld bead and thus produce a highly prestressed bead of the desired shape. The stressed state assures cracking on subsequent hydrogen charging. The autogenous EB weld is pear shaped, approximately 3 mm wide ($\frac{1}{8}$ in.) at the surface by 7.9 mm deep ($\frac{5}{16}$ in.). The profile of the bottom of the bead shows irregular spikes.

Electron-beam welding was again performed in a large Sciaky weld chamber in the Y-12 Plant. Figure 2.34 shows the vessel in the chamber positioned for the flaw welding. Weld programming was essentially the same as used before for the V-7 and V-7A notches: energy density, 190 J/mm; beam potential and current , 40.5 kV with 178 mA on the horizontal surface (deepest portion of the notch) and 182 mA on the two slopes; beam speed, 2.3 m/min (90 in./min); and vacuum chamber pressure, 0.67×10^{-3} Pa (5×10^{-6} torr).

Gaussmeter checks made after each segment was welded indicated changes in magnetic flux patterns within the notch. Adjustment of the ceramic magnets, however, restored flux levels within the unwelded portions to levels $\leqslant 2.6 \times 10^{-4}$ T before continuation of welding. The resulting EB weld bead appeared to be properly aligned in the notch.

Hydrogen charging of the EB weld bead was accomplished by the same electrolytic process used for the two previous flaws in the vessel.[2,5] A current density of about 7.8×10^{-4} A/mm^2 ($\frac{1}{2}$ A/in.^{2}), based on unmasked contact surface area, was used. The charging operations were monitored by three AE transducers spaced along the interior surface of the vessel directly below the ligament of the notch. Past vessel and prototype specimen experience implied that the crack should form in 8 to 10 hr. However, the HAZ flaw in

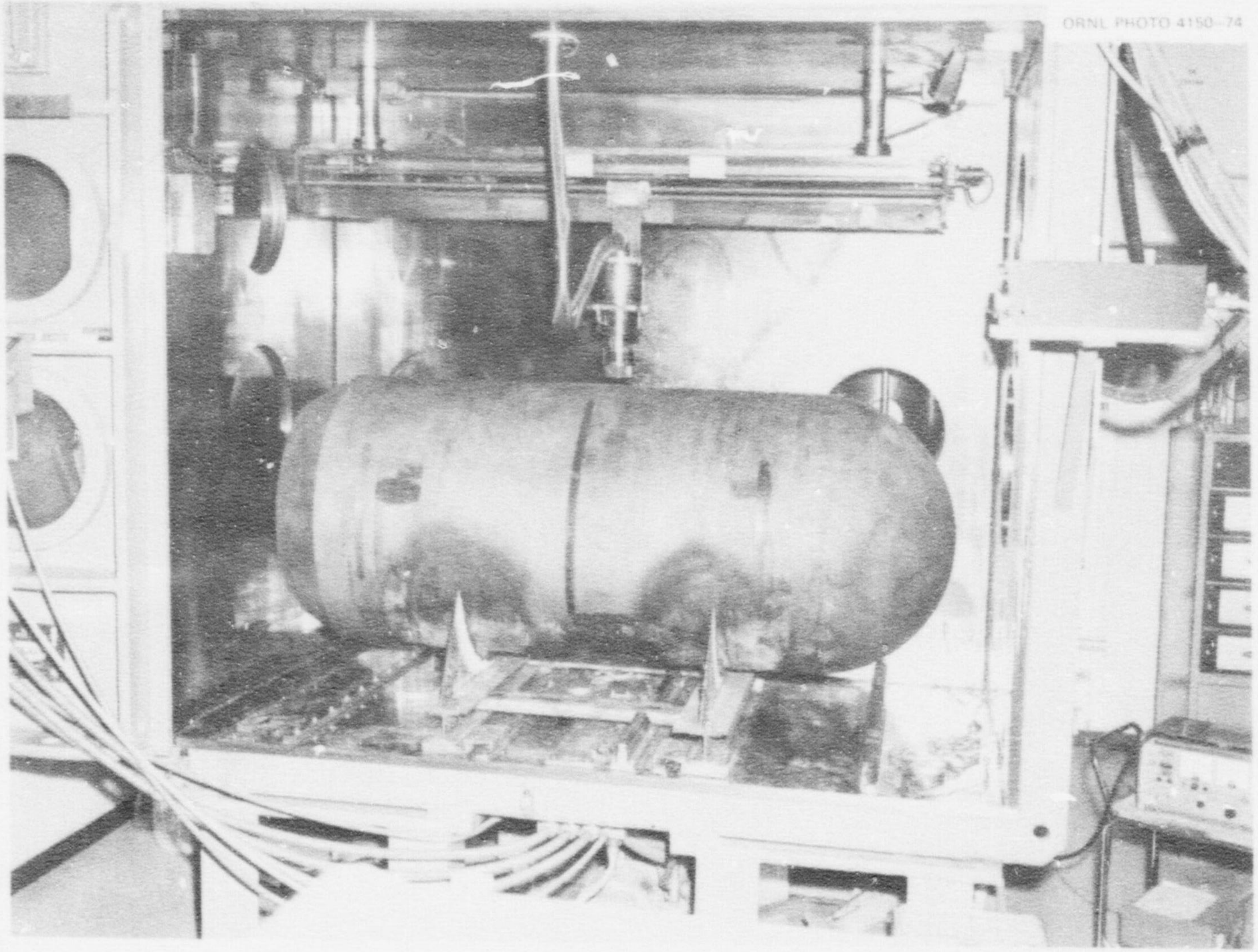

ORNL PHOTO 4150–74

Fig. 2.34. Vessel V-7B in EB weld chamber positioned for flaw welding.

V-7B appeared to have cracked after only about 4 hr of charging and emitted only about one-third of the anticipated number of acoustic pulses. Discontinuous cracks were noted along the bottom of the notch and on the slope toward the hemispherical end of the vessel. Charging was resumed since a continuous crack was not observed. Complete continuity was finally confirmed after 8 [illegible] of total charging time and after improved lighting had been installed and the notch flushed several times with a basic solution and with water.

References

1. C. E. Childress, *Fabrication and Mechanical Test Data for the Four 6-inch-thick Intermediate Test Vessels Made from Steel Plate for the Heavy Section Steel Technology Program*, Documentary Report 5, ORNL/TM-5074 (January 1976).

2. R. H. Bryan, J. G. Merkle, and G. C. Smith, *Test of 6-in.-thick Pressure Vessels, Series 3: Intermediate Test Vessel V-7A under Sustained Loading*, ORNL-NUREG-9 (February 1978).

3. W. D. Goins and D. L. Butler, *Weld Repair of Heavy Section Steel Technology Program Vessel V-7*, EPRI NP-179 (ORNL/Sub/88242-76/1), Combustion Engineering, Inc., Chattanooga, Tenn. (August 1976).

4. S. W. Wismer and P. P. Holz, *Half-Bead (Temper) Repair Welding for Heavy-Section Steel Technology Program Vessels*, ORNL/NUREG/TM-177 (June 1978).

5. J. G. Merkle et al., *Test of 6-in.-thick Pressure Vessels. Series 3: Intermediate Test Vessel V-7*, ORNL/NUREG-1 (August 1976).

6. ANSI/ASTM A-370-74, "Mechanical Testing of Steel Products," ASTM Standards, Part 10, 1977.

7. ANSI/ASTM E-399-74, "Method of Test for Plane-Strain Fracture Toughness of Metallic Materials," ASTM Standards, Part 10, 1977.

8. F. J. Witt and T. R. Mager, *A Procedure for Determining Bounding Values on Fracture Toughness, K_{Icd}, at Any Temperature*, ORNL/TM-3894 (October 1972).

9. F. J. Witt and T. R. Mager, "Fracture Toughness, K_{Ic}, Values at Temperatures up to 550°F for ASTM A533, Grade B, Class 1 Steel," *Nucl. Eng. Des.*, 7(1), 91–102 (August 1971).

10. G. C. Smith and P. P. Holz, *Repair Weld Induced Residual Stresses in Thick-Walled Steel Pressure Vessels*, ORNL/NUREG/TM-153, to be published.

11. N. J. Rendler and I. Vigness, "Hole-Drilling Strain Gage Method of Measuring Residual Stresses," *Experimental Mechanics*, December 1966, pp. 577–86.

3

Test Facility Design and Operation

3.1 Test Facility

The test site for intermediate test vessel V-7B was the same as that used for all other vessels[1–4] except V-7A, which was a pneumatic test requiring a more remote site.[5] The hydraulic testing facility is located at the old power plant adjacent to the Oak Ridge Gaseous Diffusion Plant (ORGDP), where the vessels were pressurized to failure in a concrete bunkered cell that was converted from an old steam turbine foundation. A sectional view of the test pit is shown in Fig. 3.1, and an overhead view of intermediate test vessel V-7B in the pit is shown in Fig. 3.2. The criteria for site selection and design along with a detailed description of the test facility are given in Ref. 6.

The test facility is capable of controlling vessel temperatures from −34 to 177°C (−30 to 350°F) and pressurization to 345 MPa (50,000 psi). Figure 3.3 is a schematic flow diagram of the facility showing the pressurization system normally used for intermediate vessel tests. This system was altered for V-7B to provide pressure to the patch cavity for indication of crack breakthrough prior to gross vessel pressure failure.

3.2 Instrumentation

After reviewing results of intermed[illegible]ssel tests V-7 and V-7A, the instrumentation plan for V-7B was formulated with the following changes fr[illegible]e V-7A plan.

1. The midsection crack-opening displacement (COD) gages used on V-7A were eliminated due to uncertainty of performance and insufficient time for development of a new sensor.

2. Strain gages in regions of vessel weld repairs from previous tests were reduced to a minimum. Also, gages from V-7 and V-7A at 180° remote from the midplane of the test section and experimental crack propagation gages were eliminated.

3. Outside surface COD gages remained the same but with modified mounting hardware.

The resulting instrumentation plan for V-7B included the following sensors:

1. Heating control thermocouples (8).
2. Data thermocouples (10).
3. Pressure transducers (3).
4. Pressure indicator (dial gage) (1).
5. Inner surface strain gages (weldable) (28).
6. Outer surface strain gages (foil) (31).
7. COD gages (3).

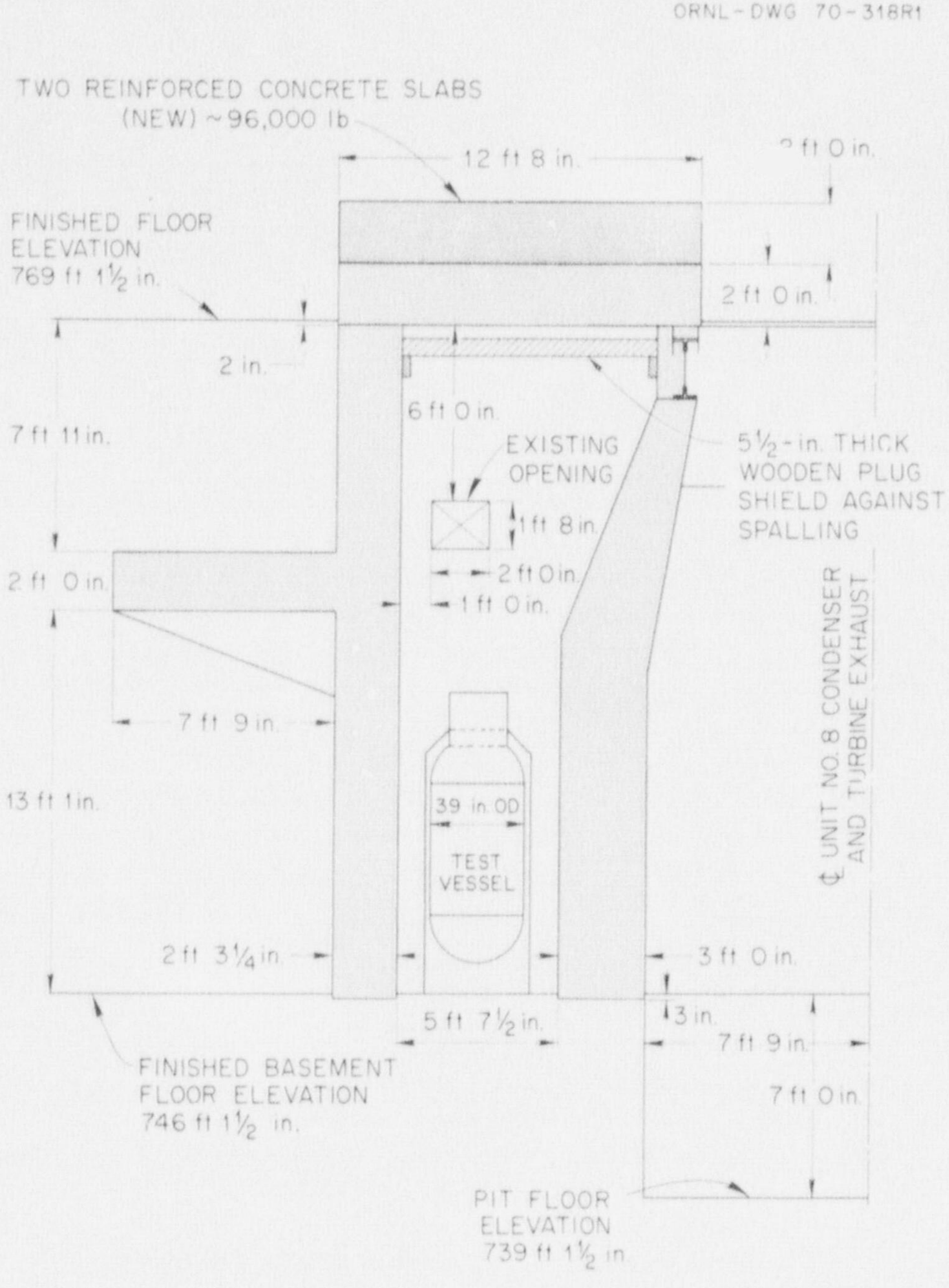

Fig. 3.1. Sectional view of intermediate vessel test pit.

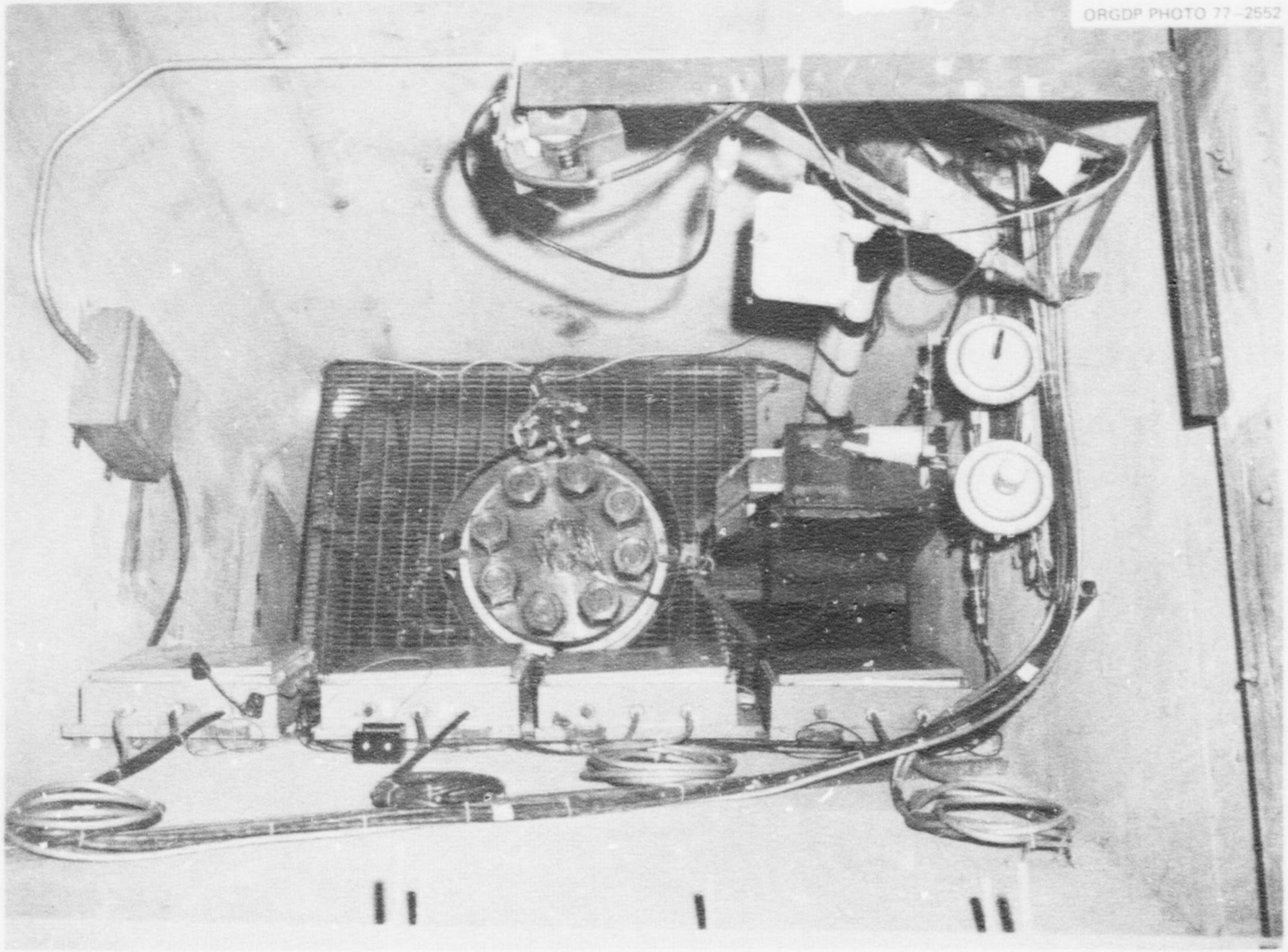

Fig. 3.2. View of V-7B in test pit.

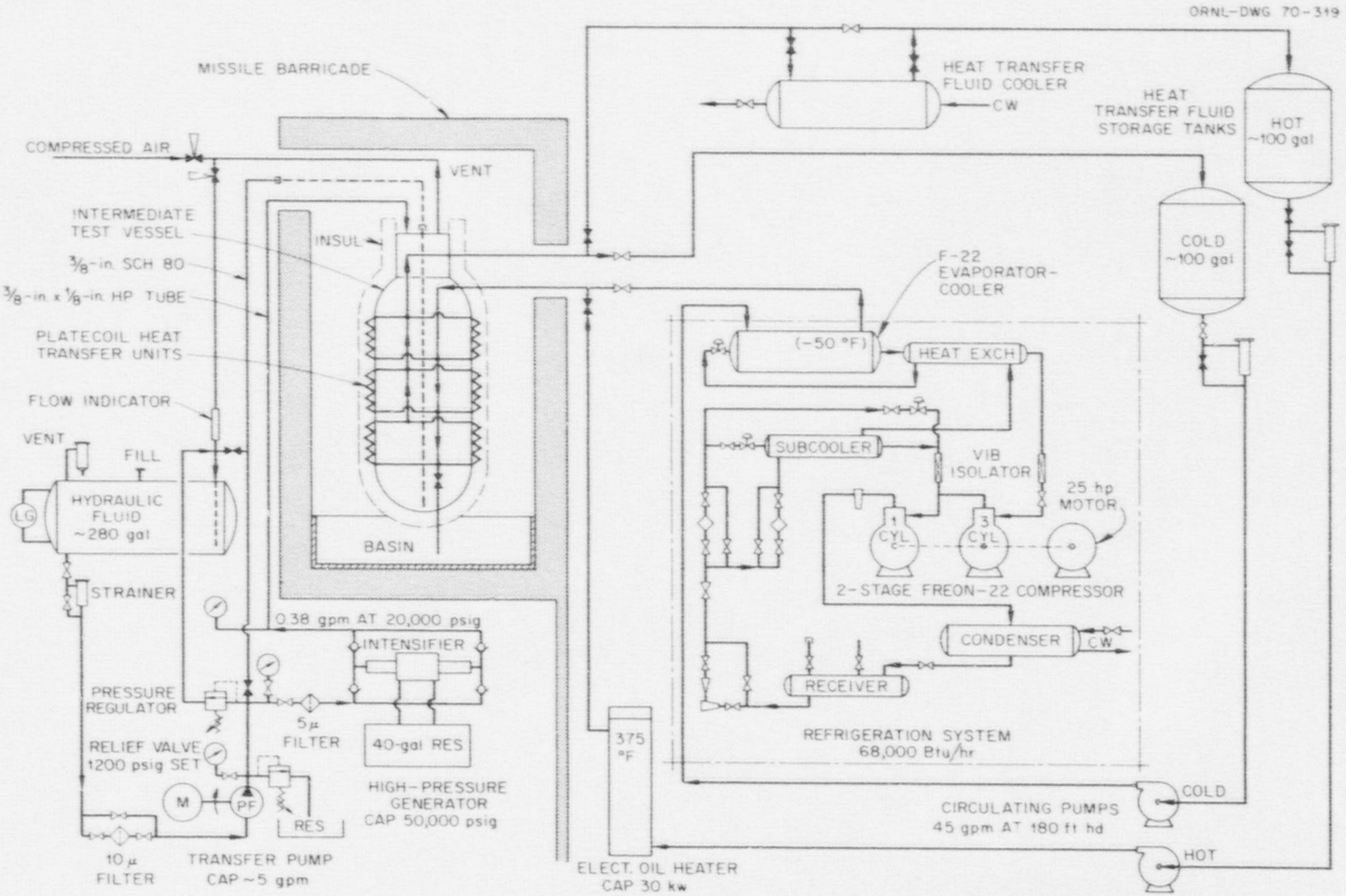

Fig. 3.3. Schematic flow diagram of intermediate vessel test facility.

Figure 3.4 depicts strain gage and thermocouple locations for V-7B. Two types of strain gages were used: Micromeasurements type EP-08-250 and Ailtech type SG 125. In both types the gage resistance was 120 Ω. The Micromeasurements foil gages are made from annealed Constantan foil on a flexible polyamide back and are used primarily where large strains are to be encountered. They were installed using M-Bond 200 cement. The Ailtech weldable gages utilize nickel-chrome gage elements encapsulated in stainless steel with MgO insulation. They are spot welded in place and have MgO-insulated stainless steel leads. The gage qualification and installation procedures were presented in Refs. 1 and 2.

Eighteen Chromel-Alumel thermocouples were used to monitor vessel temperature and insure the adequacy of the prescribed test conditions in the regions of interest. Crack-opening displacement (COD) measurements were made at three locations along the crack. Transtek linear displacement transducers, model 354-000, were mounted in supports as shown in Fig. 3.4, detail A. The supports were redesigned after some limited malfunction was detected in test V-7A. (See Ref. 5.) The COD devices performed satisfactorily on this test.

Two completely independent systems were used to measure pressure. A closed-circuit video system was used to directly view a conventional Bourdon pressure gage mounted near the high-pressure intensifier. This was a backup system to the primary strain-gage-based pressure cell (BLH) mounted in a static line connected to the vessel head. Two additional pressure cells of the same type were used, one to measure patch pressure and the other as a standby for the primary pressure cell.

Scanning closed-circuit television systems were also utilized for general surveillance of the test pit and pressurization system. A closeup view of the flaw was recorded by means of video tape during the test.

Acoustic emissions were monitored by two independent systems, one operated by Battelle Northwest and the other by ORNL personnel. The reports are included in Appendices B and C.

3.3 Data Acquisition

The primary system for data recording was a modified Datum System 70 computer-controlled data acquisition system (CCDAS). In addition to the basic 120 channels included in the CCDAS, three Hewlett-Packard dual-channel strip-chart recorders with independent conditioning and amplification circuits were utilized to maintain continuous recordings of pressures, COD gages, and selected strain gages. Two dual-pen X-Y plotters were also used for quick-look recordings of pressure vs COD gages and a selected strain gage. Ten strain gages were recorded on a separate system as a minimum data backup in the event of failure of the primary data system (the CCDAS). A Vishay/Ellis strain recording system with an integrated Texas Instruments Silent 700 recording terminal was utilized for this purpose.

In addition to the above equipment, which was located in the instrumentation trailer, signals were sent to the main control room to provide a pressure vs time recording and a digital readout of pressure. Signals from 8 of the 18 thermocouples were displayed on Honeywell recorders in the main control room. In summary, all data not recorded by the Vishay/Ellis system or Honeywell recorders were recorded using the CCDAS.

3.4 Test Procedures

3.4.1 Vessel preparation

After the vessel was flawed (see Chapter 2), it was transported to another Y-12 facility of the Engineering Technology Division for instrumentation. After all inside and part of the outside instrumentation was complete, the head was installed and the vessel was sealed and moved to the test pit. Heating coil plates were then installed, and exterior instrumentation was completed. Figure 3.5 shows the

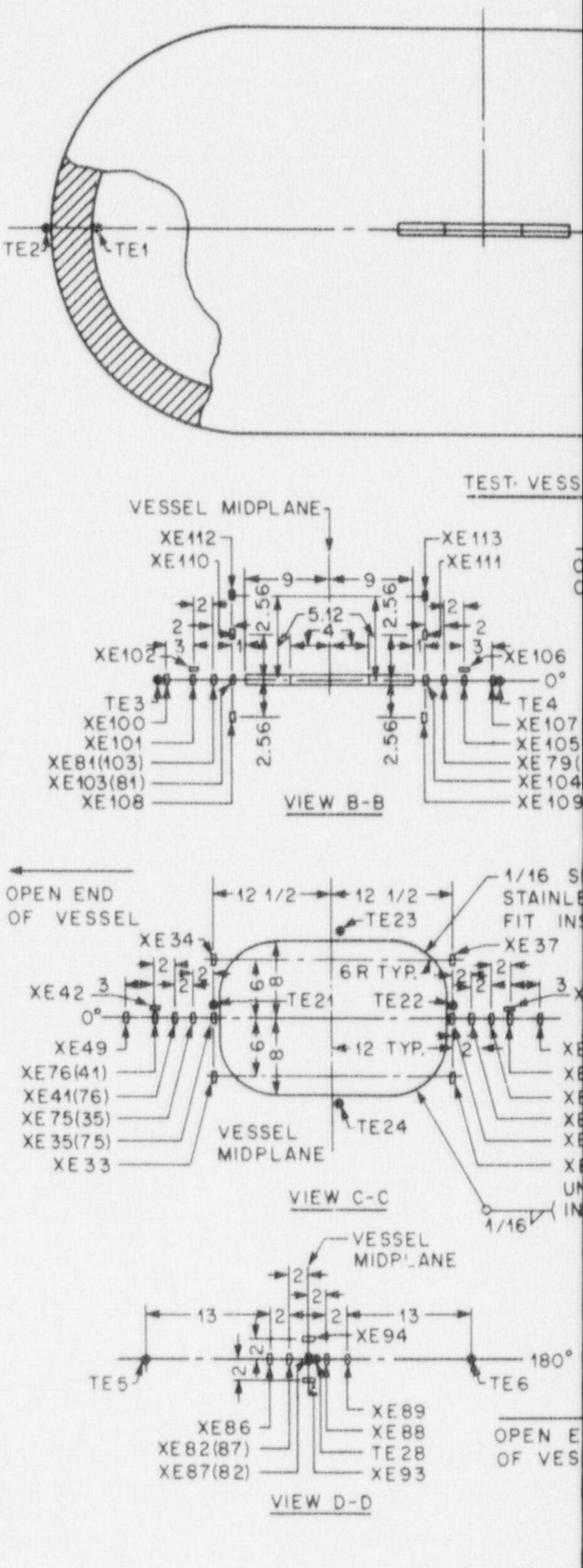

Fig. 3.4. Strain

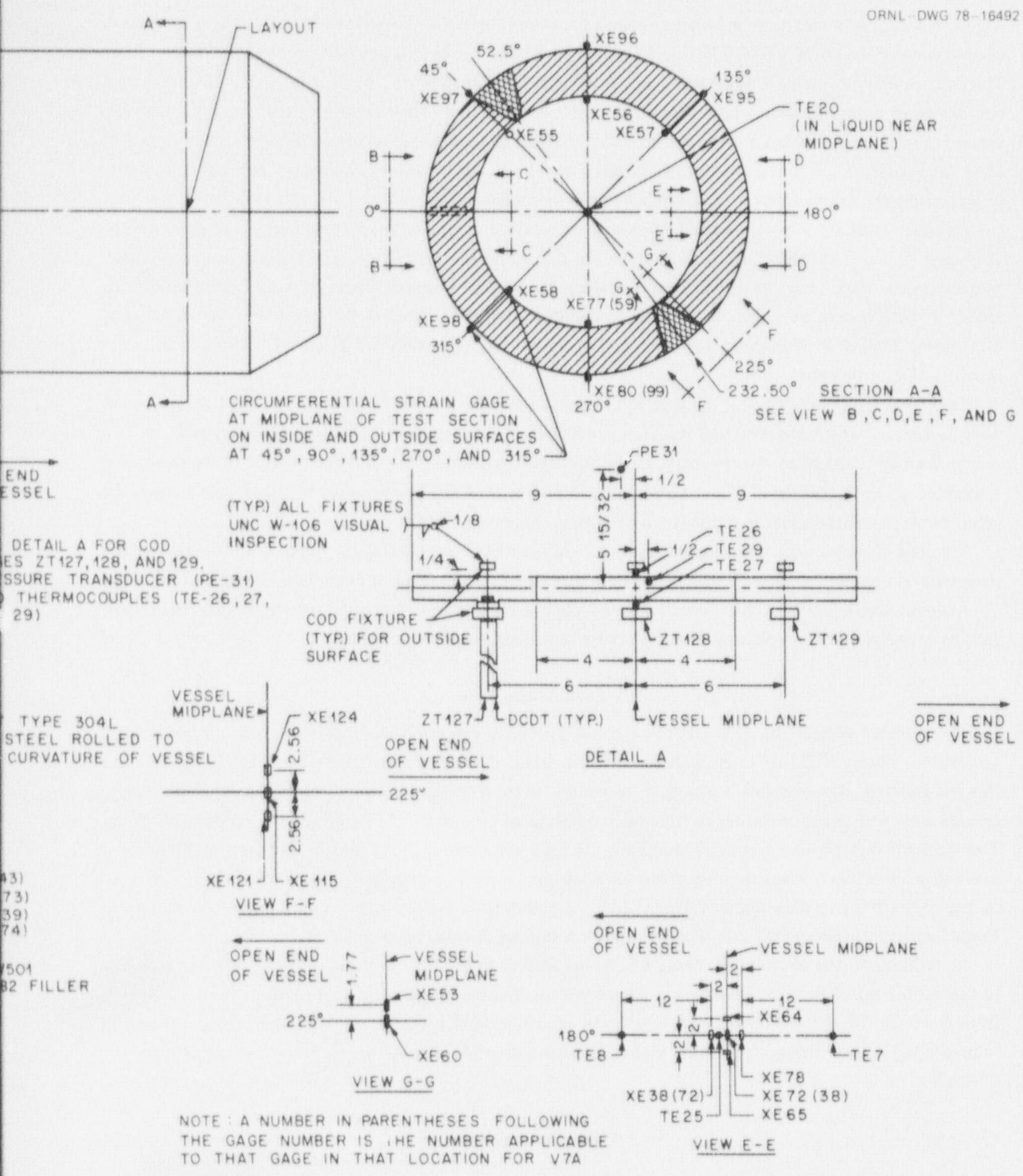

, COD transducer, and thermocouple locations for intermediate test vessel V-7B.

ORGDP PHOTO 77-2551

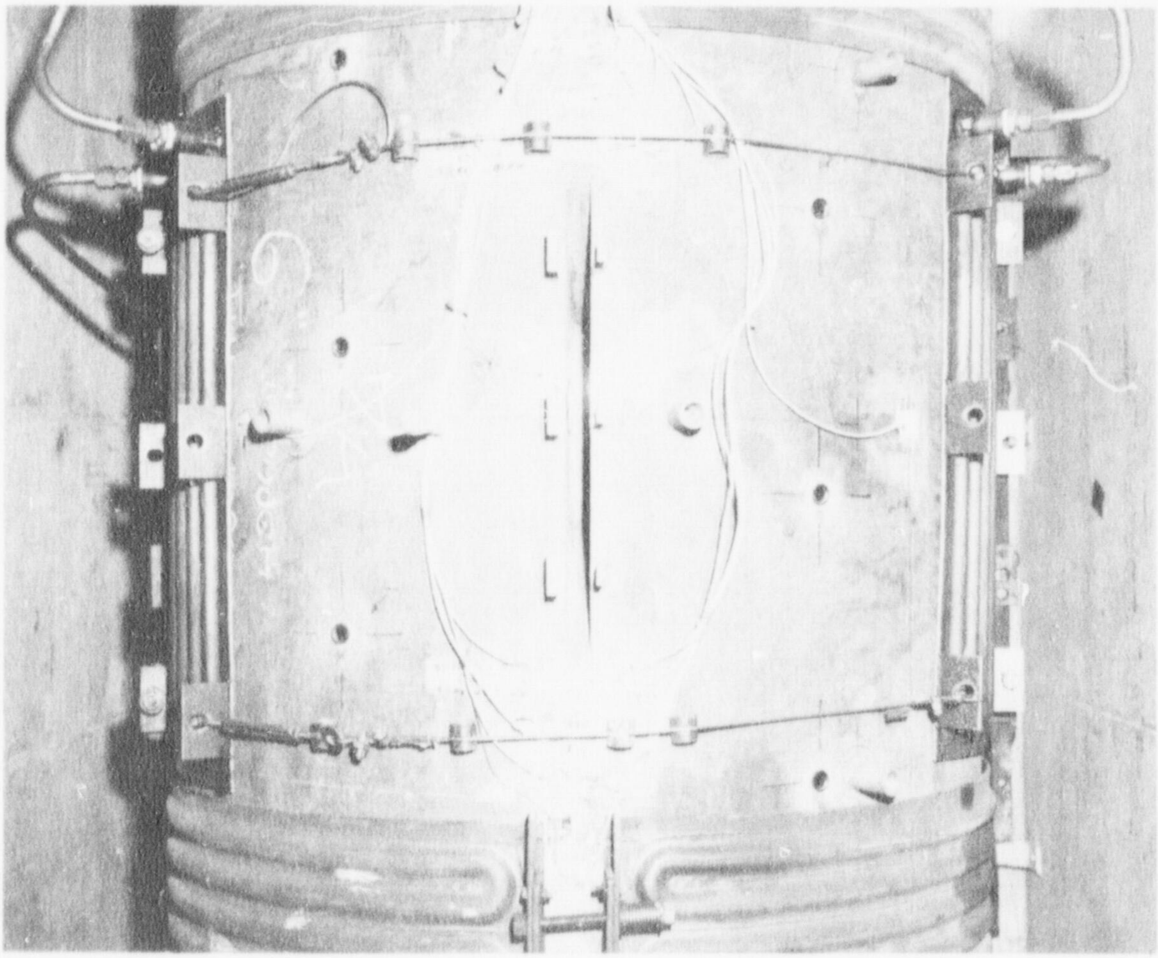

Fig. 3.5. Center of vessel V-7B in the test pit prior to test with part of exterior instrumentation.

midsection of the vessel in the test pit after the heating coils were attached. The view faces the flaw and shows some of the exterior instrumentation. After completion of the instrumentation and the connection of the lead wires to the control room, the vessel was covered with insulation and filled with demineralized water, and the pressure lines were connected. During the filling operation and while the vessel was being brought to the test temperature, installation of television and AE equipment was completed. After a final check on all data acquisition and recording equipment, the vessel was ready to test.

3.4.2 Pressure testing

The vessel was slowly brought to the testing temperature. A time vs temperature plot for the pressurization phase of a thermocouple located near the flaw is shown in Fig. 3.6. An initial set of data at zero pressure was recorded and pressurization was started. The vessel was pressurized to 72.7 MPa (10,500 psi) and then returned to zero as part of the test objective. The vessel was then repressurized to failure with scheduled hold times for evaluating data. A maximum pressure of 151.8 MPa (22.0 ksi) was attained and sustained nearly constant for about 2 min after the vessel ruptured.

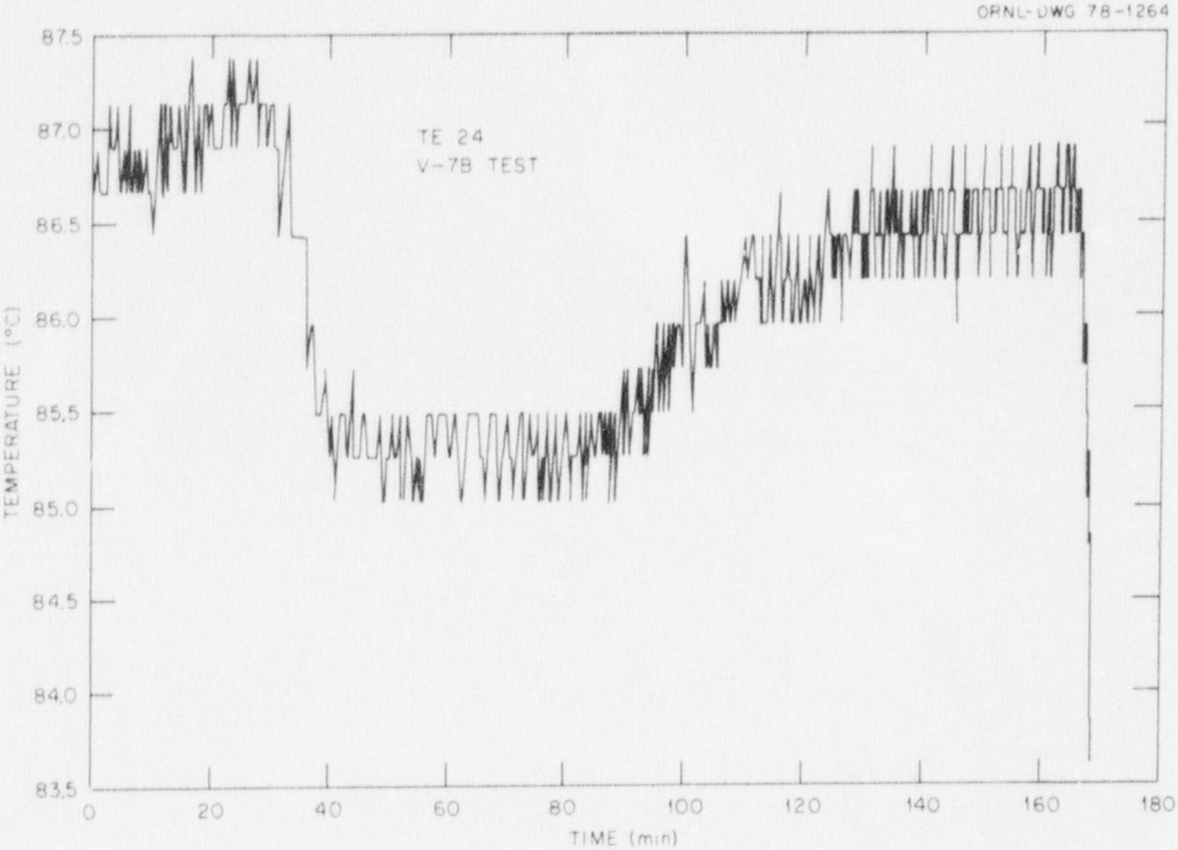

Fig. 3.6. Temperature history of V-7B test as measured by thermocouple TE 24 on inside surface near flaw.

The plan for data retrieval and intervals for the various systems is shown in Table 3.1, and a pressure vs time plot is shown in Fig. 3.7. When indications of imminent failure were observed, data were taken continuously where possible and the strip-chart recorders were speeded up. A final set of data was recorded from surviving instrumentation at zero pressure following the test.

3.5 Test Results

The test resulted in a rupture of the ligament at the time of maximum pressure. After a period of about 2 min, during which the pressure varied slightly, the pressure-retaining patch ruptured and the vessel depressurized completely through the flaw.

The COD data from the three displacement transducers are presented in Fig. 3.8. It is evident in the behavior of the COD transducer ZT 128 that this gage was affected by the rupture events, perhaps by the impact of escaping water. Figure 3.9 shows circumferential strain at 180° from the flaw, indicating gross vessel behavior.

A posttest view of vessel V-7B is given in Fig. 3.10. Permanent deformation of the flaw can be detected along with crack extension at the ends of the machined notch. Complete data from the CCDAS are shown via microfiche described in Appendix A and attached to the inside back cover.

Table 3.1. Approximate scan and output intervals for permanent records V-7B

	Intervals (Δp and Δt) for pressure (ksi) in range:					
Output	0–5	5–10	10–15	15–18	>18	Any pressure with unstable behavior[a]; depressurization
CCDAS scan, sec	1	1	1	1	1	1
CCDAS magnetic tape,[b] sec	25	25	25	10	4	4 or 2, as required
CCDAS printer,[c] psi (min)	1000 (5)	1000 (5)	500 (5)	500 (5)		Only as needed
Vishay magnetic cassette, paper tape printer and line printer,[d] psi	500	500	500	500	200	Continuous scan

[a] If strains or CODs recorded on X-YY′ plotters or strip-chart recorders show a tendency to change with little or no increase in pressure, the CCDAS should scan and record at the maximum rate. Under these conditions scanning should not be interrupted for printouts.

[b] If the test is interrupted by operational problems, the tape recording interval should be extended to 300 sec. Recording intervals longer than those specified may also be required during long periods of nearly constant pressure.

[c] Since printing interrupts recording of data, printing should be avoided as much as possible at elevated pressure. X-Y plotter output of three CODs and one strain gage is available. Also, selected data may be read directly from the CCDAS digital display. Pressure will be on a digital display continuously in the control room.

[d] Scan rate is about one point per second.

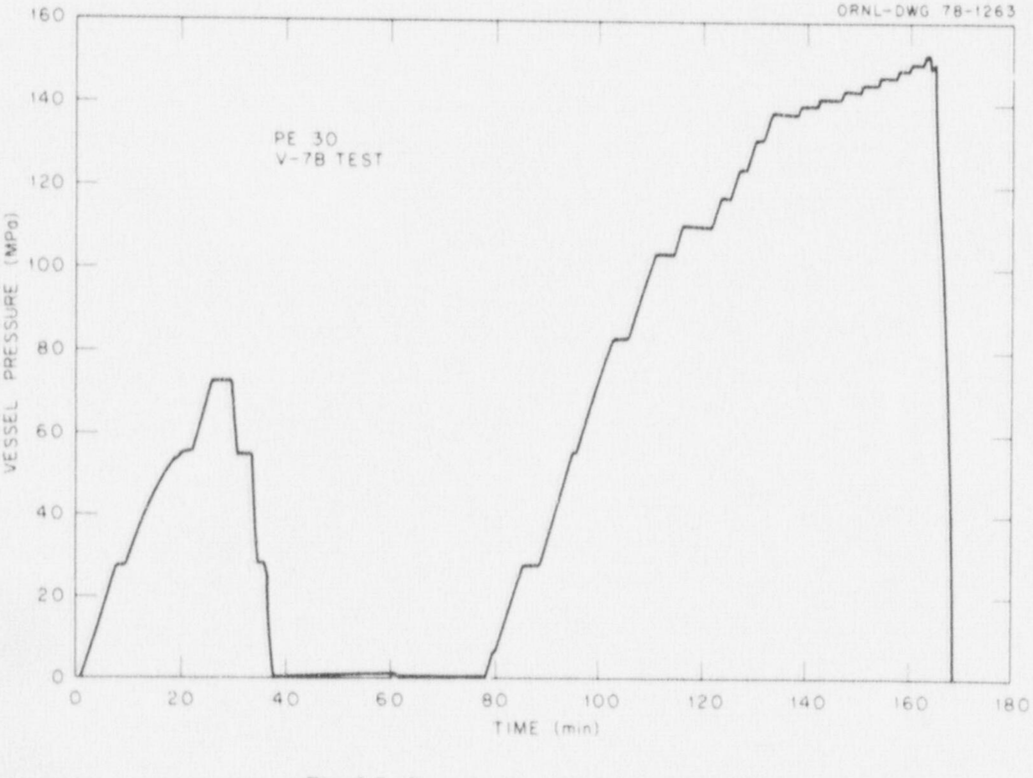

Fig. 3.7. Pressure history of V-7B test.

ORNL DWG 78 16493

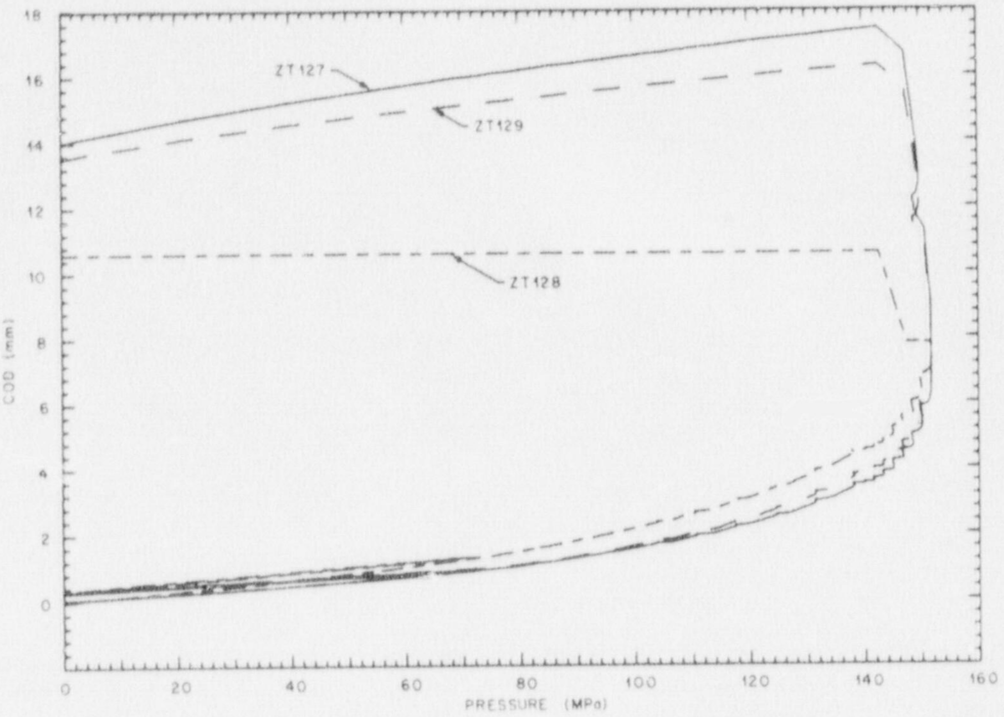

Fig. 3.8. COD vs pressure for V-7B.

ORNL DWG 78 16687

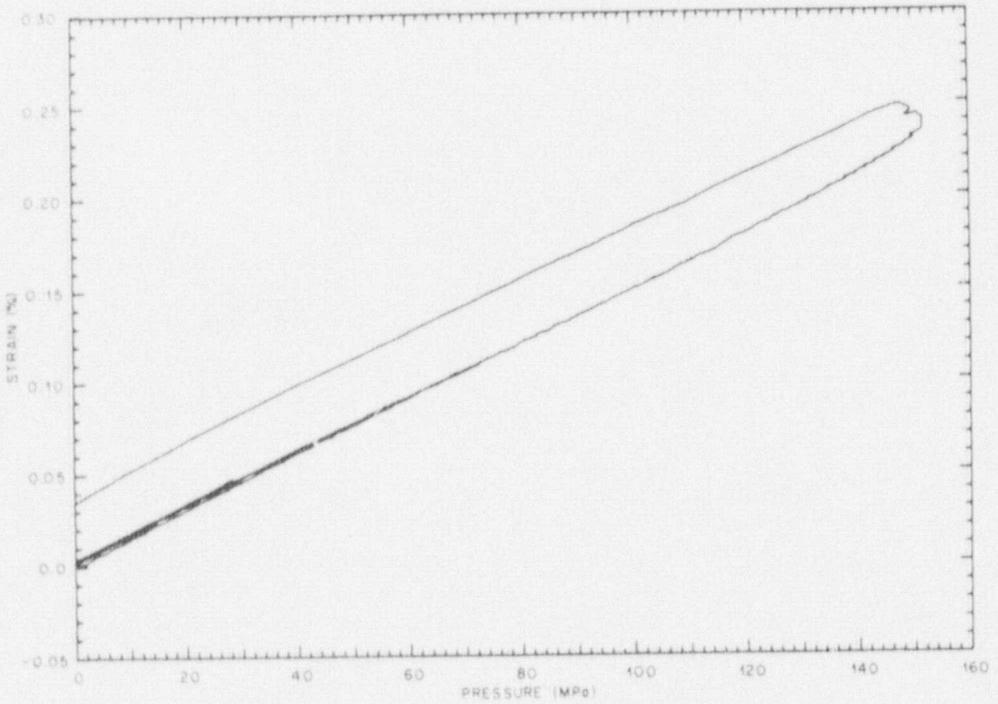

Fig. 3.9. Typical strain vs pressure for V-7B. Inside circumferential strain 180° from flaw (XE 38).

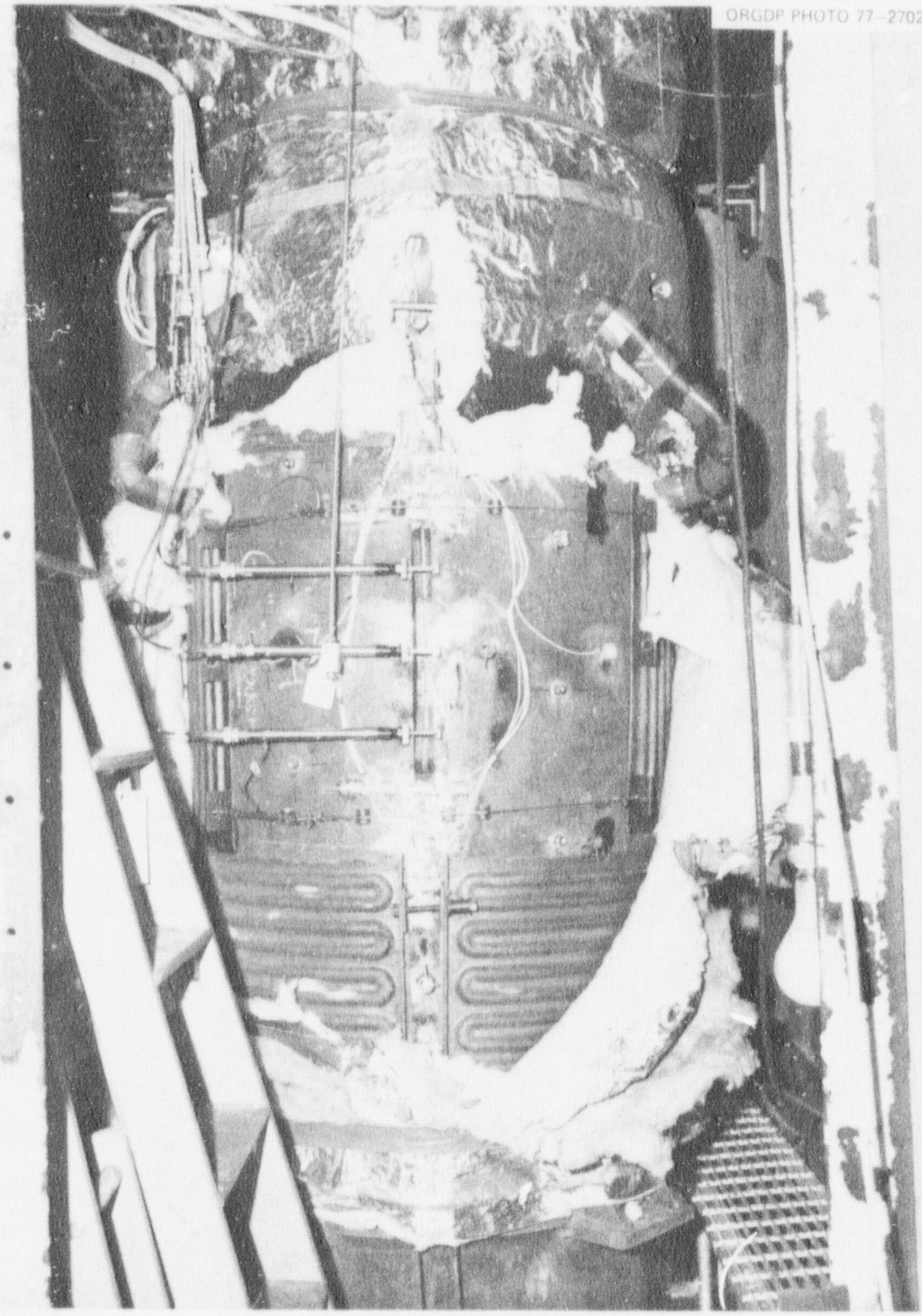

Fig. 3.10. Test vessel V-7B in pit after test.

References

1. R. W. Derby et al., *Test of 6-inch-thick Pressure Vessels. Series 1: Intermediate Test Vessels V-1 and V-2,* ORNL-4895 (February 1974).

2. R. H. Bryan et al., *Test of 6-in.-thick Pressure Vessels. Series 2: Intermediate Test Vessels V-3, V-4, and V-6,* ORNL-5059 (November 1975).

3. J. G. Merkle et al., *Test of 6-in.-thick Pressure Vessels. Series 3: Intermediate Test Vessel V-7,* ORNL/NUREG-1 (August 1976).

4. J. G. Merkle et al., *Test of 6-inch-thick Pressure Vessels. Series 4: Intermediate Test Vessels V-5 and V-9,* ORNL/NUREG-7 (August 1977).

5. R. H. Bryan et al., *Test of 6-in.-thick Pressure Vessels. Series 3: Intermediate Test Vessel V-7A Under Sustained Loading,* ORNL/NUREG-9 (February 1978).

6. C. L. Segaser, *System Design Description of the Intermediate Vessel Tests for the Heavy-Section Steel Technology Program,* ORNL/TM-2849 (June 1970), revised July 1973.

4

Pretest Fracture Analysis and Test Results

4.1 Results of Prior Tests of Vessel

The tests of vessels V-7 and V-7A were preceded by extensive analytical studies and tests of steel scale models in order (1) to investigate the modes of failure of a vessel with a long flaw, (2) to predict the mode of failure and the failure pressure, and (3) to determine the flaw dimensions that would produce the desired result.[1,2] Three types of pretest analyses are described in Ref. 1: local plastic instability, ligament rupture, and axial crack instability (burst). Further study of the burst analysis is discussed in Ref. 2. The V-7 test parameters were originally chosen with the objective that the test would be a demonstration of a leak-without-burst at a pressure not too far above the design pressure of 66.9 MPa (9710 psi). The leak pressure predicted before the first test was slightly higher than two times the design pressure.

The V-7 test was a demonstration of the expected flaw behavior with the vessel pressurized hydraulically; the vessel failed by ligament separation without bursting. The subsequent test, V-7A, was a repetition of test V-7 with an identical flaw located far from the original flaw, where the material was least affected by the first test. In the V-7A test, however, the vessel was pressurized pneumatically and the load was sustained after rupture to provide more conclusive evidence that the vessel was stable against burst at the leak pressure.

These two tests established a leakage pressure with little uncertainty, the variance deviating only 1% from the mean, as indicated in Table 4.1. They also provided an extensive set of data on the prefailure response of the vessel and the flaw to changes in pressure. The sustained-load phases of the V-7A test provided, in addition, data on the time-dependent behavior of the vessel.

This background of quantitative information on two nearly identical tests presented an opportunity for experimentally investigating a further variation of the V-7 test configuration, namely, a long, deep flaw in a

Table 4.1. Test results for vessels V-7 and V-7A

Test	P_f (MPa)	
	At time of leak	Variance from mean
V-7	147.2	1.48
V-7A	144.2	−1.48
Mean	145.7	

Section XI half-bead weld repair zone. Accordingly, the V-7B flaw was designed to be geometrically identical to the V-7 and V-7A flaws and was placed as close to the plane of the V-7A flaw as was practicable (see Figs. 2.3 and 2.33).

In the repaired and flawed vessel, V-7B, the conditions that could potentially cause the behavior of V-7B to differ from that of V-7 and V-7A were:

1. general residual deformation in the vessel, particularly near the V-7B flaw location,
2. residual stresses from the preceding tests as further modified by the repair,
3. residual stresses induced by the repair welding,
4. mechanical properties at the crack tip (in the HAZ) different from the properties of the ASTM A533, grade B, class 1 base material,
5. inhomogeneous mechanical properties near the crack.

The first two conditions could be ascertained only qualitatively from V-7 and V-7A strain data and posttest measurements. The other conditions were assessed in more quantitative terms by the residual stress and material characterization studies described in Chapter 2.

4.2 Evaluation of Expected Results

Test V-7B was planned to evaluate the strength of repair weldments containing flaws. The V-7B flaw was located in the heat-affected zone (HAZ) of the second repair weld, because that region of a weldment is particularly subject to a loss of toughness if it is not properly heat treated after welding. The plane of the flaw in V-7B was 7.5° from that in V-7A, as shown in Figs. 2.3 and 2.33. Therefore, as the data in Chapter 2 indicate, the crack tip was expected to lie initially in HAZ material of significantly higher toughness and tensile strength than either the base metal or the repair weld metal. The properties of the three zones are compared in Table 4.2.

Table 4.2. Comparative properties of various parts of the V-7B repair zone as determined from the prototypic weldment

Material	PCC$_V$ K_{Icd}[a] (MN·m$^{-3/2}$)	Yield (MPa)	Hardness (DPH)
Base	192–268	434 (center)–517 (surface)	184–207
HAZ	254–362		248–314
Repair weld	219	463–467	190–228

[a] At 93°C (200°F).

The relatively high toughness of the HAZ led to the conclusion that stable tearing of the flaw might not commence at as low a pressure as in V-7 and V-7A. The onset of tearing in these two tests was indicated ultrasonically between 90 and 105 MPa (13 and 15 ksi). According to the analysis of ligament behavior in V-7, the greater toughness of the HAZ would change the pressure for the onset of stable crack extension by about 50%. Prior to test V-7B, however, this result could not be assured since the actual location of the crack tip was uncertain.

Regardless of whether the crack was initially in the HAZ or not, its ultimate behavior was expected to be controlled by the properties of the base material and repair weld. The HAZ is generally thin, and its superiority in toughness and tensile properties over the surrounding material tends to make the crack grow into the weaker material and thereafter avoid the HAZ. This behavior had been observed in the precracked Charpy specimen, as shown in Fig. 2.21.

The vessel V-7B mode of failure was predicted to be the same as for V-7 and V-7A, that is, leak but not burst. The methods of analysis of vessel V-7, described in detail in Ref. 1, were believed to be applicable to vessel V-7B. These analyses and the actual behavior of the ligament and end regions of the flaw observed in V-7 and V-7A were the basis of the V-7B prediction. The condition of the flaw zone was known, however, to be different in two respects. First, the previous test had produced a slight permanent bulge. Second, the V-7A test had also induced residual stresses in the neighborhood of the V-7A flaw which were further modified by the preparation for repair welding and by the welding itself. These differences were taken into account.

In the assessment of the pressure at which the ligament would rupture (and the vessel would leak), it is important to note that stable crack extension through the ligament was observed ultrasonically in both V-7 and V-7A (Refs. 1 and 2). Furthermore, the ligament strains, which were measured in V-7 only, were high prior to rupture (exceeding 7%) as shown in Fig. 4.1. It was inferred from this information that stable tearing in the ligament could be considered as being controlled principally by the displacement imposed on the ligament by the deformation of the flaw region and the vessel, while the thin ligament had negligible influence on the vessel. With this conception of the tearing process, the V-7 data imply that ultimate ligament strains (i.e., at failure) would be so high that the maximum possible residual stresses would not appreciably alter the failure pressure.

The propensity for burst of vessel V-7B was evaluated on the supposition, discussed above, that the initial crack would grow stably out of the tough HAZ and thereafter be controlled by the properties of the weld or base metal. It was also presumed that stable crack extension would not be significantly different from that observed in V-7 and V-7A. The value of fracture toughness of weld metal measured before the test was in the midrange of base metal values, as shown in Table 4.2. This fact and the insensitivity of burst pressure to variations in K_{Ic} (Ref. 2) led to the conclusion that the vessel would not burst.

4.3 V-7B Test Results

This section presents measurements that generally characterize the behavior of vessel V-7B in comparison with vessel V-7A test data and analyses. The complete record of pressure, strain, crack-opening displacement (COD), and temperature data are presented on microfiche, as described in Appendix A. Results of the examination of the flaw after the test are included in this section. Complete reports on acoustic emission (AE) monitoring are included in Appendices B and C.

Vessel V-7B was tested by hydraulic pressurization through the two cycles shown in Fig. 3.7. As in the case of V-7A, the response of the vessel during the first cycle was linear except very near the flaw, where the deviations from linearity were very small. The second cycle of test V-7B, which started at atmospheric pressure, is comparable to the rising-load composite of cycles 1, 3, and 4 and the final depressurization of V-7A. Comparisons of strain and COD vs pressure in V-7A and V-7B will be made for these cycles. In the second cycle, vessel V-7B was pressurized until it leaked at 151.8 MPa (22.0 ksi). Test conditions and failure pressures in vessels V-7, V-7A, and V-7B are summarized in Table 4.3.

4.3.1 Strain behavior

The overall response of the vessels is shown by the examination of circumferential strains measured around the vessel at the circumferential midplane of the flaw. Locations of strain gages on this plane are

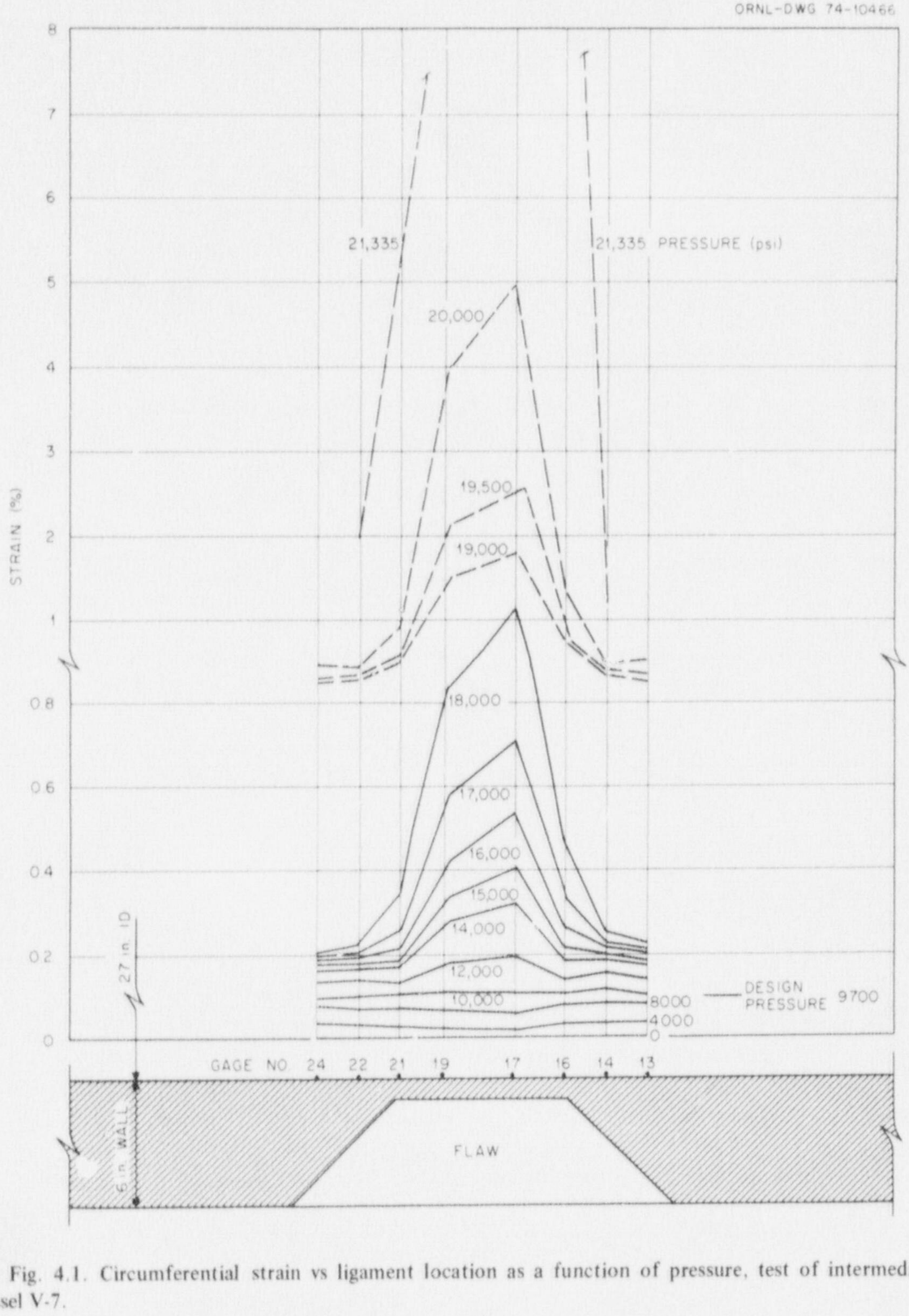

Fig. 4.1. Circumferential strain vs ligament location as a function of pressure, test of intermediate vessel V-7.

Table 4.3. Test conditions and failure pressures in vessels V-7, V-7A, and V-7B

Vessel	Pressurizing fluid	Test temperature (°C)	Failure pressure (MPa)	Mode of failure
V-7	Water	91	147.2	Leak
V-7A	Nitrogen	88	144.2	Leak with stable crack under sustained load
V-7B	Water	87	151.8	Leak with continued flaw growth under sustained load

shown in Fig. 4.2. Inside and outside strains of V-7B are compared with those of V-7A in Figs. 4.3 through 4.8.

Typical behavior of the vessel in the region of the flaw is shown by the strains at locations identified in Fig. 4.9. Strain vs pressure plots of V-7B are compared with those of V-7A in Fig. 4.10. Other strains near the flaw are shown in Figs. 4.11 to 4.13. The strains are plotted in pairs for locations that are symmetrical relative to the flaw. Since the flaw is on the boundary between weld metal and base metal, the differences in response of the two types of material are shown in Fig. 4.13*a* and *b*. There is a consistent pattern in the differences in strain at symmetrical locations; generally, strains were higher at the points of higher residual stress, whereas no differences could otherwise be attributed to the material itself.

4.3.2 COD behavior

The COD of vessel V-7B is shown in Fig. 4.14 in comparison with values calculated prior to the V-7A test. Modification of the COD mounts for test V-7B apparently improved the sensitivity and accuracy of the measurements, especially at low pressure.

The measured CODs at the center of the flaw of V-7B and V-7A are compared in Fig. 4.15. Sensors ZT127, ZT128, and ZT129 measured displacements 25.4 mm (1 in.) above the outside surface of the vessel. Sensor ZT128 was on the flaw centerline, while the other two were near opposite ends 152 mm (6 in.) from the centerline. The three CODs of vessel V-7B are shown in Fig. 4.16 as a function of rising pressure.

4.3.3 Sustained-load behavior at rupture

Vessel and patch ruptures were observed by video monitor and by strip-chart records of patch and vessel pressure. It was noted at the time of rupture that CODs were increasing rapidly, possibly indicating unstable, but slow, crack extension. Posttest data plots allowed a detailed study of several concurrent changes during the rupture phase that were too subtle and rapid to be noticed during the test. The series of plots in Figs. 4.17 through 4.20 show the changes as a function of time and lead to the conclusion that the axial tearing at constant load commenced within a few seconds of the time of ligament rupture.

Figure 4.17 covers a period of time including the last three pressurization steps. Vessel rupture as sensed by the patch pressurization system (PPS) caused the large drop in patch pressure shown in this figure. Patch rupture about 70 sec later repressurized this system and initiated the complete depressurization of the vessel. The COD measurements superimposed on the pressure plot in Fig. 4.17 show that the flaw was probably growing at constant pressure about 30 sec prior to the indication of rupture by the PPS.

The development of this apparent instability and its relationship to the actual time of rupture are seen more clearly in Figs. 4.18 and 4.19. Figure 4.18 shows that the center COD gage (ZT 128) was subjected to

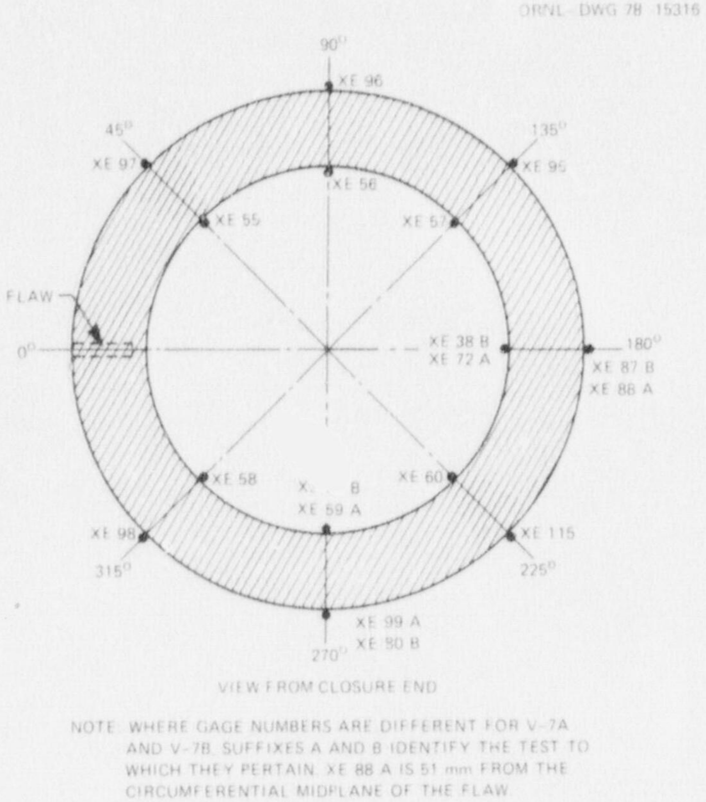

Fig. 4.2. Locations of strain gages in circumferential midplane of flaw relative to flaw location in vessels V-7A and V-7B.

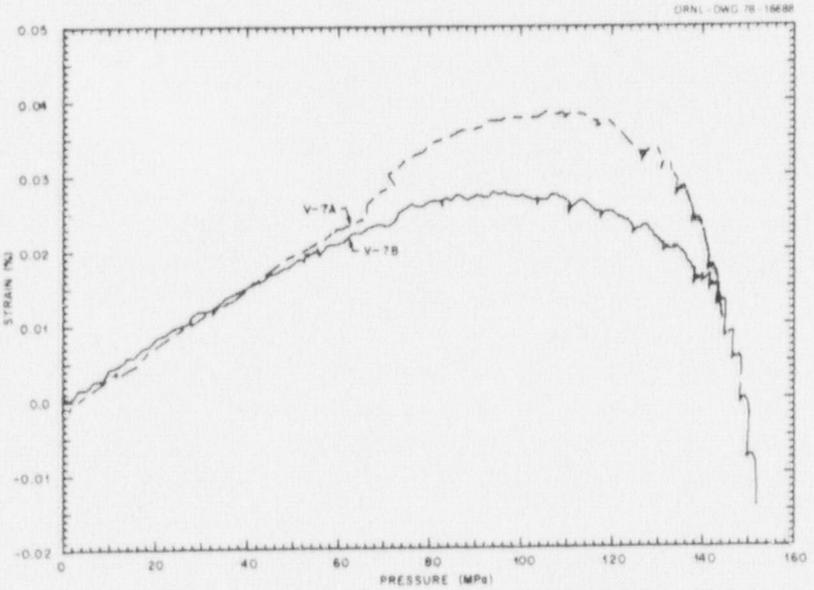

Fig. 4.3. Outside (XE 97) circumferential strain 45° from flaw vs pressure. Data plotted for rising pressure only.

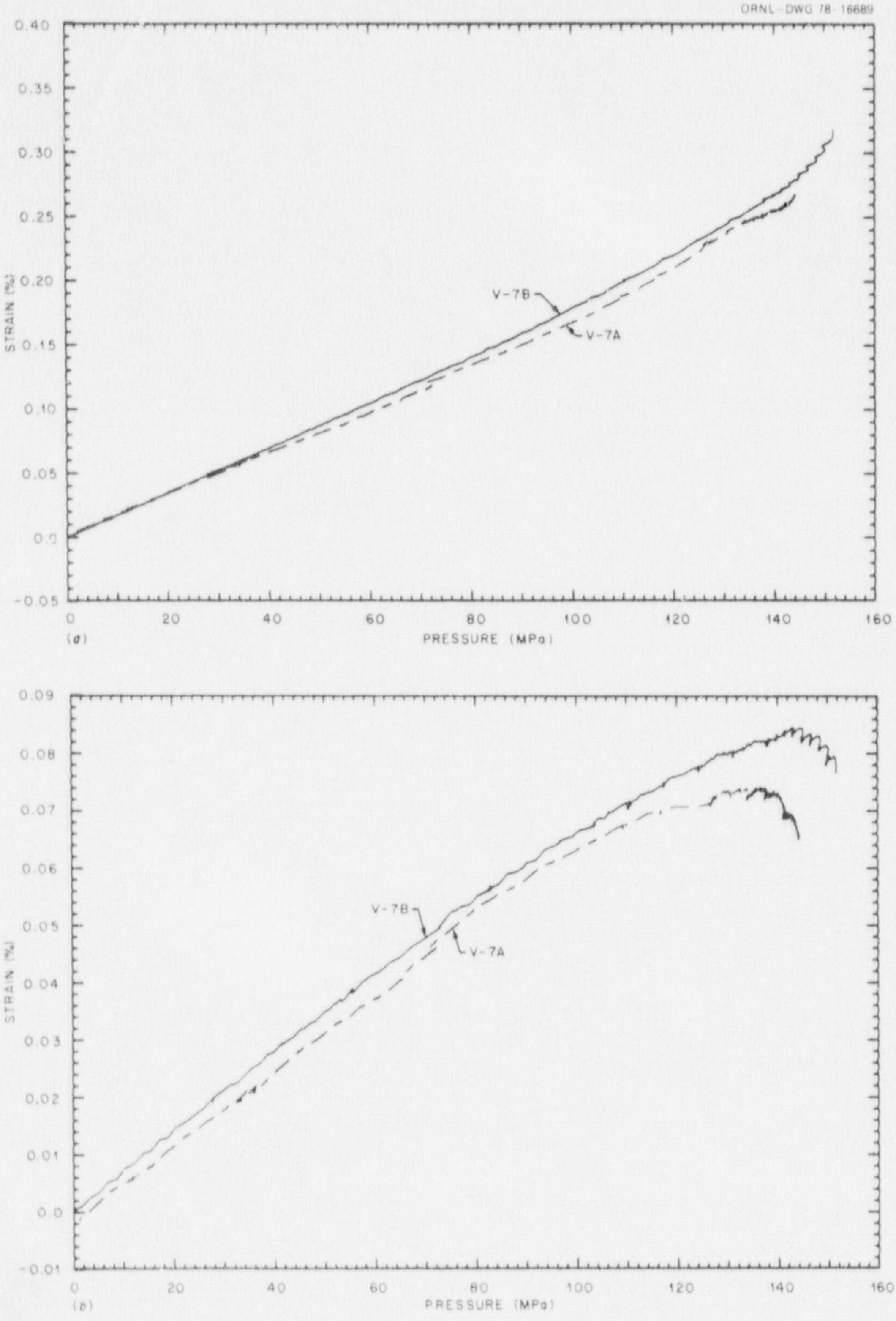

Fig. 4.4. Circumferential strain 90° from flaw vs pressure. (*a*) Inside (XE 56), (*b*) outside (XE 96). Data plotted for rising pressure only.

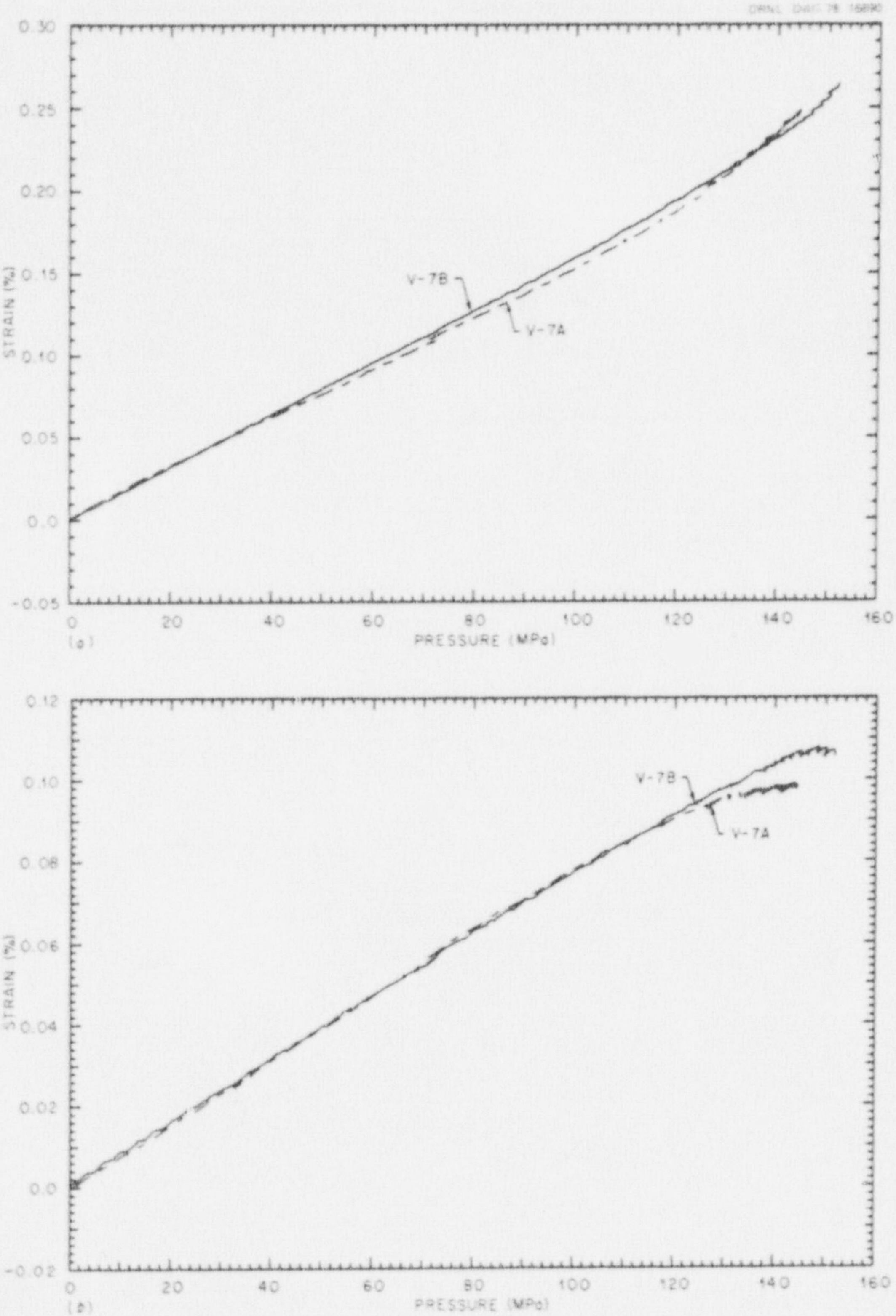

Fig. 4.5. Circumferential strain 135° from flaw vs pressure. (*a*) Inside (XE 57), (*b*) outside (XE 95). Data plotted for rising pressure only.

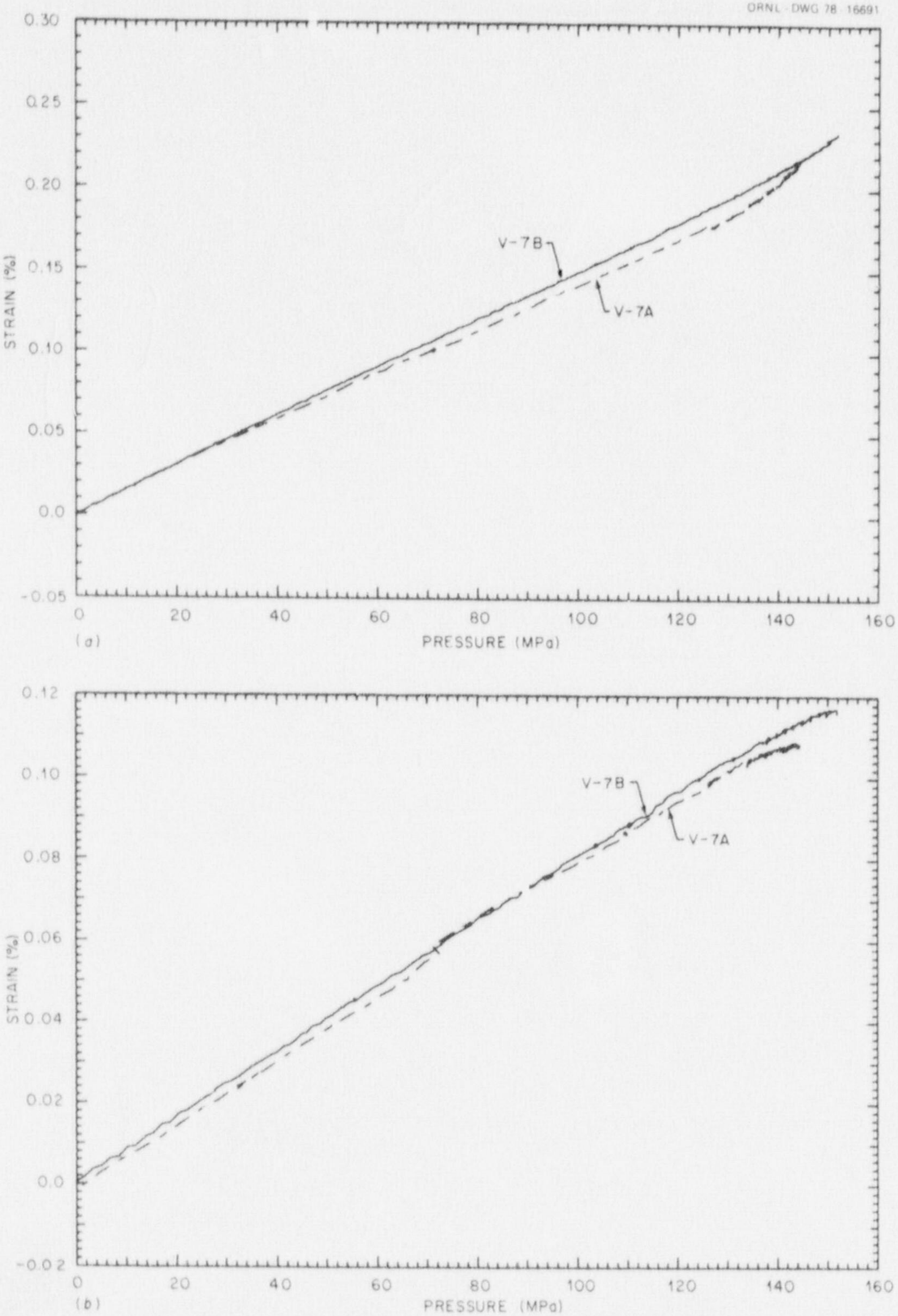

Fig. 4.6. Circumferential strain 180° from flaw vs pressure. (*a*) Inside, (*b*) outside. Data plotted for rising pressure only. Inside gages XE 72 and 38 and outside gages 88 and 87 for vessels V-7A and V-7B, respectively.

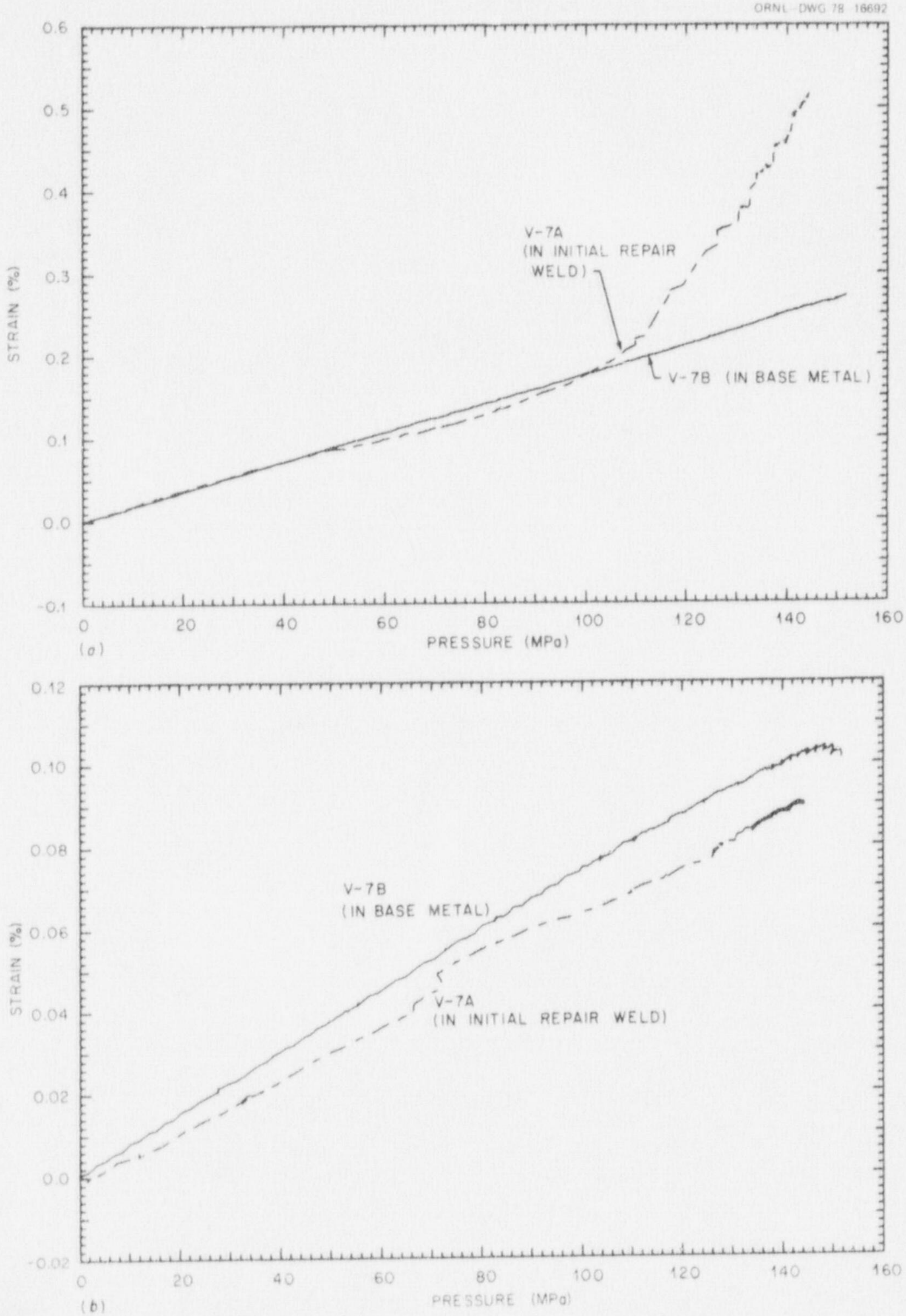

Fig. 4.7. Circumferential strain 225° from flaw vs pressure. (*a*) Inside (XE 60), (*b*) outside (XE 115). Data plotted for rising pressure only.

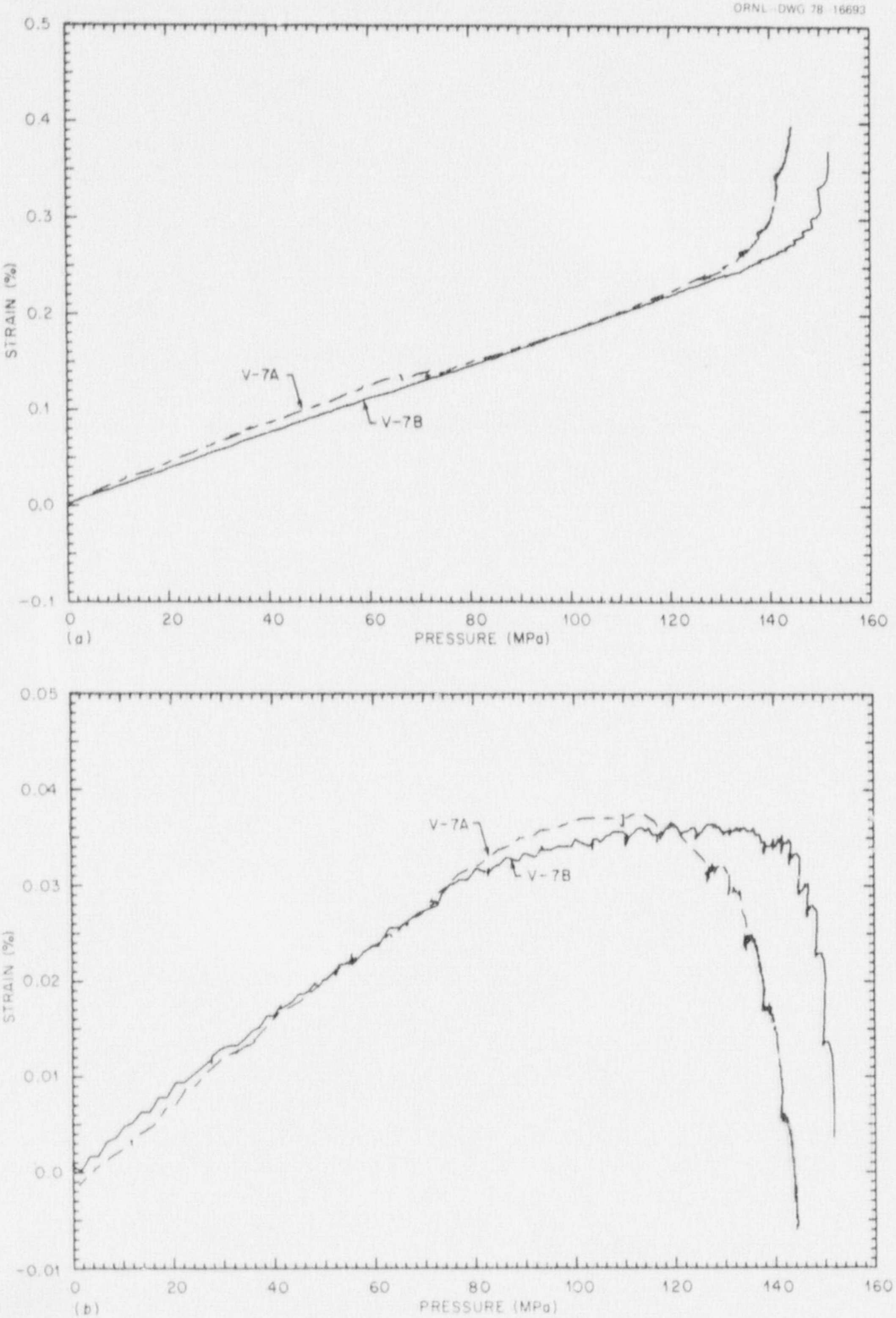

Fig. 4.8. Circumferential strain 315° from flaw vs pressure. (*a*) Inside (XE 58), (*b*) outside (XE 98). Data plotted for rising pressure only.

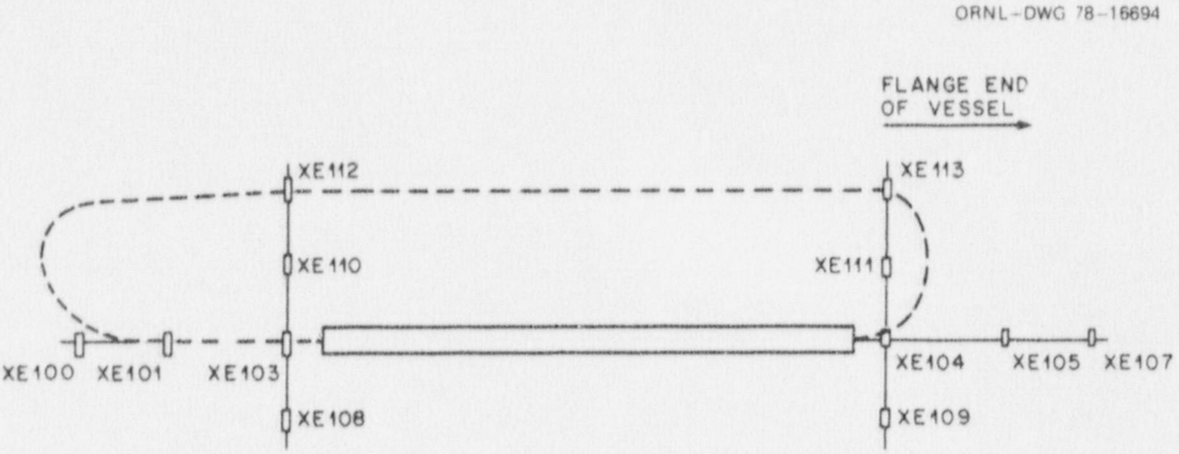

Fig. 4.9. Location of strain gages for which strains near the flaw on vessel V-7B are plotted.

an extraneous force twice within about 120 sec; the second occasion occurred coincident with the patch rupture, which released a hard stream of water against the center COD probe. The earlier perturbation in ZT 128 is believed to have been caused by a similar impact during the rupture of the vessel. Thus we consider the time of this perturbation to be the nominal time of rupture, although leakage may have started a few seconds earlier.

With this definition of nominal time of rupture as a reference point, the concurrent behavior of several variables is as shown in Fig. 4.19. The CODs were accelerating during the times after nominal rupture when vessel pressure was steady or increasing. This indicates that axial tearing of the flaw was probably taking place after rupture; this type of behavior did not occur during earlier pressurization steps or in the pneumatic V-7A test. A small temperature excursion of about 1 K (2°F) was observed near both ends of the flaw and in the ligament, as shown for one of these locations in Fig. 4.19. This occurrence is also unique to the rupture phase of the test and is consistent with the supposition that deformation and tearing at this time heated the metal. If this is the case, the ligament may have ruptured initially near one end rather than in the center since the central ligament temperature continued to increase after the nominal time of rupture until the rupture became large enough to affect the patch pressurization system. At that time the escaping fluid, chilled by expansion, cooled the notch as shown in Fig. 4.20.

The stability of the V-7B flaw relative to the V-7A flaw may be indicated by a comparison of the CODs of the two vessels at about the same pressure. Vessel V-7A attained a maximum pressure of 144.2 MPa (20.9 ksi) prior to rupture, and that pressure was sustained within about 1% for 30 min after rupture. The fourth pressure plateau prior to reaching maximum pressure in V-7B was at a comparable pressure, 145.1 MPa (21.0 ksi). Figure 4.21 shows the central CODs vs time for these two cases. This comparison suggests that at comparable loads vessel V-7B was as stable as V-7A.

4.3.4 Posttest fracture examinations

Visual and ultrasonic examinations after the test disclosed that the crack extension in V-7B was much larger than that in V-7 and V-7A. Figure 4.22 shows vessel V-7B after the test. Measurements were made by use of a thin-wire probe to determine the crack extension insofar as the crack was straight enough to allow the probe to penetrate. The vessel was examined ultrasonically to aid in determining the lines along which cuts would be made to remove the flawed region and to investigate an area nearby that was the site of high

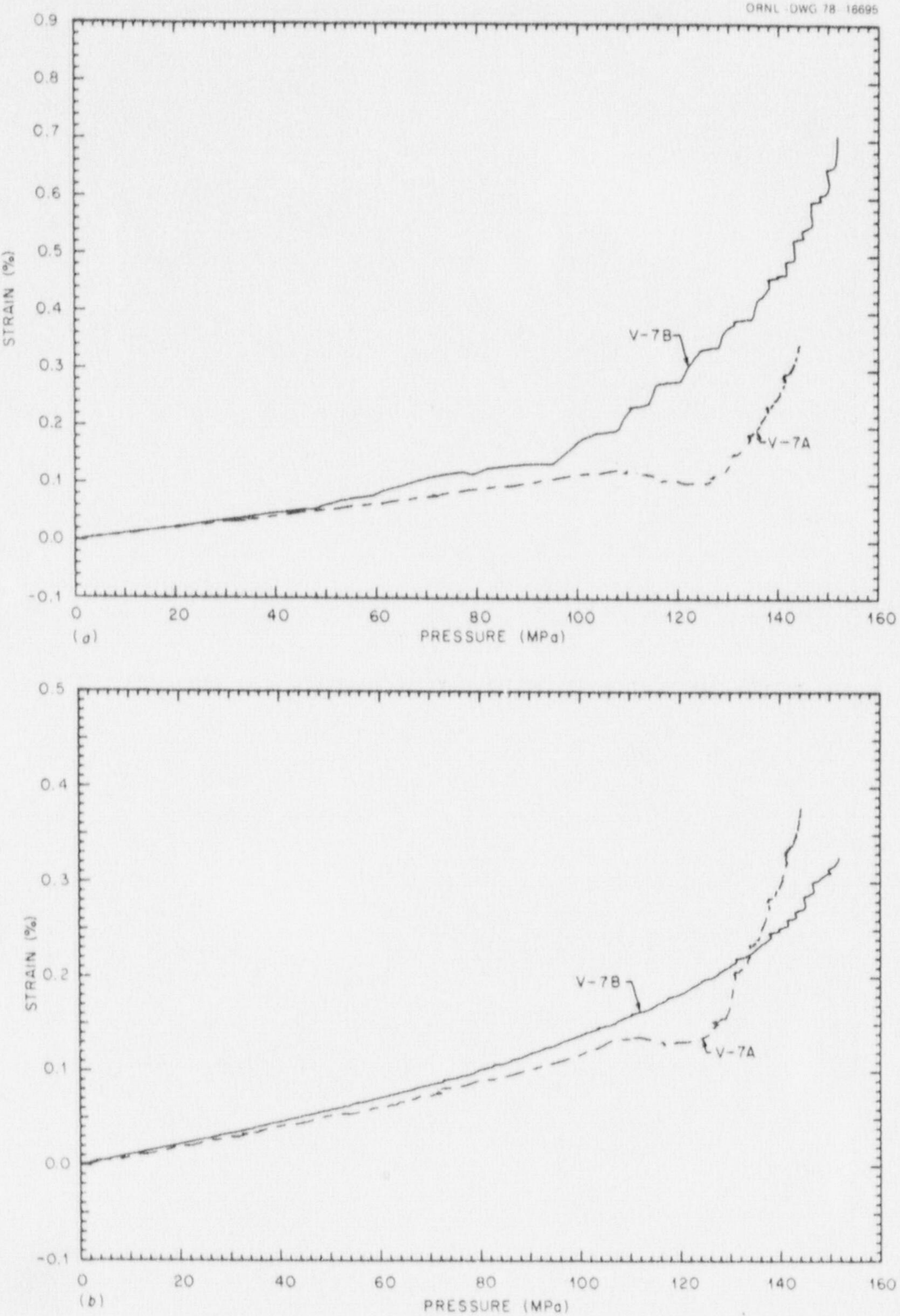

Fig. 4.10. Outside circumferential strain in the axial plane of the flaw 127 mm from the end of the machined notch vs pressure. Data plotted for rising pressure only. (*a*) XE 101 (dome end), (*b*) XE 105 (flange end).

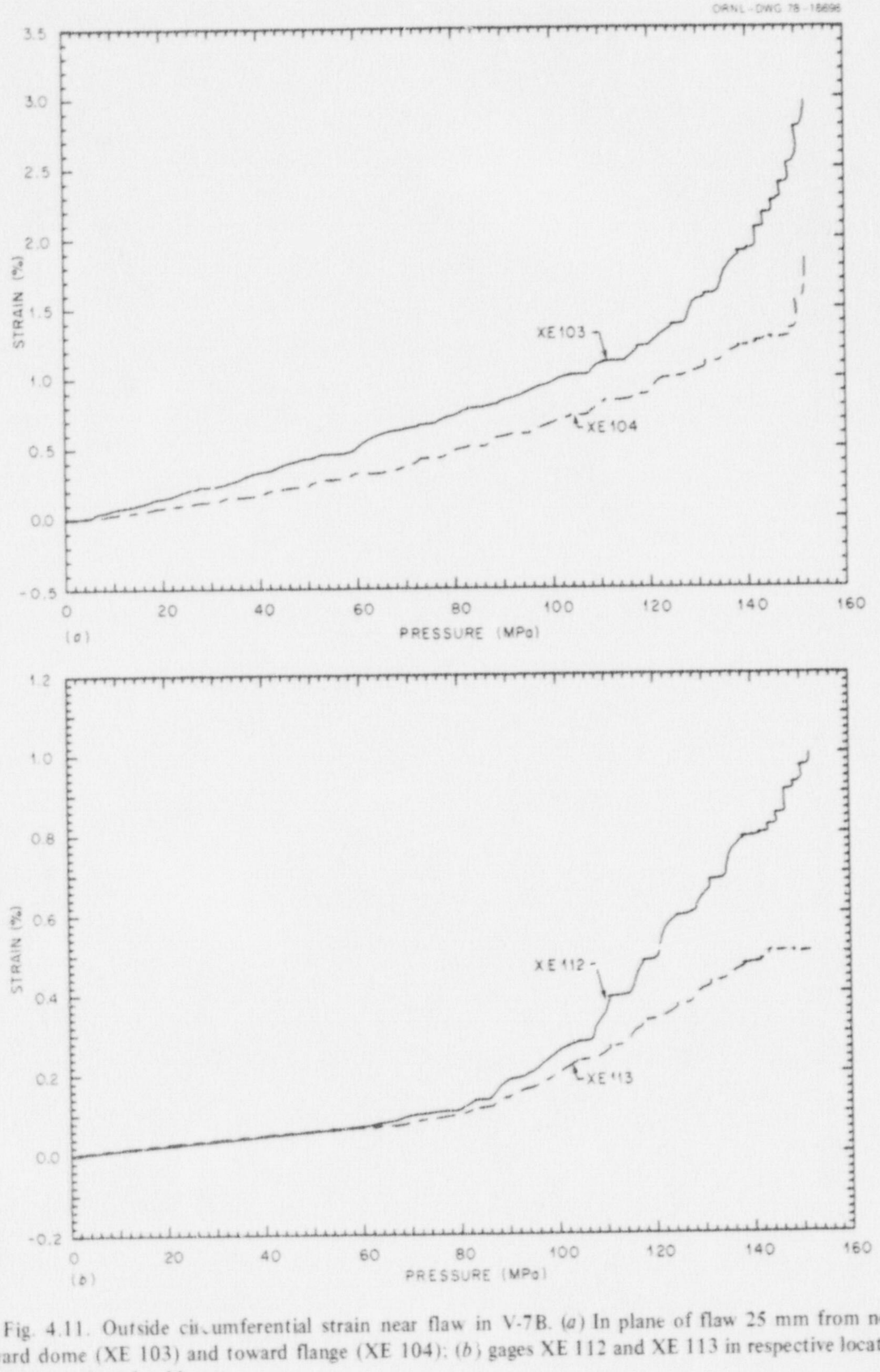

Fig. 4.11. Outside circumferential strain near flaw in V-7B. (*a*) In plane of flaw 25 mm from notch toward dome (XE 103) and toward flange (XE 104); (*b*) gages XE 112 and XE 113 in respective locations at opposite edge of weld zone.

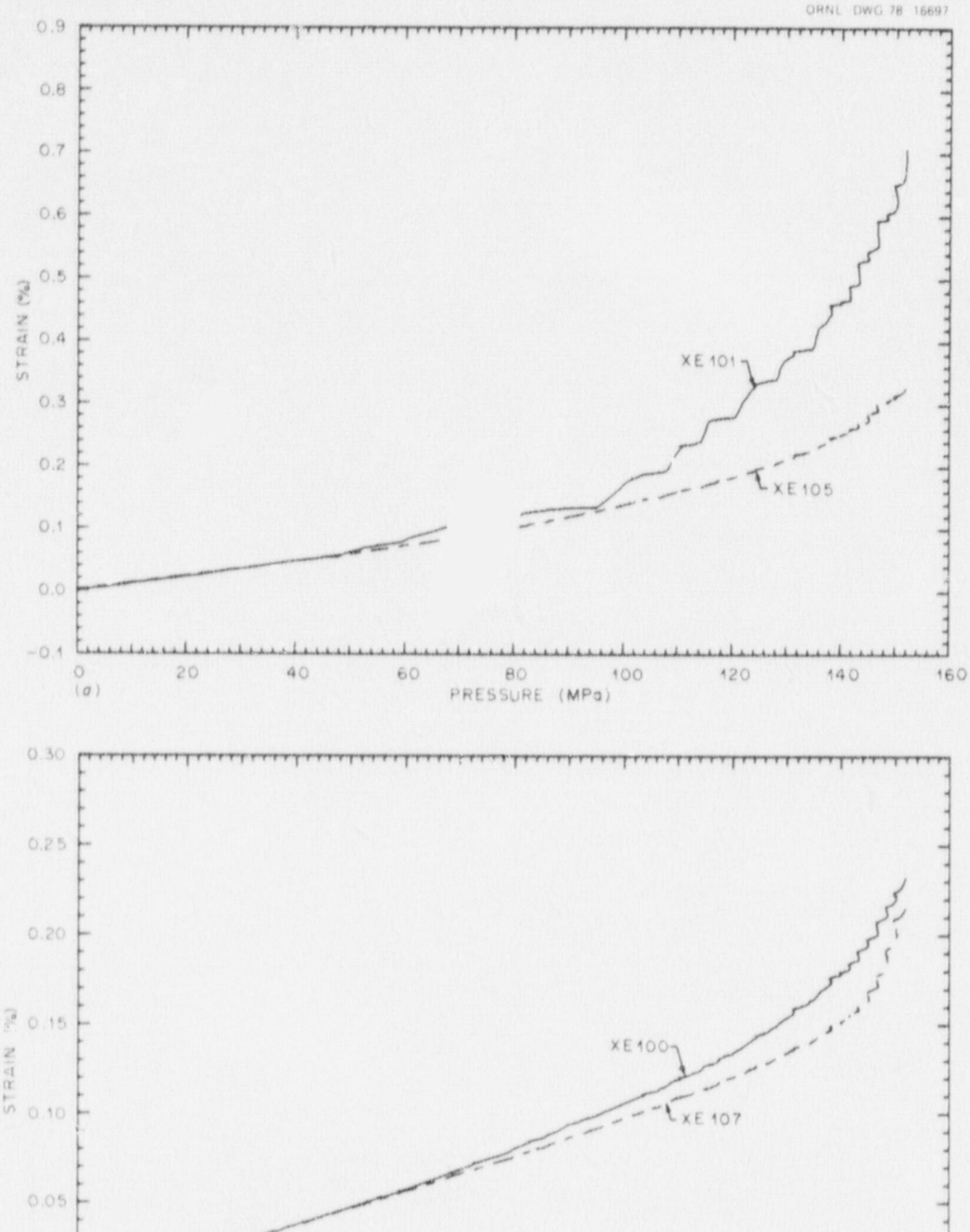

Fig. 4.12. Outside circumferential strain in plane of flaw. (*a*) 127 mm from notch toward dome (XE 101) and toward flange (XE 105); (*b*) 203 mm from notch toward dome (XE 100) and toward flange (XE 107).

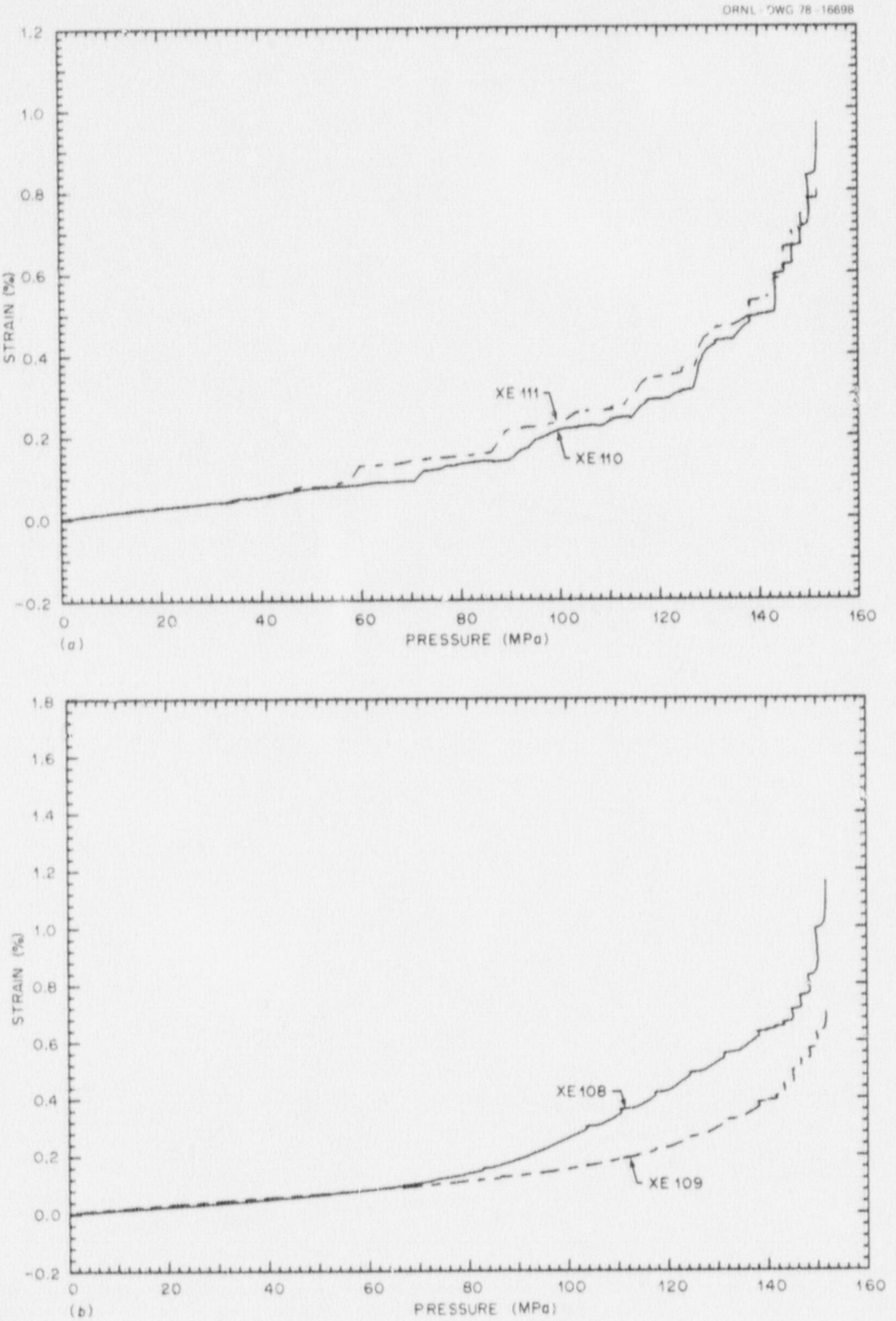

Fig. 4.13. Outside circumferential strain (*a*) on centerline of weld near flaw (XE 110 and XE 111) and (*b*) in symmetric locations on opposite side of flaw (XE 108 and XE 109).

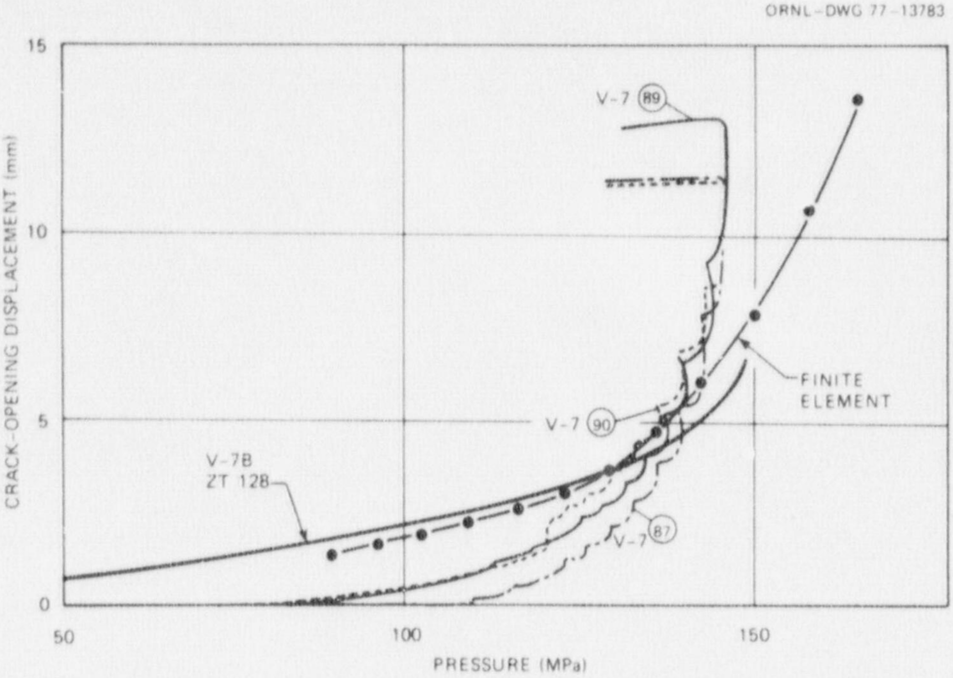

Fig. 4.14. Crack-opening displacement vs pressure recorded by transducers 87, 89, and 90 in V-7 test and ZT 128 in V-7B test compared with finite-element calculations.

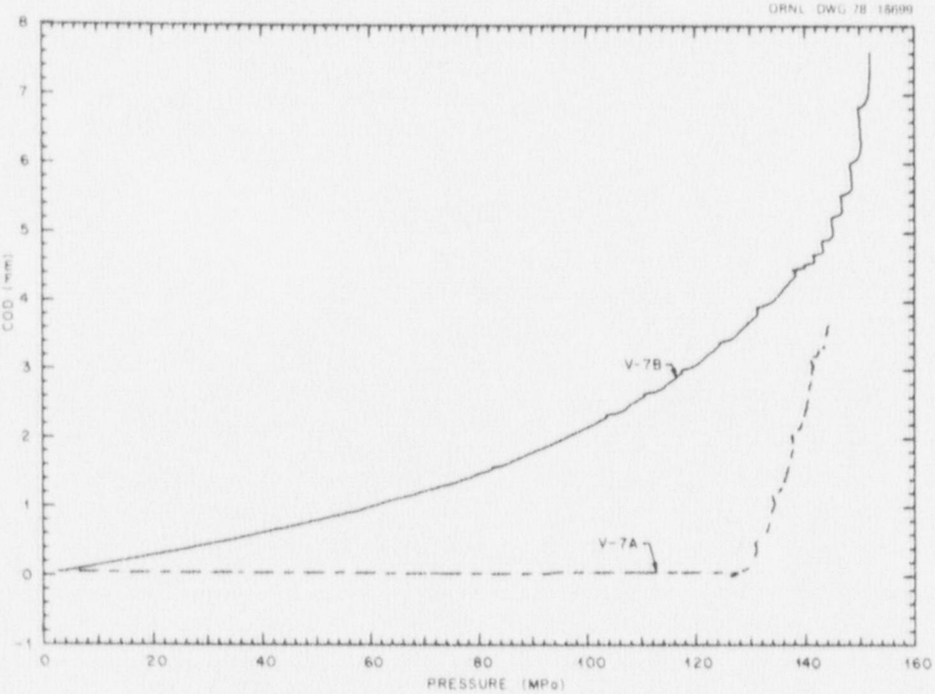

Fig. 4.15. Crack-opening displacement at midplane of flaw (ZT 128) in vessels V-7A and V-7B vs rising pressure.

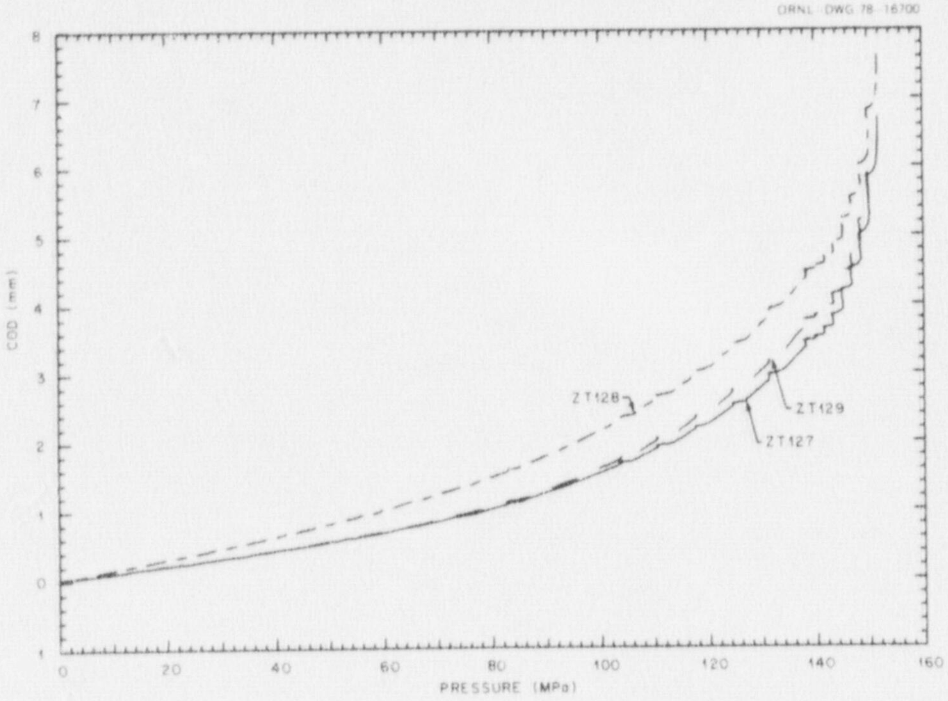

Fig. 4.16. Crack-opening displacement measurements vs rising pressure in V-7B.

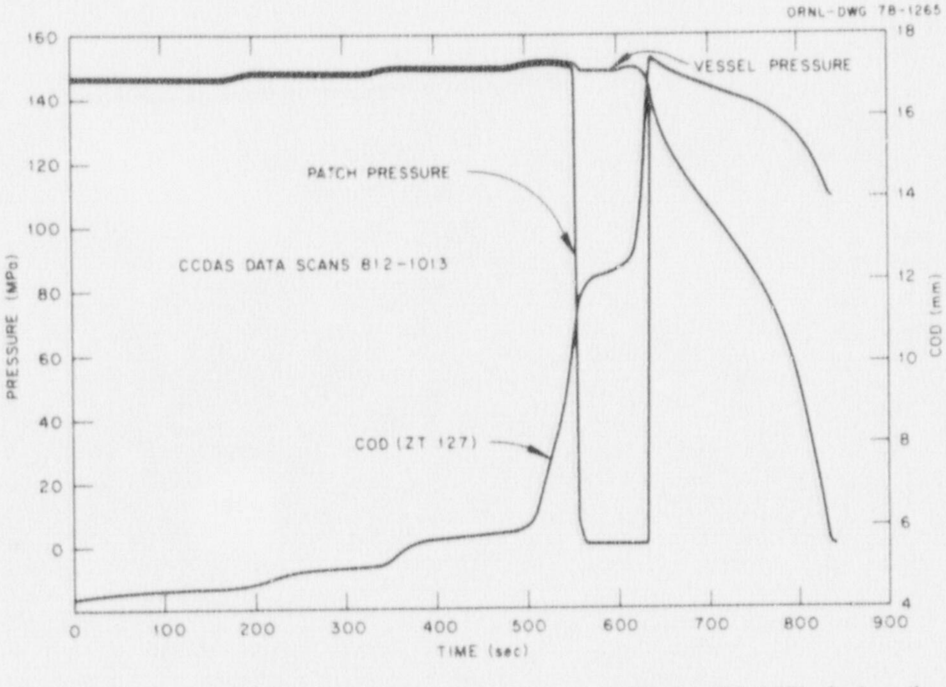

Fig. 4.17. Plots of vessel pressure, patch pressure, and COD (at ZT 127) during the last three pressurization steps, vessel rupture, and vessel depressurization. Time origin at scan 812.

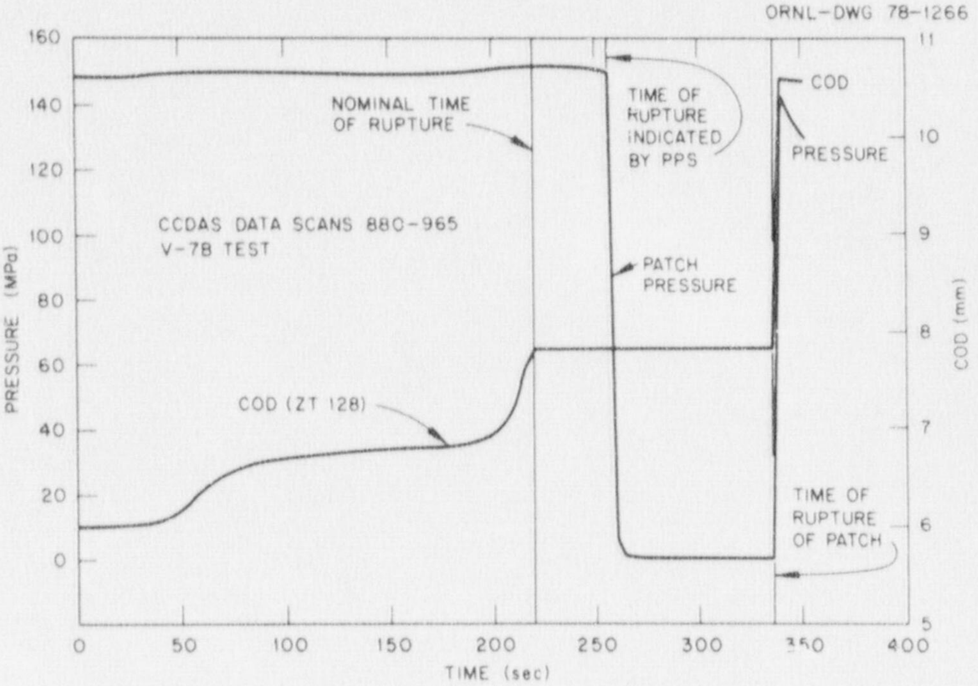

Fig. 4.18. Patch pressure and central COD (ZT 128) vs time during development of vessel rupture. Time origin at scan 880.

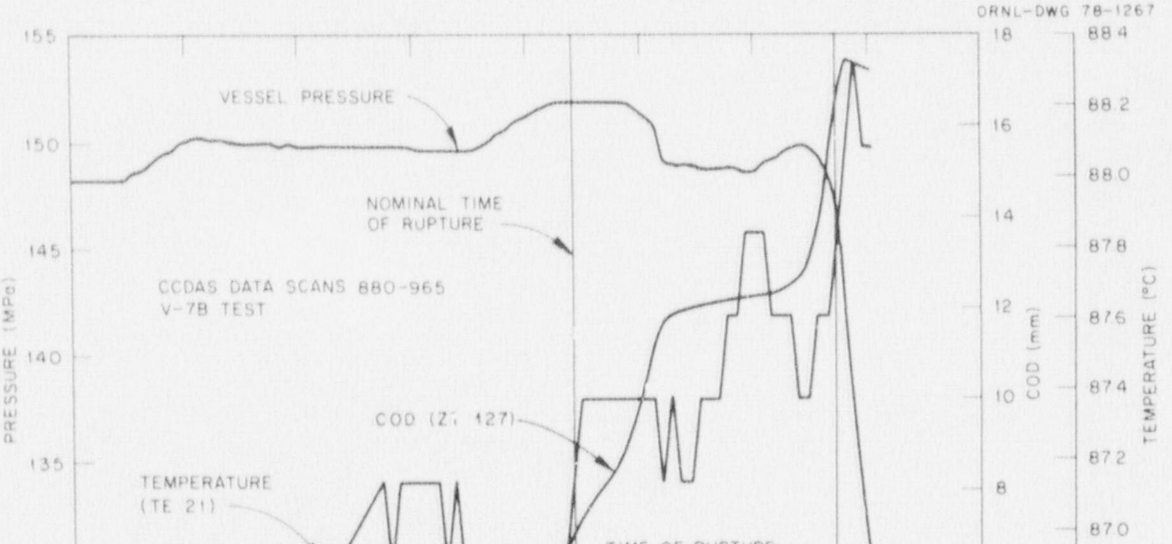

Fig. 4.19. Vessel pressure, COD (ZT 127), and metal temperature near flaw (TE 21) vs time during development of vessel rupture. Time origin at scan 880.

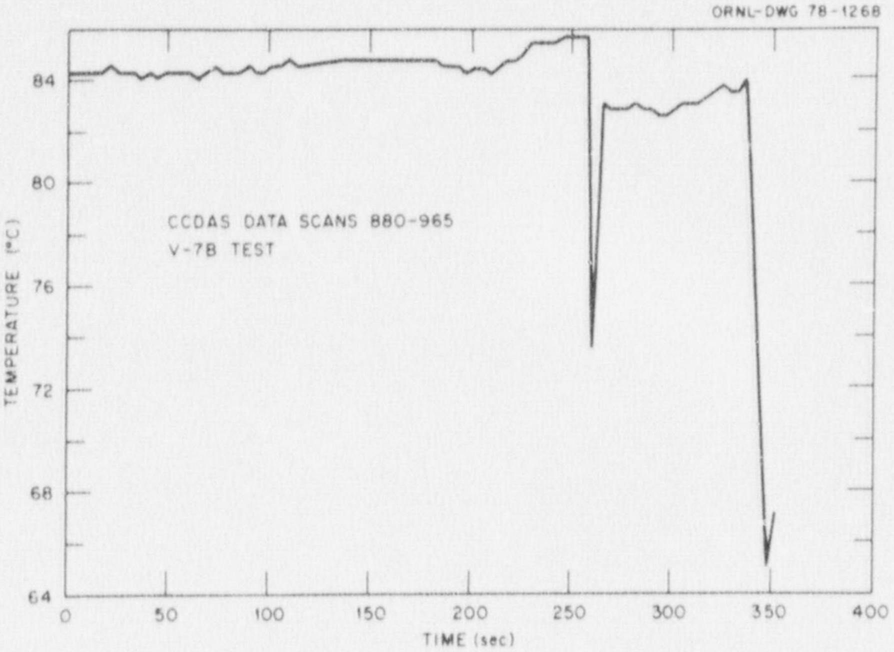

Fig. 4.20. Ligament temperature (TE 29) vs time during development of vessel rupture. Time origin at scan 880.

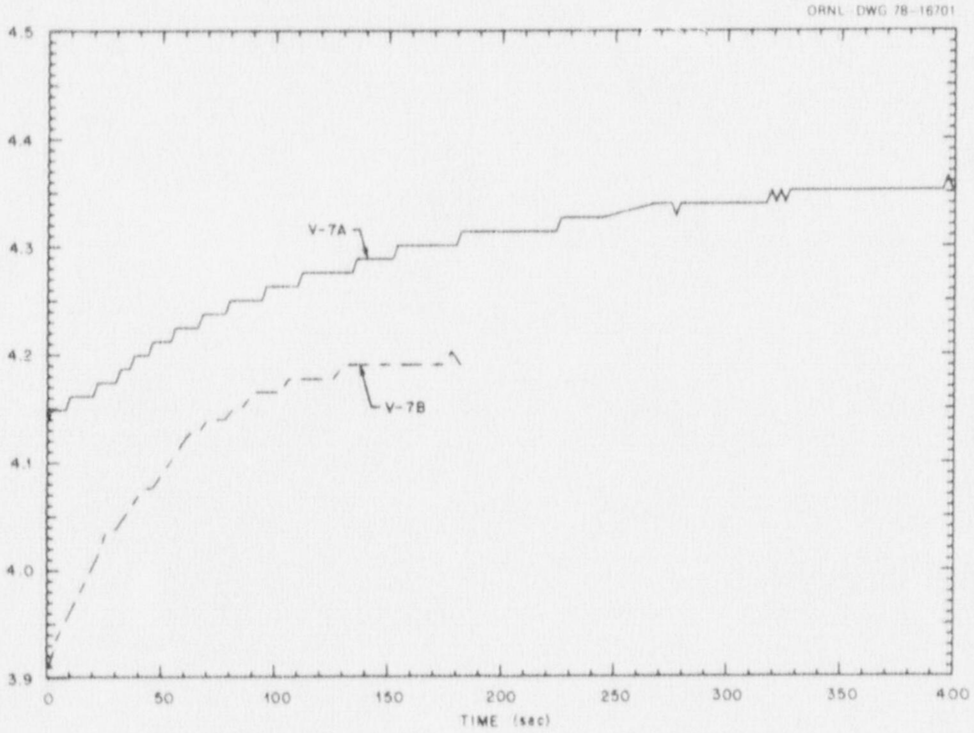

Fig. 4.21. Crack-opening displacement (ZT 127) in vessels V-7A and V-7B vs time during sustained load at about the maximum V-7A pressure (144 MPa for V-7A and 145 MPa for V-7B).

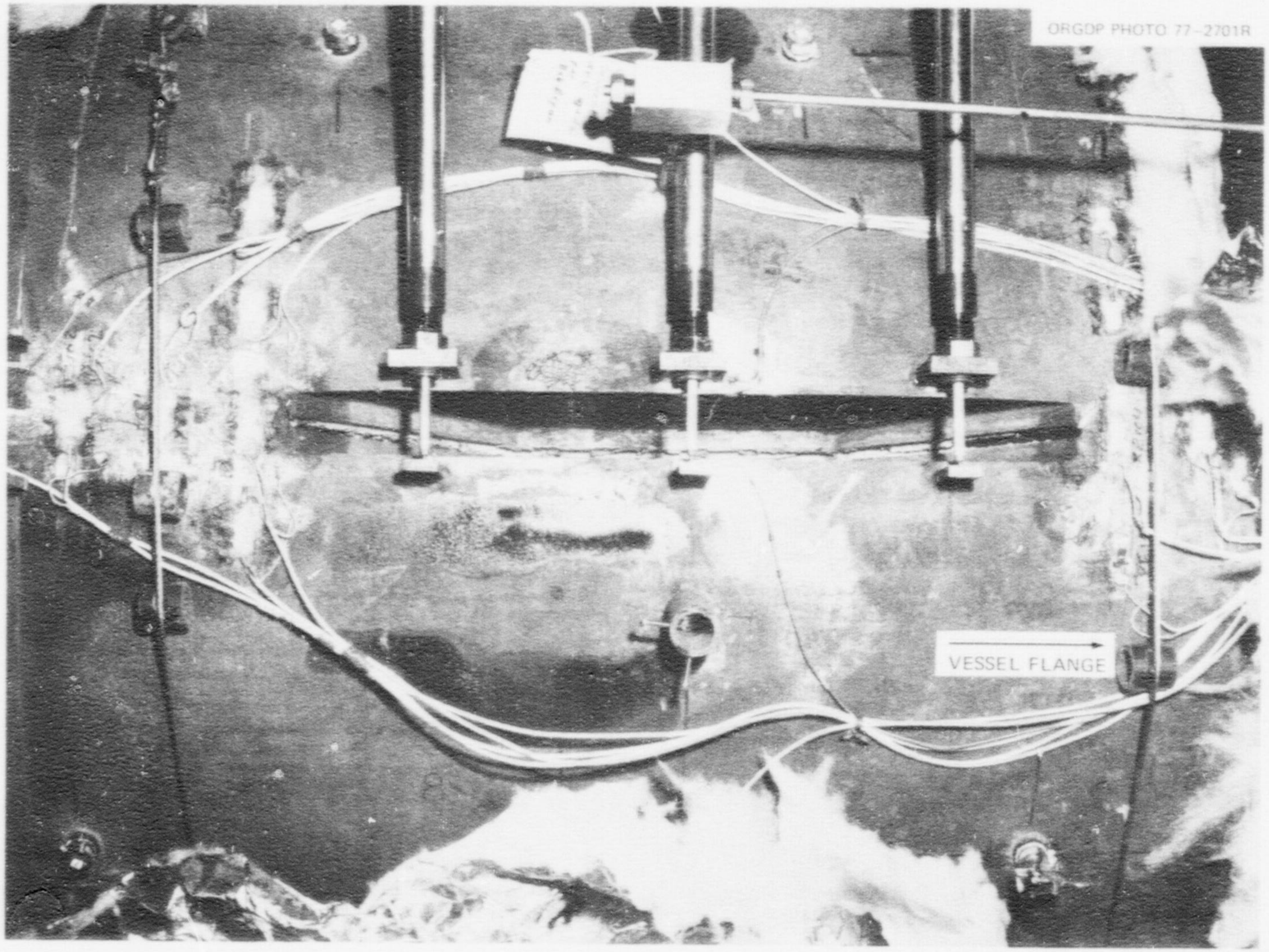

Fig. 4.22. Outside view of flaw in vessel V-7B after test. The initial EB weld crack surface that appears as a dark streak adjacent to light fracture surfaces was smooth to the expected depth of about 8 mm.

AE activity. A block containing the flaw and the weld metal was flame cut from the vessel and milled on the cut sides to permit ultrasonic (UT) examination from those surfaces. The block, about 810 mm long by 215 mm wide (32 × 8½ in.), contained the entire flaw. After UT examination was complete, the block was sectioned for metallographic study of the flaw.

The crack appearance shown in Fig. 4.22 indicated, in the initial posttest inspection, that the fracture surfaces beyond the initial electron-beam (EB) weld crack were generally rough and typical of tearing as far as one could see into the fissures [about 50 mm (2 in.) in some places]. The residual crack opening at the machined surface is about 7 to 10 mm (0.3 to 0.4 in.). Along most of the ligament the fracture runs slightly toward the base metal. At the sloping end of the machined notch toward the vessel flange, the fracture plane is visibly inclined toward the weld metal. In Fig. 4.22, short surface tears into the weld metal are evident at both ends.

The longitudinal section of the flaw in Fig. 4.23 shows the results of probe measurements and UT examination of the cut-out flaw by K. K. Klindt at ORNL. The UT examination also indicated that the deepest part of the observed crack is deflected at the flange end, about 13 mm (0.15 in.) from the longitudinal plane of symmetry of the original flaw toward the weld metal. Ultrasonic examination by the Southwest Research Institute agreed with these observations.

The rupture that caused complete depressurization of the vessel was discovered by examination of the inside surface of the vessel after the patch was removed. The sketch in Fig. 4.24 was made from rubbed impressions of the inside surface of the vessel. Two cracks were visible on the inside surface near the end of the ligament toward the flange of the vessel. The longer crack ran about 40 mm (1.6 in.) irregularly in an axial direction and was open sufficiently for light to pass straight through the wall. In contrast to V-7B, the flaws in vessels V-7 and V-7A were tightly closed after testing.

The block containing the flaw was saw cut transversely in 16 places as shown in Fig. 4.25. These cuts exposed cross-sectional views of the initial crack and the crack extension at 14 planes (28 faces). The etched faces of these cross sections show that the initial EB weld crack lay entirely within the heat-affected zone (HAZ) in the base metal adjacent to the weld repair, as had been desired (see Fig. 4.26).

The etched cross sections at several locations show the crack extension relative to the HAZ. As indicated in Figs. 4.27 and 4.28, the crack extension was entirely in the base metal in some regions, in weld metal in others, and in the HAZ only at crossover points (as in Fig. 4.27).

Some segments of the block (J, K, and L) fell in two pieces during sectioning, since they were completely fractured during the test. Segments C, M, and Q were chilled in liquid nitrogen after sectioning and broken open to expose the fracture surfaces. The two segments including the crack tips at both ends of the flaw (C and Q) are shown in Figs. 4.29 and 4.30, respectively. Visual examination of these pieces confirms the location of the crack front determined ultrasonically by K. K. Klindt (Fig. 4.23). As shown in Figs. 4.29 and 4.30, the crack extensions at the ends of the flaw conformed to and lay close to the base metal–weld metal interface. At the dome end of the flaw, from which the pieces shown in Fig. 4.29 were taken, the crack extension remained near the original plane of the flaw. At the opposite end the crack curved out of the original plane in conformance with the greater curvature of the interface at this end.

4.3.5 Crack extension relative to burst

As predicted before the test, the vessel leaked but did not burst. However, the posttest evaluation led to the conclusion that the flaw in V-7B was tearing slowly from both ends at constant pressure when maximum pressure was attained, within a few seconds of the time of ligament rupture. This behavior had not been seen in the V-7 and V-7A tests, which terminated at lower pressures.

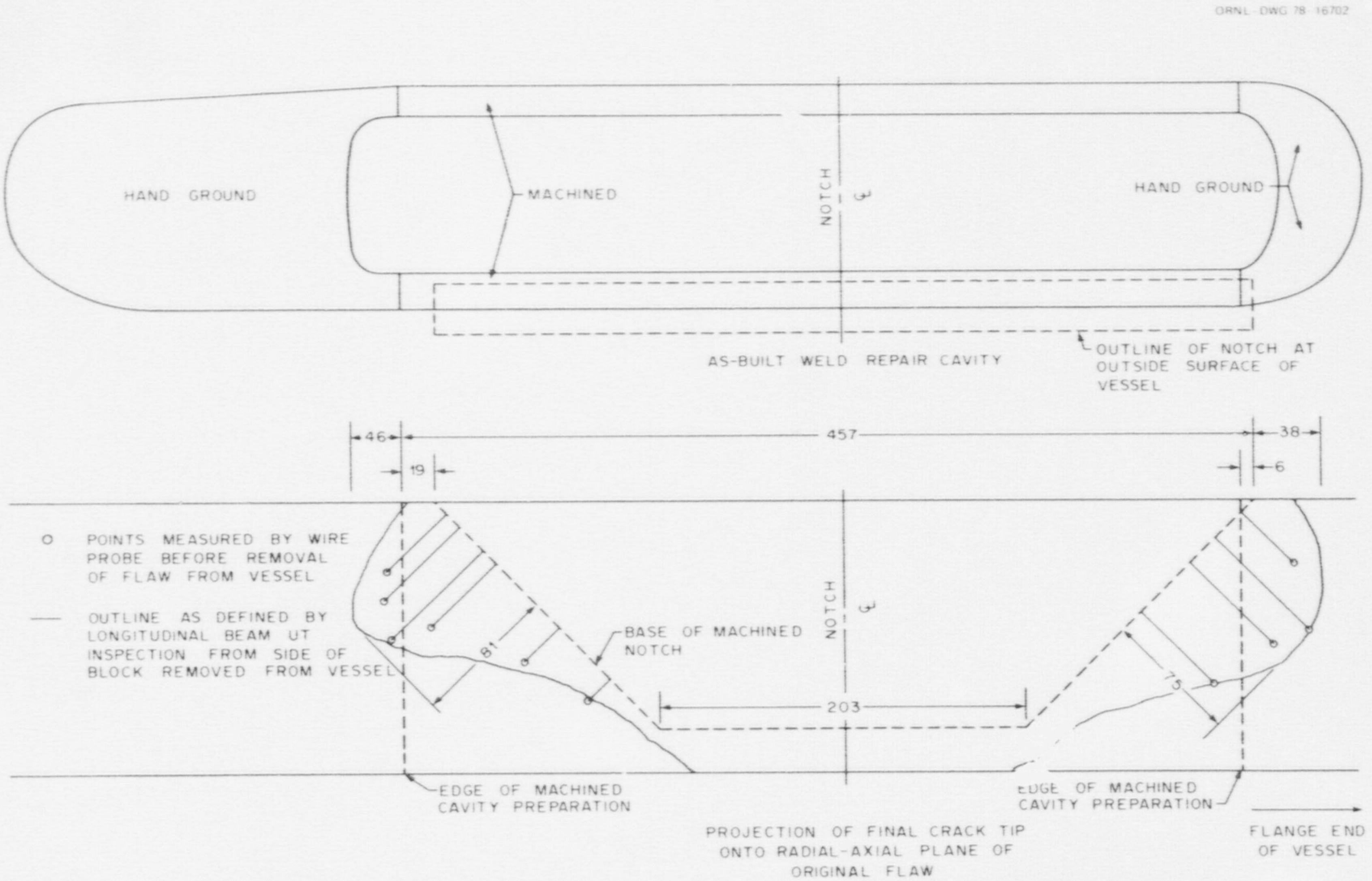

Fig. 4.23. Longitudinal section of V-7B flaw showing results of independent measurements of crack extension by wire probe and ultrasonic examination. The plan view shows the location of the crack relative to the weld.

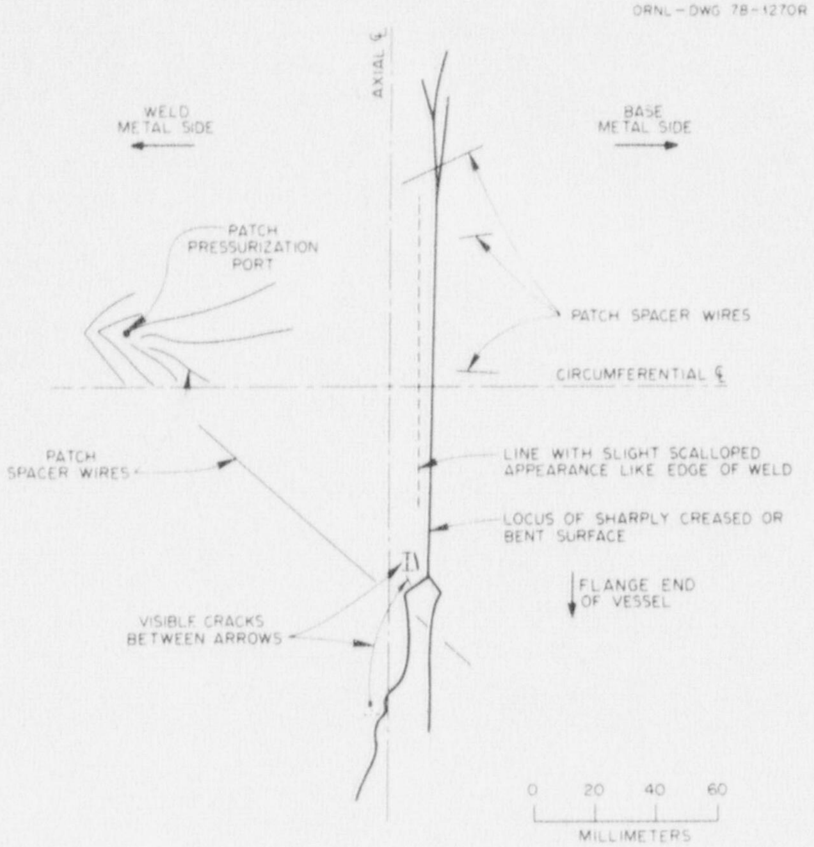

Fig. 4.24. Sketch of inside surface of vessel V-7B beneath the notch showing fissures and deformations developed during the test. Locations of features were determined by rubbed impressions on paper laid against the deformed surface.

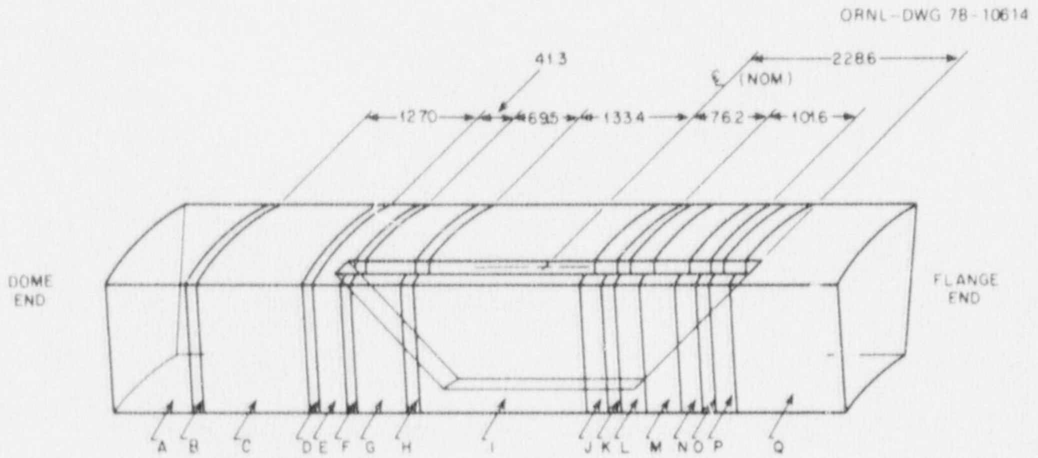

SLAB	NOMINAL THICKNESS
B,D,F,H, K,O	10
J,L,N,P	13

Fig. 4.25. Block cut from intermediate test vessel V-7B containing entire repair weld and fracture zone. Slabs A through Q were cut after all ultrasonic examinations were completed.

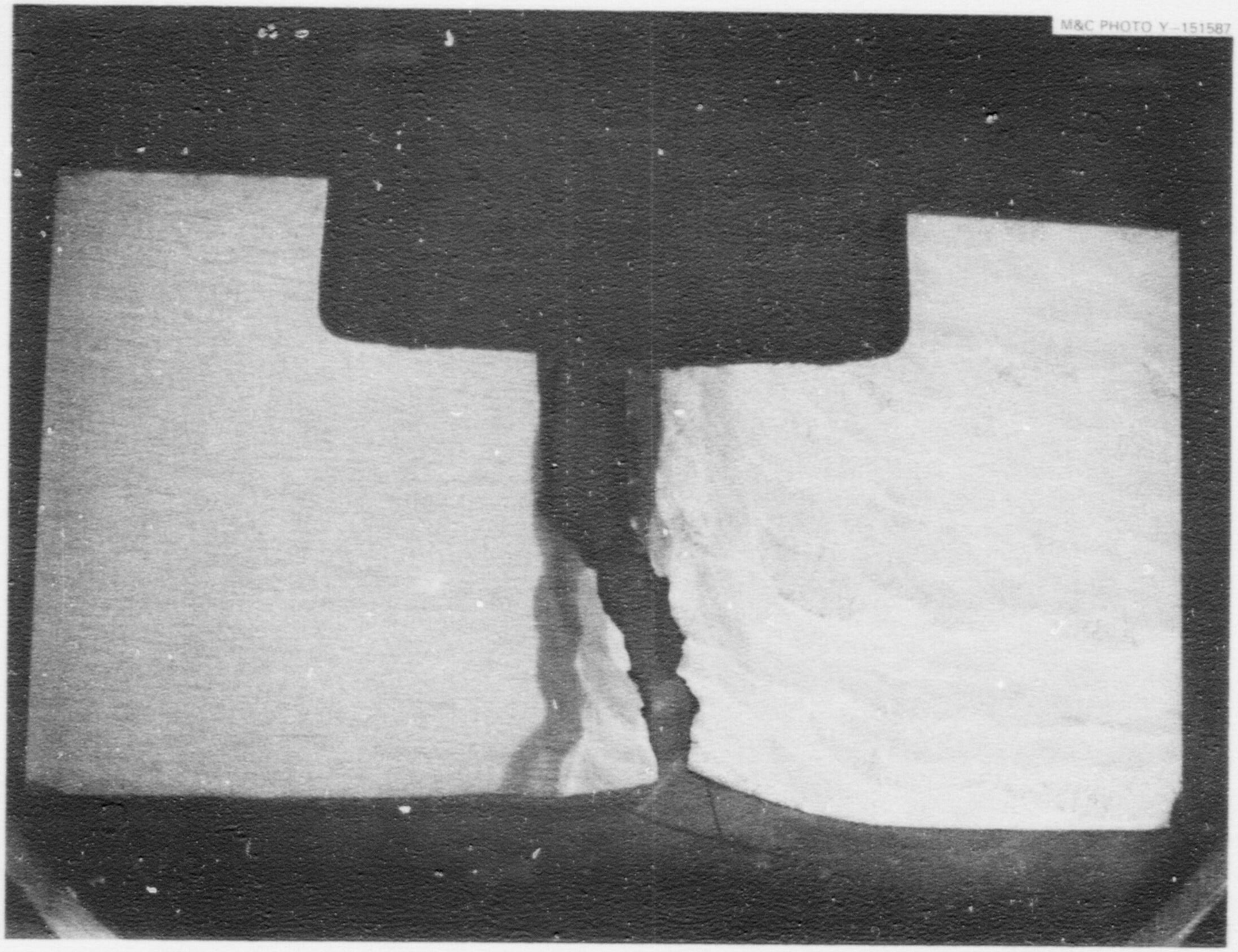

Fig. 4.26. Face K_f (the face of slab K nearest the flange end of the vessel) of cross section of V-7B fracture.

ORNL PHOTO 6543-78

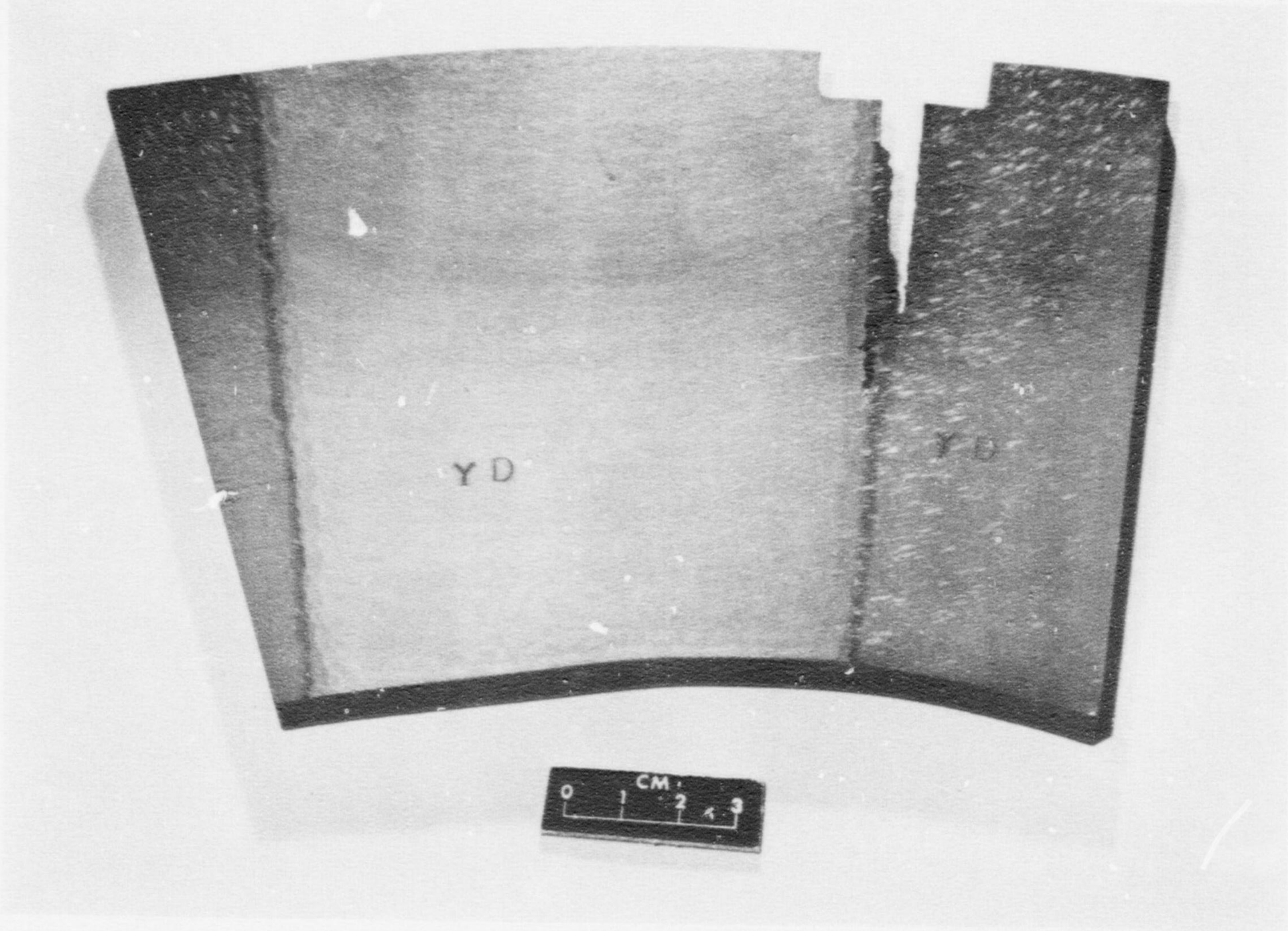

Fig. 4.27. Etched face F_d (slab F, dome side) of cross section of the flaw near the dome end of the notch in V-7B. See Fig. 4.25 for definition of cross sections.

ORNL PHOTO 6546–78

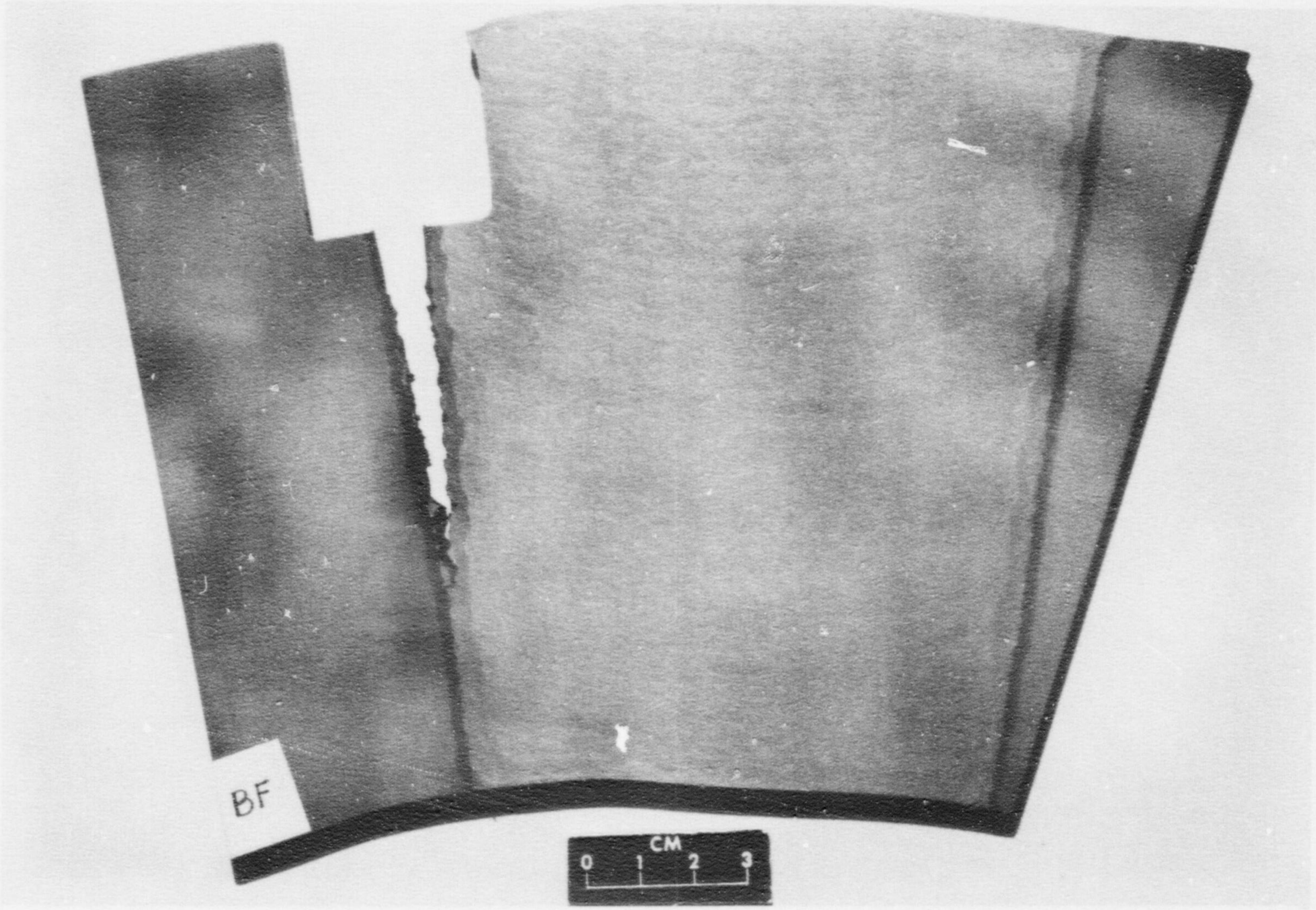

Fig. 4.28. Etched face O_f (slab O, flange side) of cross section of the flaw near the flange end of the notch in V-7B. See Fig. 4.25 for definition of cross sections.

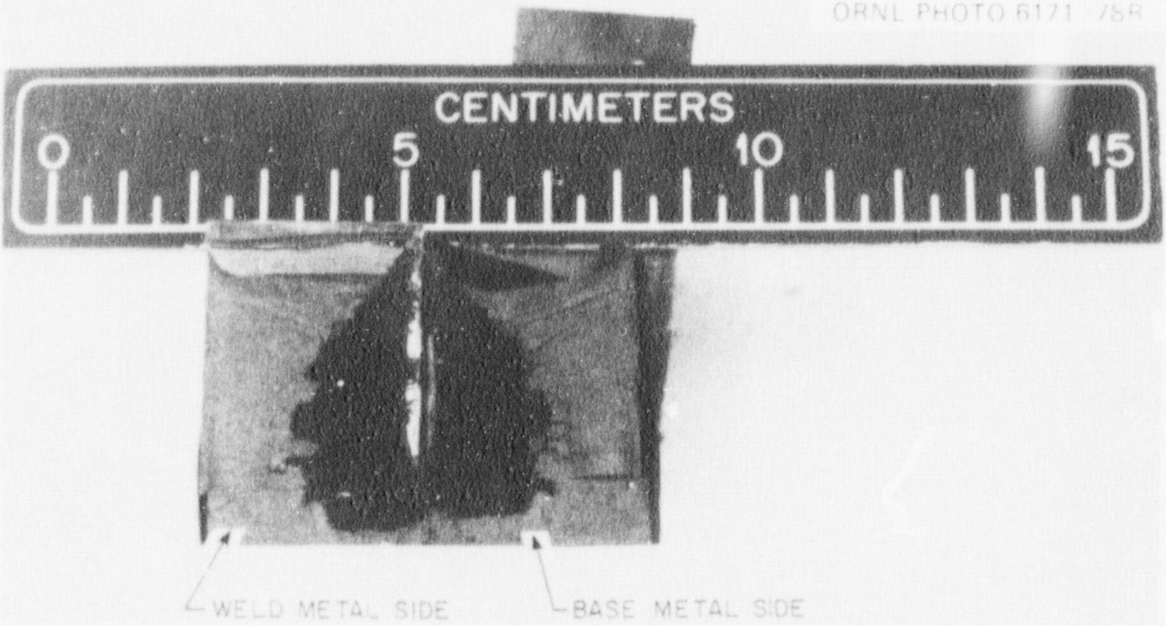

Fig. 4.29. V-7B fracture surfaces in slab C exposed by splitting the chilled slab.

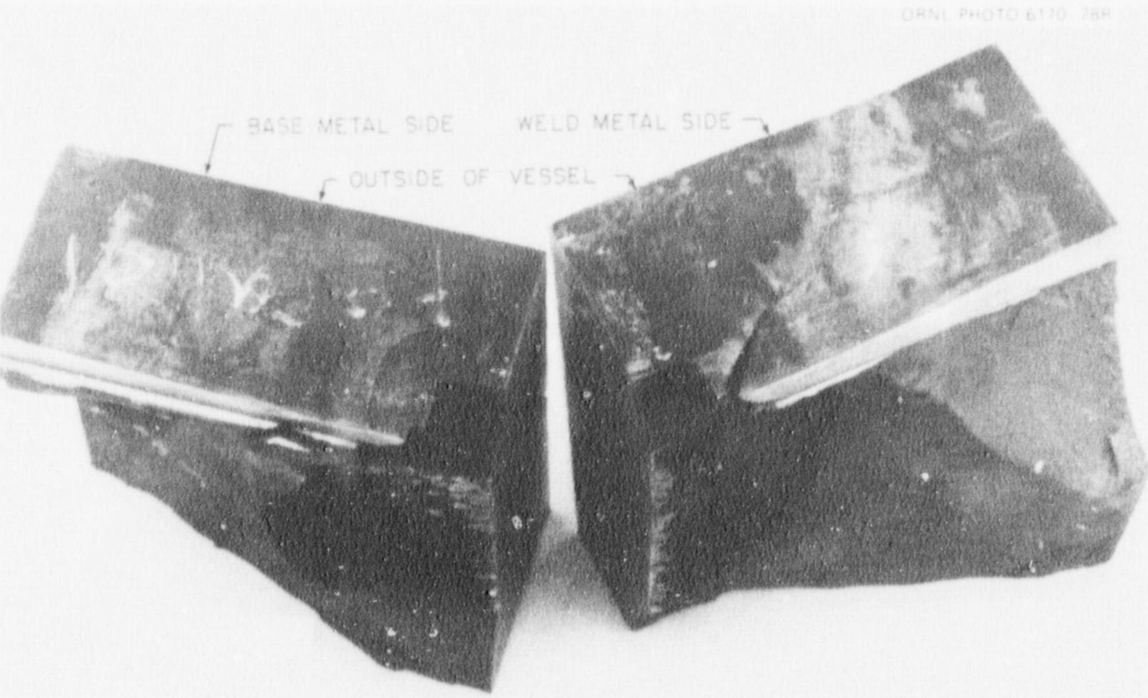

Fig. 4.30. V-7B fracture surfaces in slab Q exposed by splitting the chilled slab.

The continuing deformation of V-7B during constant load is shown in the strain and COD vs time plots of Figs. 4.31 and 4.32. Pressure changes during this interval are shown in Fig. 4.33. This behavior suggests that the structure as a whole was unstable at the maximum test pressure although the crack itself had not reached a condition conducive to fast fracture.

As indicated by pretest analyses, a burst was not expected in vessel V-7B with the initial crack length; results are shown in Fig. 4.34. Burst pressures for through-the-wall flaws in intermediate test vessels are shown by this figure to be very sensitive to the crack length for cracks at least as long as the V-7 series flaws; but variations in material toughness do not significantly affect the results. The final results of the V-7, V-7A, and V-7B tests are shown in this figure. The estimated burst conditions are consistent with the test results.

4.3.6 Effect of repair weld

The asymmetry of the repair weld relative to the flaw is shown in Fig. 4.9. One end of the V-7B flaw was near the end of the repair weld, while the repair weld extended about 200 mm (8 in.) beyond the other end of the flaw. Strains around the flaw were typically higher in locations of high residual stress (particularly at that end of the flaw where the extension of the flaw plane lay along the edge of the repair

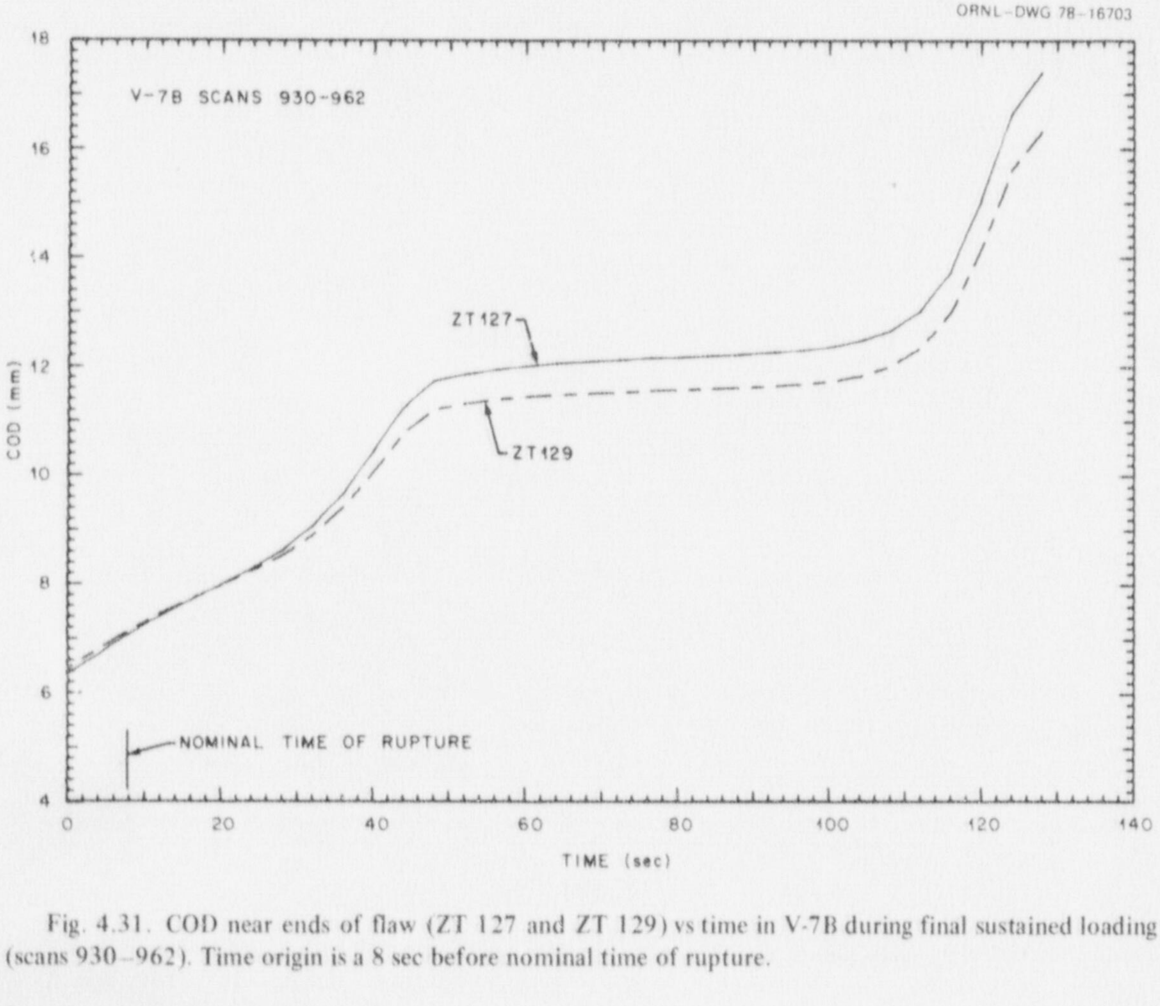

Fig. 4.31. COD near ends of flaw (ZT 127 and ZT 129) vs time in V-7B during final sustained loading (scans 930–962). Time origin is a 8 sec before nominal time of rupture.

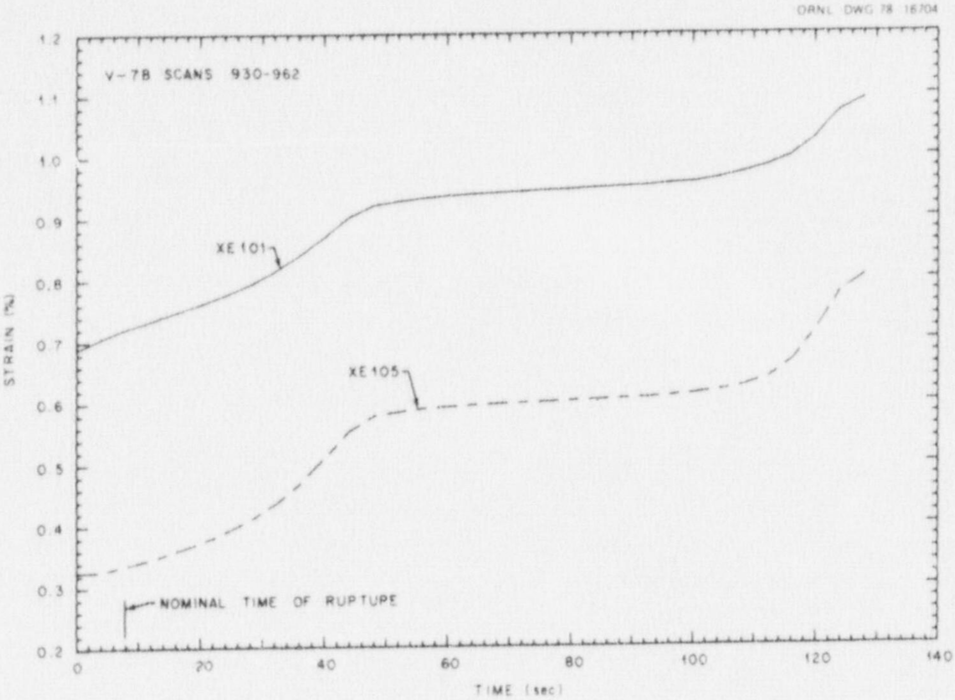

Fig. 4.32. Strain near ends of flaw (XE 101 and XE 105) vs time in V-7B during final sustained loading (scans 930–962).

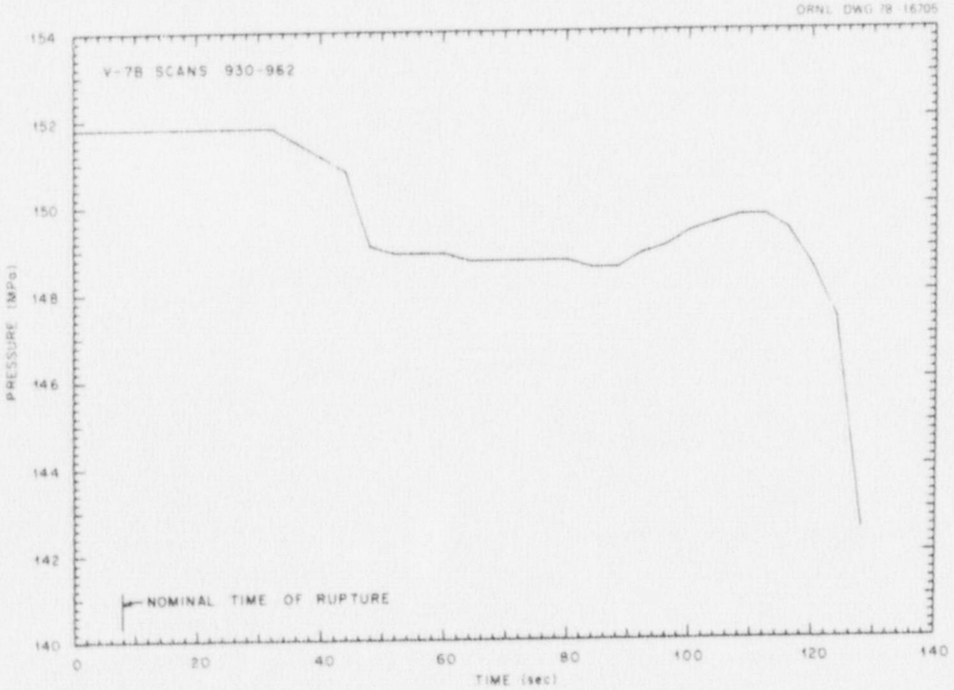

Fig. 4.33. Pressure vs time in V-7B during final sustained loading (scans 930–962).

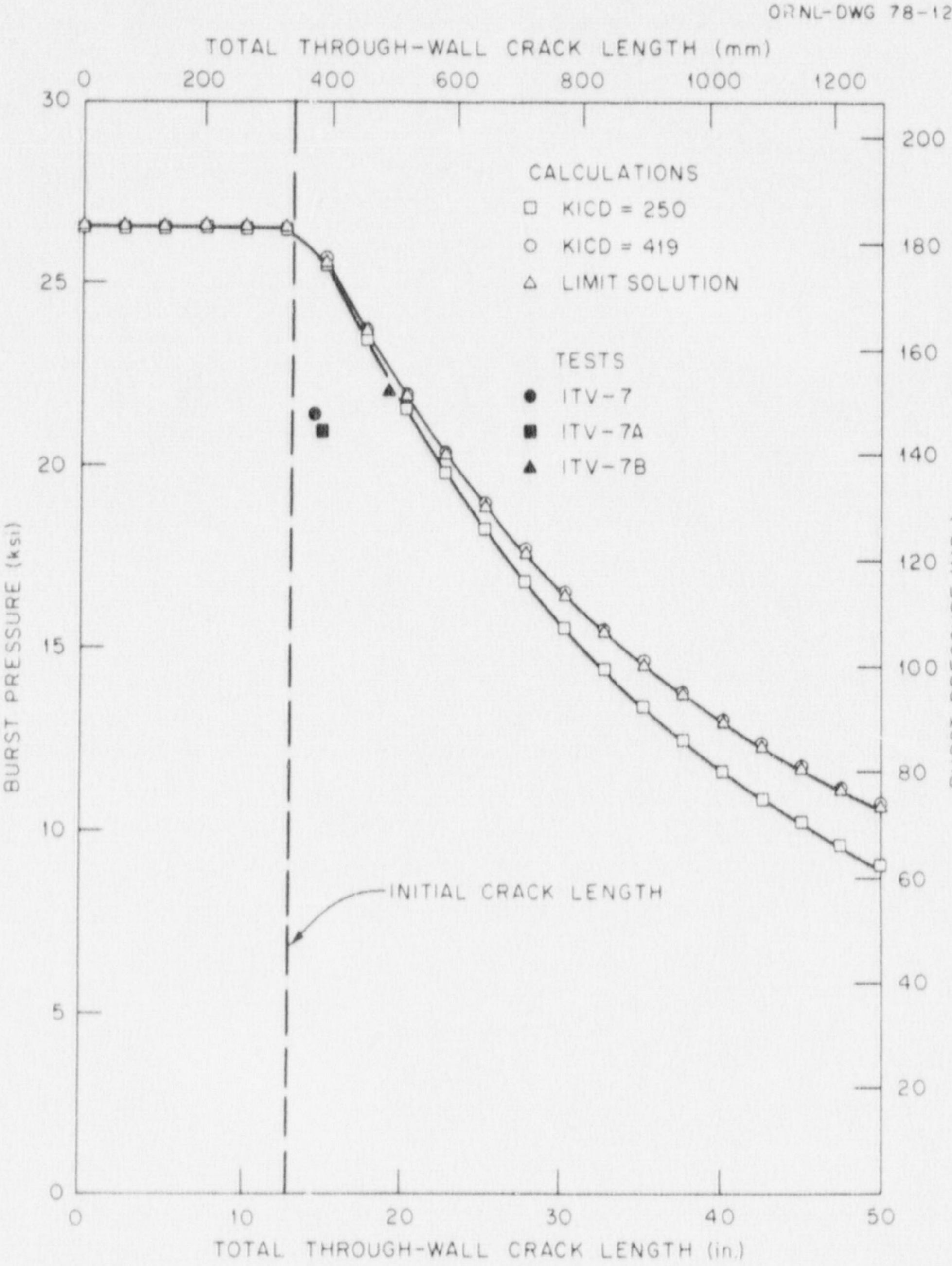

Fig. 4.34 Estimated burst pressures of an intermediate test vessel with a through-the-wall axial crack with results of tests V-7, V-7A, and V-7B.

weld) than in symmetrical but unprestressed locations. Strains in the plane of the crack in V-7A were about the same as those measured at comparable pressures in V-7B at the end of the flaw away from the repair weld (the flange end in Fig. 4.9).

Table 4.4 compares the strains at similar locations in V-7A and V-7B at a pressure of 144 MPa (20.9 ksi) (the maximum pressure in V-7A). The strains at both ends of the V-7A flaw are about the same as those at

Table 4.4. Comparison of strains at similar and symmetrical locations relative to the flaw in vessels V-7A and V-7B at 144 MPa

Gage location	Dome end of flaw (edge of weld in V-7B)			Flange end of flaw		
	Gage No.	Strain (%)		Strain (%)		Gage No.
		V-7B	V-7A	V-7B	V-7A	
In flaw plane						
203 mm from notch	XE100	0.19	0.17	0.16	0.18	XE107
127 mm from notch	XE101	0.53	0.34	0.27	0.38	XE105
25 mm from notch	XE103[a]	2.20	1.61	1.29	1.50	XE104[b]
7.5° from flaw plane[c]						
In base metal	XE108	0.67		0.45	0.81	XE109
In repair weld	XE110	0.60		0.59		XE111

[a] V-7A gage XE81.

[b] V-7A gage XE79.

[c] 13.2° in V-7A.

respective locations at the flange end of the V-7B flaw. However, the two ends of the V-7B flaw were subjected to significantly different strain conditions (see, for example, Figs. 4.11 through 4.13). Nevertheless, the crack geometry in V-7B remained approximately symmetrical throughout the test, as indicated by COD measurements (Figs. 3.8 and 4.16). These data suggest that axial tearing was not extensive until about the time of rupture and that it proceeded from both ends of the flaw almost simultaneously. Markedly different strains at the two ends of the flaw did not produce significantly different tearing.

References

1. J. G. Merkle et al., *Test of 6-inch-thick Pressure Vessels. Series 3: Intermediate Test Vessel V-7*, ORNL/NUREG-1 (August 1976).

2. R. H. Bryan, J. G. Merkle, and G. C. Smith, *Test of 6-in.-thick Pressure Vessels, Series 3: Intermediate Test Vessel V-7A under Sustained Loading*, ORNL/NUREG-9 (February 1978).

5

Summary and Conclusions

Intermediate test vessel V-7 was the seventh in a series of eight flawed 152-mm-thick (6-in.) steel vessels tested hydraulically. The test section of the vessel was fabricated of ASTM A533, grade B, class 1 steel plate. The test flaw was a trapezoid-shaped external surface flaw 135 mm deep (5.3 in.) and 457 mm long (18 in.) on the surface. A sharp crack tip was achieved by hydrogen-cracking an electron-beam (EB) weld placed around the perimeter of the flaw. After the initial test, which resulted in a leak without unstable rupture, the flawed region of the vessel was repaired in accordance with the ASME Boiler and Pressure Vessel Code, Section XI, weld repair procedure without postweld stress relief; a new flaw, identical to the original, was placed in the test section in base metal 135° from the original flaw. The repaired vessel, designated V-7A, was tested pneumatically and again resulted in a leak without rupture. The vessel was again repaired by the Section XI procedure and designated as vessel V-7B. The V-7B flaw was geometrically identical to the flaws in the two earlier tests but was placed as nearly as possible within the heat-affected zone (HAZ) of the second repair weld.

Vessel V-7B was tested hydraulically at about the same temperature [87°C (188°F)] used for V-7 and V-7A. A stainless steel patch was welded to the inside surface of the vessel beneath the flaw to prevent leakage after ligament rupture, thus allowing pressure to be sustained. The vessel was tested on July 14, 1977, through two pressure cycles, one to 72.5 MPa (10.5 ksi) and the other to 151.8 MPa (22.02 ksi). Vessels V-7 and V-7A leaked at 147 and 144 MPa, respectively. At peak pressure in vessel V-7B, a leak developed through the flaw as in the two previous tests. Thereafter the pressure was sustained relatively constant for about 2 min by means of the patch; then the patch ruptured, allowing the vessel to depressurize completely. Unlike the behavior of vessel V-7A under sustained load, the flaw in vessel V-7B apparently continued to tear in the axial direction after the rupture through the ligament became complete, indicating that a burst condition was being approached. All three tests demonstrated that the flawed vessel was structurally stable, at least up to 2.15 times design pressure; the V-7B test demonstrated stability up to 2.27 times design pressure.

Posttest ultrasonic and visual examinations of the flaw region showed that the initial sharp flaw was within the HAZ, as desired, and that both ends of the V-7B crack had extended axially by tearing an average of 76 mm (3 in.). This brought the total crack length close to the calculated instability length for the maximum test pressure achieved. This amount of axial crack tearing exceeded that previously observed in the V-7 and V-7A tests. It was also found that the path of axial tearing had proceeded immediately from the original crack tip in the repair weld HAZ into the adjacent weld or base metal, thereafter reentering the HAZ only infrequently to cross it. This behavior had also been observed in precracked Charpy V-notch specimens tested before the vessel V-7B test, indicating that the crack tearing resistance of the HAZ material was greater than that of the adjacent weld or base metal. The axial crack extensions followed the weld–base metal interface closely, even where it deviated from the plane of symmetry of the flaw.

Pretest residual stress measurements made on the inside and outside surfaces of vessel V-7B near the flaw and on through-thickness sections of companion test welds indicated circumferential residual tensile stresses of near yield point magnitude adjacent to the repair weld but considerably lower residual stresses in the repair weld itself. Measurements of strain changes induced by the machining of the V-7B notch implied that the residual circumferential stresses in the ligament were at least slightly compressive. For the high toughness conditions of the V-7B test, it was predicted that the plastic strain in the ligament would be so high prior to rupture that residual stresses in that region would not appreciably affect the leak pressure. The variance of the leak pressure in V-7B from those of the two earlier tests was, in fact, small and was probably a result of a combination of slight differences among the three tests.

This series of tests demonstrated that, provided fracture toughness is adequate, half-bead weld repairs made in accordance with Section XI of the code can perform satisfactorily under an overload even with a flaw in the repair zone. At comparable pressures the vessel response in terms of strain and crack-opening displacement was about the same in the three tests. The stability of vessel V-7B was compared to that of vessel V-7A at its maximum load. It was concluded that vessel V-7B with the flaw in the repair zone was as stable and as capable of carrying the load as were the other vessels up to their maximum test pressures. Observation of acoustic emissions indicated that the initial half-bead repair weld (unflawed) was quiescent in both the V-7A and V-7B tests and that the prepared flaws, regardless of whether they were in a repair zone or not, behaved essentially in the same manner as a source of acoustic activity.

The significantly greater axial tearing of the flaw in vessel V-7B may be the result of one or more of the following factors: (1) higher pressure, (2) residual stresses, (3) inhomogeneous material with respect to mechanical properties near the flaw plane, and (4) lower fracture toughness (possible undetected variation). The V-7B test data suggest that the major portion of the axial tearing was not promoted by the higher strains at one end of the flaw, which tends to discount localized residual stress as an important contributor. Assessment of the relative importance of the other factors would require data and methods of analysis that are not presently available.

Appendices

Appendix A

Test Data

A complete tabulation of data recorded during the vessel V-7B test has been produced on microfiche and attached inside the back cover of this report. The data recorded on the computer-controlled data acquisition system (CCDAS) consist of 1093 scans of temperature, pressure, crack-opening displacement (COD), and strain measurements recorded on magnetic tape. Ten additional channels of strain data were recorded on Vishay equipment; these data consist of 26 scans, the times and pressures of which were recorded by hand from the CCDAS.

The data on microfiche are divided into 8 tables: (1) temperature, (2) pressure and COD, (3–7) CCDAS strain, and (8) Vishay strain. Each line of a table presents a scan number, the lapsed time relative to CCDAS scan number 1, and a set of measured data in SI units. Conversions are given in Table A.1. The data tables occupy 1 fiche with 18 columns. An index to the data is given in Table A.2.

Data known to be erroneous are identified in Table A.3.

Table A.1. Conversions from SI to English units

Variable	SI unit	Multiplier of SI value to obtain English value	English unit
Pressure	MPa	0.14504	ksi
COD	mm	0.039370	in.
Strain	μm/m	1.0	μin./in.
Temperature (°F) = 9/5 [temperature (°C)] + 32			

Table A.2. Index to V-7B data on microfiche

Column No.	Table No.	Description
1–2	1	Temperature
3–4	2	Pressure and COD
5–6	3	CCDAS strain, XE33–42
7–8	4	CCDAS strain, XE43–64
9–10	5	CCDAS strain, XE65, 72, 86–96
11–12	6	CCDAS strain, XE97–107
13–14	7	CCDAS strain, XE108–124
15	8	Vishay strain, XE74–82
16–18	Blank	

Table A.3. Erroneous data

Sensor	Scan No.
XE 36, 39, 42, 55, 73, 75	All
PE30	213
XE 33	869–1093
XE 44	707–1093
XE 65	119–1093
XE 74	12
XE 102	944–1093

Appendix B

Acoustic Emission Measurements for HSST V-7B Intermediate Vessel Test

---

P. H. Hutton   J. F. Dawson*   R. J. Kurtz**

Introduction

Measurement and analysis of acoustic emissions (AE) generated during testing of the HSST V-7B intermediate vessel was performed under the auspices of the Nuclear Regulatory Commission. There were two purposes in monitoring AE: (1) to provide real-time information to the test manager of any notable indications of distress in the vessel at locations other than the machined defect, and (2) to acquire AE data for analysis relevant to development of AE/flaw relationships for inservice reactor monitoring. Two AE monitor systems were used to more effectively meet the two requirements. A Dunegan/Endevco (D/E) 1032 computerized monitor system (Fig. B.1), which provides point source location and a count of all AE signals received, was used in support of the first objective. This system should be capable of detecting AE from any point in the vessel. The BNW multiparameter digital memory AE monitor (Fig. B.2) was used to achieve the second objective. This unit measures five AE parameters (total event count and valid event count, energy, rise time, and amplitude) plus a mechanical parameter (vessel pressure) simultaneously and stores the information in the digital memories. By means of a source isolation feature, valid signals are restricted to those originating from a predetermined area – in this case, the vicinity of the machined defect. Total event count is a count of all acoustic signals detected without limitation by source isolation.

Procedure

Location of the AE sensors on the test vessel is shown in Figs. B.3 and B.4. Installed instrumentation prior to the test is shown in Fig. B.5. Pressure coupled metal wave guide sensors (8 in. long) were used with the D/E 1032 system, and surface mounted PZT-5 sensors were used with the BNW system. Since the function of the D/E 1032 system was only to detect and locate AE sources, wave guide sensors with the attendant potential for wave form distortion were chosen for insurance against temperature effects. The vessel surface was about 200°F. Wave form is more critical to the BNW system for comparison with

---

*Battelle Pacific Northwest Laboratories.

ORNL PHOTO 4860–78

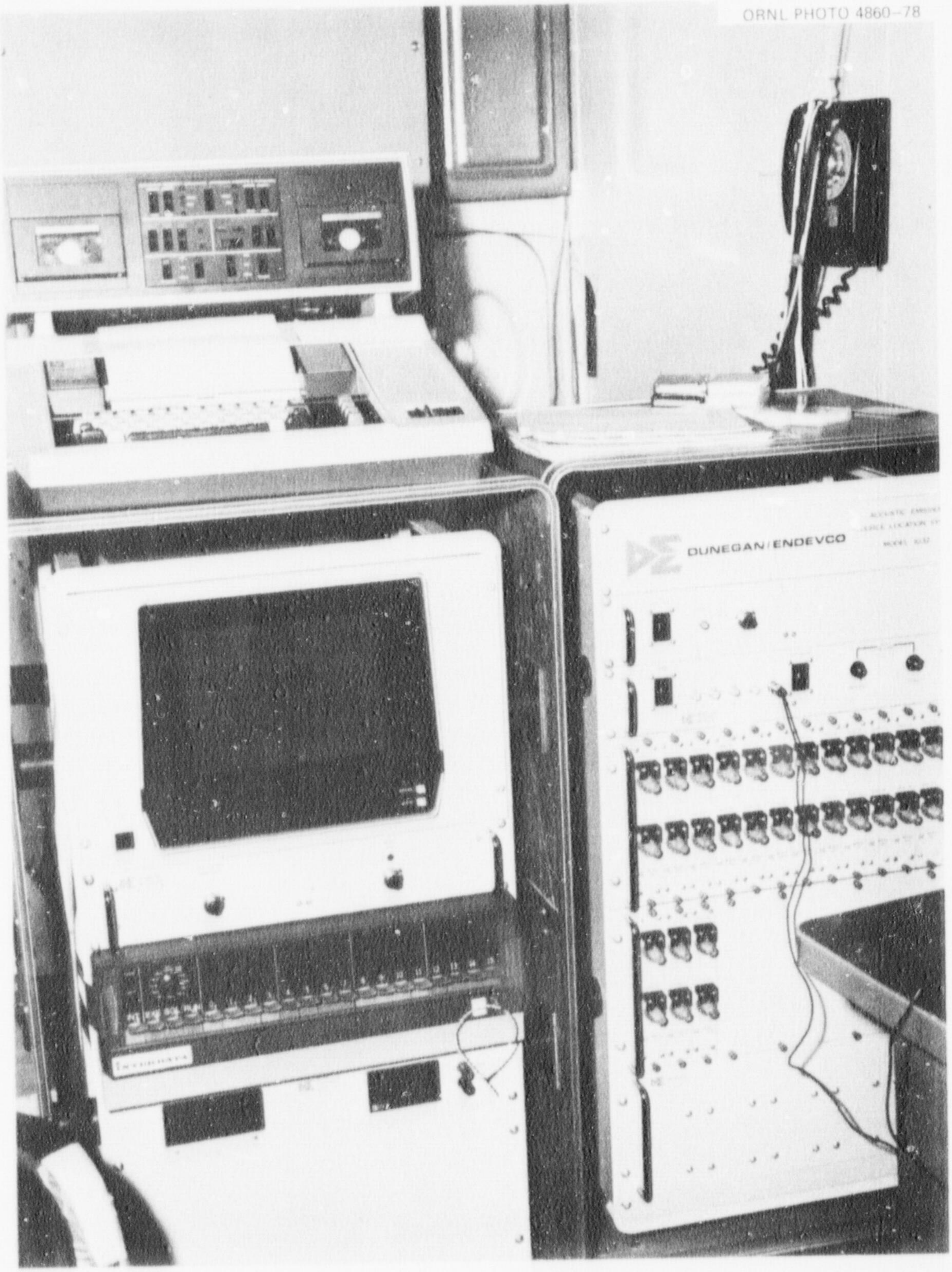

Fig. B.1. D/E 1032 AE monitor system.

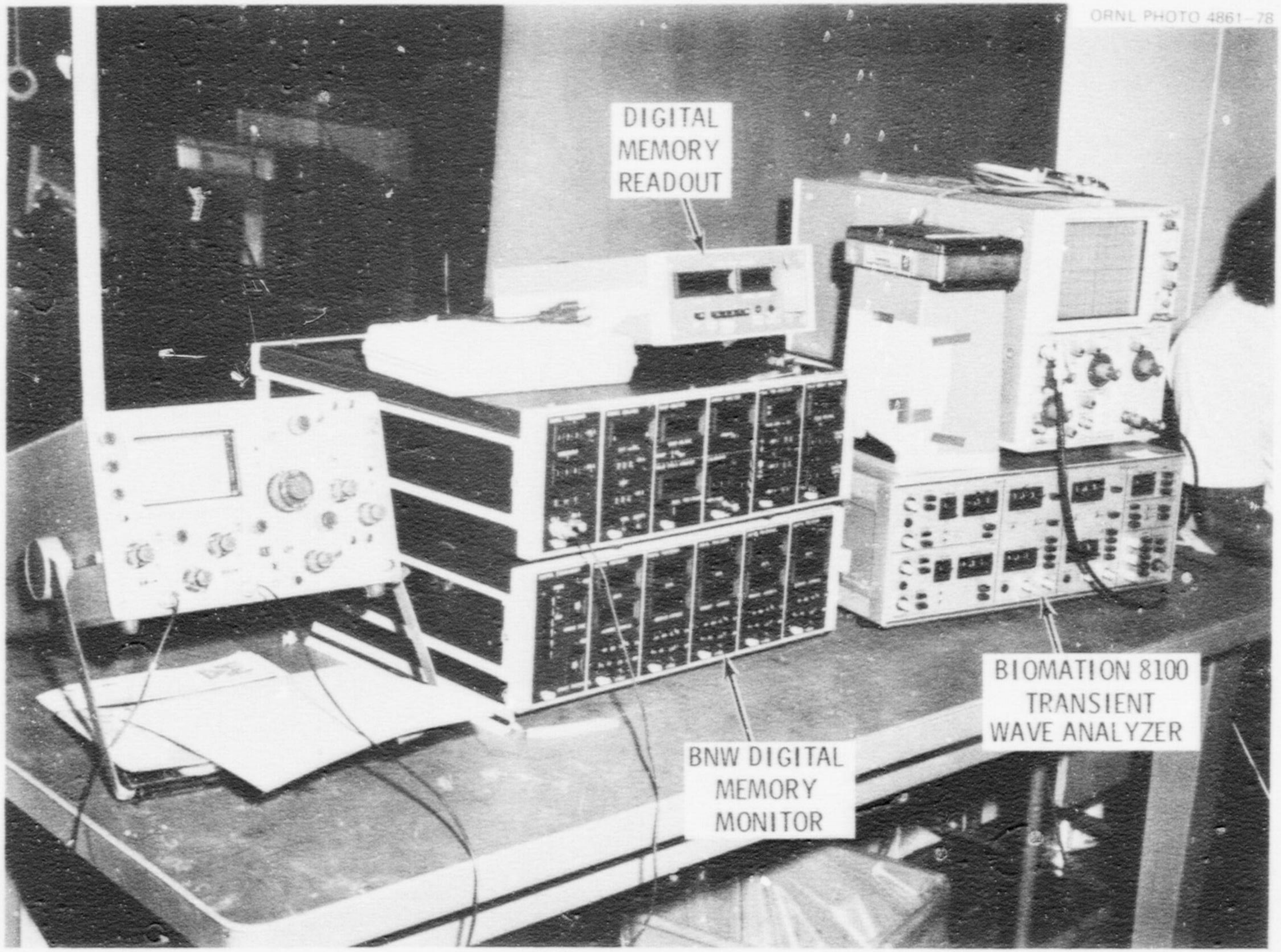
ORNL PHOTO 4861–78

Fig. B.2. BNW AE monitor system.

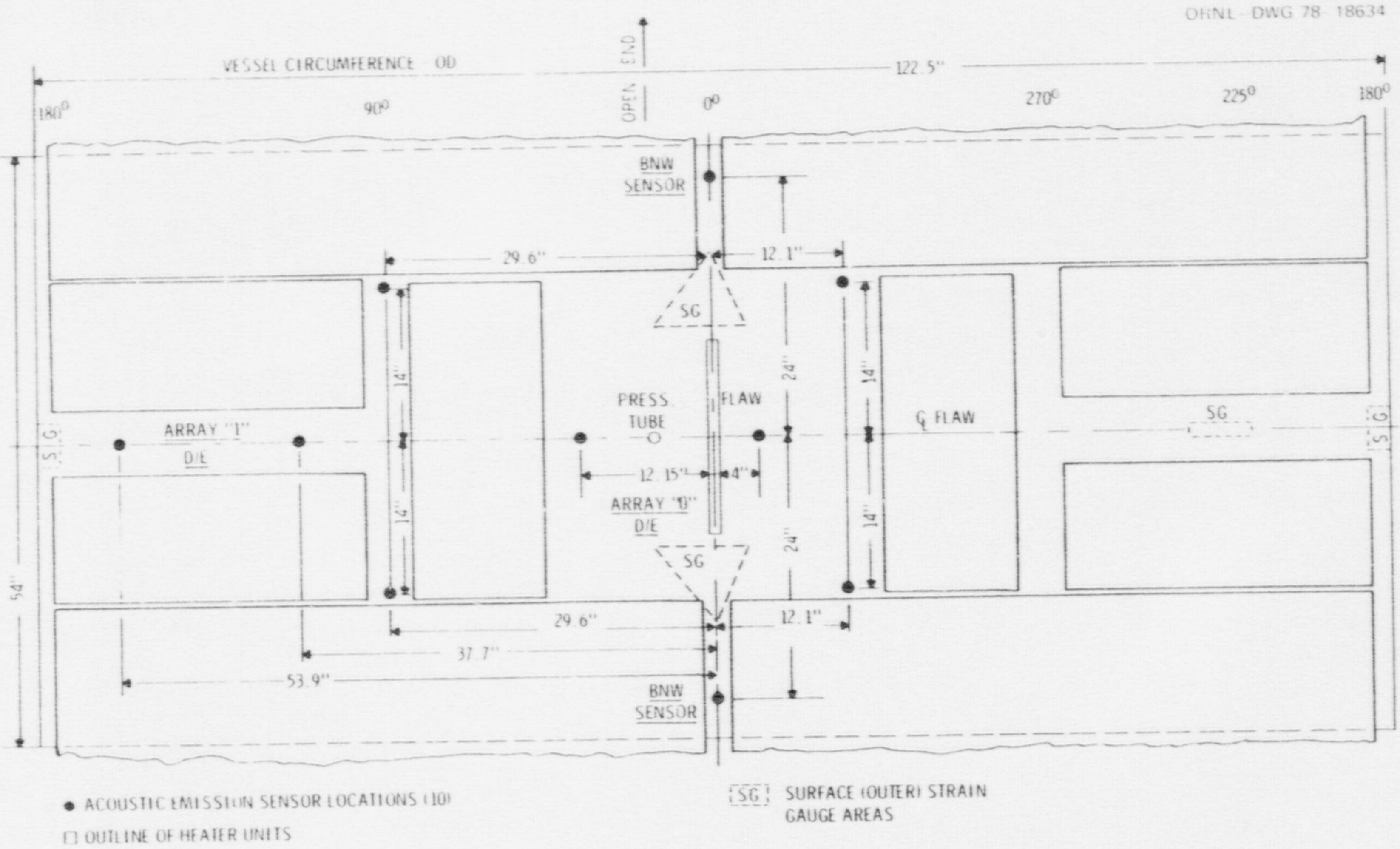

Fig. B.3. Location of AE sensors for the HSST V-7B test.

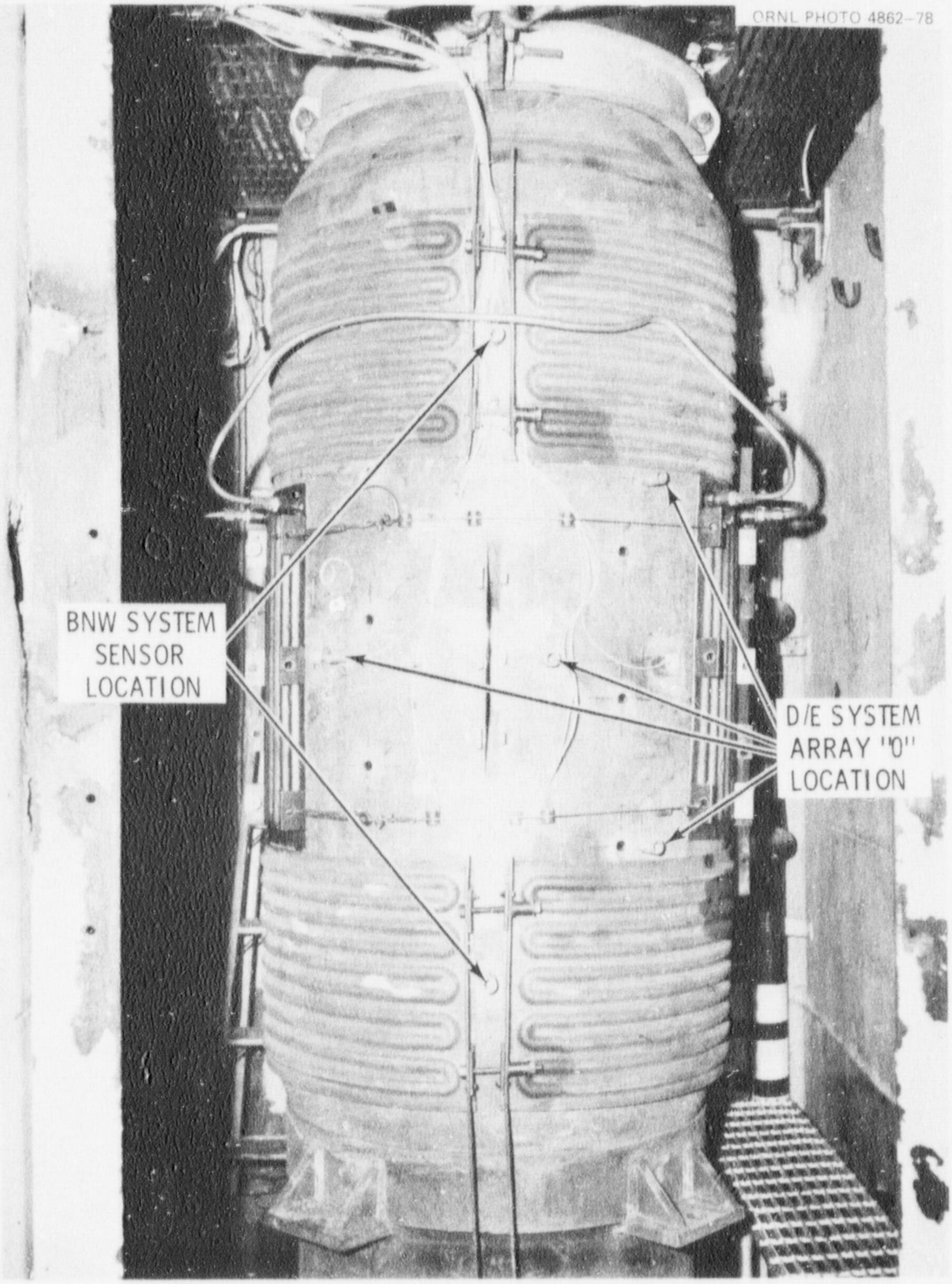

Fig. B.4. AE sensor mounts on HSST V-7B vessel.

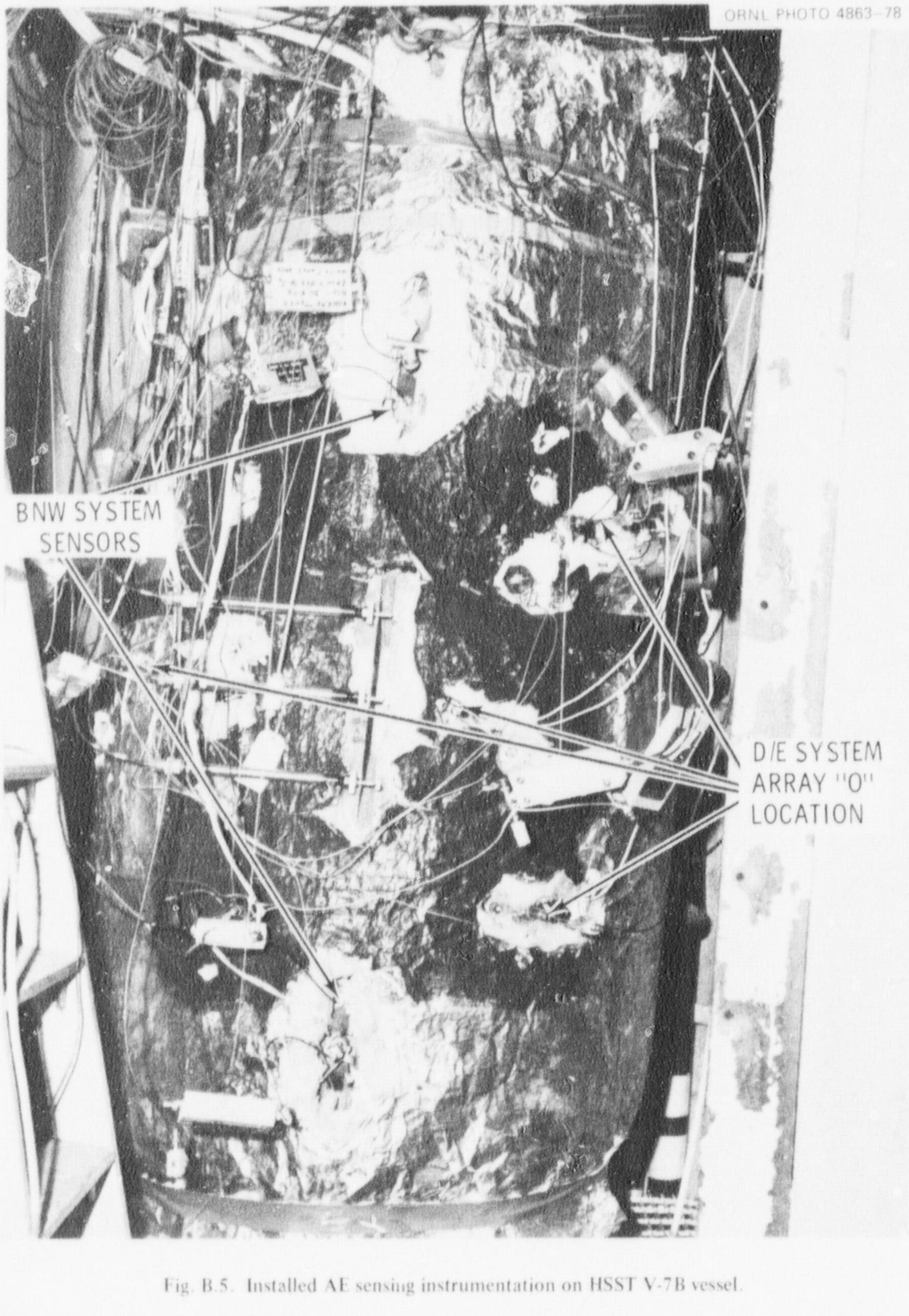

Fig. B.5. Installed AE sensing instrumentation on HSST V-7B vessel.

laboratory specimen data. Sensor calibration curves in Fig. B.6 were generated in the laboratory with the sensors mounted on a 12 × 12 × 6 in. steel block using alumina grit blast excitation.

The AE sensors were connected to preamplifiers located within 15 in. of each sensor. Output of the preamplifiers connected to the monitor systems through cables about 100 ft long.

The ASME guide for acoustic emission examination during application of pressure was followed in setting up the instrument systems preparatory to testing. An electronic pulser was used to inject acoustic signals into the vessel wall. The artificial signals served the functions of (1) verifying that the AE monitor systems were working and (2) providing a reference for setting system gains and/or detection thresholds. Operational parameters for the two AE monitor systems are presented in Table B.1.

Table B.1. Operational parameters for AE monitoring systems

Parameter	D/E 1032	BNW digital
System gain, dB	85	91
Controlling sensor sensitivity, dB (reference 1V/μbar)	−70	−70
Detection threshold (peak), V	1.5	1.4
Monitoring bandwidth, MHz	0.25–1.0	0.2–1.0
Effective sensitivity, μbar	0.27	0.14
Background noise (electronic), V(peak)		
Channel A		1.0
B		0.8
Array 0		
Channel 0	0.5	
1	0.6	
2	0.85	
3	0.5	
Array 1		
Channel 0	1.3	
1	1.2	
2	1.2	
3	0.8	
Memory update period, sec		32 (Ph. 1) 64 (Ph. 2)
Calibration value at 0.1 μsec	2400	
Maximum Δt at 0.1 μsec	2640	
Hard maximum Δt at 0.1 μsec	2800	
Delay, msec	20	
Zone isolation, μsec		
Channel A		310
Channel B		310
Zone Width, in.		19
Rise time limits, μsec		1, 5, 10
Pulse height limits, V (peak)		1.3, 2.5, 5
Parameters recorded	AE event count Δt Source coordinates AE count (ringdown) Time (36-sec increment) Pressure	AE event count (total[a] and valid[a]) Valid AE energy Valid AE rise time Valid AE amplitude Pressure

[a] Total event count is a count of all acoustic signals detected by one sensor with no source isolation control. Valid event count is a count of signals verified by source isolation limits.

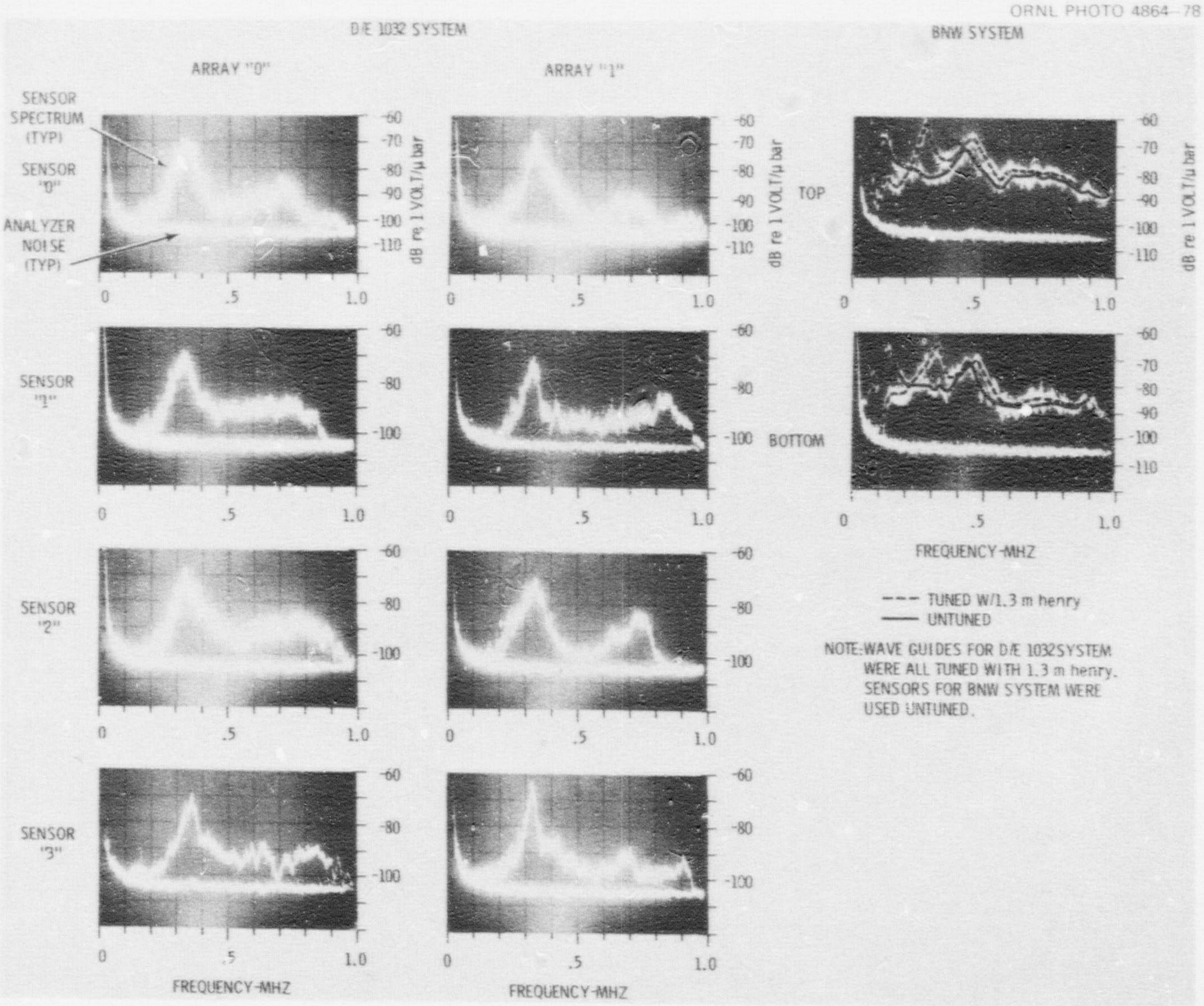

Fig. B.6. AE sensor calibration for HSST V-7B test.

Source location accuracy of the D/E 1032 system was tested using the electronic pulser. The ASME guide requires the accuracy to be within 5% of the maximum distance between the affected sensors. This would be 0.05 × 28 or ±1.4 in. in the subject test. The maximum deviation was 2.0 in. and the average for ten signals was 1.2 in.

The BNW digital system does not perform point source location. It selects AE signals on the basis of the indicated source being within a preselected area. The pulser was used to verify the source isolation zone limits.

Results

Acoustic emission data are summarized in Tables B.2 and B.3. Table B.2 gives data produced by the BNW digital system with associated vessel pressure, and Table B.3 shows data from the D/E 1032 system and corresponding crack-opening-displacement (COD) values. The column headed "Flaw area" shows the

Table B.2. HSST V-7B vessel test – BNW digital system AE data

Pressure (psig)	Total valid AE	Rise time (μsec)				Signal amplitude (V)				Total energy (10^{-5} $V^2 \cdot s$)
		<1	1–5	5–10	>10	<1.3	1.3–2.5	2.5–5	>5	
Phase 1										
0	0	0	0	0	0	0	0	0	0	0
1,000	13	6	5	1	1	7	4	1	1	1,736
2,000	21	11	7	1	2	12	4	3	2	3,247
3,000	64	33	20	8	3	34	15	6	9	9,241
4,000	126	78	31	12	5	79	21	9	17	17,111
5,000	221	128	65	22	6	136	34	27	24	29,776
6,000	324	180	100	30	14	197	46	46	35	41,665
7,000	421	228	127	45	21	255	58	62	46	54,687
8,000	516	278	159	57	22	301	73	81	61	67,318
9,000	665	369	194	70	32	389	89	102	85	84,216
10,000	782	430	230	87	35	455	97	125	105	99,168
10,500	821	448	239	98	36	475	102	135	109	103,945
Phase 2										
0	0	0	0	0	0	0	0	0	0	0
5,000	10	6	4	0	0	6	2	1	1	1,401
8,000	18	10	6	1	1	10	2	4	2	2,274
9,000	34	18	13	1	2	18	3	8	5	4,620
10,000	46	23	19	2	2	27	4	10	5	6,497
11,000	113	48	49	14	2	51	15	35	12	15,015
12,000	169	74	68	20	7	83	19	41	26	22,244
13,000	223	94	97	24	8	109	31	52	31	29,134
14,000	313	137	129	36	11	157	43	69	44	41,027
15,000	406	184	162	48	12	205	56	85	60	49,690
16,000	491	223	190	64	14	250	64	10	70	60,170
17,000	593	276	226	72	19	306	77	129	81	73,884
18,000	699	329	262	79	29	362	95	153	89	86,479
19,000	819	386	306	92	35	419	108	181	111	101,511
20,000	905	428	338	100	39	463	119	194	129	111,200
20,500	955	445	359	111	40	483	126	206	140	117,014
21,000	1067	491	407	126	43	534	137	228	168	130,307
21,500	1232	552	478	149	53	599	152	268	213	150,091
21,750	1555	734	594	165	62	779	183	321	272	195,050
Failure	1788	862	672	183	71	898	209	366	315	219,945

Table B.3. HSST V-7B vessel test – system AE data D/E 1032

Pressure (psig)	COD (mils)			AE event count	
	ZT 127	ZT 128	ZT 129	Flaw area	All array 0
Phase 1					
0	1.00	0.50	1.00	0	0
1,000	3.00	4.00	3.00	0	1
2,000	6.00	8.00	6.00	1	3
3,000	8.50	12.00	8.50	7	13
4,000	11.50	16.49	11.50	14	26
5,000				30	52
6,000	17.49	25.49	17.49	51	87
7,000	20.49	29.99	20.99	62	105
8,000	24.49	35.99	24.99	81	118
9,000	28.99	42.48	29.49	119	147
10,000	29.99	43.98	30.49	157	231
10,500	35.49	50.98	35.99	171	250
Phase 2					
0	10.50	11.50	11.0	0	0
8,000	28.99	41.48	29.99	1	1
9,000	30.99	44.98	32.49	2	2
10,000	33.99	48.98	34.99	5	9
11,000	36.99	53.48	37.99	9	15
12,000	42.98	61.98	44.48	58	70
13,000	49.48	70.47	50.98	68	82
14,000	56.48	79.97	58.49	93	114
15,000	65.98	91.97	69.47	125	152
16,000	75.97	104.46	80.47	145	178
17,000	86.97	118.46	92.97	165	200
18,000	99.46	133.95	107.96	195	232
19,000	116.96	153.94	127.45	228	269
20,000	135.95	175.94	148.45	264	327
20,500	143.45	183.93	155.44	288	353
21,000	164.94	205.42	175.94	343	429
21,500	196.93	236.41	204.92	394	498
21,750	229.92	267.90	235.41	519	666
Failure	339.38	307.89	334.38	556	711

count from array 0, which was associated with the flaw by the source coordinates given in the computer printout. The "All array 0" column shows the total count for array 0 which encompassed the flaw. Array 1 showed only limited scattered indications and is ignored for analysis. Vessel pressure is a common parameter for cross correlating information in the two tables. It is evident that the total AE event count from the D/E system is roughly one-third that from the BNW system. This is reasonable on the basis that the D/E system was purposely set up with about half the sensitivity of the BNW system. It was desirable to operate the BNW system with sensitivity similar to that used in laboratory specimen testing to facilitate data comparisons. This, however, made it subject to possible problems with unexpected vessel test system noise. With this in mind, it was decided to make the D/E system less sensitive to minimize the possibility of total loss of AE data in the event that a noise problem arose. In actuality, both systems operated without problems.

Plots of AE count and vessel pressure vs test time for each set of data are shown in Figs. B.7 and B.8. In addition to the fact that the AE count parallels the pressure curve quite well, there are two other features

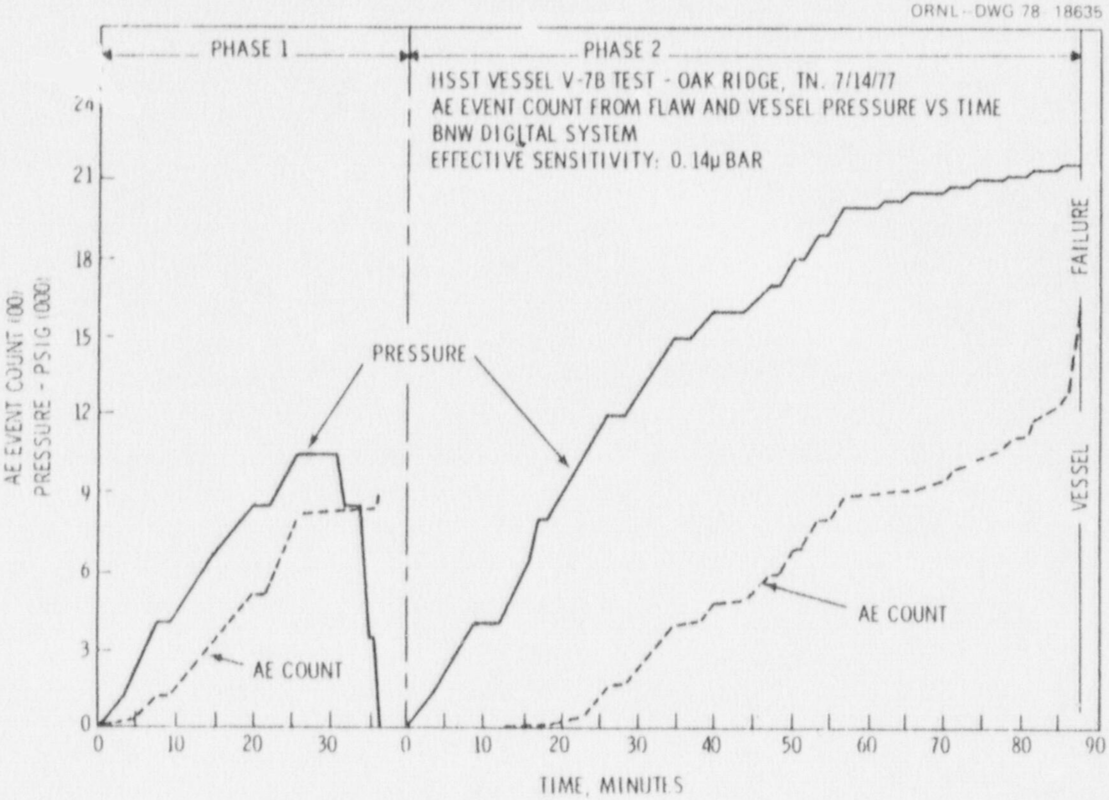

Fig. B.7. AE and pressure vs test time, HSST V-7B vessel test, BNW digital AE system.

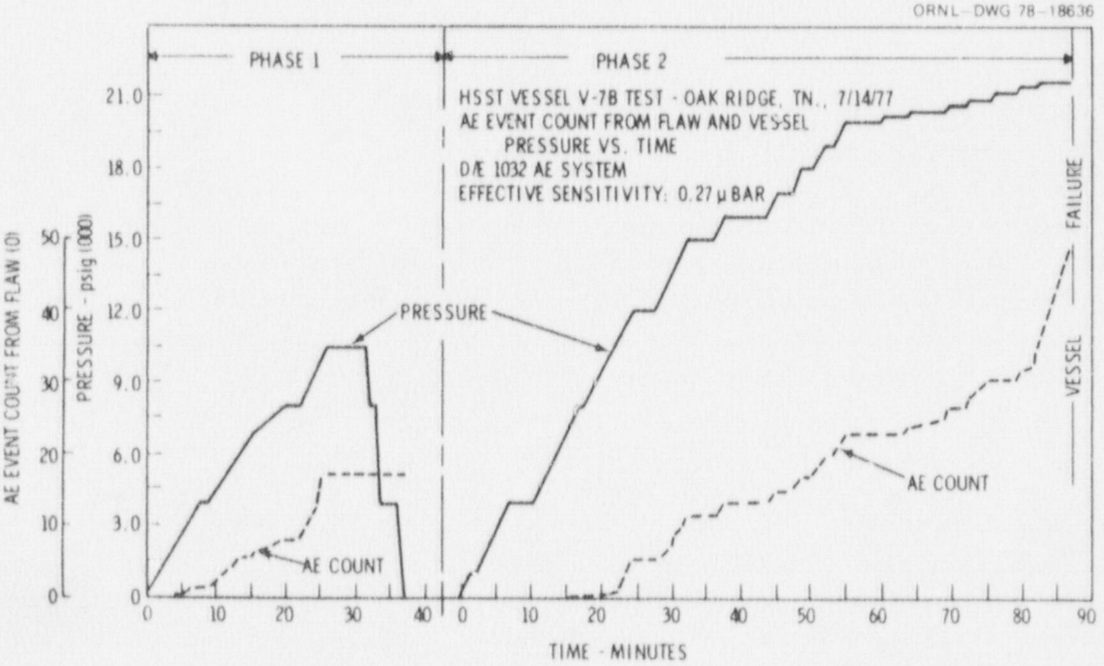

Fig. B.8. AE and pressure vs test time, HSST V-7B vessel test, D/E 1032 AE system.

to note. Going from phase 1 into phase 2, the influence of the Kaiser effect is evident. In phase 2, AE activity does not reappear to any degree until vessel pressure exceeds that of phase 1. This is an AE phenomenon associated with repeat loading within the grossly elastic range to the same stress level where most of the detectable AE will be generated in the first load cycle. Dr. Kaiser first identified this in the early fifties in Germany. Since that time, evidence has been gathered to show that the phenomenon is reversible under appropriate time and temperature conditions. Also, the effect does not hold with repeated loading to the extent that fatigue damage develops.

The other feature to note in Figs. B.7 and B.8 is the sharp increase in AE as vessel failure at the flaw is approached. This provides a finite warning of impending failure. The detailed data indicate that both systems showed the increase in AE at the same point – as the pressure exceeded 21,250 psig.

The visual display of AE source location indications on the D/E 1032 CRT screen relative to pressure increments is shown in Figs. B.9–B.16, which were generated by replaying test data from a digital cassette tape. Authenticity of the recorded data was verified by comparing the accompanying printout with the real-time printout from the test. The ΔCOD shown in the lower left corner of these illustrations is the increase in COD during a given pressure increment compared to the previous condition. In comparing Figs. B.9 and B.10, the Kaiser effect discussed previously is very evident. The same pressure range is involved with the second pressurization occurring within about 30 min of the first. The second pressurization produced very few AE indications.

The primary significance of Figs. B.9–B.16 is to demonstrate AE response to flaw development. Up to 18,000 psig, most of the AE comes from the center section of the flaw. As the pressure increases above 18,000 psig, the AE indications begin to move to the outer ends of the flaw. The last two photographs (21,000 to 21,750 psig and 21,750 psig to failure) show evidence of potential crack extension from the ends of the flaw. Figure B.17 shows that this did occur.

Signal wave forms processed by the BNW system were obtained with an associated transient wave analyzer and oscilloscope. Samples of these are presented in Fig. B.18. An important observation is the fact that these are generally similar to AE signals observed during testing laboratory specimens of the same type of material. This tends to lend credence to the usefulness of laboratory data in developing preliminary AE–fracture mechanics relationships for application to heavy-section vessels. Signal 8 is considered to be a noise signal from an unidentified source. It is classified as such on the basis of the gradual increase in amplitude without any sharply defined signal front. This is the type of signal observed previously from known noise sources such as movement at the interface of two metal objects. One noticeable difference between these signals and those observed from laboratory specimens is the predominance of lower-frequency components (∿300 kHz) in the signals from the vessel test. Signals from laboratory specimens show higher-frequency components as well as the lower frequency. This is probably a combination of the influence of high-frequency signal attenuation in the longer travel path in the vessel material and electronic system characteristics.

Analysis

A limited amount of analysis relative to flaw growth parameters has been performed at PNL. This concerns two areas – relating AE to COD measurements and relating AE to stress intensity factor.

The AE count vs COD is shown in Figs. B.19 and B.20. Figure B.19 shows the AE event count from both the BNW and the D/E systems plotted against an average of the COD values for phases 1 and 2. Figure B.20 shows AE energy data from the BNW system plotted against average COD for both phases. Except for one point corresponding to 21,750 psig, there appears to be a reasonably good linear relation between COD

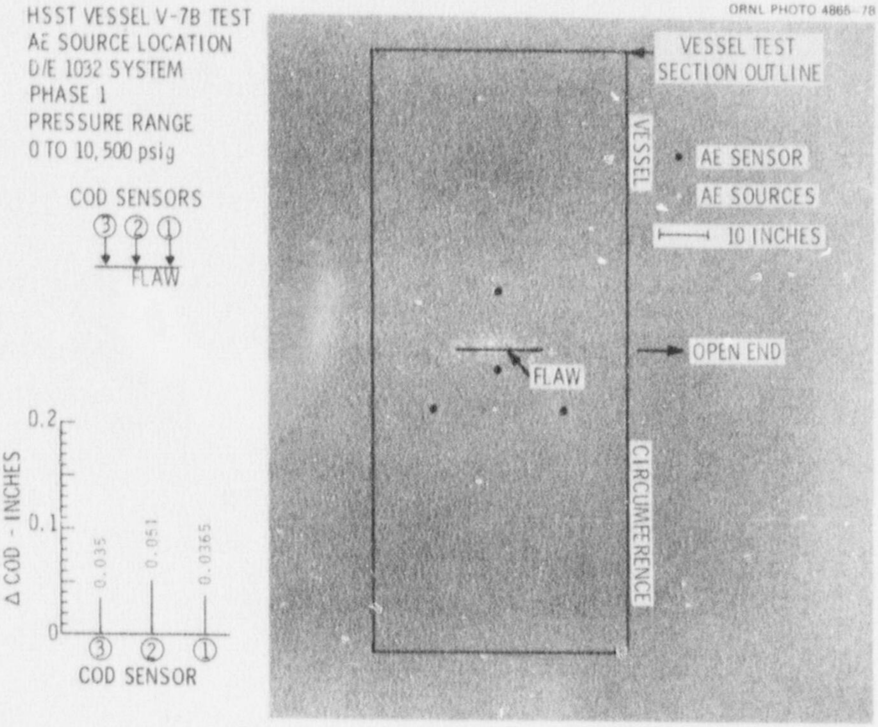

Fig. B.9. HSST V-7B test AE phase 1, 0–10,500 psig.

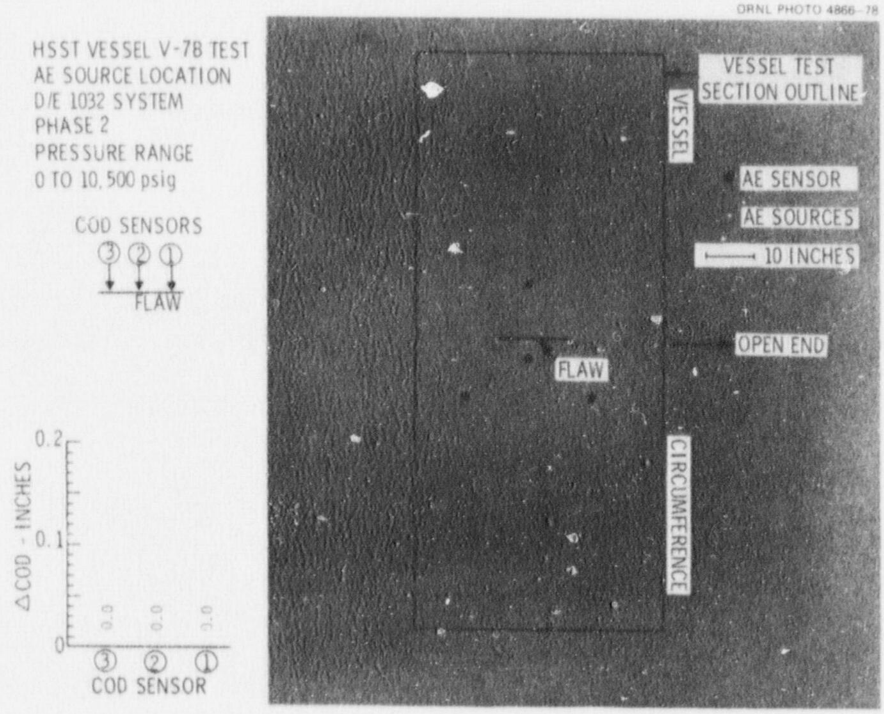

Fig. B.10. HSST V-7B test AE phase 2, 0–10,500 psig.

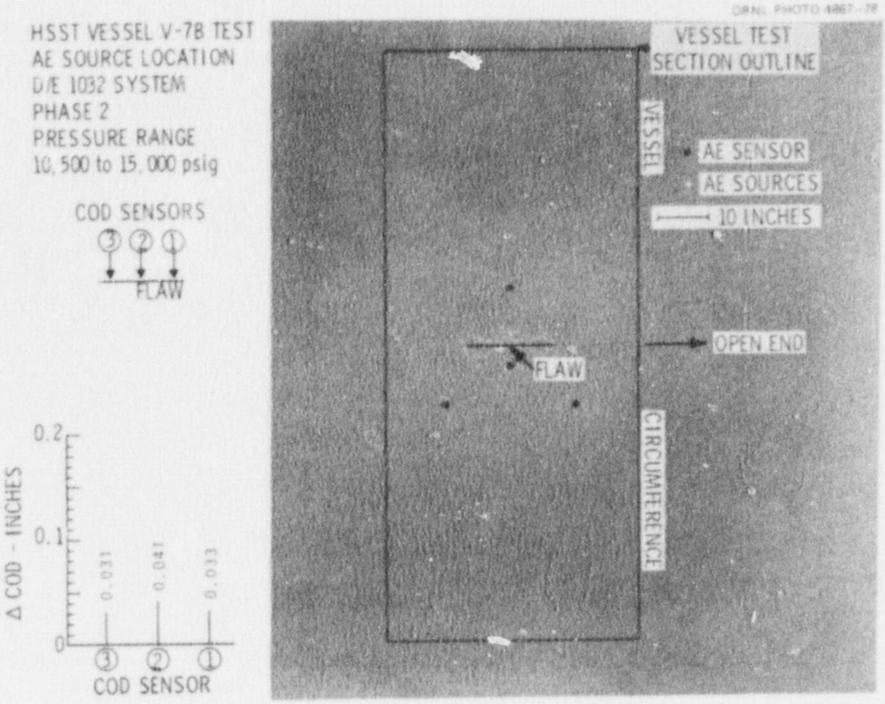

Fig. B.11. HSST V-7B test AE, phase 2, 10,500–15,000 psig.

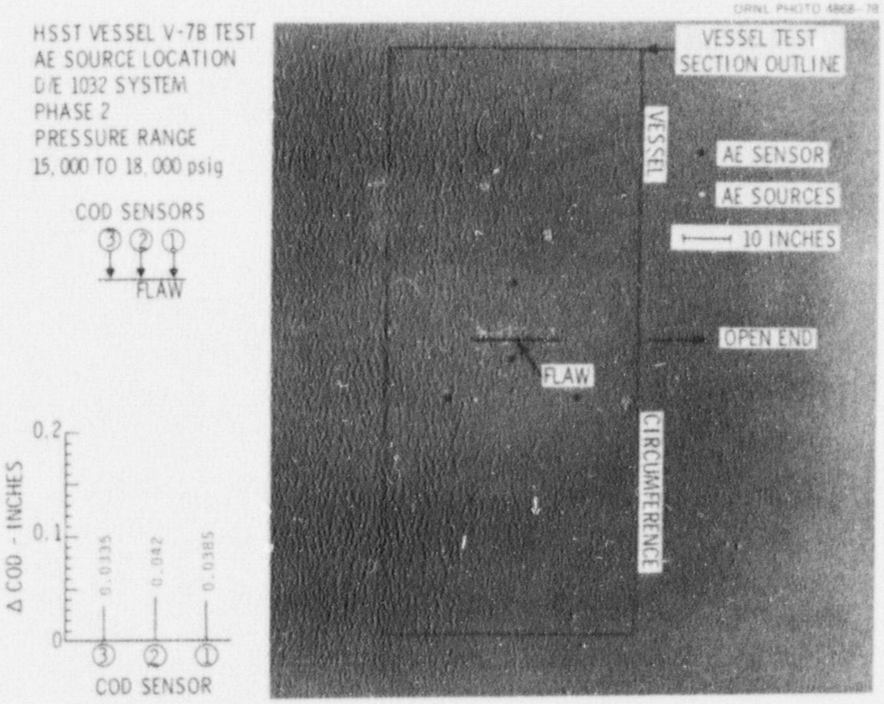

Fig. B.12. HSST V-7B test AE, phase 2, 15,000–18,000 psig.

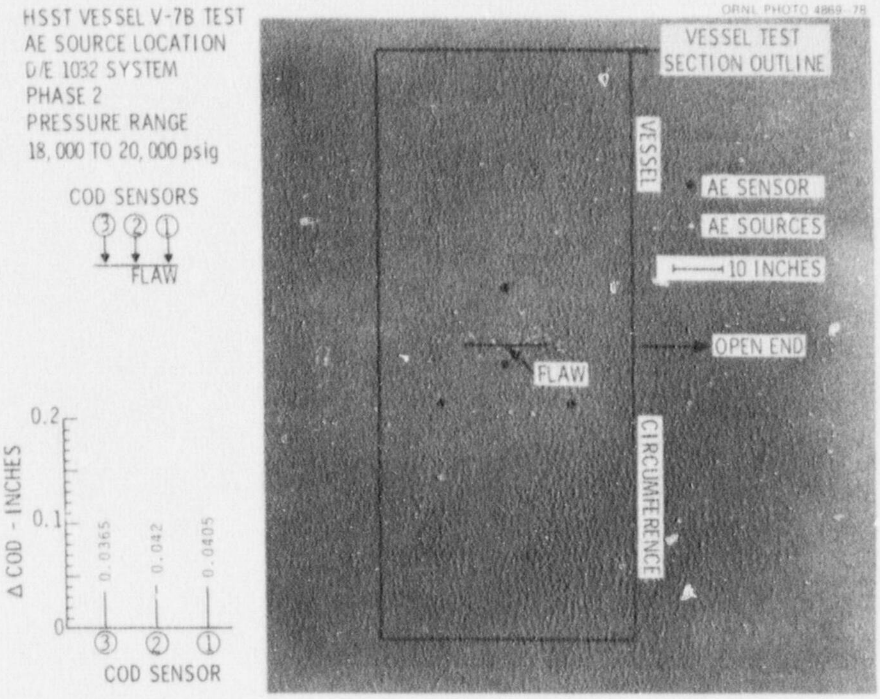

Fig. B.13. HSST V-7B test AE, phase 2, 18,000–20,000 psig.

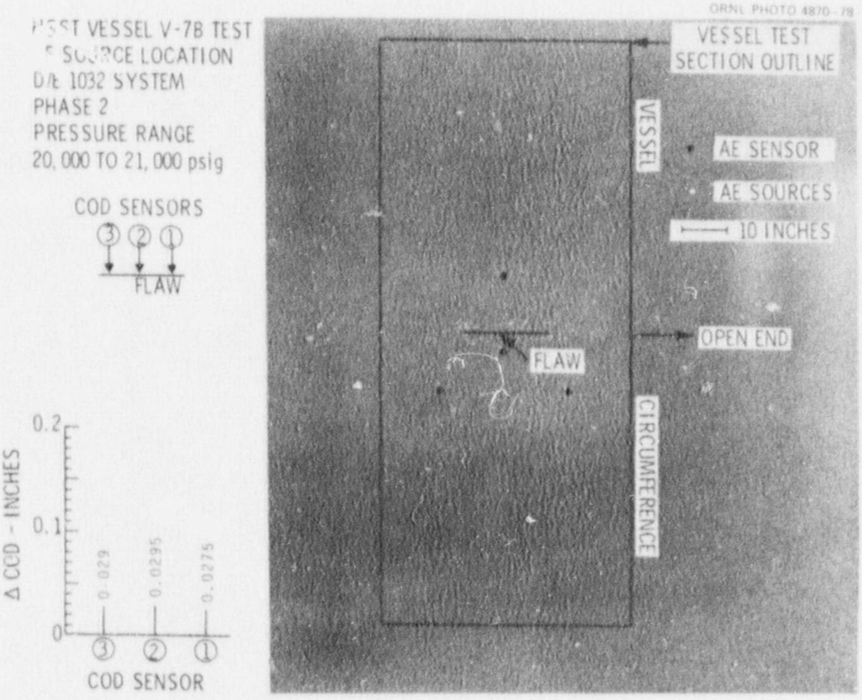

Fig. B.14. HSST V-7B test AE, phase 2, 20,000–21,000 psig.

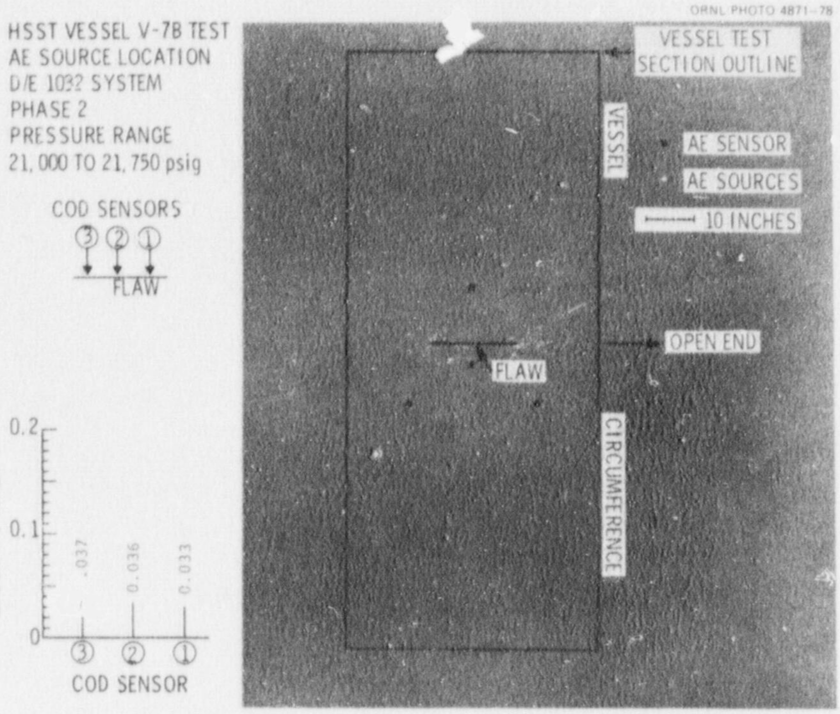

Fig. B.15. HSST V-7B test AE, phase 2, 21,000–21,750 psig.

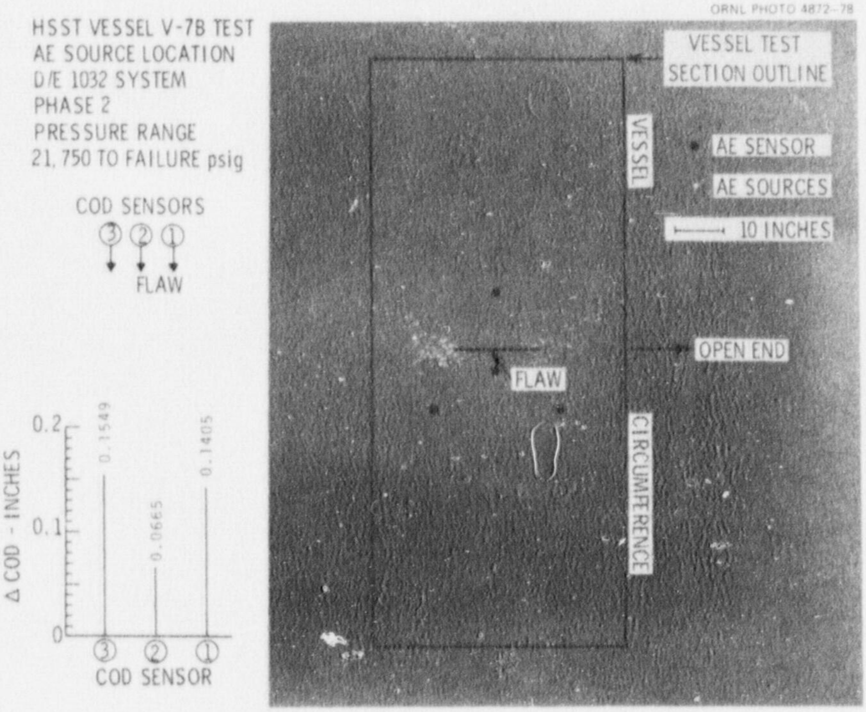

Fig. B.16. HSST V-7B test AE, phase 2, 21,750–failure psig.

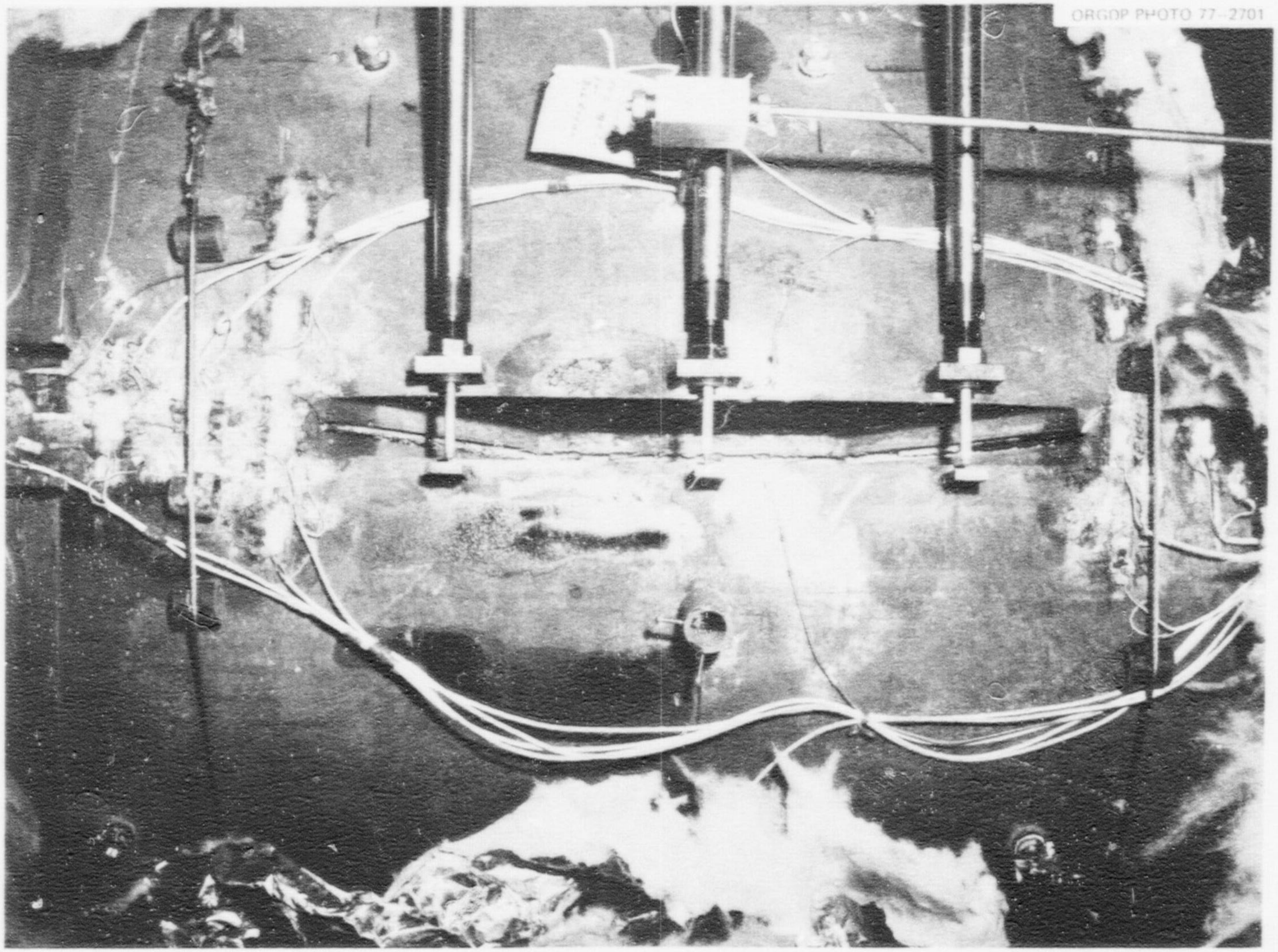
ORGDP PHOTO 77-2701

Fig. B.17. HSST V-7B vessel failure at machined flaw.

ORNL PHOTO 4873–78

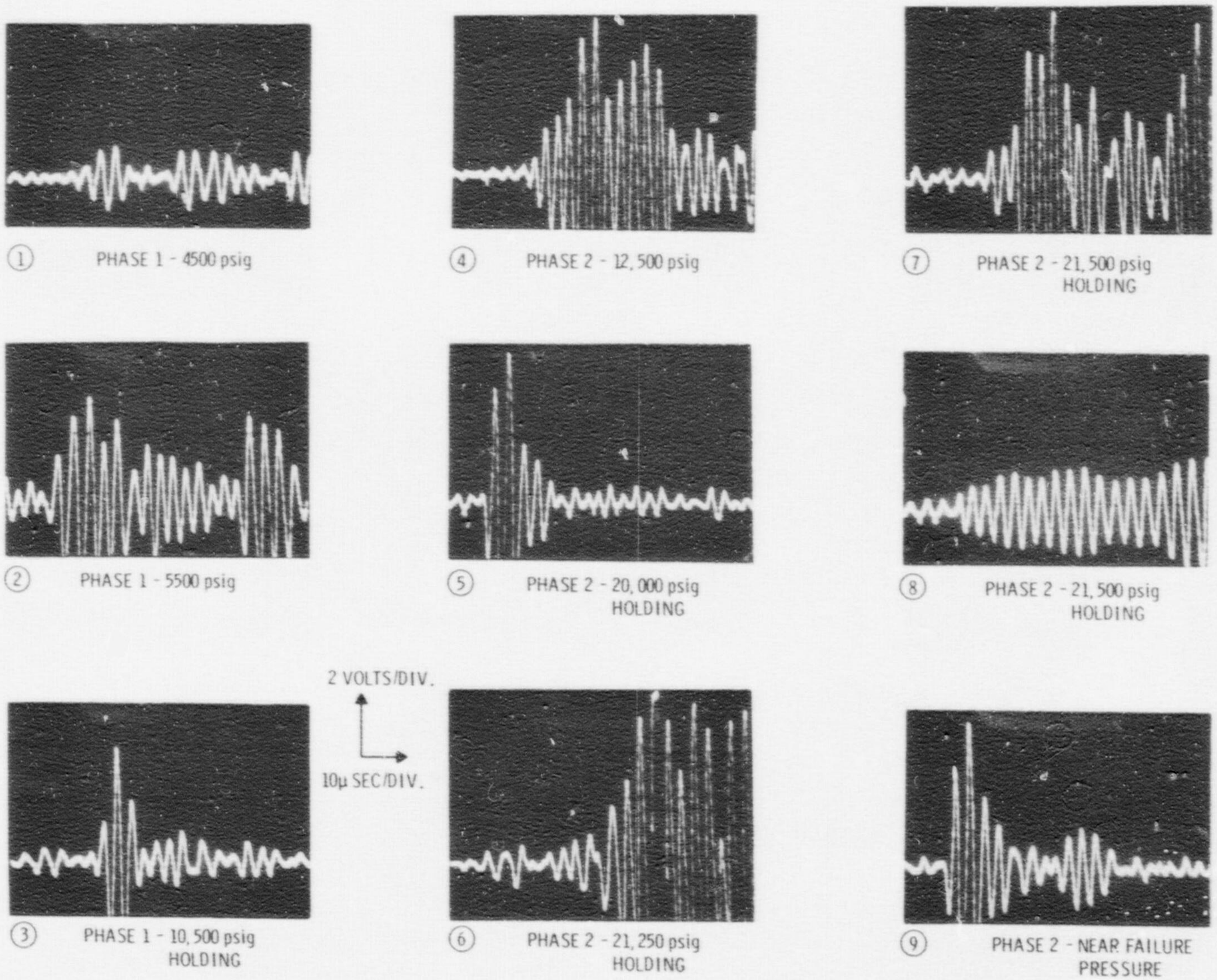

① PHASE 1 - 4500 psig

② PHASE 1 - 5500 psig

③ PHASE 1 - 10,500 psig HOLDING

④ PHASE 2 - 12,500 psig

⑤ PHASE 2 - 20,000 psig HOLDING

⑥ PHASE 2 - 21,250 psig HOLDING

⑦ PHASE 2 - 21,500 psig HOLDING

⑧ PHASE 2 - 21,500 psig HOLDING

⑨ PHASE 2 - NEAR FAILURE PRESSURE

Fig. B.18. Sample AE signals – HSST V-7B vessel test.

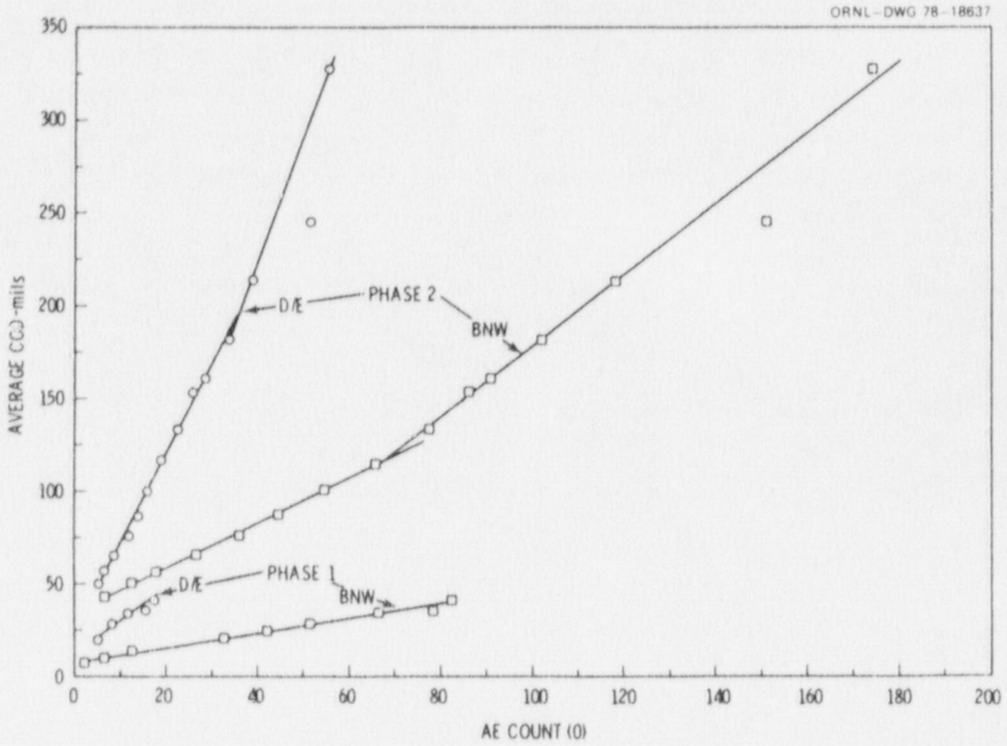

Fig. B.19. AE count vs average COD – HSST V-7B vessel test.

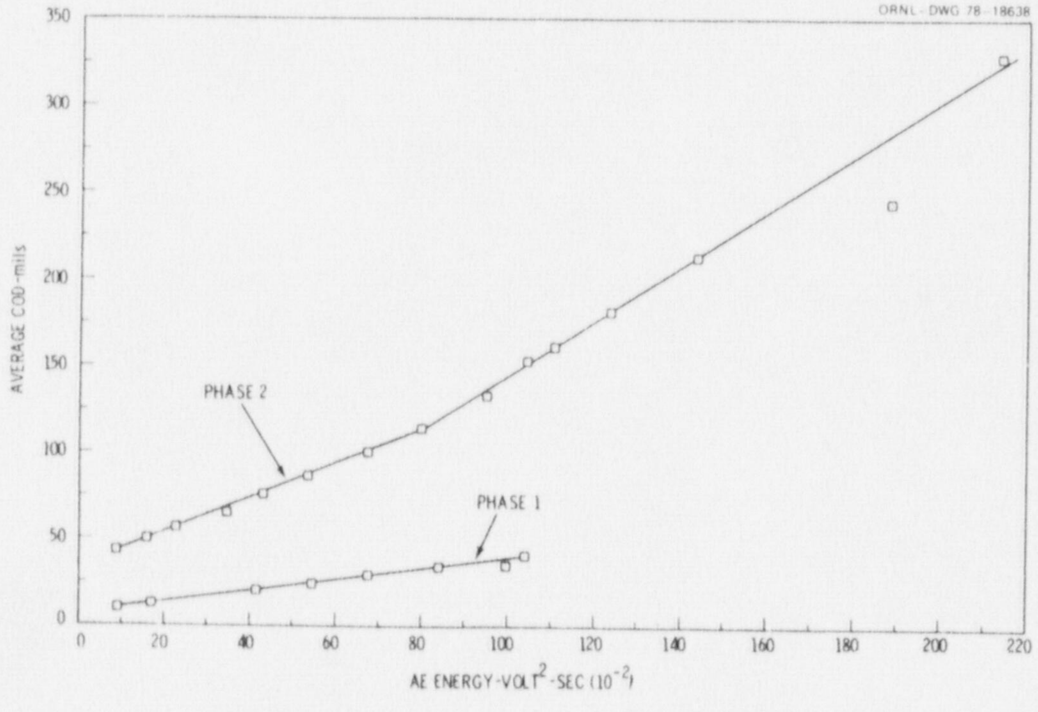

Fig. B.20. AE energy (BNW) vs average COD – HSST V-7B vessel test.

and AE. An interesting observation is the three distinct slopes to these curves. One slope is defined by the phase 1 data. For the BNW data the slope increases for phase 2 for the segment from 11,000* to 18,000 psig and then increases further for the segment from 18,000 psig to failure. The final change in slope for the D/E data appears to start at about 20,500 psig instead of 18,000. This is simply an observation at this point. We cannot yet identify a cause or attach a significance to the pattern. Further review in light of definable stages of flaw development may lend significance to the pattern.

The other area of analysis concerns relating AE to stress intensity factor. The pressure readings, calculated stress intensity factors, and reduced AE count data obtained during burst testing of vessel V-7B are given in Table B.4. The stress intensity factors were calculated by utilizing an equation developed by Merkle et al:[1]

$$K_I = C\left(\frac{r}{t}\right)p\,\sqrt{\pi a}\,, \tag{1}$$

where C is the elastic shape factor for the flaw (1.572), r is the vessel radius (13.5 in.), t is the wall

---

*Phase 2 data from 0 to 11,000 psig were not included because this is a nonrepresentative area AE due to the effects of previous loading to 10,500 psig on phase 1.

Table B.4. Acoustic emission and fracture mechanics data on HSST vessel V-7B burst test[a]

Pressure (psig)	K_I (ksi $\sqrt{\text{in.}}$)	BNW AE count									BNW energy (10^{-5} V^2·s)	D/E AE count	
		Total valid	Rise time (μsec)				Signal amplitude (V)					Flaw	Total array
			<1	1–5	5–10	>10	<1.3	1.3–2.5	2.5–5	>5			
0	0	0	0	0	0	0	0	0	0	0	0	0	0
1,000	14.45	13	6	5	1	1	7	4	1	1	1,736	0	1
2,000	28.90	21	11	7	1	2	12	4	3	2	3,247	1	3
3,000	43.35	64	33	20	8	3	34	15	6	9	9,241	7	13
4,000	57.80	126	78	31	12	5	79	21	9	17	17,111	14	26
5,000	72.25	221	128	65	22	6	136	34	27	24	29,776	30	52
6,000	86.70	324	180	100	30	14	197	46	46	35	41,665	51	87
7,000	101.2	421	228	127	45	21	255	58	62	46	54,687	62	105
8,000	115.6	516	278	159	57	22	301	73	81	61	67,318	81	116
9,000	130.1	665	369	194	70	32	389	89	102	85	84,216	119	178
10,000	144.5	782	430	230	87	35	455	97	125	105	92,168	157	231
10,500	151.7	821	448	239	98	36	475	102	135	109	103,945	171	248
11,000	159.0	854	460	254	104	36	487	107	147	112	108,204	173	251
12,000	173.4	910	486	273	110	41	519	111	153	126	115,433	222	306
13,000	187.9	964	506	302	114	42	545	123	164	131	122,323	232	318
14,000	202.3	1054	549	334	126	45	593	135	181	144	134,216	257	350
15,000	216.8	1147	596	367	138	46	641	148	197	160	142,879	285	383
16,000	231.2	1232	635	395	154	48	686	156	219	170	153,359	307	412
17,000	245.7	1334	688	431	162	53	742	169	241	181	167,073	329	430
18,000	260.1	1440	741	467	169	63	798	187	265	189	179,668	354	462
19,000	274.6	1560	798	511	182	69	855	200	293	211	194,700	387	500
20,000	289.0	1646	840	543	190	73	899	211	306	229	204,200	425	558
20,500	293.2	1696	857	564	201	74	919	218	318	240	210,203	442	578
21,000	303.5	1808	903	612	216	77	970	229	340	268	223,496	481	625
21,500	310.7	1973	964	683	239	87	1035	244	380	313	243,280	534	700
21,750	314.3	2296	1146	799	255	96	1215	275	433	372	288,239	609	807
22,020	318.2	2529	1274	877	273	105	1334	301	478	415	313,134	720	953

[a] The AE data represent the cumulative AE obtained during two pressurization runs on vessel V-7B. During the first run the vessel was pressurized to 10,500 psi and then unloaded. On the next run the vessel was pressurized to failure. All AE data obtained below 10,500 psi on the second pressurization were subtracted from the accumulated AE obtained at higher pressures.

thickness (6 in.), a is the flaw depth (5.31 in.), and p is the internal pressure. Substituting the above values into Eq. (1) yields

$$K_I = 14.45\,p\,. \tag{2}$$

In order to delineate the relationship between AE and a fracture mechanics parameter, graphs of AE count vs the stress intensity factor were made (Fig. B.21). The D/E counts are plotted in Fig. B.21 as total array count and flaw count. The total array count represents the total AE count obtained in array 0 regardless of source location. The flaw count represents a manual accumulation of AE count in array 0 from sources near the flaw as determined by their source coordinates. A linear relationship between AE count and stress intensity factor seems to exist over a broad range in stress intensity factor. Deviation from linearity occurs at the extreme low and high ends of the stress intensity factor range. Deviation at high stress intensity factor values is influenced by increasing AE associated with incipient fast fracture. The characteristic of rapidly increasing AE as a precursor to fast fracture has been observed by a number of AE investigators in several materials.[1–3]

The lines drawn on Fig. B.21 were obtained by a least-mean-squares fitting on the data to an equation of the form

$$\Sigma \mathrm{AE} = a + bK_I\,. \tag{3}$$

The calculated regression coefficients and the square of the correlation coefficients are listed in Table B.5. It is evident from the data in Table B.5 that all AE parameters plotted in Fig. B.21 correlate well with the stress intensity factor. In addition, linear regression analysis was performed on BNW AE count data that were partitioned with respect to rise time and signal amplitude. The objective is to contribute to identification of AE parameters which most strongly relate to flaw growth. Table B.5 indicates that all the partitioned AE, except the slow rise time (>10 μsec) and high amplitude (>5 V), correlate well with stress intensity factor. This is consistent with results obtained to date in laboratory specimen testing under the NRC-sponsored AE flaw characterization program at PNL.

Table B.5. Least-squares regression coefficients and correlation coefficients for AE vs K_I curves[a]

	BNW AE count									BNW energy (10^{-5} V^2·s)	D/E AE count	
	Total valid	Rise time (μsec)				Signal amplitude (V)					Flaw	Total array
		<1	1–5	5–10	>10	<1.3	1.3–2.5	2.5–5	>5			
a	−221.8	−86.6	−94.7	−31.1	−9.3	−94.4	−23.0	−63.5	−40.5	−24,791	−105.0	−113.6
b	6.478	3.220	2.193	0.788	0.277	3.462	0.805	1.270	0.936	797.8	1.815	2.303
r^2	0.995	0.992	0.994	0.994	0.979	0.994	0.996	0.993	0.988	0.995	0.990	0.992

[a] $\Sigma\mathrm{AE} = a + bK_I$ for K_I between 43.35 and 303.5 ksi $\sqrt{\mathrm{in.}}$

Again, the absolute significance of these results to flaw evaluation by AE has not been established. They constitute an important input to the AE flaw characterization program, however, because they were derived from a test involving a vessel configuration with a relatively thick wall (6 in.). The current AE flaw characterization work by necessity uses primarily laboratory specimens up to 1½ to 2 in. thick. The subject data contribute to assuring that laboratory results are valid and applicable in the context of a reactor vessel.

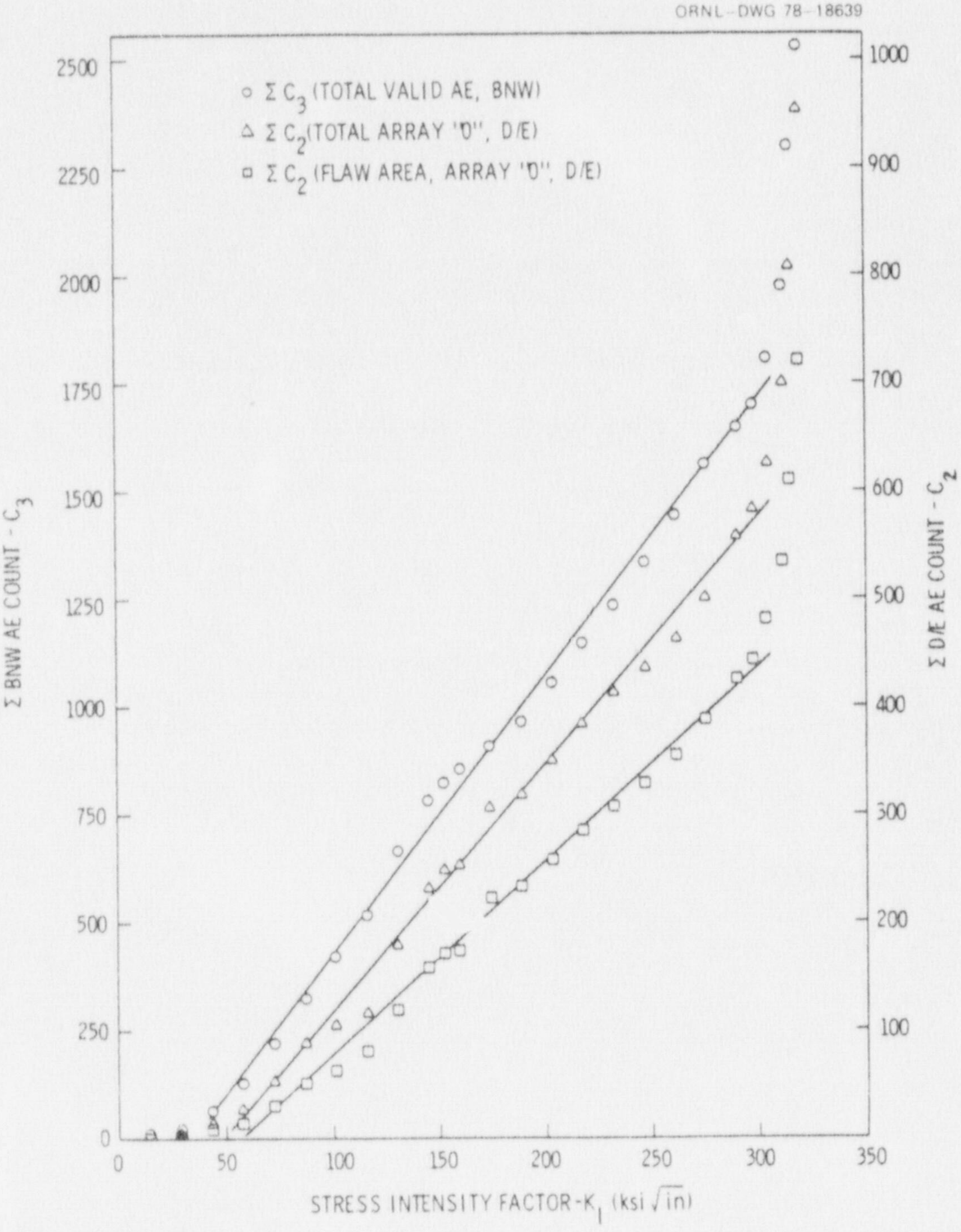

Fig. B.21. AE count vs stress intensity factor – HSST V-7B vessel test.

Conclusions

Conclusions which can be drawn from the AE results include:

1. AE source location information which is indicative of flaw development can be obtained in the circumstances of this test.

2. Growth of a flaw in 6 in. thick A533B class 1 material at 200°F produced readily detectable AE.

3. The AE signals detected from the V-7B vessel are similar to those observed in laboratory testing of thinner laboratory specimens of similar material.

4. AE data show a good correlation with fracture mechanics parameters associated with development of the machined defect in the vessel wall.

5. There was no AE indication of distress in the vessel at locations other than the machined defect detected.

References

1. J. G. Merkle et al., *Test of 6-in.-thick Pressure Vessels. Series 3: Intermediate Test Vessel V-7,* ORNL/NUREG-1 (August 1976).

2. P. G. Bentley et al. "Acoustic Emission Test on a 25-mm-thick Mild Steel Pressure Vessel with Inserted Defects," *Journal Institute of Mechanical Engineers* (June 1976).

3. N. O. Cross, *Display and Analysis of Real Time Data from Acoustic Emission Tests of Pressure Vessels,* Exxon Research and Engineering Co., Florham Park, N.J., presented at the Second Acoustic Emission Symposium, Tokyo, Japan, September 1974.

Appendix C

Acoustic Emission Monitoring of HSST Intermediate Vessel V-7B

D. J. Naus

Introduction

Techniques for nondestructive testing of nuclear power facilities to evaluate safety and to assure maximum availability have included dye penetration, computerized remote ultrasonic evaluation, holographic techniques, and remote television coverage.[1] Application of many of these techniques is quite time consuming and costly. Relatively recent advancements in nondestructive testing utilizing acoustic emission (AE) techniques have made this technique potentially viable for in-service monitoring of the structural integrity of pressure vessels.

Acoustic emissions are small-amplitude elastic stress waves generated during material deformation (plastic deformation or nucleation and growth of flaws) resulting from mechanical or thermal stimulus. The stress waves are detected by transducers as small displacements of the specimen surface. The emissions may be of two types, continuous or burst. Continuous acoustic emissions are low-level, high-signal-density emissions such as might be observed during a tensile test of an unflawed specimen. Burst AEs are generated when a plastic zone or microcracks form in the vicinity of a stress concentration. Characterization of the stress wave emissions provides an insight into the type of inelastic deformation occurring. That is, rate of emissions indicates immediacy of fracture instability; amplitude (oscillation counts) indicates magnitude of the inelastic phenomena; total AE energy may be used as an indicator of structural integrity; and rate of emission per unit time indicates the rate of flaw propagation. The capability of AE for monitoring the thick-walled pressure vessels tested under the Heavy-Section Steel Technology (HSST) Program is being evaluated as a secondary purpose of the program.

HSST intermediate test vessel V-7B was fabricated from ASTM A533, grade B, class 1 steel plate. The test vessel had an outside diameter of 99 cm (39 in.) and an inside diameter of 68.6 cm (27 in.). A flaw formed by hydrogen charging of an electron-beam weld in the heat-affected zone of a previous weld repair was the region of interest. Details of the test vessel and flaw are presented in Figs. C.1 and C.2, respectively. This section of the report presents AE data obtained using an in-house Trodyne multisensor comprehensive data (MSCD) system. Results were obtained during the two pressurization cycles of the flawed vessel.

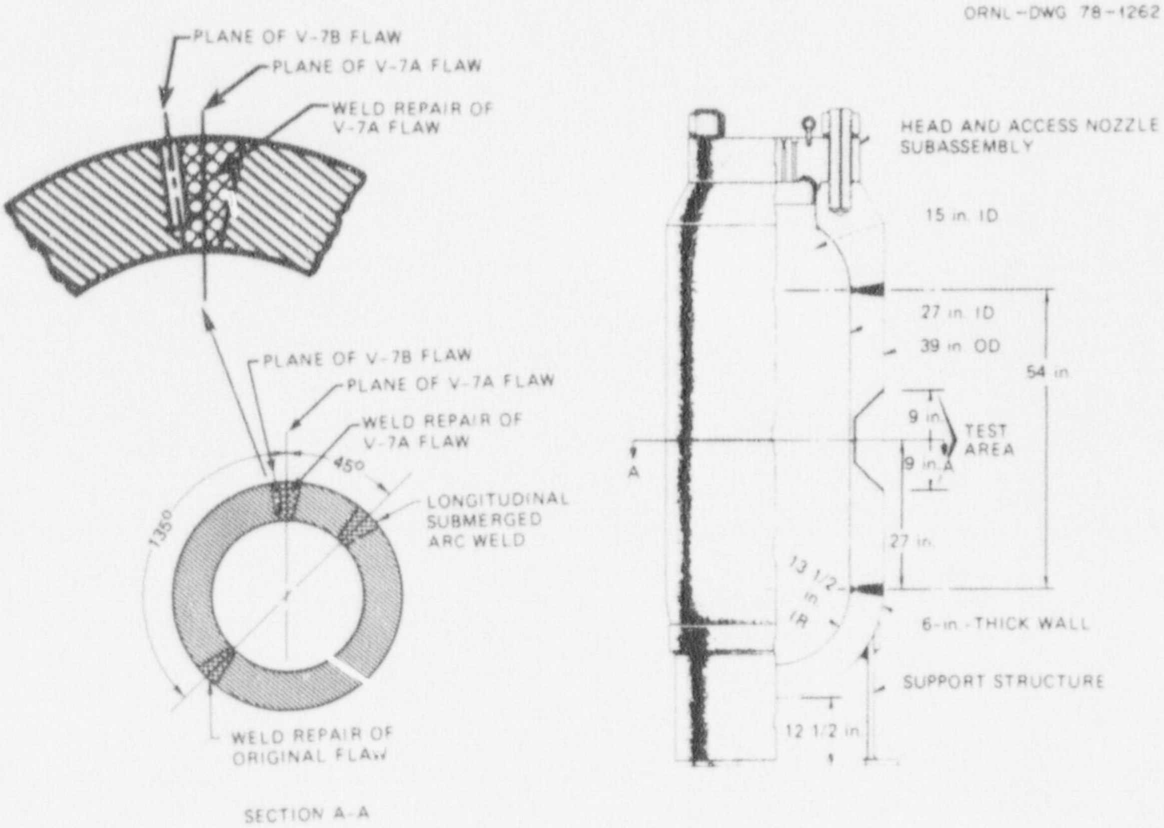

Fig. C.1. Intermediate test vessel V-7B.

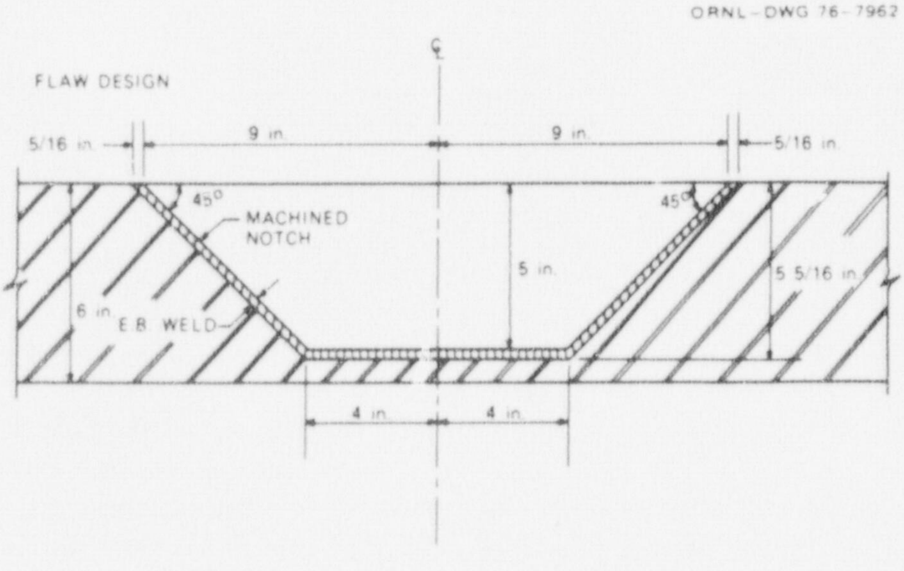

Fig. C.2. Flaw design for V-7, V-7A, and V-7B.

Instrumentation

The Trodyne MSCD system shown in Fig. C.3 was used for AE monitoring of intermediate test vessel V-7B. Each input channel of the system consisted of a sensor, preamplifier, and amplifier. The amplified and filtered signals were fed into a processor which derived the individual AE parameters from the detected signal, stored the data sets and their transfer to the computer, generated the control parameters for the


ORGDP PHOTO 77–2696

Fig. C.3. Acoustic emission instrumentation.

entire MSCD system, and performed discrimination functions. Discrimination functions consisted of sensor activity detection (which establishes reset time to clear the system for the next data set), exclusion signals (which accept only valid sensor arrival sequences), and range gate (which assures that signals are grouped in complete sets within the instantaneous array). The MSCD measured the magnitude of acoustic emission events as a function of their location, time of occurrence, and parametric value. All derived AE parameters were processed, stored for off-line analysis, and displayed on the CRT screen in real time as either raw data, activity distribution, or magnitude distribution. Permanent records of the CRT screen contents were obtained during the test as desired.

Experimental Procedure

The cylindrical test section of vessel V-7B was instrumented with eight transducers. Six of the transducers were used as active sensors and two were used as slave sensors to lock the system out to events occurring outside the flawed region of interest. Transducer positions and locations relative to the flaw are presented in Fig. C.4. Monitoring of the entire cylindrical section of the vessel could not be accomplished during this test because the required heating elements covered most of the surface. Transducers were attached to the vessel by means of epoxy shoes which had been glued to the vessel surface using an elevated-temperature epoxy (Barco Bond MB-100X epoxy adhesive from the Astro Chemical Company). The location of active transducers (1–6) and slave transducers (S1,S2) are shown in Fig. C.5. Coupling of the epoxy shoe and the transducer was provided by a thin layer of Dow Corning 340 silicone heat sink

ORNL–DWG 78–15317

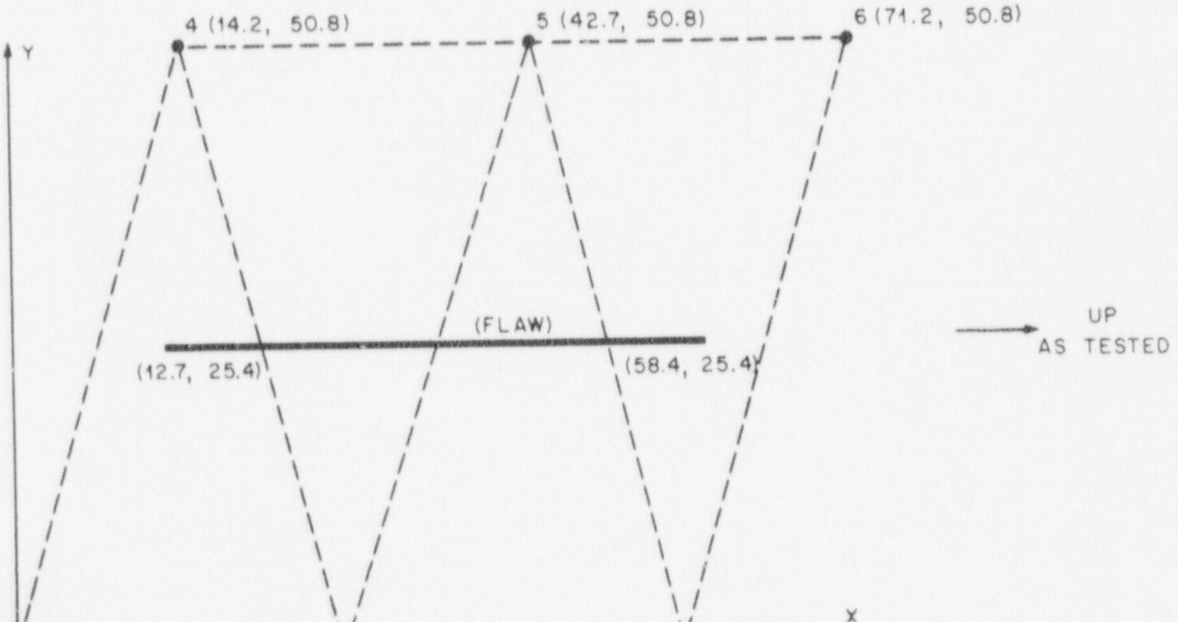

Fig. C.4. Transducer locations relative to flaw.

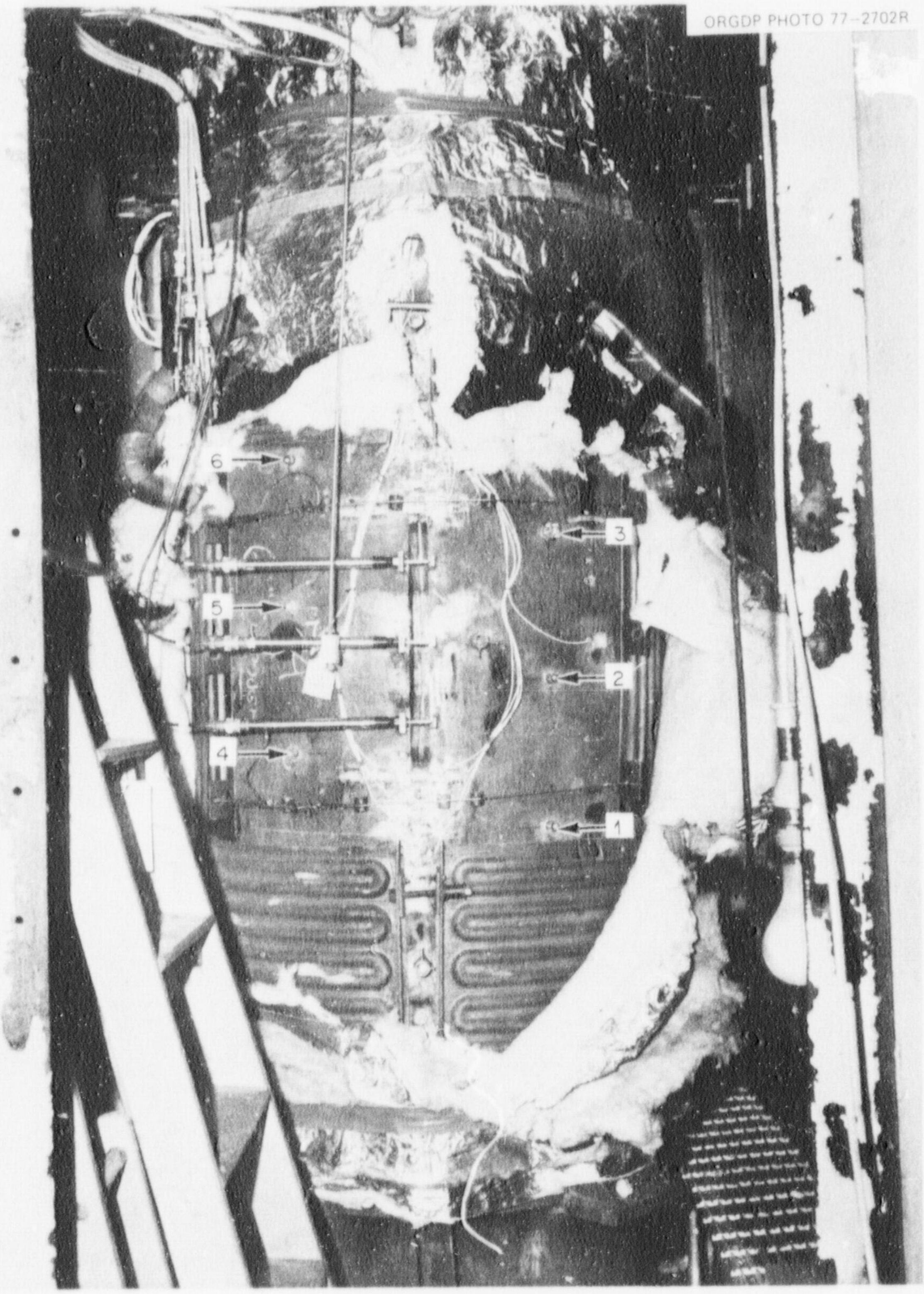

Fig. C.5. Transducer positioning on test vessel.

compound. MSCD system specifications during the test were as follows:

Transducers: 250 kHz resonant frequence, single-ended
Filters: 100–400 kHz
Preamplifier gain: 40 dB
Signal conditioner gain:*
    Channel 1 – 44 dB (84 dB total)
    Channel 2 – 47 dB (87 dB total)
    Channel 3 – 47 dB (87 dB total)
    Channel 4 – 55 dB(95 dB total)
    Channel 5 – 43 dB (83 dB total)
    Channel 6 – 44 dB (84 dB total)
    Channel 7 – 43 dB (83 dB total)
    Channel 8 – 56 dB (96 dB total)
Arrival time resolution: 1 μsec
Sensor activity constant: 1 msec
Threshold: 400 mV
ΔT range selector: 200 μsec
Wave propagation velocity:† 250,000 cm/sec

Pressure was monitored throughout the test using a parametric input to the MSCD from a pressure transducer.

Vessel temperature during the test was maintained at approximately 87°C. Testing of vessel V-7B was done hydraulically in two pressurization cycles as shown in Fig. C.6. The first cycle was to 72.4 MPa, and the second was to failure at 152 MPa. Acoustic emission data were obtained during both cycles.

Test Results

Cycle 1: Pressurization to 72.4 MPa

The initial loading cycle consisted of pressurization to 72.4 MPa with intermediate pressure holds at 27.6 and 55.3 MPa for instrument scans. Acoustic emission data were obtained throughout the cycle, and a total of 448 valid events were detected. Figure C.7 presents a histogram of event occurrence for each 3.4-MPa loading interval, and Fig. C.8 summarizes occurrence and COD gage output as a function of pressure. Figure C.9 presents a summation of event magnitude voltages as a function of elapsed time‡ and pressure. A two-dimensional grid displaying sensor and flaw locations and events and event magnitudes at conclusion of the initial pressurization cycle are presented in Fig. C.10. The 20.3-cm base of the flawed region is noted as a solid line, and the flawed region extending from the base to the vessel outer surface is noted by the dashed line. Each square of the grid where events have been noted contains two numbers: the upper number corresponds to the total number of accepted events and the lower number to the summation of the voltage magnitudes for the events. Regions with the most intense activity have been highlighted in the figure by shading (dots). It can be noted that all but one of these regions were adjacent to the flaw and

---

*Signal conditioner gain was established by balancing channels for equivalent background noise intensity.

†Established using software program.

‡Elapsed time corresponds to elapsed time as recorded by clock in the AE system.

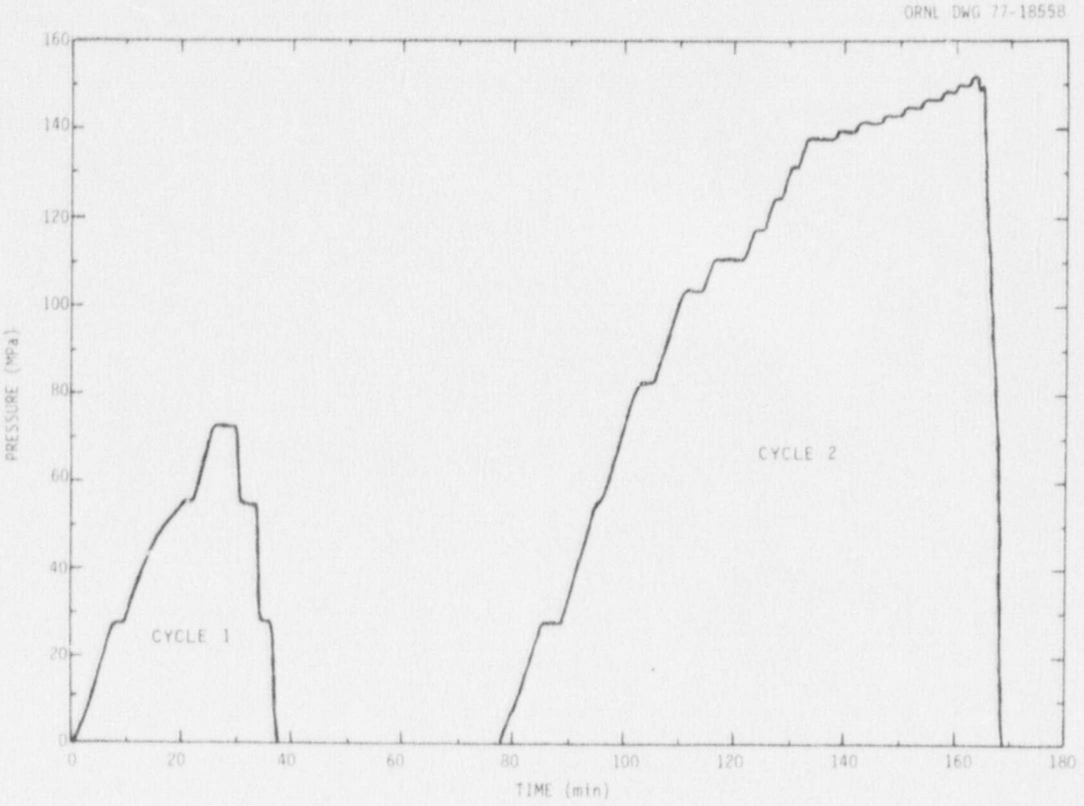

Fig. C.6. Vessel pressurization cycles.

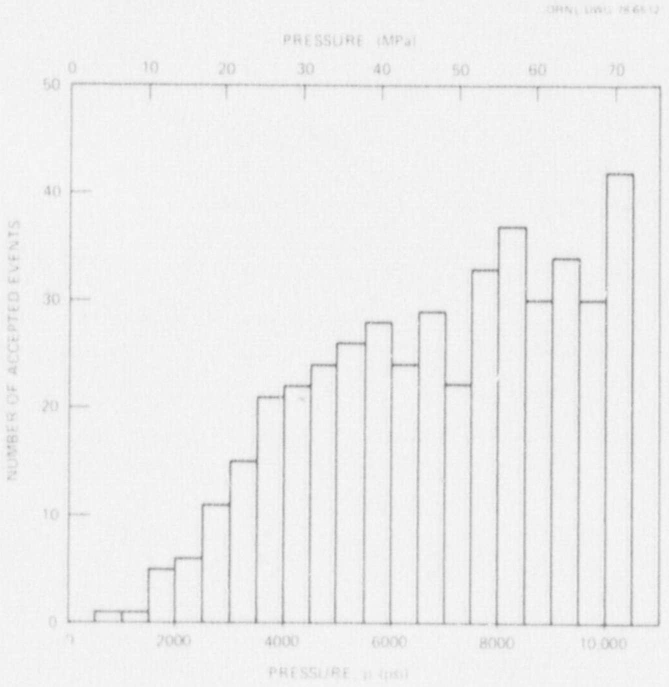

Fig. C.7. Event occurrence histogram: cycle 1.

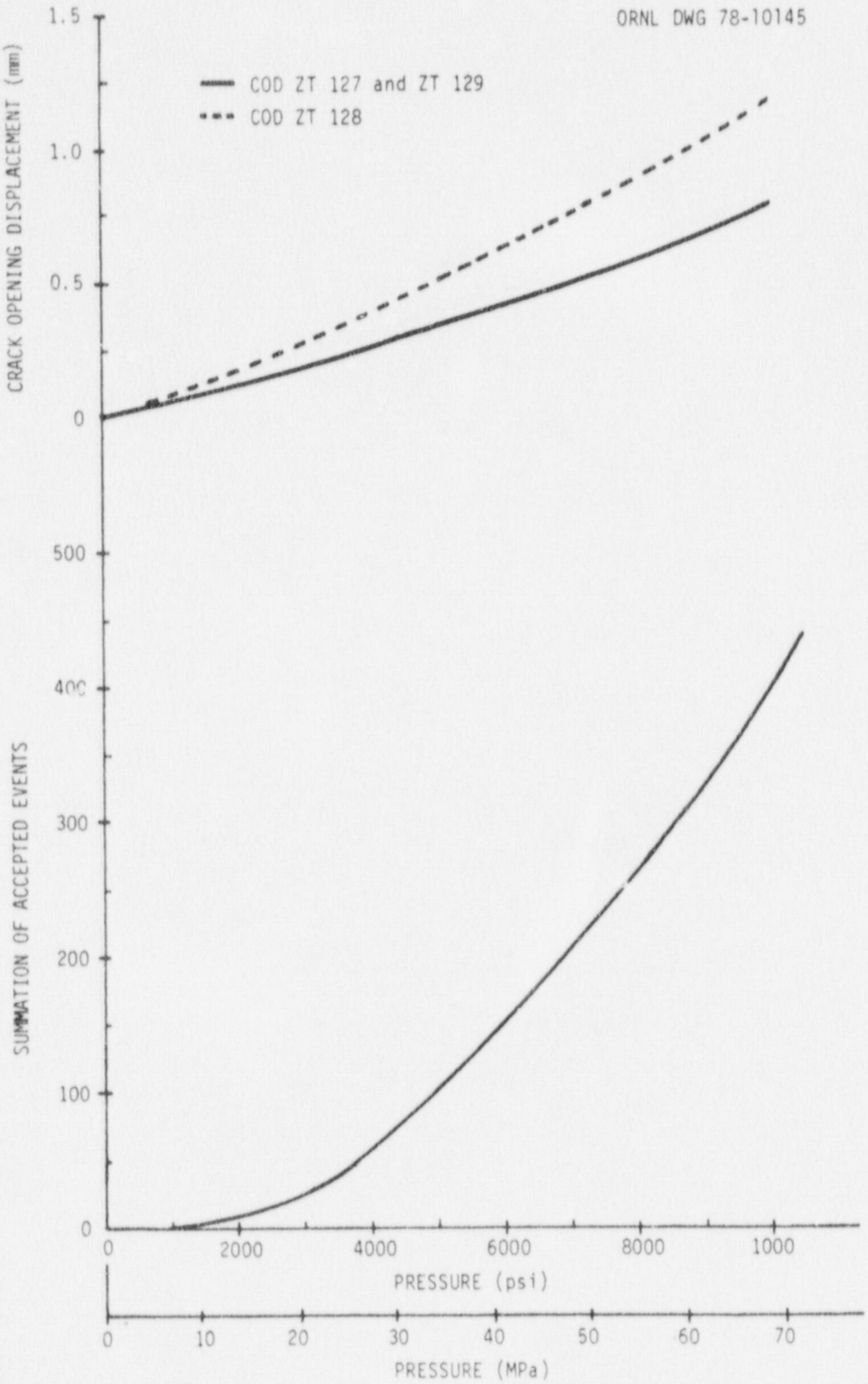

Fig. C.8. COD and summation of events vs pressure: cycle 1.

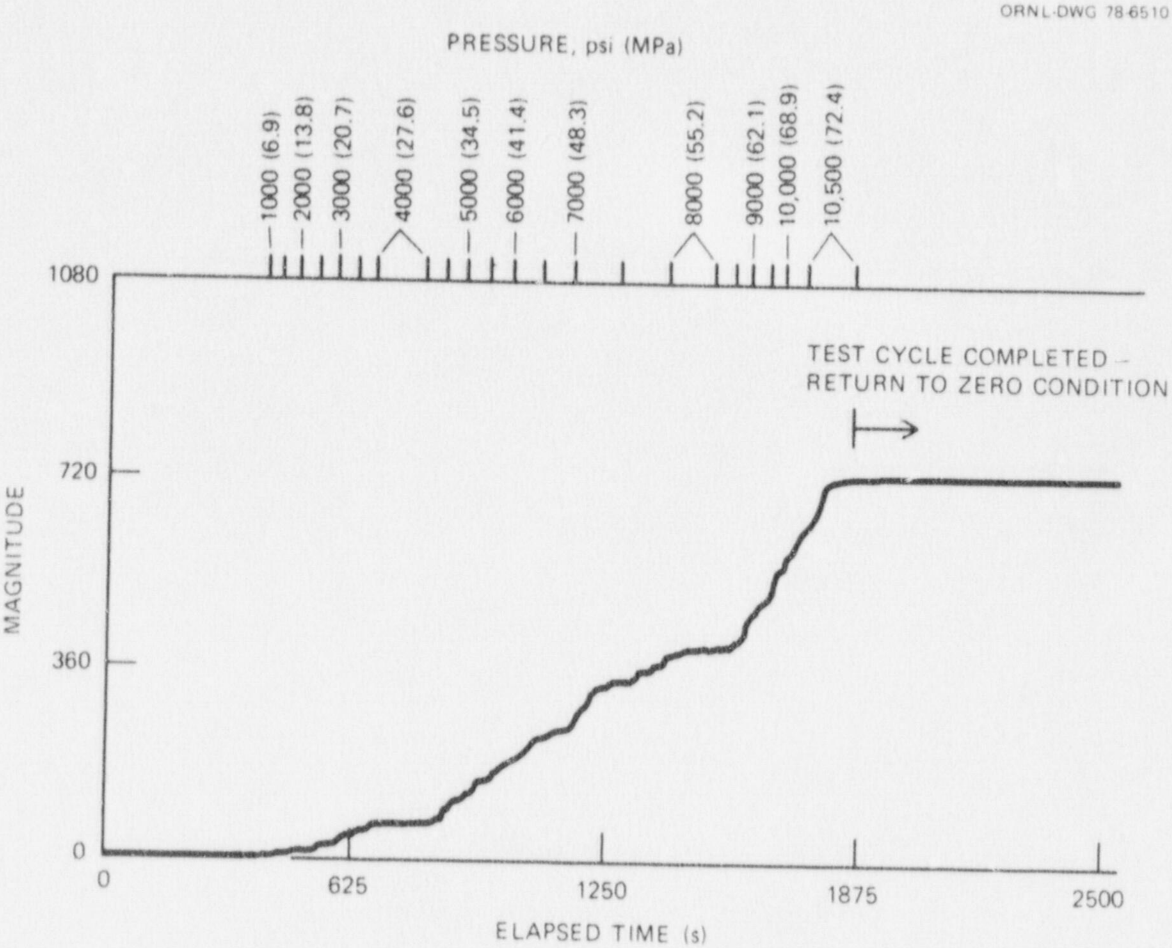

Fig. C.9. Event magnitude vs elapsed time and pressure: cycle 1.

there appeared to be more activity for the upper part of the flaw than for the lower. The one region not adjacent to the flaw, showing intense activity, corresponds to the position where the stainless steel patch was fillet welded to the inner surface of the vessel, and this activity may be associated with a weld defect.

Cycle 2: Pressurization to Failure

During the second pressurization cycle, the vessel was loaded as shown in Fig. C.6 until a leak developed through the vessel wall at the flaw. The pressure was held constant for short intervals intermittently during the test while instrument scans were taken. For the first cycle, AE data were obtained throughout the loading cycle, and a total of 931 valid events were detected. Figure C.11 presents a histogram of event occurrence for each 3.4 MPa of load. Crack-opening displacements and summation of accepted events as a function of pressure are presented in Fig. C.12. It can be noted that the curves are of the same general shape in that both the displacements and number of events increase rapidly as failure is approached. Figure C.13 presents a summation of event magnitude voltages as a function of elapsed time* and pressure.

---

*As recorded by clock in the AE system.

ORNL DWG 78 10169

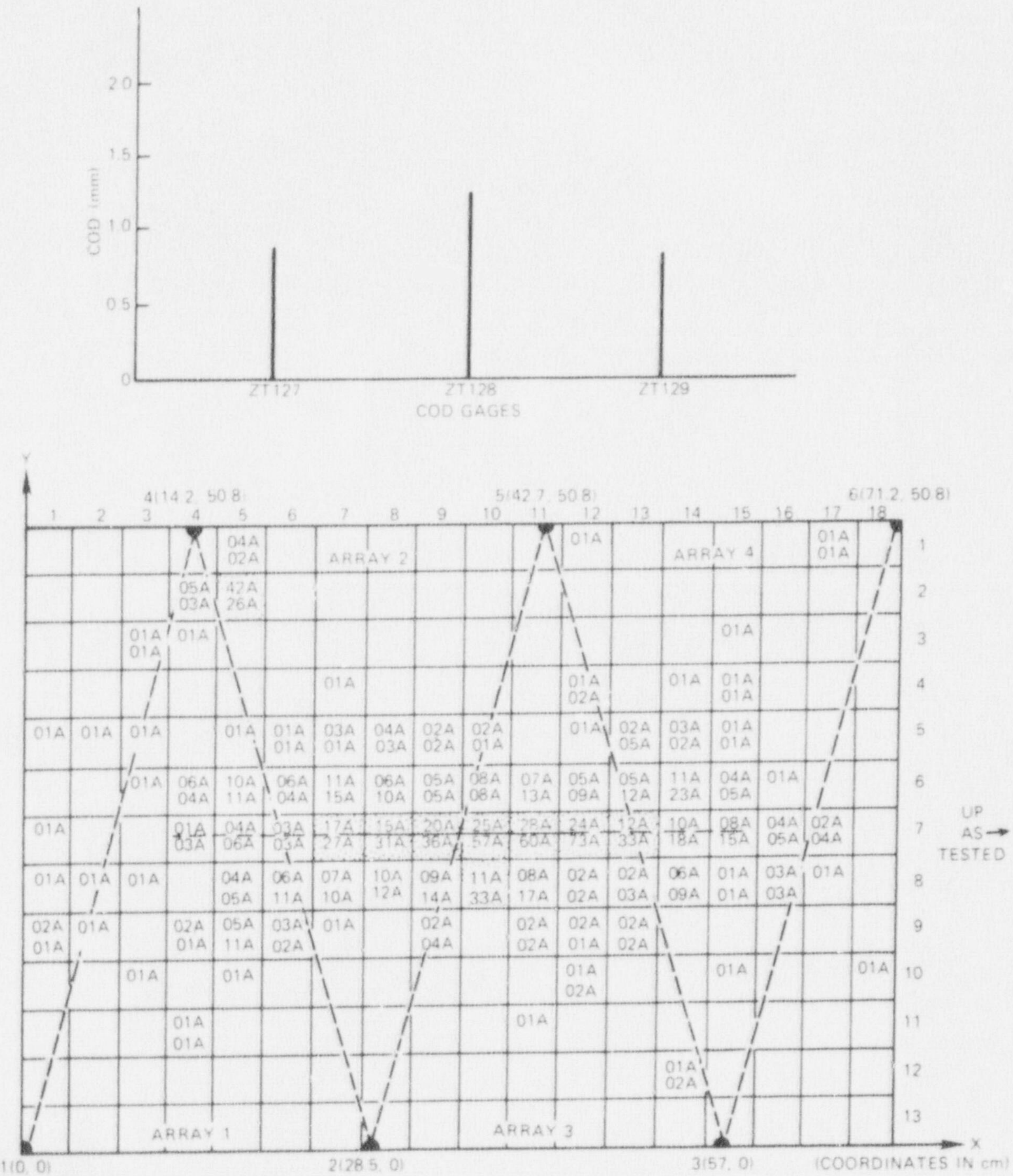

	1	2	3	4	5	6	7	8	9	10	11	12	13	14	15	16	17	18
1					04A 02A							01A					01A 01A	
2				05A 03A	42A 26A													
3			01A 01A	01A											01A			
4							01A					01A 02A		01A	01A 01A			
5	01A	01A	01A		01A	01A 01A	03A 01A	04A 03A	02A 02A	02A 01A		01A	02A 05A	03A 02A	01A 01A			
6			01A	06A 04A	10A 11A	06A 04A	11A 15A	06A 10A	05A 05A	08A 08A	07A 13A	05A 09A	05A 12A	11A 23A	04A 05A	01A		
7	01A			01A 03A	04A 06A	03A 03A	17A 27A	15A 31A	20A 36A	25A 57A	28A 60A	24A 73A	12A 33A	10A 18A	08A 15A	04A 05A	02A 04A	
8	01A	01A	01A		04A 05A	06A 11A	07A 10A	10A 12A	09A 14A	11A 33A	08A 17A	02A 02A	02A 03A	06A 09A	01A 01A	03A 03A	01A	
9	02A 01A	01A		02A 01A	05A 11A	03A 02A	01A		02A 04A		02A 02A	02A 01A	02A 02A					
10			01A		01A							01A 02A			01A			01A
11				01A 01A							01A							
12														01A 02A				
13																		

Fig. C.10. Grid display initial pressurization cycle, 448 events.

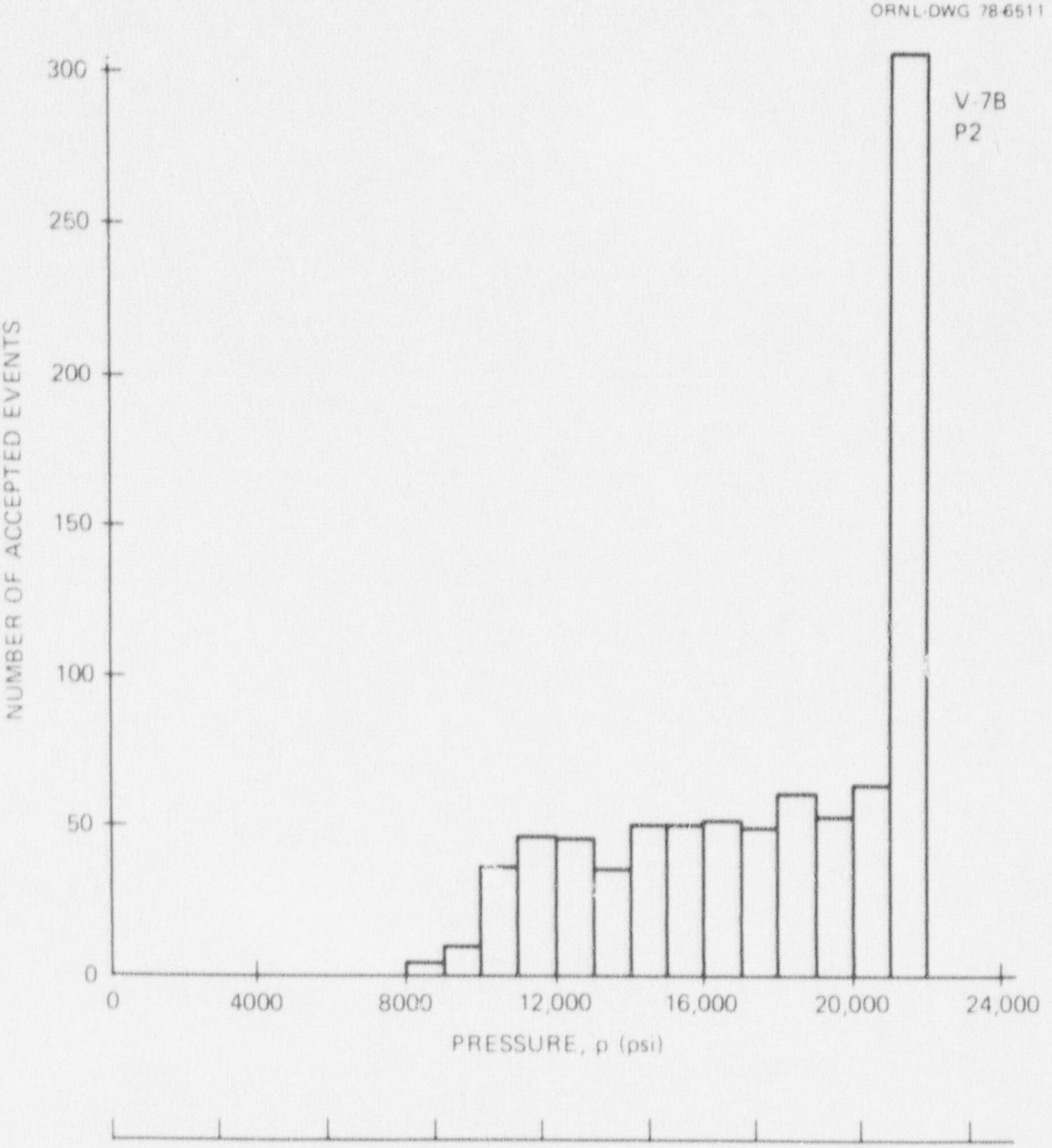

Fig. C.11. Event occurrence histogram: cycle 2.

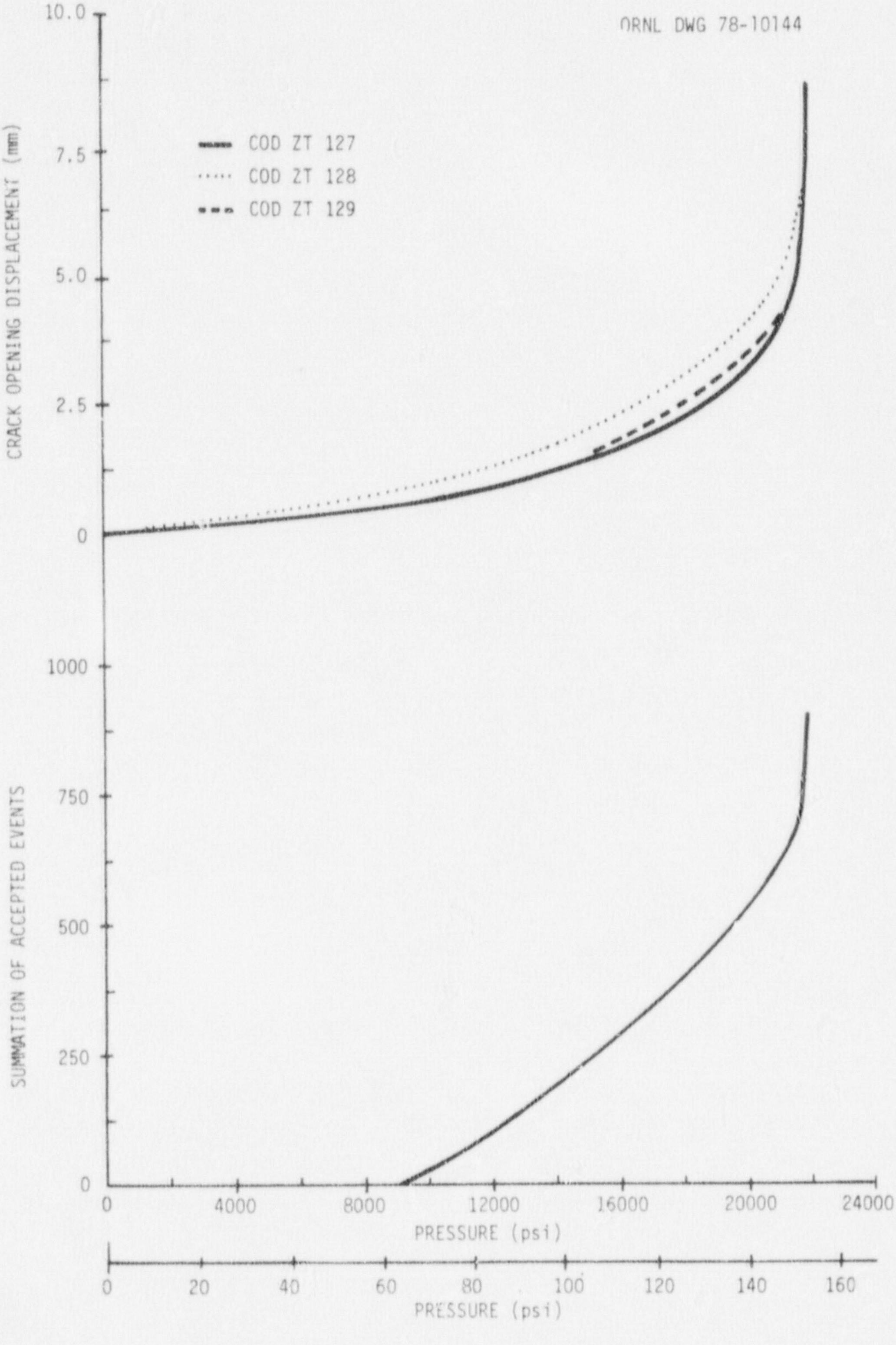

Fig. C.12. COD and summation of events vs pressure: cycle 2.

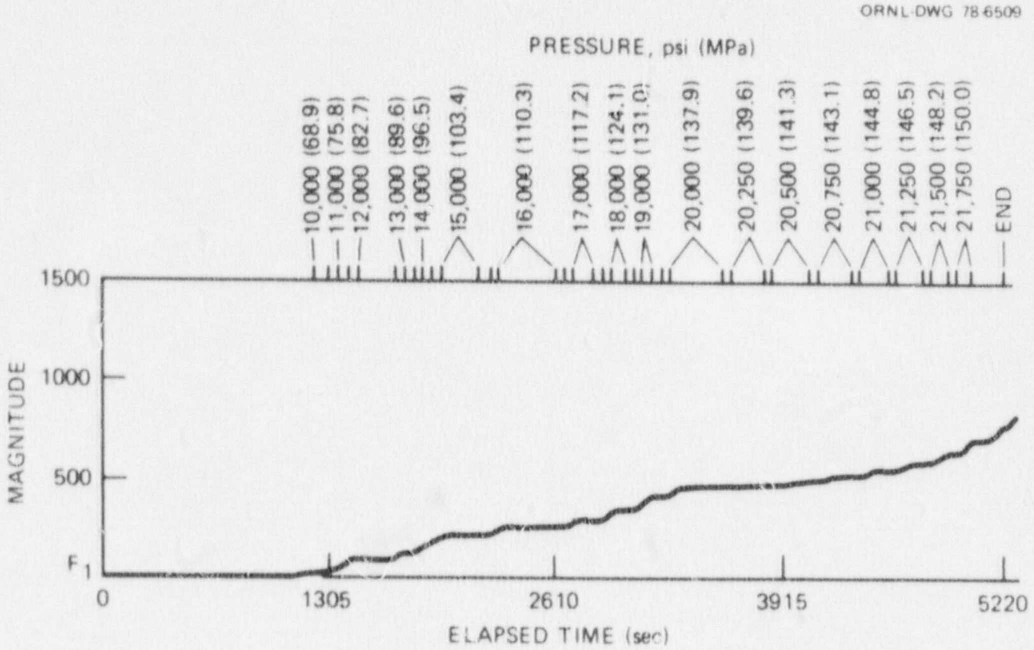

Fig. C.13. Event magnitude vs elapsed time and pressure: cycle 2.

Two-dimensional grid displays were obtained for the second pressurization cycle both during and after completion of the test. Figures C.14 to C.19 present displays of events and voltage magnitudes as a function of location for pressures corresponding to 124.1, 144.8, 146.5, 148.2, 150 MPa, and at the conclusion of the test, respectively. Notations in these figures are the same as for Fig. C.10. Significant event occurrence by location* as a function of pressure interval is presented in Fig. C.20. As noted in the figures, regions of primary activity were adjacent to the flaw.

Conclusions

The following conclusions may be drawn from AE monitoring of HSST vessel V-7B.

1. Primary AE activity was adjacent to the flaw. Some activity was noted at a location corresponding approximately to the region where the stainless steel patch was fillet welded to the inner surface of the vessel. Data scatter may be attributable to both specimen geometry and the relatively close proximity of the transducers. (Spacing of transducers was less than five times the vessel thickness.^{2})

2. Plots of COD gages and summation of events as a function of pressure were geometrically similar.

3. At impending failure, the slope of the summation of events as a function of pressure changed drastically. This provides a possible technique for monitoring the vessel so that pressurization may be halted prior to failure. Also, as failure was approached, the magnitude of the emissions increased.

4. Results of this test tend to indicate that AE was able to identify regions where significant activity was occurring.

---

*Significant event occurrence by location is defined to be a grid square in the figure where at least four events or an event with a magnitude greater than 3.0 V has occurred during the pressure interval defined.

ORNL DWG 78 10170

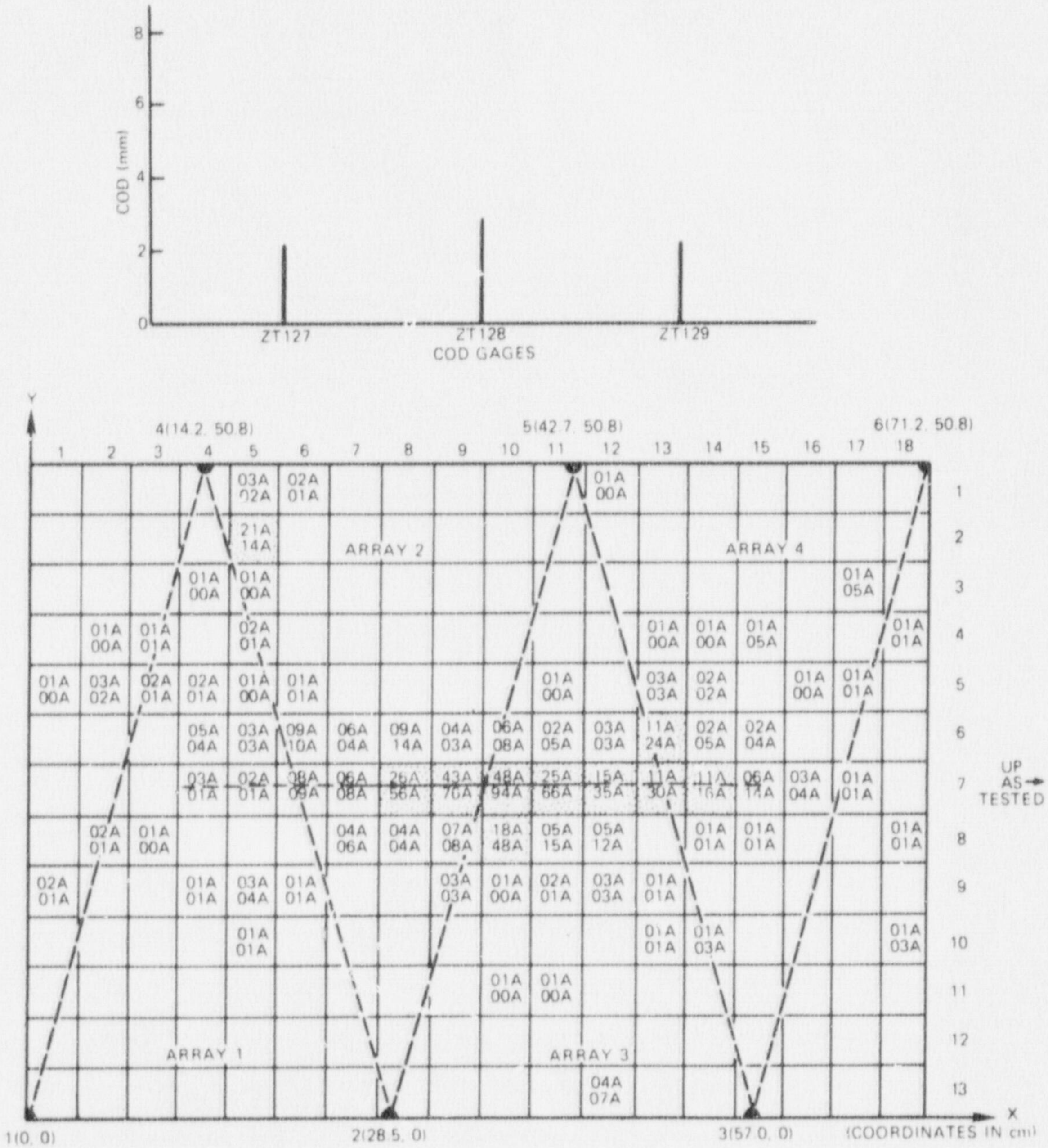

	1	2	3	4	5	6	7	8	9	10	11	12	13	14	15	16	17	18
1					03A 02A	02A 01A						01A 00A						
2					21A 14A													
3				01A 00A	01A 00A												01A 05A	
4		01A 00A	01A 01A		02A 01A								01A 00A	01A 00A	01A 05A			01A 01A
5	01A 00A	03A 02A	02A 01A	02A 01A	01A 00A	01A 01A					01A 00A		03A 03A	02A 02A		01A 00A	01A 01A	
6				05A 04A	03A 03A	09A 10A	06A 04A	09A 14A	04A 03A	06A 08A	02A 05A	03A 03A	11A 24A	02A 05A	02A 04A			
7				03A 01A	02A 01A	08A 09A	06A 08A	26A 56A	43A 76A	48A 94A	25A 66A	15A 35A	11A 30A	11A 16A	06A 14A	03A 04A	01A 01A	
8		02A 01A	01A 00A				04A 06A	04A 04A	07A 08A	18A 48A	05A 15A	05A 12A		01A 01A	01A 01A			01A 01A
9	02A 01A			01A 01A	03A 04A	01A 01A			03A 03A	01A 00A	02A 01A	03A 03A	01A 01A					
10					01A 01A								01A 01A	01A 03A				01A 03A
11										01A 00A	01A 00A							
12																		
13												04A 07A						

Fig. C.14. Grid display pressure cycle 2: P = 124.1 MPa, 402 events.

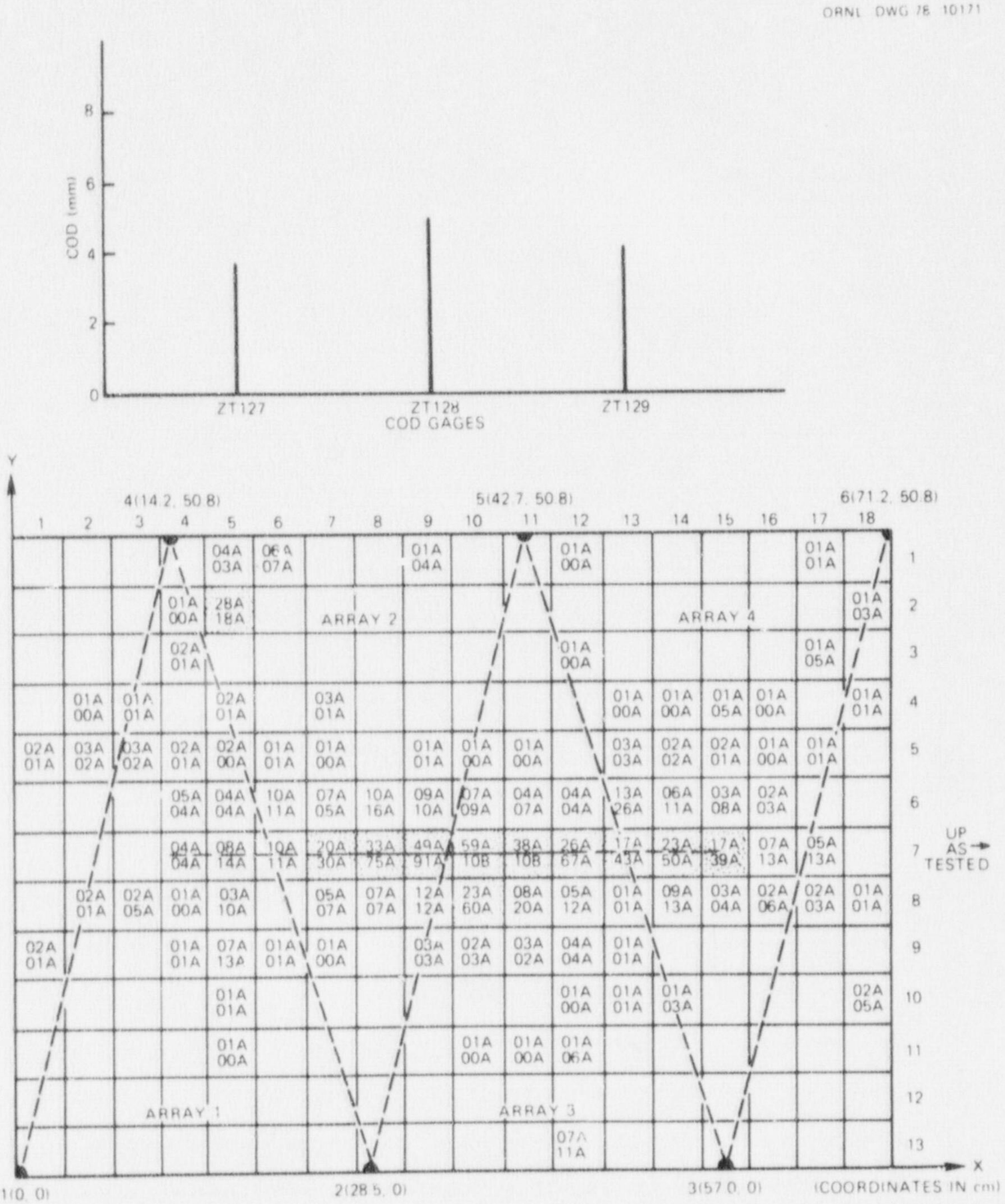

	1	2	3	4	5	6	7	8	9	10	11	12	13	14	15	16	17	18
1					04A 03A	06A 07A			01A 04A			01A 00A					01A 01A	
2				01A 00A	28A 18A													01A 03A
3				02A 01A								01A 00A					01A 05A	
4		01A 00A	01A 01A		02A 01A		03A 01A						01A 00A	01A 00A	01A 05A	01A 00A		01A 01A
5	02A 01A	03A 02A	03A 02A	02A 01A	02A 00A	01A 01A	01A 00A		01A 01A	01A 00A	01A 00A		03A 03A	02A 02A	02A 01A	01A 00A	01A 01A	
6				05A 04A	04A 04A	10A 11A	07A 05A	10A 16A	09A 10A	07A 09A	04A 07A	04A 04A	13A 26A	06A 11A	03A 08A	02A 03A		
7				04A 04A	08A 14A	10A 11A	20A 30A	33A 75A	49A 91A	59A 10B	38A 10B	26A 67A	17A 43A	23A 50A	17A 39A	07A 13A	05A 13A	
8		02A 01A	02A 05A	01A 00A	03A 10A		05A 07A	07A 07A	12A 12A	23A 60A	08A 20A	05A 12A	01A 01A	09A 13A	03A 04A	02A 06A	02A 03A	01A 01A
9	02A 01A			01A 01A	07A 13A	01A 01A	01A 00A		03A 03A	02A 03A	03A 02A	04A 04A	01A 01A					
10					01A 01A							01A 00A	01A 01A	01A 03A				02A 05A
11					01A 00A					01A 00A	01A 00A	01A 06A						
12																		
13												07A 11A						

Fig. C.15. Grid display pressure cycle 2: P = 144.8 MPa, 614 events.

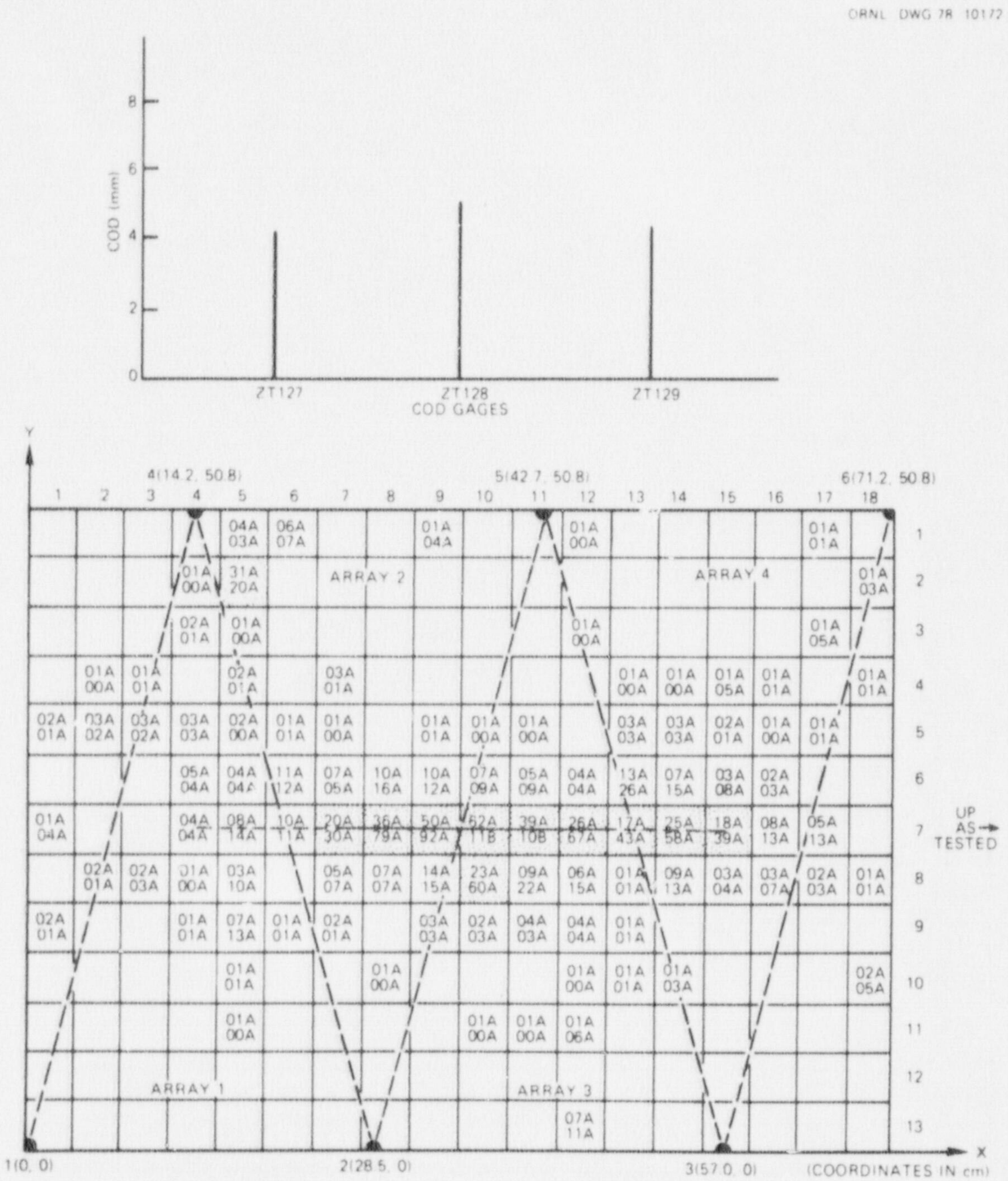

	1	2	3	4	5	6	7	8	9	10	11	12	13	14	15	16	17	18
1					04A 03A	06A 07A			01A 04A			01A 00A					01A 01A	
2				01A 00A	31A 20A													01A 03A
3				02A 01A	01A 00A							01A 00A					01A 05A	
4		01A 00A	01A 01A		02A 01A		03A 01A						01A 00A	01A 00A	01A 05A	01A 01A		01A 01A
5	02A 01A	03A 02A	03A 02A	03A 03A	02A 00A	01A 01A	01A 00A		01A 01A	01A 00A	01A 00A		03A 03A	03A 03A	02A 01A	01A 00A	01A 01A	
6				05A 04A	04A 04A	11A 12A	07A 05A	10A 16A	10A 12A	07A 09A	05A 09A	04A 04A	13A 26A	07A 15A	03A 08A	02A 03A		
7	01A 04A			04A 04A	08A 14A	10A 11A	20A 30A	36A 79A	50A 92A	62A 11B	39A 10B	26A 67A	17A 43A	25A 58A	18A 39A	08A 13A	05A 13A	
8		02A 01A	02A 03A	01A 00A	03A 10A		05A 07A	07A 07A	14A 15A	23A 60A	09A 22A	06A 15A	01A 01A	09A 13A	03A 04A	03A 07A	02A 03A	01A 01A
9	02A 01A			01A 01A	07A 13A	01A 01A	02A 01A		03A 03A	02A 03A	04A 03A	04A 04A	01A 01A					
10					01A 01A			01A 00A				01A 00A	01A 01A	01A 03A				02A 05A
11					01A 00A					01A 00A	01A 00A	01A 06A						
12																		
13												07A 11A						

Fig. C.16. Grid display pressure cycle 2: P = 146.5 MPa, 644 events.

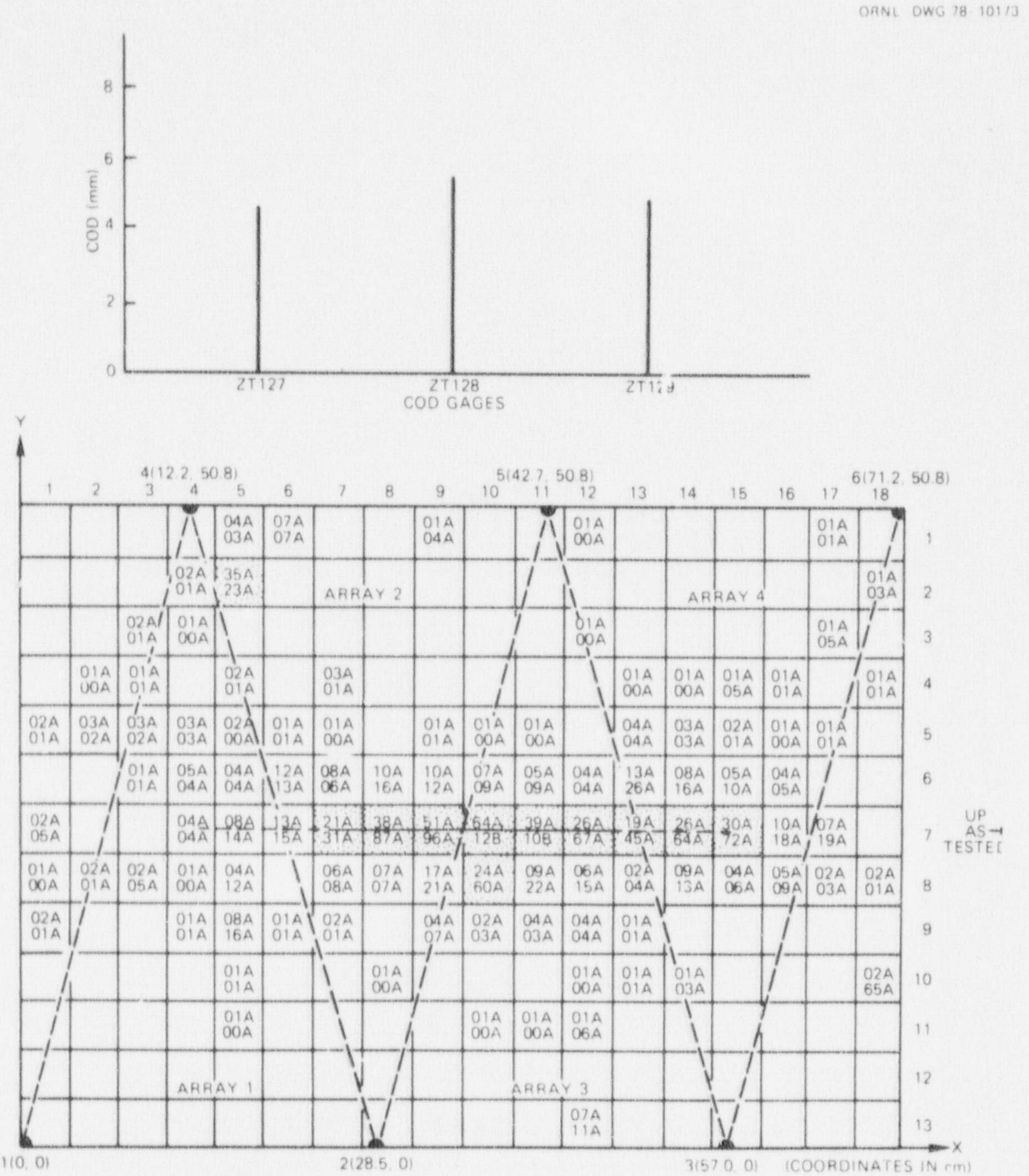

1	2	3	4	5	6	7	8	9	10	11	12	13	14	15	16	17	18	
				04A 03A	07A 07A			01A 04A			01A 00A					01A 01A		1
			02A 01A	35A 23A													01A 03A	2
		02A 01A	01A 00A								01A 00A					01A 05A		3
	01A 00A	01A 01A		02A 01A		03A 01A						01A 00A	01A 00A	01A 05A	01A 01A		01A 01A	4
02A 01A	03A 02A	03A 02A	03A 03A	02A 00A	01A 01A	01A 00A		01A 01A	01A 00A	01A 00A		04A 04A	03A 03A	02A 01A	01A 00A	01A 01A		5
		01A 01A	05A 04A	04A 04A	12A 13A	08A 06A	10A 16A	10A 12A	07A 09A	05A 09A	04A 04A	13A 26A	08A 16A	05A 10A	04A 05A			6
02A 05A			04A 04A	08A 14A	13A 15A	21A 31A	38A 87A	51A 96A	64A 12B	39A 10B	26A 67A	19A 45A	26A 64A	30A 72A	10A 18A	07A 19A		7
01A 00A	02A 01A	02A 05A	01A 00A	04A 12A		06A 08A	07A 07A	17A 21A	24A 60A	09A 22A	06A 15A	02A 04A	09A 13A	04A 06A	05A 09A	02A 03A	02A 01A	8
02A 01A			01A 01A	08A 16A	01A 01A	02A 01A		04A 07A	02A 03A	04A 03A	04A 04A	01A 01A						9
				01A 01A			01A 00A				01A 00A	01A 01A	01A 03A				02A 65A	10
				01A 00A					01A 00A	01A 00A	01A 06A							11
																		12
											07A 11A							13

Fig. C.17. Grid display pressure cycle 2: P = 148.2 MPa, 702 events.

ORNL DWG 78-10174

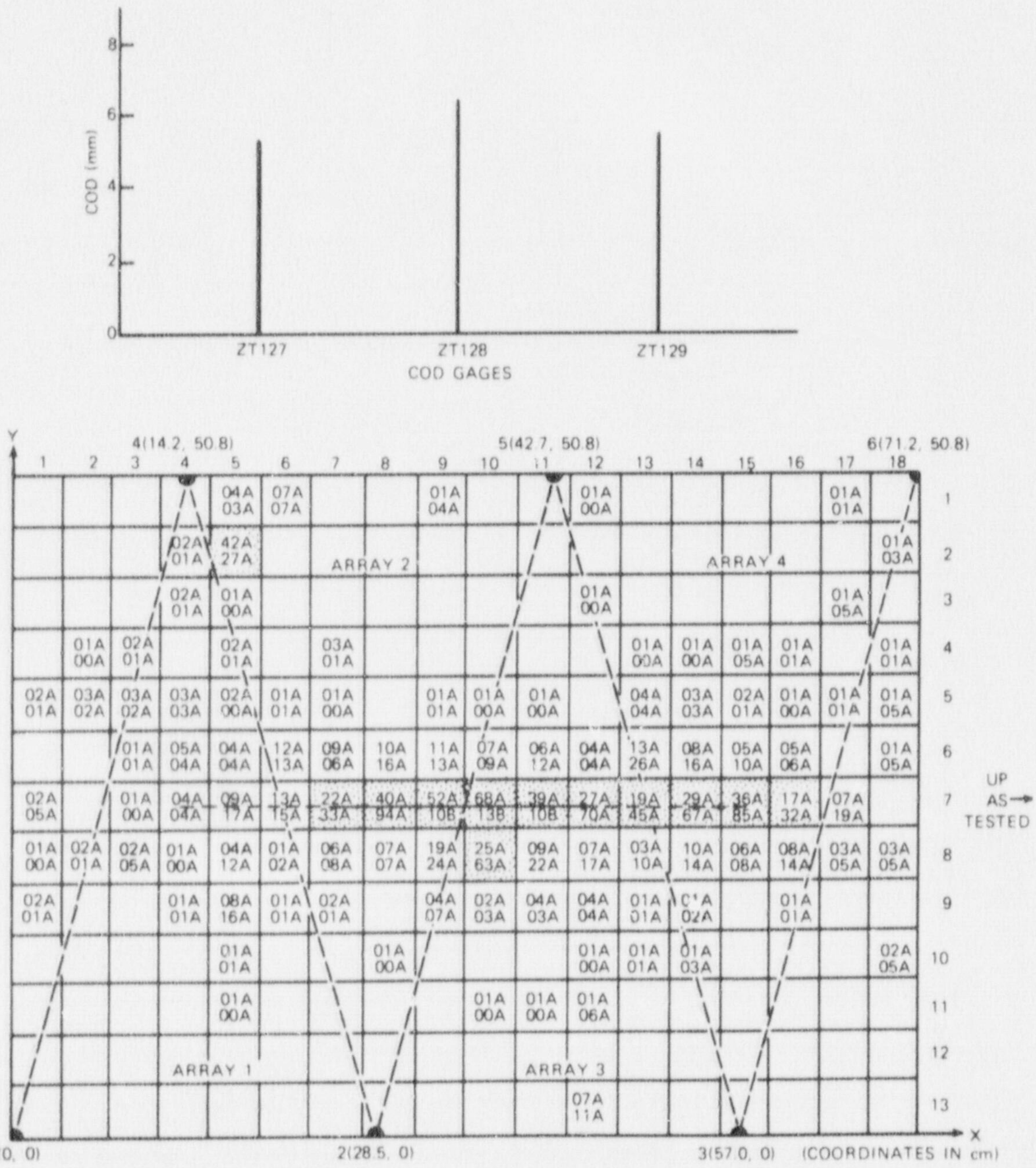

	1	2	3	4	5	6	7	8	9	10	11	12	13	14	15	16	17	18
1					04A 03A	07A 07A			01A 04A			01A 00A					01A 01A	
2				02A 01A	42A 27A													01A 03A
3				02A 01A	01A 00A							01A 00A					01A 05A	
4		01A 00A	02A 01A		02A 01A		03A 01A						01A 00A	01A 00A	01A 05A	01A 01A		01A 01A
5	02A 01A	03A 02A	03A 02A	03A 03A	02A 00A	01A 01A	01A 00A		01A 01A	01A 00A	01A 00A		04A 04A	03A 03A	02A 01A	01A 00A	01A 01A	01A 05A
6			01A 01A	05A 04A	04A 04A	12A 13A	09A 06A	10A 16A	11A 13A	07A 09A	06A 12A	04A 04A	13A 26A	08A 16A	05A 10A	05A 06A		01A 05A
7	02A 05A		01A 00A	04A 04A	09A 17A	13A 15A	22A 33A	40A 94A	52A 10B	68A 13B	39A 10B	27A 70A	19A 45A	29A 67A	36A 85A	17A 32A	07A 19A	
8	01A 00A	02A 01A	02A 05A	01A 00A	04A 12A	01A 02A	06A 08A	07A 07A	19A 24A	25A 63A	09A 22A	07A 17A	03A 10A	10A 14A	06A 08A	08A 14A	03A 05A	03A 05A
9	02A 01A			01A 01A	08A 16A	01A 01A	02A 01A		04A 07A	02A 03A	04A 03A	04A 04A	01A 01A	01A 02A		01A 01A		
10					01A 01A			01A 00A				01A 00A	01A 01A	01A 03A				02A 05A
11					01A 00A					01A 00A	01A 00A	01A 06A						
12																		
13												07A 11A						

Fig. C.18. Grid display pressure cycle 2: P = 150.0 MPa, 759 events.

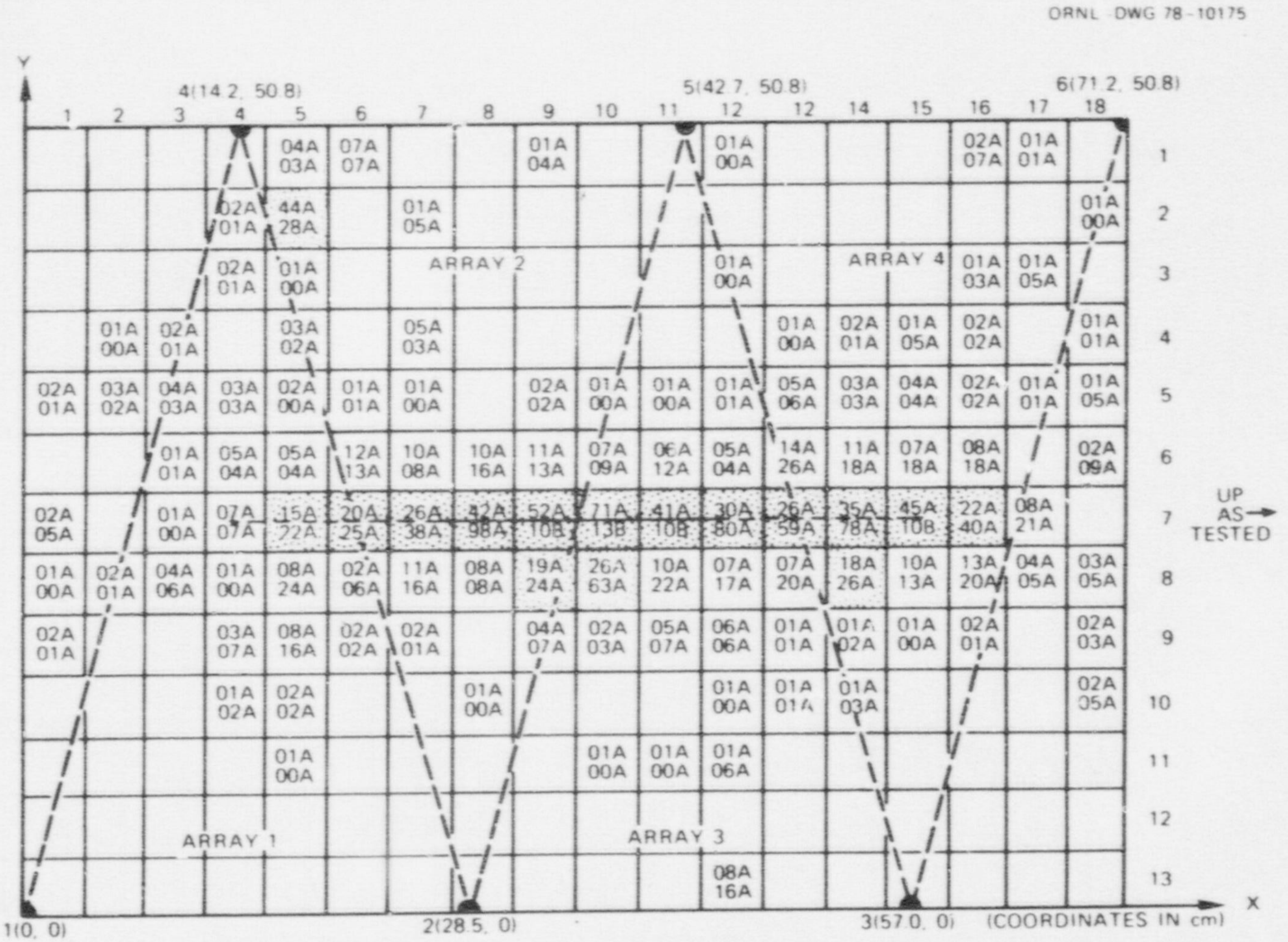

	1	2	3	4	5	6	7	8	9	10	11	12	12	14	15	16	17	18
1					04A 03A	07A 07A			01A 04A			01A 00A				02A 07A	01A 01A	
2				02A 01A	44A 28A		01A 05A											01A 00A
3				02A 01A	01A 00A							01A 00A				01A 03A	01A 05A	
4		01A 00A	02A 01A		03A 02A		05A 03A						01A 00A	02A 01A	01A 05A	02A 02A		01A 01A
5	02A 01A	03A 02A	04A 03A	03A 03A	02A 00A	01A 01A	01A 00A		02A 02A	01A 00A	01A 00A	01A 01A	05A 06A	03A 03A	04A 04A	02A 02A	01A 01A	01A 05A
6			01A 01A	05A 04A	05A 04A	12A 13A	10A 08A	10A 16A	11A 13A	07A 09A	06A 12A	05A 04A	14A 26A	11A 18A	07A 18A	08A 18A		02A 09A
7	02A 05A		01A 00A	07A 07A	15A 22A	20A 25A	26A 38A	42A 98A	52A 10B	71A 13B	41A 10B	30A 80A	26A 59A	35A 78A	45A 10B	22A 40A	08A 21A	
8	01A 00A	02A 01A	04A 06A	01A 00A	08A 24A	02A 06A	11A 16A	08A 08A	19A 24A	26A 63A	10A 22A	07A 17A	07A 20A	18A 26A	10A 13A	13A 20A	04A 05A	03A 05A
9	02A 01A			03A 07A	08A 16A	02A 02A	02A 01A		04A 07A	02A 03A	05A 07A	06A 06A	01A 01A	01A 02A	01A 00A	02A 01A		02A 03A
10				01A 02A	02A 02A			01A 00A				01A 00A	01A 01A	01A 03A				02A 05A
11					01A 00A					01A 00A	01A 00A	01A 06A						
12																		
13												08A 16A						

Fig. C.19. Grid display pressure cycle 2: test conclusion· 931 events.

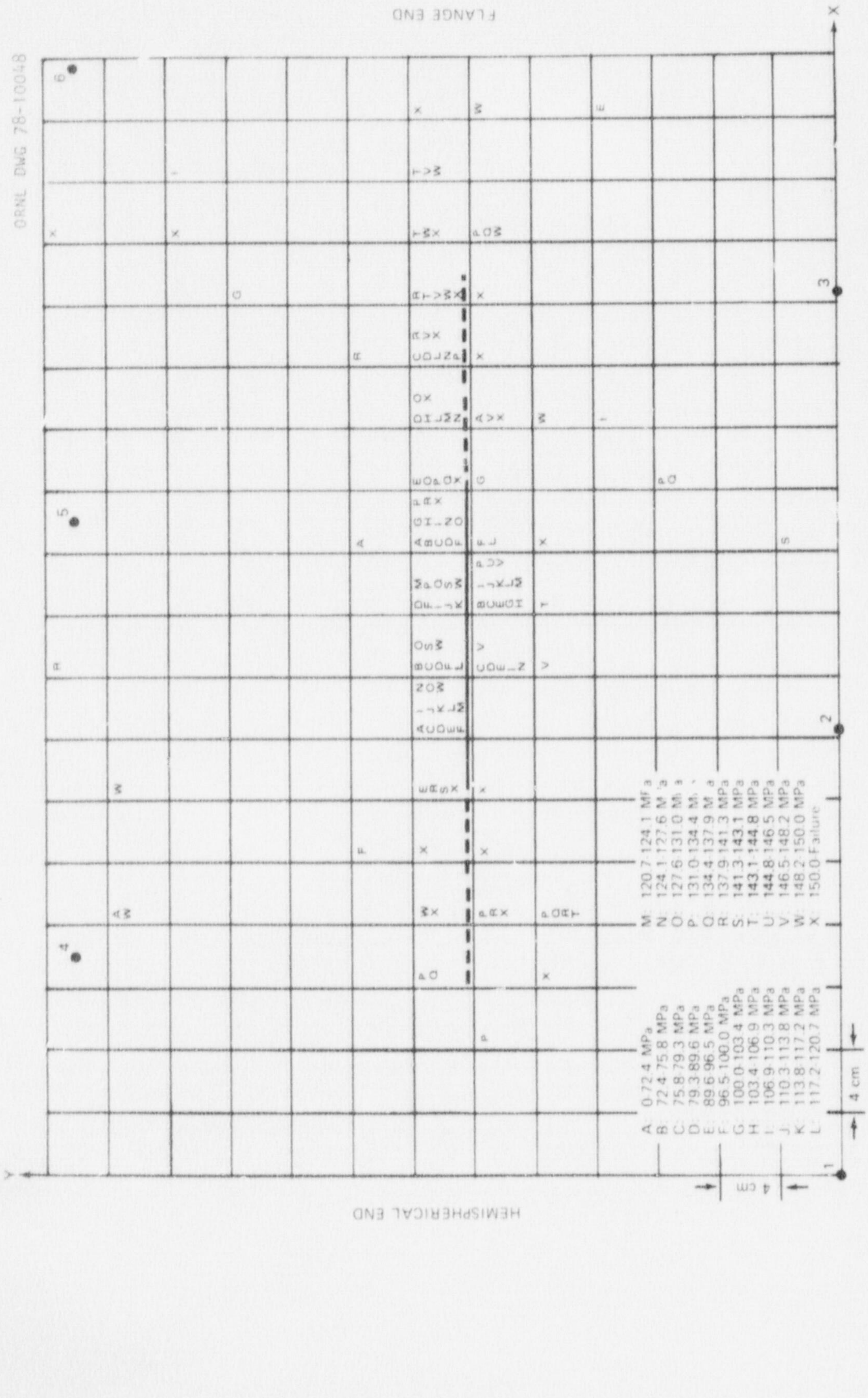

Fig. C.20. Significant event occurrence as a function of loading interval.

References

1. R. L. Bell, *A Progress Report on the Use of Acoustic Emission to Detect Incipient Failure in Nuclear Pressure Vessels*, DE-74-1 Dunegan/Endevco (January 1974).

2. M. P. Kelley and R. J. Schlamp, *Acoustic Emission Monitoring of HSST Intermediate Test Vessel V-7A*, Dunegan/Endevco (July 1976).

Conversion factors[a]

SI unit	English unit	Factor
mm	in.	0.0393701
cm	in.	0.393701
m	ft	3.28084
MPa	ksi	0.145038
$MN \cdot m^{-3/2}$	$ksi\sqrt{in.}$	0.910048
J	ft-lb	0.737562
K	°F or °R	1.8
kJ/m^2	$in.-lb/in.^2$	5.71015
m^3	gal	264.17
$m^3 \cdot s^{-1}$	gph	15850
kPa	ft (H_2O)	0.33456
W	Btu/hr	3.4121
kW	hp	1.3405
T	G	10^4
T(°F) = 1.8 T(°C) + 32		

[a] Multiply SI quantity by given factor to obtain English quantity.

NUREG/CR-0309
ORNL/NUREG-38
Dist. Category R5

Internal Distribution

1. R. G. Berggren
2. S. E. Bolt
3. R. H. Bryan
4. J. P. Callahan
5. D. A. Canonico
6. R. D. Cheverton
7. J. M. Corum
8. W. B. Cottrell
9. M. H. Fontana
10. W. L. Greenstreet
11. R. C. Gwaltney
12. R. F. Hibbs
13. P. P. Holz
14. H. W. Hoffman
15. S. K. Iskander
16. K. K. Klindt
17. Milton Levenson
18. R. E. MacPherson
19. J. R. McGuffey
20. J. G. Merkle
21. C. A. Mills
22. S. E. Moore
23. F. R. Mynatt
24. H. A. Pohto (Y-12)
25. H. Postma
26. G. C. Robinson
27. C. D. St. Onge (Y-12)
28. Myrtleen Sheldon
29. G. M. Slaughter
30. J. E. Smith
31. I. Spiewak
32. W. J. Stelzman
33. D. G. Thomas
34. D. B. Trauger
35. H. E. Trammell
36. J. R. Weir, Jr.

37–39. G. D. Whitman

40. Patent Office

41–42. Central Research Library

43. Document Reference Section

44–47. Laboratory Records

48. Laboratory Records, RC

External Distribution

49. C. Z. Serpan, RSR, Nuclear Regulatory Commission, Washington, D.C. 20555
50. Director, Research and Technical Support Division, Department of Energy, Oak Ridge Operations Office

51–107. Special ORNL distribution (by NRC)

108–275. Special HSST distribution (by NRC)

276–570. Given distribution in category R5 (TIC-2, NTIS-25)